Lecture Notes in Civil Engineering

Guoqiang Zhang
N. D. Kaushika
S. C. Kaushik
R. K. Tomar *Editors*

Advances in Energy and Built Environment

Select Proceedings of TRACE 2018

Springer

Lecture Notes in Civil Engineering

Volume 36

Lecture Notes in Civil Engineering (LNCE) publishes the latest developments in Civil Engineering - quickly, informally and in top quality. Though original research reported in proceedings and post-proceedings represents the core of LNCE, edited volumes of exceptionally high quality and interest may also be considered for publication. Volumes published in LNCE embrace all aspects and subfields of, as well as new challenges in, Civil Engineering. Topics in the series include:

- Construction and Structural Mechanics
- Building Materials
- Concrete, Steel and Timber Structures
- Geotechnical Engineering
- Earthquake Engineering
- Coastal Engineering
- Hydraulics, Hydrology and Water Resources Engineering
- Environmental Engineering and Sustainability
- Structural Health and Monitoring
- Surveying and Geographical Information Systems
- Heating, Ventilation and Air Conditioning (HVAC)
- Transportation and Traffic
- Risk Analysis
- Safety and Security

To submit a proposal or request further information, please contact the appropriate Springer Editor:

– Mr. Pierpaolo Riva at pierpaolo.riva@springer.com (Europe and Americas);
– Ms. Swati Meherishi at swati.meherishi@springer.com (India);
– Ms. Li Shen at li.shen@springer.com (China);
– Dr. Loyola D'Silva at loyola.dsilva@springer.com (S-E Asia and Australia/NZ).

Indexed by Scopus

More information about this series at http://www.springer.com/series/15087

Guoqiang Zhang · N. D. Kaushika ·
S. C. Kaushik · R. K. Tomar
Editors

Advances in Energy and Built Environment

Select Proceedings of TRACE 2018

Springer

Editors
Guoqiang Zhang
Hunan University
Changsha, China

N. D. Kaushika
Siksha 'O' Anusandhan University
Bhubaneswar, India

S. C. Kaushik
Indian Institute of Technology Delhi
New Delhi, India

R. K. Tomar
Amity University
Noida, India

ISSN 2366-2557 ISSN 2366-2565 (electronic)
Lecture Notes in Civil Engineering
ISBN 978-981-13-7556-9 ISBN 978-981-13-7557-6 (eBook)
https://doi.org/10.1007/978-981-13-7557-6

This Springer imprint is published by the registered company Springer Nature Singapore Pte Ltd.
The registered company address is: 152 Beach Road, #21-01/04 Gateway East, Singapore 189721, Singapore

Preface

The present global objective in civil engineering is to meet the ever-growing demand to handle rising population, various energy and environmental concerns and safety of structures and inhabitants. The Second International Conference on "Trends and Recent Advancement in Civil Engineering" (TRACE) was hosted by the Department of Civil Engineering on 23rd and 24th August 2018 at Amity University, Noida, Uttar Pradesh, India.

TRACE 2018 focused on advances and rapid evolution of various areas in civil engineering. The conference witnessed participation and presentation of research papers (topical reviews and original articles) from academia, industry experts and researchers from R&D centres from India and abroad. The conference proceedings were classified into five titles:

- Advances in Energy and Built Environment
- Advances in Transportation Engineering
- Advances in Structural Engineering and Rehabilitation
- Advances in Water Resources Engineering and Management
- Advances in Sustainable Construction Materials and Geotechnical Engineering.

The title *Advances in Energy and Built Environment* covers papers on contemporary renewable energy and built environment technologies which include microgrid, rural electrification, viability and reliability aspects of solar photovoltaic, greening of buildings using rooftop solar PV systems and heating and cooling of buildings. For the sake of completeness, the papers on exergy analysis and solar radiation estimation have also been included. All twenty-two papers have been selected for publication. It is believed that this collection will be useful for a fairly wide spectrum of audiences like researchers, application engineers and industry managers.

Changsha, China — Guoqiang Zhang
Bhubaneswar, India — N. D. Kaushika
New Delhi, India — S. C. Kaushik
Noida, India — R. K. Tomar

Acknowledgements

The conference was organized to fulfil the vision of Honourable Dr. Ashok K. Chauhan, Founder President of Ritnand Balved Education Foundation (RBEF), and under the able leadership of Honourable Dr. Atul Chauhan, Chancellor, Amity University, Noida, Uttar Pradesh, India. I am honoured to organize this prestigious conference which connected the world's foremost industries with the topmost academia.

I express my sincerest thanks to all the lead speakers and authors of original research papers for their contribution. I also express my thanks to all the reviewers for their cooperation in the review process. I am happy to express my deep sense of gratitude to our publication sponsor Springer for publishing the conference proceedings.

I express my warm gratitude towards all our sponsors: academic partners: Liverpool John Moores University, UK; National University of Malaysia; industry partner: Defence Infrastructure Planning and Management (DIPM) Council of India; knowledge partners: Institution of Civil Engineers, UK; Indian Association of Structural Engineers (IAStuctE); Women in Science & Engineering (WiSE), India; Indian Geotechnical Society (IGS); and Indian Buildings Congress (IBC); platinum sponsor: Ministry of Water Resources, River Development and Ganga Rejuvenation, Government of India; gold sponsor; J K Cement Ltd.; supporting sponsor: Bentley; HEICO; VCL Group; BL Goel & Co.; Subham Builders; Innovative Construction and Consultants; Satya Sai Builders and Contractors Pvt. Ltd.; Megde India Projects (OPC) Pvt. Ltd., etc.

Finally, I compliment my team for their hard work and enthusiasm to make TRACE a success story. I am confident that TRACE 2018 will allow exciting and meaningful conversations, partnerships and collaborations in construction technology and infrastructure growth.

Dr. R. K. Tomar
General Chair, TRACE 2018
Head, Department of Civil Engineering
Amity School of Engineering and Technology
Amity University, Noida
Uttar Pradesh, India

Contents

About the Editors

Dr. Guoqiang Zhang is a professor at Hunan University, China, where he is currently the dean of Institute for Sustainable Urbanization and Construction Innovation. He is also the director of the National Center for International Research Collaboration in Building Safety and Environment of Ministry of Science and Technology of China, and the deputy director of Key Lab of Building Safety and Energy Efficiency of Ministry of Education of China. He is also a member of the academic committee of Hunan University, and an editorial member of the Journal of Hunan University. Due to his contribution to Sustainable Built Environment Education, Research and Practice, Dr. Zhang received special government allowance from the State Council in China. He has made valuable contributions towards sustainable education and science communication, research, social service and commercialization of scientific and technological achievements.

Dr. N. D. Kaushika formerly professor, Centre for Energy Studies, Indian Institute of Technology Delhi, and subsequently director of reputed engineering institutions in Delhi and National Capital Region, is a specialist in renewable energy and environment. He is a recipient of the Hariom Prerit S. S. Bhatnagar Research Endowment Award for research in energy conservation in 1987. Currently, he is a visiting research professor at the Institute of Technological Engineering and Research of SOA University, Bhubaneswar, India. He is an author of five books and has contributed articles in several reputed journals and books chapters in several books by international publishers.

Dr. S. C. Kaushik received his Ph.D. in Plasma Science from IIT Delhi after his distinguished First Position in Master's degree in science (electronics) from Meerut University. His fields of research include plasma science, thermal science and engineering, energy conservation and heat recovery, solar refrigeration and air conditioning, solar architecture, and thermal storage and power generation. He has made significant contributions in these fields as evident by his about 500 research articles in journals of repute at the national and international level. He is a pioneer in exergy analysis and finite time thermodynamics of energy systems, and a leading

expert on alternative refrigeration and air conditioning technologies. Dr. Kaushik has co-authored ten books and also edited two volumes. His specific contributions to energy systems have been recognized by several awards to his credit viz. Young Scientist UNESCO Award, Hariom Prerit S. S. Bhatnagar Award, Divyajyoti Science and Technology Award, Top Academic Research Performer in Energy, Dr. A. P. J. Abdul Kalam Gold Medal Research Award and outstanding Research Faculty Award in India. He is Member of ISES (Australia) and IIR (France), and a Life Member of various other professional societies like SESI, PSSI, ISTE, ISHRAE and ISME. He has been former Head, Centre for Energy Studies 2007–2010 and at present Emeritus Professor at CES, IIT Delhi.

Dr. R. K. Tomar received his Ph.D. from the Indian Institute of Technology (IIT) Delhi and is currently, Head of the Department of Civil Engineering, Amity School of Engineering and Technology, Amity University, India. His research interests include artificial intelligence applications in buildings and sustainable built environment. He has a combined experience of 27 years in industry and academia in various capacities. He has published several research articles in international peer-reviewed journals.

Comparative Study of Earth Air Tunnel and Borehole Heat Exchanger Applied for Building Space Conditioning

Shiv Lal and S. C. Kaushik

Abstract In this communication, energy and exergy analysis of building-integrated "earth air tunnel heat exchanger" (EATHE) and "borehole heat exchanger" (BHE) has been studied for a composite climate of Delhi. A mathematical model has been developed to predict the energy and exergy of the system. Computational fluid dynamics software has been used to compare the exergetic performance of both the systems. This work is the extension of Kaushik et al. (J Renew Sustain Energy 6(1), 2014 [1]) and Lal et al. (J Renew Sustain Energy 6(2), 023123, 2014 [2]) where economic analysis has been done for both the systems using year-round performance analysis method. It is found that the borehole heat exchanger is more economical in fixed cost and recurring cost and gives improved year-round performance than earth air tunnel heat exchanger.

Keywords Earth air tunnel heat exchanger · Borehole heat exchanger · Exergy · Economic analysis

1 Introduction

The building sector is the highest energy-demanding sector in present time in USA. And its percentage is also increasing drastically in developing countries in recent years. It is estimated that the overall energy consumption in buildings is around 40% of the global energy use. The conventional processes for providing thermal comforts are mainly powered by fossil fuel; it is accounted to be 28% of the world's overall energy consumption [3]. The energy demand in buildings for realizing indoor thermal comfort has increased considerably in current scenario due to economic growth and infrastructure development for rising living standard. This increment in energy demand is one of the causes of greenhouse gas (GHG) emissions. From the

S. Lal (✉)
Department of Mechanical Engineering, Rajasthan Technical University, Kota 324010, India
e-mail: shivlal1@gmail.com

S. C. Kaushik
Centre for Energy Studies, Indian Institute of Technology, Delhi, New Delhi 110016, India

G. Zhang et al. (eds.), *Advances in Energy and Built Environment*, Lecture Notes in Civil Engineering 36, https://doi.org/10.1007/978-981-13-7557-6_1

fourth IPCC report, the GHG emissions have increased by an average of 1.6% per year and CO_2 emissions at a rate of 1.9% per year (due to fossil fuel consumption in power plant). Switching to passive concepts for providing indoor thermal comfort, decreasing the energy consumption in the buildings and using low-carbon fuels are a few measures to reduce GHG emissions from buildings [4].

The passive concepts for cooling or heating are used to provide indoor thermal comfort by using natural sources of thermal energy. Direct or indirect coupling of buildings with the earth is one of the passive concepts for achieving indoor thermal comfort and one of the ways of decreasing energy consumption in heating, ventilation and air conditioning (HVAC) [5]. It is well known that the subsoil temperature fluctuates with depth and becomes almost constant at a base of 3–4 m or high [6]. This invariable warmth is higher than the winter seasonal ambient average warmth and lower than the summer seasonal ambient average temperature. This invariable ground temperature (thermal energy) is used for providing indoor thermal comfort through earth air tunnel and borehole heat exchanger systems. The effectiveness of an EATHE system hinges upon the temperature and moisture disposal in the ground as well as the surface conditions. The earth air tunnel heat exchanger (EATHE) is promising option to reduce energy demand adding a root of sustainable development which has gained significant importance during the last three decades [6–9].

In India, a first scientific attempt on constructing earth air tunnel was made at Clara Swain Hospital, Bareilly, India [5]. It developed a simple theoretical model to evaluate an EATHE effectiveness, located at Mathura, UP, India. The system is made up of by 80-m-length tunnel having 0.528 m^2 cross-sectional area. It was observed that the system's cooling and heating capacity is 512 and 269 kWh, respectively, at an air velocity of 4.89 m/s. The earth tunnel was coupled with the conventional air conditioner to reduce the cooling load of AC and found the substantially increased effectiveness [10]. Singh [11] analysed and improved the EATHE system for space cooling based upon room warmth and environmental conditions. Trombe and Serres [12] experimentally analysed and simulated an air earth heat exchanger in France. Based upon the different ground surface boundary conditions, Santamouris et al. [8] investigated the effectiveness of a single and parallel EATHE. An EATHE system was developed by Thanu et al. [13] at the Gulmohar farm house, Gurgaon, India, for monitoring the relative humidity and temperature at both inlet and exit of the system. Mathur and Bansal [14] extended their experiments of EATHE using evaporative cooling and found the better cooling results in summer.

Zukowski et al. [15] used PVC pipe and reported that the building temperature was reduced by 1.9 °C and cooling load reduced by 595 kWh. Bansal et al. [16] developed a fleeting and definite model based on computational fluid dynamics to predict the thermal performance and cooling/heating capacity of earth air pipe heat exchanger systems. Lal et al. [17] reviewed the various theoretical and experimental studies on earth air tunnel. It has evaluated the performance analysis of an earth air tunnel situated at Gwal Pahari, Gurgaon, India. The energy conservation potential and CO_2 mitigation also carried out during the study [1].

The earth air tunnel is a horizontal ground-coupled system, and borehole is a vertical ground-coupled system. The weather affected the buried pipe's depth by

2–3 °C as par the peak seasonal climate. But the 3–4 m depth is found feasible as concerned with economics of EATHE. This system has the limitation of land requirement. So the borehole heat exchanger (BHE) required less land, and it felt into the depth of ground. The shallow geothermal energy wells have been studied by Sanner [18], and he found that geothermal temperature reduces (up to annual mean ambient temperature) till 20 m depth and thereafter temperature increases on average 3 °C for each 100 m depth.

Sharqawy et al. [19] developed a mathematical model to predict the effective pipe to borehole thermal resistance and compared their results with modelling results of Gu and O'Neal [20], Remund [21] and Shonder and Beck [22]. Gustafsson and Westerlund [23] simulated the thermal resistance in a U-tube BHE through CFD technique. Lee and Lam [24] developed a modified multi-ground level model with heterogeneous groundwater flow. The borehole thermal resistance varied with relative ground water flow velocity and tables. The Indian energy scenario has not shown any data related to the BHE application.

The energy and exergy analysis of both the passive systems is found to be at preliminary stage. The exergy analysis of both EATHE and BHE has been carried out for experimental systems. As concerned with the energy conservation, BHE is one of the good options for space conditioning. The comparative studies on EATHE and BHE performance are carried out for the same configuration (same length and diameter of heat exchanger pipe) through mathematical and CFD simulation in ANSYS.

2 Materials and Methods

2.1 Theoretical Modelling and

2.1.1 Governing Equations for EATHE

Bansal and Sodha [10] developed a mathematical model for tunnel output temperature calculation, and its results have been validated from experimental result of EATHE at Mathura, India. The assumptions of this model are as: tunnel was of uniform cross section, surrounding surface temperatures changes uniformly, homogeneous material and uniform temperature distribution. This model is used for the outlet temperature from EATHE in this study. The earth air tunnel outlet temperature is expressed by Bansal and Sodha [10];

$$T_{\text{out}} = T_g\left(1 - \mathrm{e}^{-\left(\frac{2\pi r_1 h_{\text{fa}}}{\dot{m}_a C_a}\right)L}\right) + T_{\text{in}}\,\mathrm{e}^{-\left(\frac{2\pi r_1 h_{\text{fa}}}{\dot{m}_a C_a}\right)L} \tag{1}$$

From the simple thermohydraulic design (from log mean temperature difference and energy equation) of borehole heat exchanger, the outlet temperature is given by Sanner [18];

$$T_{o\_\mathrm{BHE}} = T_{\mathrm{wall}} + (T_{\mathrm{in}} - T_{\mathrm{wall}}).\mathrm{e}^{-(hA/\dot{m}_a C_a)} \tag{2}$$

2.1.2 Exergy Analysis

The rate of heat discharge by the EATHE in the cooling mode is calculated from the equation,

$$\dot{Q}_c = \dot{m}_a\left(h_{a,\mathrm{in}} - h_{a,\mathrm{out}}\right) \tag{3}$$

where

$$h_{a,\mathrm{in}} = (h_a)_{\mathrm{in}} + w_{\mathrm{in}}(h_v)_{\mathrm{in}} \text{ and } h_{a,\mathrm{out}} = (h_a)_{\mathrm{out}} + w_{\mathrm{out}}(h_v)_{\mathrm{out}} \tag{4}$$

The heat rejected from EATHE can be expressed by:

$$\dot{Q}_c = \bar{h}_a A\left(T_a - T_p\right) \tag{5}$$

where $\bar{h}_a = \frac{N_u k}{D}$,

And

$$N_u = 0.023 Re^{0.8} P_r^{0,1/3} \tag{6}$$

where $\bar{h}_a$ is the convective heat transfer coefficient of air which depends upon the Reynolds number, shape and roughness of the pipe for turbulent flow; A is the surface area of the EATHE; T_p is the temperature of pipe surface; T_a is the average temperature of air flowing in buried pipe; k is the thermal conductivity of the pipe, and D is the hydraulic diameter of the pipe.

The work input to the blower is given by

$$\dot{W}_b = \frac{\dot{m}_a\left(h_{b,\mathrm{in}} - h_{b,\mathrm{out}}\right)}{\eta_{\mathrm{mech}}} \tag{7}$$

Or

$$\dot{W}_b = \frac{\nabla P.V}{\eta_{\mathrm{mech}}} \tag{8}$$

where ∇P is the pressure loss, V is the volumetric flow rate of air, and η_{mech} is the mechanical efficiency of the blower. The pressure loss can be calculated from

$$\nabla P = 0.5 f \frac{L}{D} \rho U^2 + \sum \zeta \tag{9}$$

where U is the velocity, f is the friction losses, ζ is the particular resistance losses, and L is the pipe length. Hence, the coefficient of performance (COP) of the system can be calculated as

$$\mathrm{COP} = \frac{\dot{Q}_c}{\dot{W}_b} \tag{10}$$

The COP of the system is the ratio of heat transfer to the work consumption by the blower.

The physical exergy is considered for this analysis, and other types of exergies are neglected. The general exergy balance equation is given as follows:

$$\underbrace{\dot{E}_{x\mathrm{in}} - \dot{E}_{x\mathrm{out}}}_{\substack{\text{Rate of net exergy transfer} \\ \text{by heat, work and mass}}} = \underbrace{\dot{E}_{x\mathrm{dest}}}_{\substack{\text{Rate of exergy} \\ \text{destruction}}} \tag{11}$$

Or

$$\dot{E}_{x\mathrm{heat}} - \dot{E}_{x\mathrm{work}} + \dot{E}_{x\mathrm{mass,in}} - \dot{E}_{x\mathrm{mass,out}} = \dot{E}_{x\mathrm{dest}} \tag{12}$$

This equation can be written as:

$$\sum\left(1 - \frac{T_o}{T_x}\right)\dot{Q}_x - \dot{W} + \sum \dot{m}_{\mathrm{in}} E_{x,\mathrm{in}} - \sum \dot{m}_{\mathrm{out}} E_{x,\mathrm{out}} = \dot{E}_{x\mathrm{dest}} \tag{13}$$

where $\dot{Q}_x$ is the heat transfer rate through the boundary at temperature T_x at location x, $\dot{W}$ is the work rate, and the subscription zero indicates the properties at reference dead state. The total flow exergy of air is evaluated from Eq. (11) [24]

$$E_{x,a} = \left[\left(C_{\mathrm{pa}} + \omega C_{\mathrm{pv}}\right)\right](T - T_o) - T_o\left[\left(C_{\mathrm{pa}} + \omega C_{\mathrm{pv}}\right)\ln\left(\frac{T}{T_o}\right) - \left(R_a + \omega R_v\right)\ln\left(\frac{P}{P_o}\right)\right] + T_o[(R_a + \omega R_v)\ln[(1 + 1.6078\omega_o)/(1 + 1.6078\omega)] + 1.6078\omega R_a \ln(\omega/\omega_o)] \tag{14}$$

For ease of calculations, some assumptions have to be made as: $C_{\mathrm{pm}} = C_{\mathrm{pa}} + \omega C_{\mathrm{pv}}$, where C_{pm} is the specific heat of humid air and it is equal to 1.0216 kJ/kg K, ω is the moisture content in the air, the gas constant of water vapour is equal to $R_v = 0.461$ kJ/kg. K and for dry air $R_a = 0.2871$ kJ/kg K,

$$E_{x,a} = 1.0216(T - T_o) - T_o\left[1.0216\ln\left(\frac{T}{T_o}\right) - (0.2871 + 0.461\omega)\ln\left(\frac{P}{P_o}\right)\right] + T_o[(0.2871 + 0.461\omega)\ln[(1 + 1.6078\omega_o)/(1 + 1.6078\omega)] + 1.6078\omega R_a \ln(\omega/\omega_o)] \tag{15}$$

where ω is the specific humidity ratio and it is defined by:

$$\omega = \dot{m}_w/\dot{m}_a \tag{16}$$

The exergy can be evaluated by the multiplying specific exergy and mass flow rate.

$$\dot{E}_{x\text{heat}} = \dot{m}_a E_{x,a} \tag{17}$$

$$\eta_{ex} = \frac{\dot{E}_{x\text{out}}}{\dot{E}_{x\text{in}}} = 1 - \frac{\dot{E}_{x\text{dest}}}{\dot{E}_{x\text{in}}} \tag{18}$$

It can be written as [25]:

$$\eta_{2,R} = \frac{\dot{E}_{x\text{heat}}}{\dot{W}_{\text{act,in}}} = \frac{\dot{m}_a\left(E_{xa,\text{in}} - E_{xa,\text{out}}\right)}{\dot{W}_{\text{act,in}}} \tag{19}$$

2.1.3 Economic Assessment

The following assumptions are made for economic assessment of solar chimney:

i. Interest rate (i) 10%
ii. Repair and maintenance (R_m) 5% of the capital cost of solar chimney
iii. Life span (n) 5 year.

The net present value (NPV) can be calculated as follows

$$\text{NPV} = -C_o + (A_{\text{es}} - R_m)\left[\frac{(1+i)^n - 1}{i(1+i)^n}\right] \tag{20a}$$

The payback period is defined by the ratio of cost of solar chimney to the annual energy saving. It can be calculated as follows:

$$\text{PP} = \left[\frac{C_o}{A_{\text{cs}} - R_m}\right] \tag{20b}$$

where PP is payback period, C_o is the cost of solar chimney, and A_{es} is annual energy saving in heating and ventilation.

3 Result and Discussion

3.1 Exergy Analysis of Experimental EATHE

The exergy analysis is carried out by Eq. (19) for both cooling and heating modes and presented in Figs. 1 and 2. The maximum and minimum exergy efficiency in month of June is estimated as 7.87 and 4.15, respectively. And the maximum and

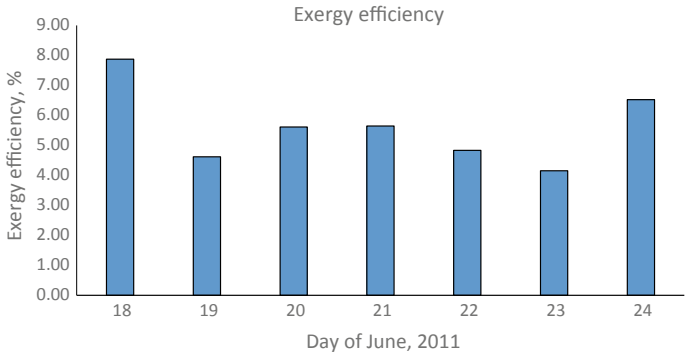

Fig. 1 Exergy efficiency of EATHE for a week of June

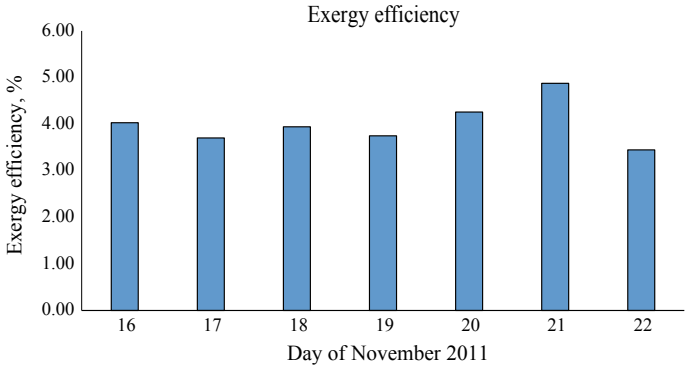

Fig. 2 Exergy efficiency of EATHE for a week of November

minimum exergy efficiency in month of November is estimated by 4.87 and 3.45, respectively. The exergy efficiency is reduced when increasing the inlet temperature and decreasing the relative humidity difference between inlet and outlet positions. Therefore, the exergy fluctuation in summer month observed higher than the winter.

3.2 Exergy Analysis of Experimental Borehole Heat Exchanger

The exergy analysis has been done for borehole heat exchanger for both seasons like summer and winter. Figure 3, expressed the exergy efficiency variation of Borehole Heat Exchanger (BHE) for a week in summer season. It is seen that the minimum exergy efficiency has observed by 3.00 on May 23 and maximum by 4.43 on May 17. The daily average exergy for the experimental time has been observed in summer by 3.5–3.80.

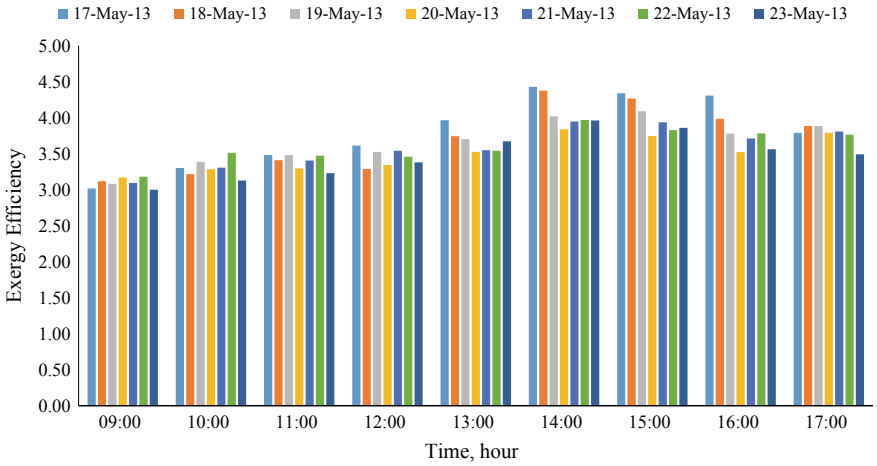

Fig. 3 Exergy analysis of borehole heat exchanger for May. The exergy efficiency for a week of December is presented in Fig. 4. It is found that the exergy efficiency increases when the ambient temperature decreases. It is found higher in morning and evening as compared to middle of the day. But in reverse of that the higher exergy efficiency has evaluated in mid of the day in summer, when ambient temperature goes highest. The average exergy efficiency in experimental time has been observed by 2.69–6.38. The minimum exergy efficiency estimated by 1.34 on December 27 and maximum by 7.59 on December 31. The minimum exergy at middle of the day and higher exergy efficiency observed in morning and evening hours in winter season

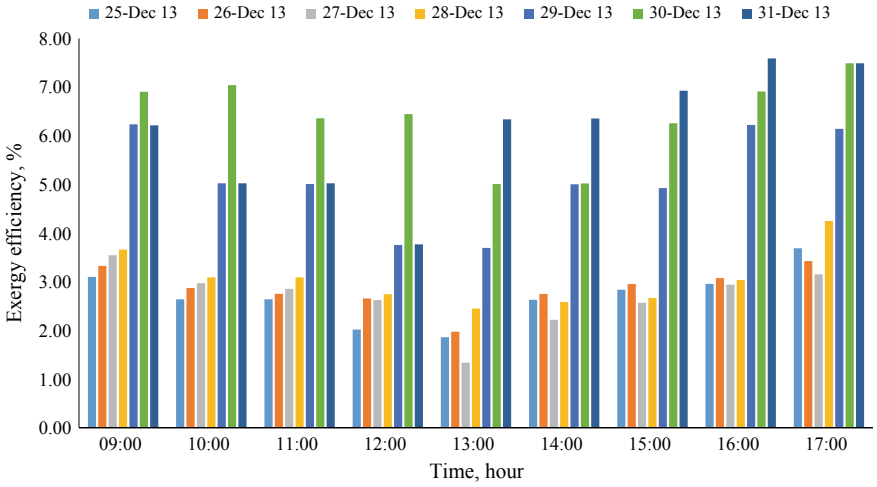

Fig. 4 Exergy analysis of borehole heat exchanger for December

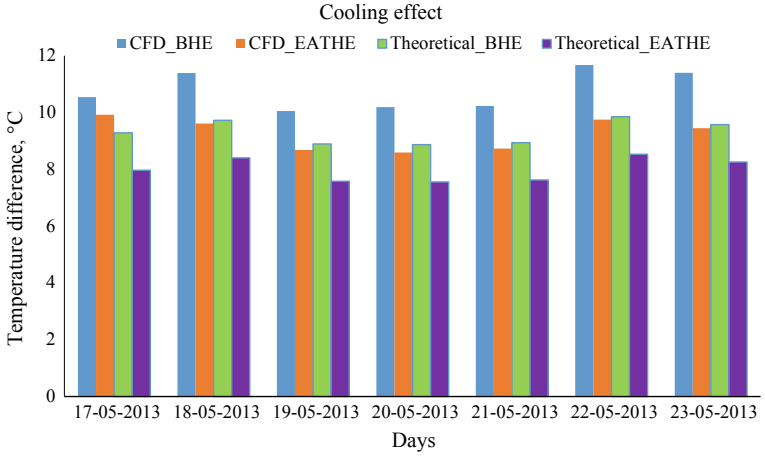

Fig. 5 Cooling effect of BHE and EATHE

3.3 Comparative Study of BHE and EATHE

The earth air tunnel heat exchanger generally buried at a depth of 3–4 m because it is a feasible solution due to economic considerations [6]. At 3–4 m depth, ground temperature is varying 2–3 °C with the annual mean ambient temperature. The stable and ground temperature have mate at the depth of 20 m, and it is equal to annual average ambient temperature. From the analytical study, it is found that the ground temperature at EATHE depth differs than the BHE depth. At the bottom of borehole depth, the ground temperature found stable.

For the comparison of the performance of BHE and EATHE, exactly similar configuration systems are used for the study. Both the tubes are having 2 inch in diameter and 120 ft. long. The EATHE was buried at 3 m depth (horizontal) and the BHE bored up to 18 m depth (vertical). Figure 5 shows the cooling effect of BHE and EATHE and found that the BHE produces higher cooling effect than EATHE. Figure 6 shows the heating effect in winter season and found that the BHE produces more heating effect than EATHE. It is found that the BHE gives approximately 20 kWh higher cooling effect than EATHE. In winter season, the BHE gives almost 10 kWh higher heating effect than EATHE. It is concluded that the BHE is a better solution than EATHE for both the effects. The COP of BHE system is found higher than the EATHE system for similar configurations, and it is estimated 1.13 and 0.59 higher than the EATHE in cooling and heating modes, respectively.

Due to more land area required for EATHE, using BHE is more economical option. The total cost of BHE system is slightly higher if land cost does not considered. If land cost is considered than the EATHE, project cost is approximately ten times higher than BHE project cost. The BHE as a superior than EATHE is that, the BHE required small land area to establish the system than EATHE and will give higher

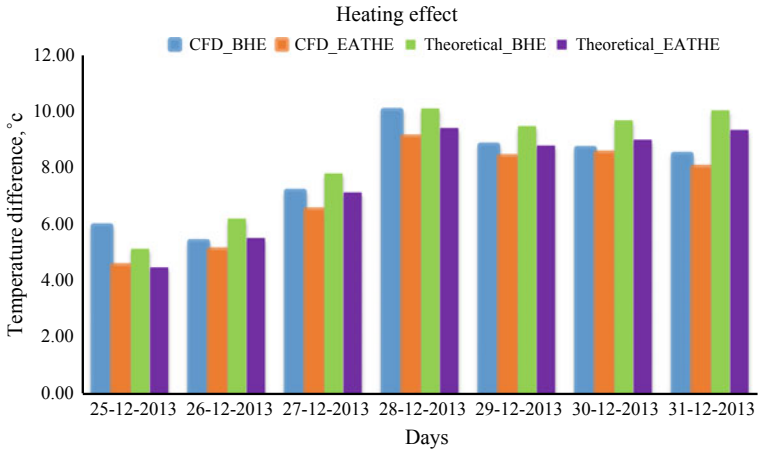

Fig. 6 Heating effect of BHE and EATHE

Table 1 Cost of an EATHE (Rs. 61.25 USD-1 as on 15 January 2014)

S. No.	Material and on as on/misc. charge	Cost (Rs)	USD
1	G.I. pipe (40 m) @331 Rs per feet	13,240	216.16
2	G.I. pipe fittings	1000	16.33
3	Blower (variable speed)	10,000	163.27
4	Excavation and filling of sand (57 cu. M)	10,000	163.27
5	Labour charge	3000	48.98
	Total cost	37,240	608.00
6	Cost of land (25×2 m^2), 30,000Rs@m2	1,500,000	24,489.80
Total			25,097.80

performance for both space heating and cooling. From the cost analysis from Tables 1 and 2, the system cost of BHE is slightly higher but the overall project cost of BHE is many times higher than the BHE. In the metropolitan cities, the EATHE is not a feasible solution as par the cost considerations, in this condition BHE plays an important role and found feasible.

The NPV and the payback period have been calculated by using Eqs. (20a and 20b). It is found that the NPV is greater than one; it means the project is economically feasible. The payback period is evaluated as approximately one year.

Table 2 Cost of a BHE (Rs. 61.25 USD-1 as on 15 January 2014)

S. No.	Material and on as on/misc. charge	Cost (Rs)	USD
1	G.I. pipe (40 m) @331 Rs per feet	13,240	216.16
2	G.I. pipe fittings	1000	16.33
3	0.2032-m-diameter and 19-m-long perforated PVC pipe for borehole	18,000	293.88
4	Blower (variable speed)	10,000	163.27
5	Drilling of 19-m-deep borehole	6000	97.96
6	Labour charge	3000	48.98
	Total cost	51,240	836.57
7	Cost of land (2×2 m^2), 30,000Rs@m2	120,000	1959.18
Total			2795.76

4 Conclusions

The NPV is found to be many times higher than one which shows that the project is economically feasible. The payback period is evaluated as approximately one year. It is observed that BHE is a good option for space cooling. From the comparative study of BHE and EATHE, it is found that the BHE is having higher cooling and heating potential than EATHE. The COP of BHE system is found to be higher than the EATHE system for similar configurations. It is estimated as 1.13 and 0.59 higher than the EATHE in cooling and heating modes, respectively.

References

1. Kaushik SC, Garg T, Lal S (2014) Thermal performance prediction and energy conservation potential of earth air tunnel heat exchanger for thermal comfort in India. J Renew Sustain Energy 6. https://doi.org/10.1063/1.4861782
2. Lal S, Balam NB, Jain HK (2014) Performance evaluation, energy conservation potential, and parametric study of borehole heat exchanger for space cooling in building. J Renew Sustain Energy 6:023123. http://dx.doi.org/10.1063/1.4872362
3. Lal S, Saushik SC, Bhargava PK (2012) A study on stack ventilation system and integrated approaches. In: Emerging trends of energy conservation in buildings. CBRI, India, pp 255–263
4. Alter L (2011) The trombe wall: low tech solar design makes a comeback. Available at: http://www.treehugger.com/sustainable-product-design/the-trombe-wall-low-tech-solar-design-makes-a-comeback.html/ (Assesses on Oct 2012)
5. Sodha MS, Sharma AK, Singh SP, Bansal NK, Kumar A (1985) Evaluation of an earth-air tunnel system for cooling/heating of a hospital complex. Build Environ 20(2):115–122. https://doi.org/10.1016/0360-1323(85)90005-8
6. Sharan G, Sahu RK, Jadhav R (2001) Earth-tube heat exchanger based air-conditioning for tiger dwellings. Zoos Print 16 [5], May (RNI2:8)

7. Kumar R, Ramesh S, Kaushik SC (2003) Performance evaluation and energy conservation potential of earth–air–tunnel system coupled with non-air-conditioned building. Build Environ 38(6):807–813. https://doi.org/10.1016/S0360-1323(03)00024-6
8. Santamouris M, Mihalakakou G, Lewis JO, Asimakopoulos D (1997) On the application of the energy balance equation to predict ground temperature profiles. Sol Energy 60:181–190. https://doi.org/10.1016/S0038-092X(97)00012-1
9. Sawhney RL, Buddhi D, ThanuN M (1990) An experimental study of summer performance of a recirculation type underground air pipe air conditioning system. Build Environ 34:189–196
10. Bansal NK, Sodha MS (1986) An earth-air tunnel system for cooling buildings. Tunn Undergr Space Technol 1(2):177–182. https://doi.org/10.1016/0886-7798(86)90057-X
11. Singh SP (1994) Optimization of earth air tunnel system for space cooling. Energy Convers Manag 35(8):721–725. https://doi.org/10.1016/0196-8904(94)90057-4
12. Trombe A, Serres L (1994) Air-earth exchanger study in real site experimentation and simulation. Energy Build 21(2):155–162. https://doi.org/10.1016/0378-7788(94)90008-6
13. Thanu NM, Sawhney RL, Khare RN, Buddhi D (2001) An experimental study of the thermal performance of an earth-air-pipe system in single pass mode. Sol Energy 71(6):353–364. https://doi.org/10.1016/S0038-092X(01)00072-X
14. Mathur J, Bansal V (2009) Performance enhancement of earth air tunnel heat exchanger using evaporative cooling. Int J Low Carbon Technol 4:150–158
15. Zukowski M, Sadowska B, Sarosiek W (2011) Assessment of the cooling potential of an earth-tube heat exchanger in residential buildings. In: The 8th international conference on environmental engineering, Vilnius, Lithuania, pp 830–834
16. Bansal V, Mishra R, Agrawal GD, Mathur J (2013) Derating factor new concept for evaluating thermal performance of earth air tunnel heat exchanger: a transient CFD model. Appl Energy 102:412–426. https://doi.org/10.1016/j.apenergy.2012.07.027
17. Kaushik SC, Lal S, Bhargava PK (2013) Earth–air tunnel heat exchanger for building space conditioning: a critical review. Nanomaterials and Energy (ICE), vol 2, in press, https://doi.org/10.1680/nme.13.00007
18. Sanner B (2001) Shallow geothermal energy. GHC Bulletin, pp 19–25
19. Sharqawy MH, Mokheimer EM, Badr HM (2009) Effective pipe-to-borehole thermal resistance for vertical ground heat exchangers. Geothermics 38:271–277. https://doi.org/10.1016/j.geothermics.2009.02.001
20. Gu Y, O'Neal DL (1998) Development of an equivalent diameter expression for vertical U-tubes used in ground-coupled heat pumps. ASHRAE Transactions 104:347–355
21. Remund CP (1999) Borehole thermal resistance: laboratory and field studies. ASHRAE Transactions 105:439–445
22. Shonder JA, Beck JV (1999) Field test of a new method for determining soil formation thermal conductivity and borehole resistance. ASHRAE Trans 106:843–850
23. Gustafsson AM, Westerlund L (2010) Simulation of the thermal borehole resistance in groundwater filled borehole heat exchanger using CFD. Int J Energy Environ 1(3):399–410
24. Lee CK, Lam HN (2012) A modified multi-layer model for borehole ground heat exchangers with an inhomogeneous groundwater flow. Energy, 47:378–387. https://doi.org/10.1016/j.energy.2012.09.056
25. Dincer I, Sahin AZ (2004) 2004, A new model for thermodynamic analysis of a drying process. Int J Heat Mass Transf 47(4):645–652

Advances in Reliability of Solar PV Systems

Anil K. Rai

Abstract The problems of solar PV system reliability and its improvements have been addressed in this paper. Reliability is the ability of solar PV system to perform adequately without failure during the intended period of time under the operating environmental condition encountered. It also considers the capability of the system to cater the needs of the load that it has been designed for. In this situation, the energy balance between the energy generating unit (array), storage unit (battery bank) and load becomes important. However, the consideration of unit array output instead of equivalent hour full sunlight (EHFS) can ameliorate the system capability to serve the load at a particular location and effective unit array output (EUAO) for a wider region. The consideration of quality and redundancy is also found to significantly help the improvement of reliability.

Keywords Module characteristics · System reliability · EHFS and EUAO

1 Introduction

Solar photovoltaics, solar thermal electric and wind power have global potential and advanced technologies. In solar photovoltaic, the conversion of incident solar energy into electricity takes place directly (no intermediate stages). Over the past 4–5 decades, an extensive research effort has been carried out for efficiency amelioration and cost reduction, but relatively less attention has been paid on system reliability parameters. The system reliability can be defined as the probability of a system to function adequately for the intended period under the existing operating conditions. In this regard, three factors of reliability (1) redundancy at subsystem level, (2) mismatch losses at component and subsystem level and (3) design have been considered to combat the variability of solar radiation during year-round cycle.

A. K. Rai (✉)
Ajay Kumar Garg Engineering College, Ghaziabad, India
e-mail: anilkrai@yahoo.com

G. Zhang et al. (eds.), *Advances in Energy and Built Environment*, Lecture Notes in Civil Engineering 36, https://doi.org/10.1007/978-981-13-7557-6_2

2 Power Loss and Developments of Hot Spot

Around the world, over the past 4–5 decades extensive efforts were made at research, development, testing and demonstration of solar PV power technology. It has been observed that in the field condition, module/array generated power was lower than the nameplate rating of modules/array at STC (1000 W/m^2, 25 °C) may be due to a variety of reasons [1, 2]. Sundareswaran et al. [3] have discussed the enhanced energy output from a PV system under non-uniform solar radiation conditions through artificial bee colony algorithm. Different solar cells have different current–voltage characteristics due to manufacturer's tolerances despite several controls and all automations. These variations in current–voltage characteristics particularly at maximum power point ($I_{\max,}$ $V_{\max}$) exhibit statistical distribution. In series-connected solar cells, series string current will be limited by the lowest current generated by a solar cell, and similar results would occur when solar cells are connected in parallel. These variations in $I_{\max}$ and $V_{\max}$ lead to power loss in the network, and this kind of power loss has been investigated by Kaushika and Rai [4]. They have also concluded that these losses tend to increase with time due to soiling of solar cell.

The environmental stress includes power loss in a solar cell network resulting from opening of a string. This power loss results in excessive heating of regions known as hot spots and leads failure of operation of solar cell. The solar cells are subjected to shadow problems from predictable and unpredictable sources in the field conditions. The shadowed cell blocks the flow of current in a series string, and string becomes reverse biased; in spite of delivering power to load, it starts dissipating power, and consequently, regions of excessive heating are developed in the solar cell which is shadowed. These excessive heating regions can cause module failure and also damage the encapsulation. It has been investigated that the percentage of power loss is much higher than the percentage area of array which is shadowed. When solar cell operates at low voltage, the cell operating at low voltage becomes reverse biased due to low voltage output which exhibits hot spot regions. These excessive heating regions can cause module failure and also damage the encapsulation; therefore, 'safe operating regions' are specified by some manufacturers for their modules.

3 System Reliability Improvements

3.1 Subsystem Level

The system reliability can be affected by quality and redundancy. The component and their physical material used in the system as well as manufacturing process, testing and calibration are quality concerned and depend on the quality and experience of personnel involved and working environment. In the early development of solar cell, the quality concerns were cost-intensive for solar PV system and were only adopted in space applications. The redundancy is oversize of the system and is of two types:

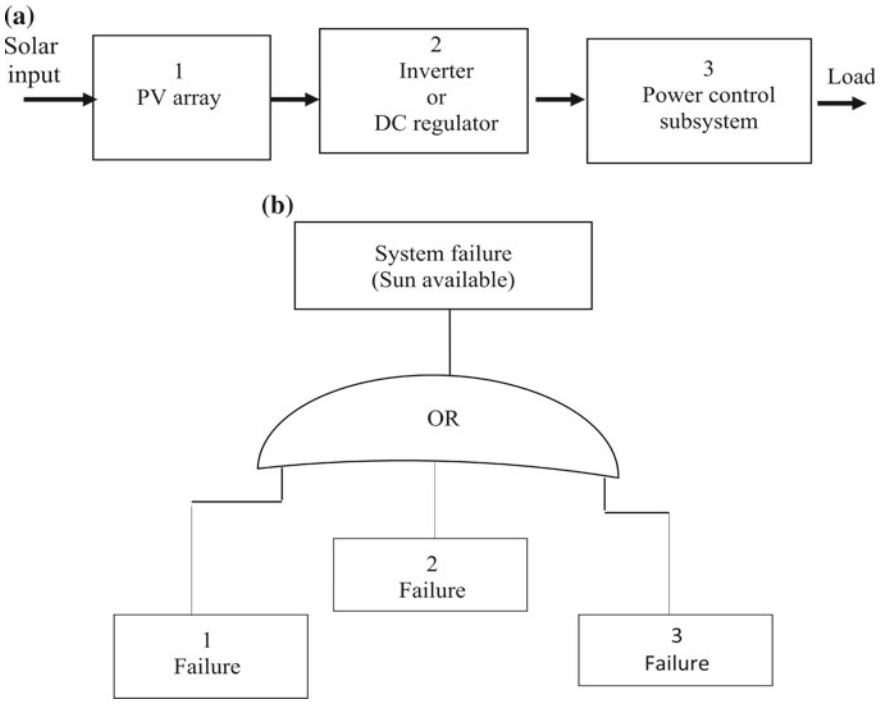

Fig. 1 **a** Schematic diagram of standalone solar PV system. **b** Fault tree standalone solar PV system

active or parallel and standby. In active redundancy, system components share the normal function amongst themselves. In case of failure of component, the activity is automatically taken care by another component.

In standby redundancy, the redundant component remains in standby state and puts into action when main operating component fails. The improvement in reliability requires additional investment, and Billinton and Allan [5] have shown that cost increases as reliability level increases. Therefore, in decision-making process, cost and reliability are two conflicting parameters. Therefore, efficacy of redundancy in terrestrial solar PV system has been examined in following section:

The interconnections of components of standalone solar PV system at subsystem level are shown in Fig. 1a and can be analysed following Stember [6] and Billinton and Allan [5].

In the consequence of the failure of each system, the fault tree and fault mode effect analysis are shown in Fig. 1b and Table 1, respectively. The system under consideration has all components connected in series and failure of any component of the system results in failure of the system. Consequently, the output is only delivered to the load if all the subsystems are operational.

The above system as shown in Fig. 1a is further considered with standby PV array. The fault tree and fault mode effect analysis are shown in Fig. 2b and Table 2,

Table 1 Fault mode effect analysis for standalone system

Subsystem state			Failure of system sun available
PV array	Inverter	Power control	
Operational	Operational	Operational	Operational
Operational	Operational	Failed	Failed
Operational	Failed	Operational	Failed
Failed	Operational	Operational	Failed

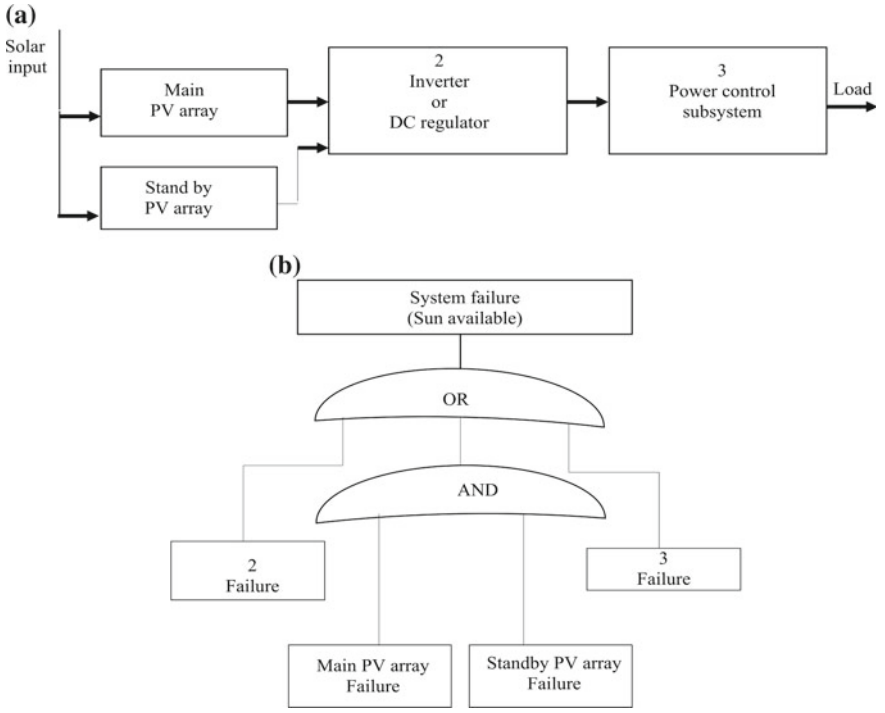

Fig. 2 **a** Solar PV system with redundant array. **b** Fault tree for solar PV system with redundant array

respectively. In this case, it clearly shows that failure of the system happens if both the PV arrays fail. Therefore, due to redundancy at subsystem level, the failure mode is significantly reduced, but it is not a cost-effective option.

Table 2 Fault mode effects analysis for system with redundant PV array

Subsystem state				System failure sun available
Main PV array	Standby PV array	Inverter or DC regulator	Power control	
Operational	Operational	Operational	Operational	Operational
Operational	Operational	Operational	Failed	Failed
Operational	Failed	Operational	Operational	Operational
Operational	Operational	Failed	Operational	Failed
Failed	Operational	Operational	Operational	Operational
Operational	Operational	Failed	Failed	Failed
Operational	Failed	operating	Failed	Failed
Failed	Operational	Operational	Failed	Failed
Operational	Failed	Failed	Operational	Failed
Failed	Operational	Failed	Operational	Failed
Failed	Failed	Operational	Operational	Failed

3.2 Component Level

The reliability of the PV system can be improved by the development of fault-tolerant circuitry to combat the fault arises due to shadow problem. It was first investigated in satellite applications; in these applications, solar PV array cannot be oriented and stabilized for optimum illumination of solar panels. The performance of solar PV system can be improved significantly by the use of bypass diode across parallel string [7]. Subsequently by junction application of shunt diode, power loss can be reduced on terrestrial solar cell arrays [8, 9]. In the present day, most of the manufacturer of solar cell module uses bypass diode across each module or in some cases, across sections of module to ameliorate the shadow effect and malfunction of solar cell. The bypass diode functions as a standby redundancy. Simultaneously, it has been realized that by proper arrangement of interconnections of solar cell in the module, power output from a shadowed array can be improved substantially. Several authors [10–13] have proposed several interconnection schemes for the reliability improvement. The interconnection schemes hold promise of cost-effectiveness and will also function as an active redundancy. In what follows, different interconnection schemes (Fig. 3) were investigated using mathematical network analysis approach. Computations based on numerical analysis show the mismatch loss in bridge-linked array is inversely proportional to the total number of cells, and in case of series–parallel array, it is more nearly to square root of total number of cells.

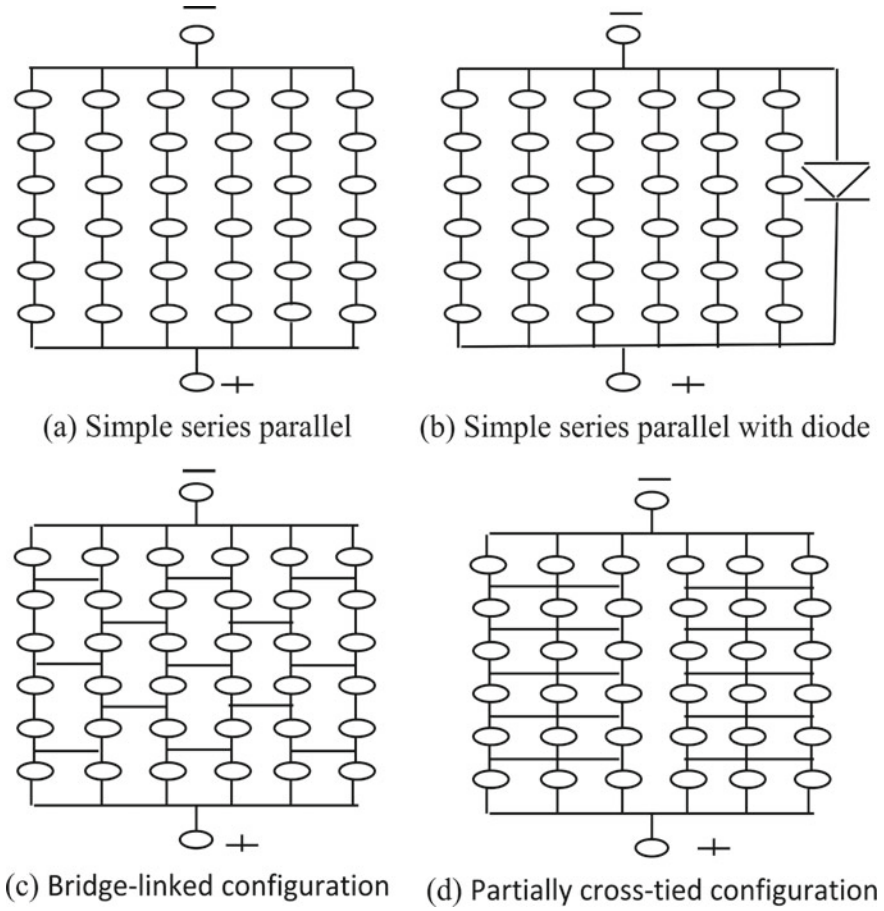

Fig. 3 Interconnection schemes for solar PV array

3.3 System Design Level

The system reliability also depends upon the selection of suitable design parameter because the performance of solar energy conversion devices exclusively depends upon site parameters. The objective of selection of design parameter is to combine both array characteristics and site parameters into one parameter known as EUAO and expressing this as a function of latitude and longitude. The system capacity is not considered due to modular nature of solar PV system.

The energy generating from the solar PV array is the product of array peak power at STC and number of hours the solar incident radiation is of 1000 W/m^2 (EHFS). The performance of solar cell is adversely affected by rising of cell operating temperature above STC (25 °C). For Indian climate, the nominal cell operating temperature

(NOCT) is taken as 45 °C. The relationship between cell junction temperature, ambient temperature and NOCT is given as [2]

$$T_{\text{jun}} - T_{\text{amb}} = \text{NOCT} - 20$$
$$\text{or, } T_{\text{jun}} = \text{NOCT} + T_{\text{amb}} - 20$$
$$\text{or, } T_{\text{jun}} = T_{\text{amb}} + 25$$

where

T_{jun} Solar cell junction temperature (°C)
T_{amb} Ambient air temperature (°C).

Due to effect of cell operating temperature, array power degraded with per degree rise in cell operating temperature above Standard Test Condition (25 °C). To incorporate the temperature effect and ensure a sufficient margin of safety in design of the system, unit array output (UAO) is considered in place of EHFS. The UAO is expressed in Wh/Wp/day [14]. The expression for UAO is given as

$$\text{UAO} = \text{EHFS} \times \left[1 - \frac{\%\ \text{Temp. coefficient}}{100} \times (\text{Maximum ambient air temp. in a month})\right]$$

The array energy output is given by

$$\text{Output energy from array} = W_p \text{ rating of array} \times \text{UAO}$$

To make the design parameter more reliable, a rigorous approach has been carried out and simulation model was developed [15] for the development of single design parameter known as equivalent unit array output (EUAO) and simulation model flow chart is shown in Fig. 4. The design parameter EUAO was calculated for autonomy days 3 in Indian region, and its variations with geographical coordinates were carried out (Fig. 5a and b). It is observed from the figures that variation of EUAO exhibits more scattered with latitude as compared to longitude due to specific geometry of Indian peninsula. Therefore, the arid and non-arid zones in Indian region are considered separately to obtain more statistically significant polynomial fits (Fig. 5b).

4 Conclusions

This paper addresses the problems of system reliability and improvements. It considers the reliability improvements at subsystem and component levels. Subsystem-level reliability is not cost-intensive due to cost of PV array and is not considered as an attractive option. In practical situation, the system reliability is influenced by faults at component levels, and therefore, different interconnection schemes to improve the reliability of the system are investigated. The cross-tie configuration of PV array

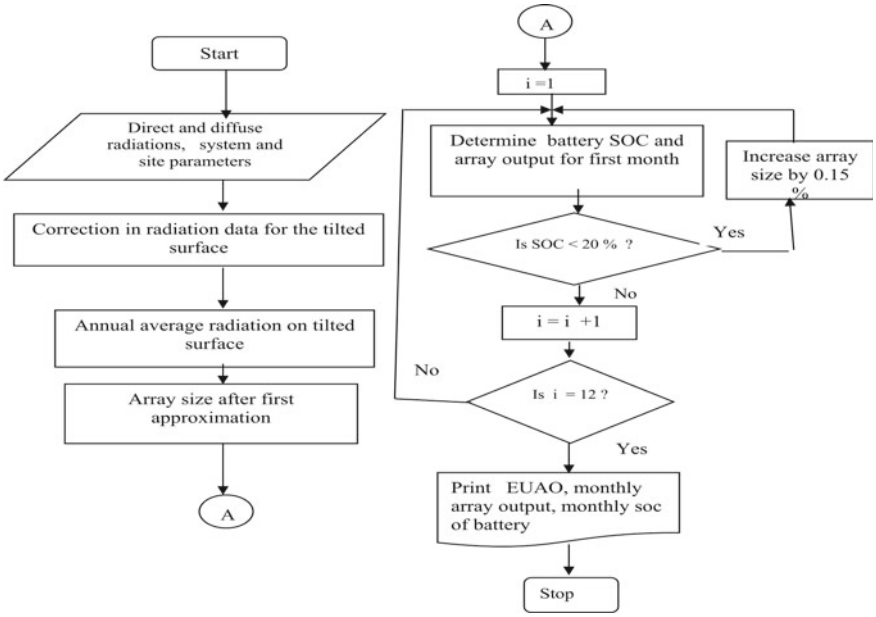

Fig. 4 Simulation model flow chart to calculate effective unit array output (EUAO)

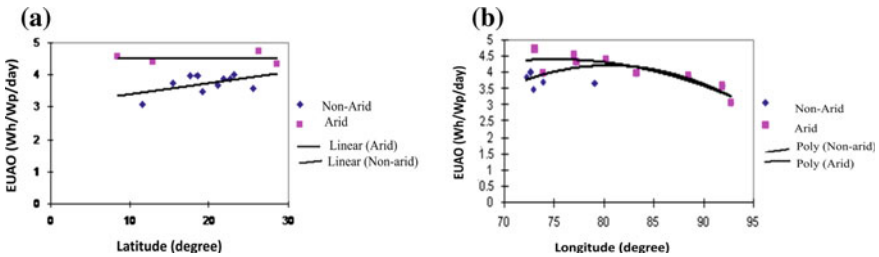

Fig. 5 **a** EUAO versus latitude variation. **b** EUAO versus longitude variation

excels over other interconnection schemes. The selection of suitable design parameter, EUAO, will also increase the reliability of the system.

Acknowledgements Sincere thanks are due to Prof. N.D. Kaushika Ex-Professor, IIT Delhi, for guiding me in preparation of this paper.

References

1. Kaushika ND (1996) 50 kW solar PV power plant in Rajasthan TEFR. Sun Source of India Ltd
2. Treble FC (1991) Generating electricity from Sun Pergamon press, New York

3. Sundareswaran K, Sankar P, Nayak PSR, Simon Sishaj P, Sankaran P (2015) Enhanced energy output from a PV system under partial shaded conditions through artificial bee colony. IEEE Trans Sustain Energy 6(1):198–209
4. Kaushika ND, Rai AK (2007) An investigation of mismatch losses in solar Photovoltaic cell networks. Energy 32:755–759
5. Billinton R, Allan RN (1992) Reliability evaluation of engineering systems: concepts and techniques. Plenum Press, New York, USA
6. Stember LH (1981) Reliability considerations in the design of solar photovoltaic power system. Solar Cells 3:269–285
7. Raushenbach SH (1971) Electrical output of shadowed solar cell arrays". IEEE Trans Electron Devices 18:483
8. Sayed M, Partin L (1975) Effect of shading on CDs/Cu_xS solar cell array design. IEEE Trans Energy Convers 14:61
9. Swalesh MS, Green MA (1982) Effect of shunt resistance and bypass diode on the shadow tolerance of solar cell modules. Solar Cells 5:183
10. Brandstetter A (1984) Solar cell arrays studies. In: Proceedings of the solar world congress. Permagon Press, Australia 4:1549
11. Gautam NK, Kaushika ND (2001) Network analysis of fault-tolerant solar photovoltaic arrays. Sol Energy Mater Sol Cell 69:25–42
12. Satpathy PR, Renu S, Sasmita J (2017) A shade dispersion interconnection scheme for partially shaded modules in a solar PV array network. Energy 139:350–365
13. Singer S, Rosenshtein B, Surazi S (1984) Characterization of PV array output using a small number of measured parameter. Sol Energy 32:603
14. Bhattacharya T (1998) Terrestrial solar photovoltaic. Narosa Publishing House, New Delhi
15. Kaushika ND, Mishra A, Rai AK (2018) Solar photovoltaics: technology, system design, reliability and viability. Springer Nature Publication

Exergy Analysis of Dedicated Mechanically Subcooled Vapour Compression Refrigeration Cycle Using HFC-R134a, HFO-R1234ze and R1234yf

Shyam Agarwal, Akhilesh Arora and B. B. Arora

Abstract The current work presents the exergy analysis of dedicated mechanically subcooled vapour compression refrigeration system. It involves the performance comparison of dedicated mechanically subcooled cycle (DSC), overall cycle (OC), subcooler cycle (SC) and simple VCR cycle using HFO-R1234ze, R1234yf and HFC-R134a. A computational formulation model has been developed in the EES software for the computation of various performance parameters, viz. COP, exergetic efficiency, exergy destruction rate and exergy destruction ratio. The effect of variation of effectiveness of subcooler (0.3–1.0) and isentropic efficiency of compressors (0.1–1.0) has been investigated on the performance of the cycles. Exergy destruction in each system component has also been checked. It has been observed that performance wise, the dedicated mechanically subcooled VCR cycle is an improved version of simple VCR cycle. The overall cycle also performs better than simple VCR cycle. The HFO-R1234ze competes with HFC-R134a and supersedes R1234yf. It proves itself a good alternate to R134a being a friend of the environment. Condenser1 is the most sensitive system component of dedicated mechanically subcooled VCR cycle for the refrigerants considered.

Keywords VCR · Subcool · Exergetic efficiency · COP · HFO · HFO-R1234ze

Nomenclature

Abbreviations and Symbols

Comp.	Compressor
Cond.	Condenser
COP	Coefficient of performance
DOS	Degree of subcooling

S. Agarwal · A. Arora (✉) · B. B. Arora
Department of Mechanical Engineering, Delhi Technological University, Delhi 110042, India
e-mail: profakhilesharora@gamil.com

G. Zhang et al. (eds.), *Advances in Energy and Built Environment*, Lecture Notes in Civil Engineering 36, https://doi.org/10.1007/978-981-13-7557-6_3

DSC	Dedicated mechanically subcooler VCR
$(\Delta T)_{sc}$	Degree of subcooling
$\dot{E}_D$	Exergy destruction rate (kW)
ED	Exergy destruction
EDR	Exergy destruction ratio
EES	Energy equation solver
$\dot{E}$	Rate of exergy (kW)
E.V.	Expansion valve
Ex.	Expansion
GWP	Global warming potential
h	Specific enthalpy (kJ/kg)
HFC	Hydrofluorocarbon
HFO	Hydrofluoroolefin
$\dot{m}_r$	Mass flow rate of refrigerant (kg/s)
ODP	Ozone depleting potential
P	Pressure (kPa)
SVCR	Simple vapour compression refrigeration
$\dot{Q}_e$	Rate of net refrigerating effect (kW)
s	Specific entropy (kJ/kg °C)
T	Temperature (°C)
T_b	Boundary temperature (°C)
T_e	Evaporator temperature (°C)
T_0	Dead state temperature (°C)
VCR	Vapour compression refrigeration
$\dot{W}$	Work rate (kW)

Greek Symbols

ε	Effectiveness
η	Efficiency
Σ	Summation

Subscripts

0	Dead state
C	Condenser
Comp.	Compressor
Cond.	Condenser
e	Evaporator
ex	Exergetic
SC	Subcooler cycle, subcooler

OC	Overall cycle
i	Input
o	Output

1 Introduction

The efficient and eco-sustainable refrigeration systems are in current demand. The developing countries like India have hunger demand of electricity especially in summer season due to increasing refrigeration and air-conditioning load. In order to fulfil the need of high grade energy during peak load, efficient refrigeration systems are required. The price of high grade energy is also growing continuously. The protection of the environment from high GWP HFCs which are used in refrigeration and air-conditioning systems is a current issue. The high GWP HFCs have to be phased out as per the European Union (EU) regulation [1] No 517/2014 2006). Sarbu [2] presented the current status of alternative refrigerant development related to vapour compression-based refrigeration, air-conditioning and heat pump units through total equivalent warming impact (TEWI) analysis. Many researchers have proved that the mechanically subcooling of vapour compression refrigeration (VCR) cycle improves its performance. Park et al. [3] studied advanced vapour compression cycle technologies, which include subcooling cycles, expansion loss recovery cycles and multi-stage cycles.

The subcooling is focused on a suction-line heat exchanger, thermoelectric subcooler and mechanical subcooler. The expansion loss recovery cycles are mainly focused on utilizing an expander and ejector. The multi-stage cycle includes a vapour or liquid refrigerant injection cycle and two-phase refrigerant injection cycle. They have recommended the need of future research for these cycles. Qureshi and Zubair [4, 5] and Qureshi et al. [6] observed the effect of refrigerant combination on the performance of dedicated mechanically subcooler vapour compression refrigeration cycle. They also reviewed the future aspects of mechanical subcooling in vapour compression refrigeration cycle. They analysed that the load carrying capacity of the evaporator increased by approximately 0.5 kW when R22 was subcooled in the main cycle by 5–8 °C. They noted that using the subcooling, the second-law efficiency of the cycle increased by an average 21% and this percentage increase is directly proportional to the ambient temperature. Zubair [7, 8] and Zubair et al. [9] have investigated a dedicated and a integrated mechanical subcooling system from the thermodynamic standpoint. In these studies, it was found that the system performance had improved when operating in situations where the difference between the condensing and evaporating temperatures is large. Qureshi et al. [6] analysed that the load carrying capacity of the evaporator increased by approximately 0.5 kW when R22 was subcooled in the main cycle by 5–8 °C. They noted that using the subcooling, the second-law efficiency of the cycle increased by an average 21% and this percentage increase is directly proportional to the ambient temperature. Pottker and Hrnjak [10] performed experimental study to observe the effect of condensing

subcooling on the performance of an air-conditioning system operating with R134a and R1234yf, under the same operating conditions. They observed that the system COP increased up to 18% for R1234yf and 9% for R134a. Arora [11] and Arora et al. [12–14], 2008 have investigated vapour absorption and vapour compression refrigeration systems for performance improvement using liquid–vapour heat exchanger subcooling techniques energetically and exergetically. They observed that the subcooling of vapour compression refrigeration cycle enhances the COP and exergetic efficiency of the cycle. They have also analysed half effect water lithium bromide and double effect parallel flow vapour absorption refrigeration system on the basis of energy and exergy. Dixit et al. [15, 16] analysed waste heat-driven triple effect vapour absorption system and absorption–compression cascade refrigeration system for the energy and exergy performance of the system. Kalla et al. [17] reviewed vapour compression refrigeration system for alternative refrigerants.

The literature survey collected from different established data sources, viz. Science Direct, Google Scholar and ResearchGate, depicts that the vast research has been done on simple VCR cycle for performance improvement. According to some research studies out of these, dedicated mechanical subcooling incorporated to VCR cycle improves its performance. Few research studies explore the performance of dedicated mechanical subcooler VCR cycle using HFO refrigerants, viz. R1234ze and R1234yf.

2 System Description and Modelling

2.1 System Description

Figures 1 and 2 illustrate the schematic and P-h and T-s diagrams of dedicated mechanically subcooled vapour compression refrigeration system, respectively. It comprises of two sections, i.e. subcooled and subcooler vapour compression refrigeration cycles. The evaporator of subcooler VCR cycle receives the heat rejected by the condensate liquid refrigerant of subcooled VCR cycle and acts as subcooler. In this way, the two cycles are coupled together through subcooler or evaporator 2 in order to achieve low temperature in evaporator 1. The refrigerants considered for the energy and exergy analysis of the system are R134a, R1234yf and R1234ze. The same refrigerant has been considered in the two sections simultaneously.

The subcooled VCR cycle is in lower section which consists of compressor 1, evaporator 1, expansion valve 1, subcooler and condenser 1, and the subcooler VCR cycle is in upper section which consists of compressor 2, condenser 2, expansion valve 2 and evaporator 2 or subcooler. The vapour refrigerant leaving the evaporator 1 of subcooled VCR cycle at state point 1 enters into the compressor 1 and is being compressed. The refrigerant at high temperature and pressure leaving the compressor 1 at state point 2 enters into the condenser 1. The liquid condensate has been subcooled from state points 3–3a by the evaporator 2 of the subcooler cycle. The subcooled

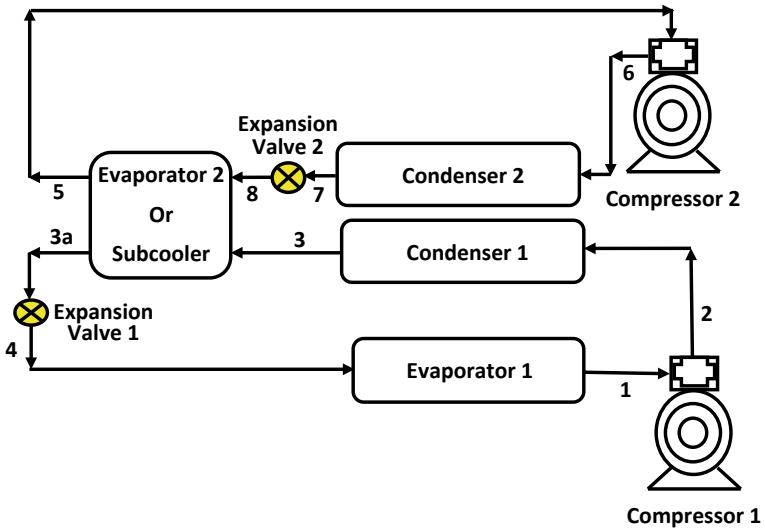

Fig. 1 Schematic diagram of dedicated mechanically subcooled vapour compression refrigeration cycle

liquid refrigerant is throttled by the expansion valve 1 from state points 3a–4. The low-temperature liquid–vapour mixture of refrigerant enters into the evaporator 1, and the low temperature is achieved in the evaporator 1.

Similarly, the saturated vapour of the refrigerant leaving the evaporator 2 or subcooler at state point 5 enters into the compressor 2. The compressed high-pressure, high-temperature vapour refrigerant enters into the condenser 2 at state point 6. The vapour phase of the refrigerant is converted into liquid in the condenser 2. The liquid condensate refrigerant leaving the condenser 2 at state point 7 is expanded freely by the expansion valve 2 from state points 7–8. The low-temperature liquid–vapour mixture of refrigerant enters into the evaporator 2 or subcooler and absorbs heat from the condensate of condenser 1 from state points 8–5 and is transformed into saturated vapour.

Thus, the mechanical subcooling is produced by the subcooler VCR cycle in the subcooler from state points 3–3a. The evaporator temperature ($T_{e,SC}$) of the subcooler cycle is more than the evaporator temperature of subcooled cycle. The subcooling of liquid condensate refrigerant of subcooled cycle enhances the net specific refrigerating effect as shown in Fig. 2 from state points 4–1. The increase in refrigerating effect enhances the coefficient of performance (COP) of the subcooled cycle. However, the compressor work of the subcooler cycle reduces the COP of the overall cycle.

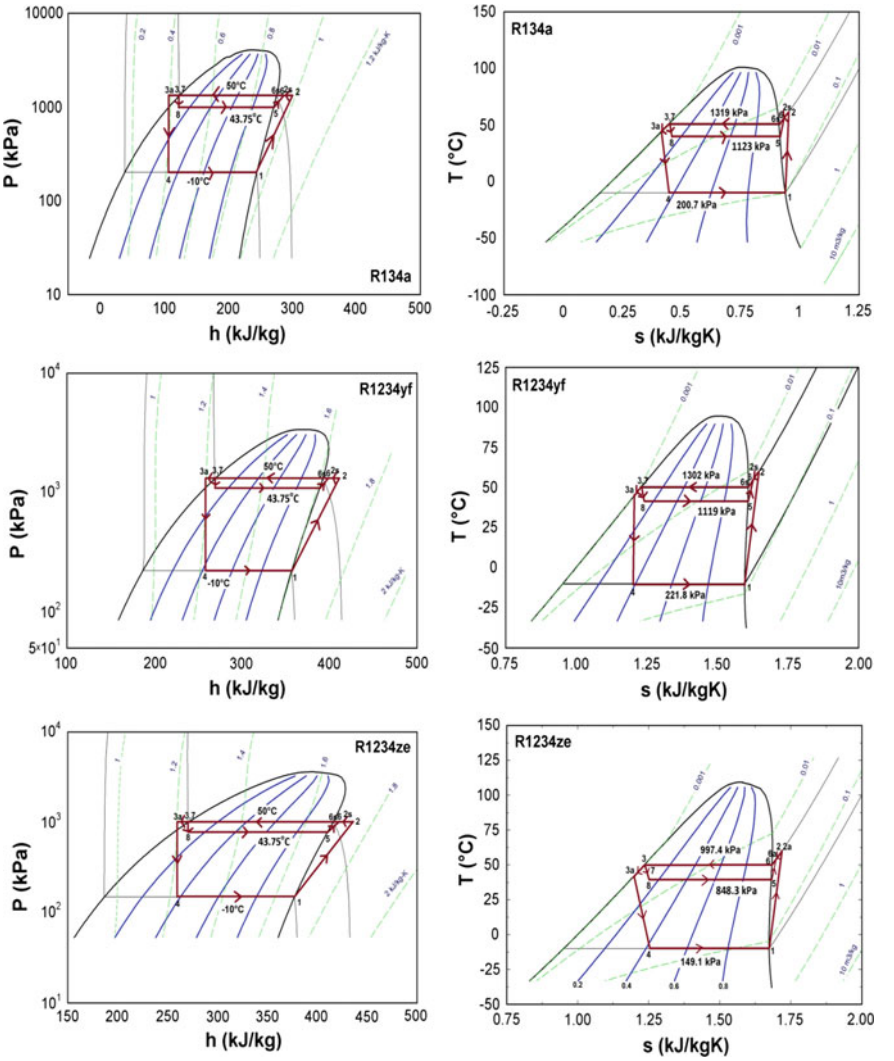

Fig. 2 Pressure–enthalpy (P-h) and temperature–entropy (T-s) state diagrams of R134a, R1234yf and R1234ze

2.2 System Modelling

The present work analysed the dedicated mechanically subcooled vapour compression cycle energy exegetically using R134a, R1234yf and R1234ze refrigerants, in which the subcooler VCR cycle produces mechanical subcooling in the subcooled VCR cycle through subcooler. The various performance parameters, viz. compressor work, COP, exergetic efficiency, total exergy destruction rate and exergy destruction

ratio (EDR), have been investigated for different variables, viz. effectiveness of subcooler and isentropic efficiency of compressor. The exergy destruction rate in each system component has also been explored.

A computer program has been formulated in Engineering Equation Solver (EES) to compute the performance parameters involved in the analysis. The current analysis has been done on the basis of the first law and second law of thermodynamics using steady-state governing equations.

2.2.1 Energy Analysis

The first law based on work, energy and mass conservation principles is presented in Eqs. (1) and (2).

$$\sum \dot{Q} - \sum \dot{W} = \sum \dot{m}_{\mathrm{o}} h_{\mathrm{o}} - \sum \dot{m}_{\mathrm{i}} h_{\mathrm{i}} \tag{1}$$

$$\sum \dot{m}_{\mathrm{i}} - \sum \dot{m}_{\mathrm{o}} = 0 \tag{2}$$

where $\dot{Q}$, $\dot{W}$ and $\dot{m}$ are the rate of heat, work and mass transfer crossing the boundary of the system, respectively.

The coefficient of performance (COP) of simple, dedicated mechanically subcooled, subcooler and overall VCR cycles is given by Eqs. (3)–(9).

$$\mathrm{COP}_{\mathrm{SVCR}} = \frac{\dot{Q}_{\mathrm{e}}}{\dot{W}_{\mathrm{comp}}} \tag{3}$$

where $\dot{Q}_{\mathrm{e}}$ is the net refrigeration effect produced and $\dot{W}_{\mathrm{comp}}$ is the actual work of the compressor.

$$\mathrm{COP}_{\mathrm{DSC}} = \frac{\dot{Q}_{\mathrm{e,DSC}}}{\dot{W}_{\mathrm{comp1}}} \tag{4}$$

$$\dot{Q}_{\mathrm{e,DSC}} = \dot{m}_{\mathrm{r,DSC}}(h_1 - h_4) \tag{5}$$

$$\dot{W}_{\mathrm{comp1}} = \dot{m}_{\mathrm{r,DSC}}(h_2 - h_1) \tag{6}$$

$$\mathrm{COP}_{\mathrm{SC}} = \frac{\dot{Q}_{\mathrm{e,SC}}}{\dot{W}_{\mathrm{comp2}}} \tag{7}$$

$$\dot{W}_{\mathrm{comp2}} = \dot{m}_{\mathrm{r,SC}}(h_6 - h_5) \tag{8}$$

$$\mathrm{COP}_{\mathrm{OC}} = \frac{\dot{Q}_{\mathrm{e,DSC}}}{\dot{W}_{\mathrm{comp1}} + \dot{W}_{\mathrm{comp2}}} \tag{9}$$

where $\dot{Q}_{e,DSC}$, $\dot{Q}_{e,SC}$, $\dot{W}_{comp1}$, $\dot{W}_{comp2}$, $\dot{m}_{r,DSC}$ and $\dot{m}_{r,SC}$ are net refrigerant effect, net compressor work and mass flow rate of dedicated mechanically subcooled and subcooler VCR cycles, respectively.

The effectiveness of subcooler ε_{SC} is the ratio of the minimum heat transfer to the maximum heat transfer.

$$\varepsilon_{SC} = \frac{T_3 - T_{3a}}{T_3 - T_8} \tag{10}$$

where ε_{SC} is the effectiveness of subcooler and T_3, T_5 and T_8 are temperatures at respective state points.

The energy balance in the subcooler is given by Eq. (11):

$$\dot{m}_{r,DSC}(h_3 - h_{3a}) = \dot{m}_{r,SC}(h_5 - h_8) \tag{11}$$

2.2.2 Exergy Analysis

The second law of thermodynamics expresses the concept of exergy. The exergy is defined as the degree measure of quality or usefulness of energy to impact the environment. The maximum useful work which can be extracted from a system as it reversibly comes into equilibrium with its environment (Bejan et al. [18] and Arora and Kaushik [19]).

For the refrigerant flowing in a refrigerating system, the exergy is defined as follows [18]:

$$\dot{E} = \dot{m}_r[(h - h_0) - T_0(s - s_0)] \tag{12}$$

where h_0 and s_0 are the enthalpy and entropy values of the refrigerant at dead state pressure P_0 and temperature T_0.

Exergy destruction $\left(\dot{E}_D\right)$ or internal exergy destruction losses which are caused by irreversibilities of the system are the algebraic sum of total exergy at the inlet and outlet of the system. General exergy balance is given by Dincer and Kanoglu [20]:

$$\dot{E}_D = \dot{E}_{in} - \dot{E}_{out} \tag{13}$$

where $\dot{E}_D$ is the rate of exergy destruction and $\dot{E}_{in}$ and $\dot{E}_{out}$ are the total exergy transferred by heat, work and mass.

Exergy Destruction ($\dot{E}_{\mathrm{D}}$) in the Components of Dedicated Mechanically Subcooled (DSC) Vapour Compression Refrigeration Cycle

The exergy destruction in each component of the dedicated mechanically subcooled vapour compression refrigeration cycle is given by the following equations:

Evaporator 1

$$\left(\dot{E}_{\mathrm{D}}\right)_{\mathrm{e,DSC}} = \dot{E}_{\mathrm{X4}} + \dot{Q}_{\mathrm{e,DSC}}\left(1 - \frac{T_0}{T_{\mathrm{b,DSC}}}\right) - \dot{E}_{\mathrm{X1}} = \dot{m}_{\mathrm{r,DSC}}(h_4 - T_0 s_4) + \dot{Q}_{\mathrm{e,DSC}}\left(1 - \frac{T_0}{T_{\mathrm{b}}}\right) - \dot{m}_{\mathrm{r,DSC}}(h_1 - T_0 s_1) \tag{14}$$

Compressor 1

$$\left(\dot{E}_{\mathrm{D}}\right)_{\mathrm{comp1}} = \dot{E}_{\mathrm{X_1}} + \dot{W}_{\mathrm{comp1}} - \dot{E}_{\mathrm{X_2}} = \dot{m}_{\mathrm{r,DSC}}(h_1 - T_0 s_1) + \dot{W}_{\mathrm{comp1}} - \dot{m}_{\mathrm{r,DSC}}(h_2 - T_0 s_2) \tag{15}$$

Condenser 1

$$\left(\dot{E}_{\mathrm{D}}\right)_{\mathrm{cond1}} = \dot{E}_{\mathrm{X_2}} - \dot{E}_{\mathrm{X_3}} = \dot{m}_{\mathrm{r,DSC}}(h_2 - T_0 s_2) - \dot{m}_{\mathrm{r,DSC}}(h_3 - T_0 s_3) \tag{16}$$

Expansion valve 1

$$\left(\dot{E}_{\mathrm{D}}\right)_{\mathrm{Ex.valve1}} = \dot{E}_{\mathrm{X_3}} - \dot{E}_{\mathrm{X_{3a}}} = \dot{m}_{\mathrm{r,DSC}}(h_{3\mathrm{a}} - T_0 s_{3\mathrm{a}}) - \dot{m}_{\mathrm{r,DSC}}(h_4 T_0 s_4) = \dot{m}_{\mathrm{r,DSC}} T_0 (s_4 - s_{3\mathrm{a}}) \tag{17}$$

Subcooler

$$\left(\dot{E}_{\mathrm{D}}\right)_{\mathrm{SC}} = (\dot{E}_{\mathrm{X_8}} - \dot{E}_{\mathrm{X_5}}) + \left(\dot{E}_{\mathrm{X_3}} - \dot{E}_{\mathrm{X_{3a}}}\right) = \dot{m}_{\mathrm{r,SC}}\{(h_8 - h_5) - T_0(s_8 - s_5)\} + \dot{m}_{\mathrm{r,DSC}}\{(h_3 - h_{3\mathrm{a}}) - T_0(s_3 - s_{3\mathrm{a}})\} \tag{18}$$

Compressor 2

$$\left(\dot{E}_{\mathrm{D}}\right)_{\mathrm{comp2}} = \dot{E}_{\mathrm{X_5}} + \dot{W}_{\mathrm{comp2}} - \dot{E}_{\mathrm{X_6}} = \dot{m}_{\mathrm{r,SC}}(h_5 - T_0 s_5) + \dot{W}_{\mathrm{comp2}} - \dot{m}_{\mathrm{r,SC}}(h_6 - T_0 s_6) \tag{19}$$

Condenser 2

$$\left(\dot{E}_{\mathrm{D}}\right)_{\mathrm{cond2}} = \dot{E}_{\mathrm{X}_6} - \dot{E}_{\mathrm{X}_7} = \dot{m}_{\mathrm{r,SC}}(h_6 - T_0 s_6) - \dot{m}_{\mathrm{r,SC}}(h_7 - T_0 s_7) \tag{20}$$

Expansion valve 2

$$\left(\dot{E}_{\mathrm{D}}\right)_{\mathrm{Ex.valve2}} = \dot{E}_{\mathrm{X}_7} - \dot{E}_{\mathrm{X}_8} = \dot{m}_{\mathrm{r,SC}}(h_7 - T_0 s_7) - \dot{m}_{\mathrm{r,SC}}(h_8 - T_0 s_8) = \dot{m}_{\mathrm{r,SC}} T_0 (s_8 - s_7) \tag{21}$$

Evaporator 2

$$\begin{aligned}\left(\dot{E}_{\mathrm{D}}\right)_{\mathrm{e,Sc}} = \dot{E}_{\mathrm{X}_8} + \dot{Q}_{\mathrm{e,SC}}\left(1 - \frac{T_0}{T_{\mathrm{b,SC}}}\right) - \dot{E}_{\mathrm{X}_5} = \dot{m}_{\mathrm{r,SC}}(h_8 - T_0 s_8) \\ + \dot{Q}_{\mathrm{e,SC}}\left(1 - \frac{T_0}{T_{\mathrm{b,SC}}}\right) - \dot{m}_{\mathrm{r,SC}}(h_5 - T_0 s_5)\end{aligned} \tag{22}$$

where $\dot{E}_{\mathrm{D}}$, $\dot{E}_{\mathrm{X}}$, $\dot{m}_{\mathrm{r}}$ and T_{b} are the exergy destruction rate, exergy rate, mass flow rate and temperature of space to be cooled for the dedicated mechanically subcooled and subcooler cycles, respectively. T_0, h_0 and s_0 are the temperature, enthalpy and entropy of dead state.

Total Exergy Destruction

Total exergy destruction of the system is the sum of exergy destruction in each component of the system.

The total exergy destruction in dedicated mechanically subcooled vapour compression refrigeration cycle (DSC) is given by:

$$\sum\left(\dot{E}_{\mathrm{D}}\right)_{\mathrm{DSC}} = \left(\dot{E}_{\mathrm{D}}\right)_{\mathrm{e,DSC}} + \left(\dot{E}_{\mathrm{D}}\right)_{\mathrm{comp1}} + \left(\dot{E}_{\mathrm{D}}\right)_{\mathrm{cond1}} + \left(\dot{E}_{\mathrm{D}}\right)_{\mathrm{Ex.valve1}} \tag{23}$$

$$\sum\left(\dot{E}_{\mathrm{D}}\right)_{\mathrm{SC}} = \left(\dot{E}_{\mathrm{D}}\right)_{\mathrm{e,Sc}} + \left(\dot{E}_{\mathrm{D}}\right)_{\mathrm{comp2}} + \left(\dot{E}_{\mathrm{D}}\right)_{\mathrm{cond2}} + \left(\dot{E}_{\mathrm{D}}\right)_{\mathrm{Ex.valve2}} \tag{24}$$

$$\begin{aligned}\sum\left(\dot{E}_{\mathrm{D}}\right)_{\mathrm{OC}} = \left(\dot{E}_{\mathrm{D}}\right)_{\mathrm{e,DSC}} + \left(\dot{E}_{\mathrm{D}}\right)_{\mathrm{comp1}} + \left(\dot{E}_{\mathrm{D}}\right)_{\mathrm{cond1}} \\ + \left(\dot{E}_{\mathrm{D}}\right)_{\mathrm{Ex.valve1}} + \left(\dot{E}_{\mathrm{D}}\right)_{\mathrm{SC}} + \left(\dot{E}_{\mathrm{D}}\right)_{\mathrm{comp2}} + \left(\dot{E}_{\mathrm{D}}\right)_{\mathrm{cond2}} + \left(\dot{E}_{\mathrm{D}}\right)_{\mathrm{Ex.valve2}}\end{aligned} \tag{25}$$

Exergetic Efficiency

The exergetic efficiency is the ratio of the total exergy recovered to the total exergy supplied and is given by Dincer and Kanoglu [20]:

$$\eta_{ex} = \frac{\sum \dot{E}_{out}}{\sum \dot{E}_{in}} = 1 - \frac{\sum \dot{E}_{D}}{\sum \dot{E}_{in}} \tag{26}$$

where η_{ex} is the exergetic efficiency of the cycle. $\sum \dot{E}_{out}$, $\sum \dot{E}_{in}$ and $\sum \dot{E}_{D}$ are the total exergy recovered, supplied and destructed, respectively.

The exergetic efficiency of vapour compression refrigeration system is defined as the ratio of the exergy of heat absorbed in the evaporator from the space to be cooled at temperature T_b to the actual compressor work input ($\dot{W}_{comp}$) [19]. The exergetic efficiency is the ratio of exergy in products to the exergy of fuel. The exergetic efficiency of dedicated mechanically subcooled, subcooler and overall VCR cycles is given by Eqs. (27)–(29).

$$\eta_{ex(DSC)} = \frac{\left|\dot{Q}_{e,DSC}\left(1 - \frac{T_0}{T_{b,DSC}}\right)\right|}{\dot{W}_{comp1}} \tag{27}$$

$$\eta_{ex(SC)} = \frac{\left|\dot{Q}_{e,SC}\left(1 - \frac{T_0}{T_{b,SC}}\right)\right|}{\dot{W}_{comp2}} \tag{28}$$

$$\eta_{ex(OC)} = \frac{\left|\dot{Q}_{e,DSC}\left(1 - \frac{T_0}{T_{b,DSC}}\right)\right|}{\dot{W}_{comp1} + \dot{W}_{comp2}} \tag{29}$$

where T_0 is the ambient or dead state temperature.

Exergy Destruction Ratio (EDR)

The EDR is the total exergy destruction in the system to the exergy in the products [19] and is given by Eq. (30).

$$EDR = \frac{\dot{E}_{D,total}}{\dot{E}_{P}} = \frac{1}{\eta_{ex}} - 1 \tag{30}$$

The exergy destruction ratio for the dedicated mechanically subcooled, subcooler and overall VCR cycles is given in the following Eqs. (31)–(33).

$$EDR_{DSC} = \frac{\sum(\dot{E}_{D})_{DSC}}{\dot{E}_{P,DSC}} = \frac{\sum(\dot{E}_{D})_{DSC}}{\left|\dot{Q}_{e,DSC}\left(1 - \frac{T_0}{T_{b,DSC}}\right)\right|} \tag{31}$$

$$\mathrm{EDR_{SC}} = \frac{\sum\left(\dot{E}_{\mathrm{D}}\right)_{\mathrm{SC}}}{\dot{E}_{\mathrm{P,SC}}} = \frac{\sum\left(\dot{E}_{\mathrm{D}}\right)_{\mathrm{SC}}}{\left|\dot{Q}_{\mathrm{e,SC}}\left(1 - \frac{T_0}{T_{\mathrm{b,SC}}}\right)\right|} \tag{32}$$

$$\mathrm{EDR_{OC}} = \frac{\sum\left(\dot{E}_{\mathrm{D}}\right)_{\mathrm{OC}}}{\dot{E}_{\mathrm{P,DSC}}} = \frac{\sum\left(\dot{E}_{\mathrm{D}}\right)_{\mathrm{OC}}}{\left|\dot{Q}_{\mathrm{e,DSC}}\left(1 - \frac{T_0}{T_{\mathrm{b,DSC}}}\right)\right|} \tag{33}$$

2.3 Assumptions

The current work explores the performance improvement of dedicated mechanically subcooled (DSC) vapour compression refrigeration cycle exergetically. The mathematical formulation of thermodynamic relations has been carried out considering mass, energy and work conservation principles for system and system components.

The following assumptions has been considered to formulate the complex thermodynamic model of dedicated mechanically subcooled (DSC) vapour compression refrigeration cycle except where the variation of physical parameters is involved.

- It is assumed that the state of refrigerant is dry and saturated at the entry of compressor at state points 1 and 5.
- The difference between evaporator temperature and the temperature of space to be cooled ($T_{\mathrm{b,DSC}} - T_{\mathrm{e,DSC}}$, $T_{\mathrm{b,SC}} - T_{\mathrm{e,SC}}$) is 5 °C.
- The range of variation of evaporator 1 temperature ($T_{\mathrm{e,DSC}}$) is −20 to 10 °C.
- The range of variation of condenser 1 temperature ($T_{\mathrm{e,SC}}$) is 30–50 °C.
- The heat losses and pressure losses from the system and system components are negligible. The whole system operates in a steady-state condition.
- The range of degree of subcooling $(\Delta T)_{\mathrm{SC}}$ is 5 to 30 °C.
- The pressure drop in evaporator (δ_{e}) and condenser (δ_{c}) is assumed to be zero.

3 Results and Discussions

Energy and exergy analysis of dedicated mechanically subcooled (DSC) vapour compression refrigeration cycle has been performed using a computer software-based program in Engineering Equation Solver (EES) [21] as shown in Fig. 1. The considered refrigerants for the analysis are R134a, R1234yf and R1234ze. The computation of the various performance parameters, viz. Compressor work, COP, exergetic efficiency, total exergy destruction rate and exergy destruction ratio (EDR), has been done by calling built-in functions (i.e. specific entropy, specific enthalpy, temperature and pressure) of the EES library.

The results from the present analysis have been compared with the results of Arora and Kaushik [19]. It is observed that the difference in the value of COP and exergetic efficiency is within a range of ±1%. The difference in results may be due to the pressure drop in evaporator and condenser is assumed to be zero.

Table 1 Input variable considered except where the variation of these system variables involved [12, 19]

S. No.	Input variables	Values
1	Evaporator 1 temperature ($T_{e,DSC}$)	−10 °C
2	Degree of subcooling ($(\Delta T)_{sc}$)(3–3a)	5 °C
3	Condenser 1 and condenser 2 temperature ($T_{c,DSC}$ & $T_{c,SC}$), assuming summer conditions in a country near the equator line	50 °C
4	Isentropic efficiency of compressor (η_{comp1}, η_{comp2})	80%
5	Effectiveness of subcooler (ε_{SC})	0.8
6	Net refrigerating effect ($\dot{Q}_{e,DSC}$)	3.5167 kW
7	Ambient or dead state temperature (T_0) and pressure (P_0)	25 °C & 101.325 kPa

3.1 Effect of Subcooler Effectiveness

The effect of effectiveness of subcooler (ε_{SC}) on various performance parameters, viz. degree of subcooling $(\Delta T)_{sc}$, compressor work $\left(\dot{W}_C\right)$, $COP_{max.}$, exergetic efficiency (η_{ex}), total exergy destruction rate $\left(\dot{E}_{D,Total}\right)$ and

exergy destruction ratio (EDR), for the considered refrigerants R1234ze, R1234yf and R134a has been illustrated in Fig. 3a–f).

Figure 3a shows that the effect of effectiveness of subcooler (ε_{SC}) on degree of subcooling $(\Delta T)_{sc}$. The degree of subcooling increases with increase in effectiveness of subcooler. The effectiveness is given by $\varepsilon_{SC} = \frac{T_3 - T_{3a}}{T_3 - T_8}$ (Eq. 10), where degree of subcooling is $T_3 - T_{3a}$, which is directly proportional to the ε_{SC}. Hence, the value of $(\Delta T)_{sc}$ increases with increase in effectiveness of subcooler. It has been observed that the maximum value of DOS (28.84) is for R1234ze. However, the minimum value (9.48) is for R134a.

Figure 3b illustrates the variation of compressor work $\left(\dot{W}_C\right)$ with effectiveness of subcooler (ε_{SC}) for DSC, OC, SC and SVCR. The value of $\left(\dot{W}_C\right)$ decreases with increase in effectiveness of subcooler for DSC and OC. However, compressor work increases with increase in (ε_{SC}) for subcooler cycle. For the refrigerating load $\dot{Q}_{e,DSC} = 3.5167$ kW (Table 1), the mass flow rate of refrigerant decreases with increase in $(\Delta T)_{sc}$ and the value of $(\Delta T)_{sc}$ increases with increase in (ε_{SC}). Therefore, the compressor work of DSC and OC decreases for constant value of $T_{e,DSC}$ and $T_{c,DSC}$ with increase in effectiveness of subcooler. However, the cooling load of subcooler cycle increases with increase in DOS ($(\Delta T)_{sc}$), by which the mass flow rate of refrigerant increases with increase in effectiveness of subcooler. Hence, the compressor work of subcooler cycle (SC) increases with increase in ε_{SC}. It can be observed that the maximum compressor work of DSC and OC is less than that of simple VCR (SVCR). The maximum value compressor work is for R1234yf and minimum for R1234ze in DSC and OC.

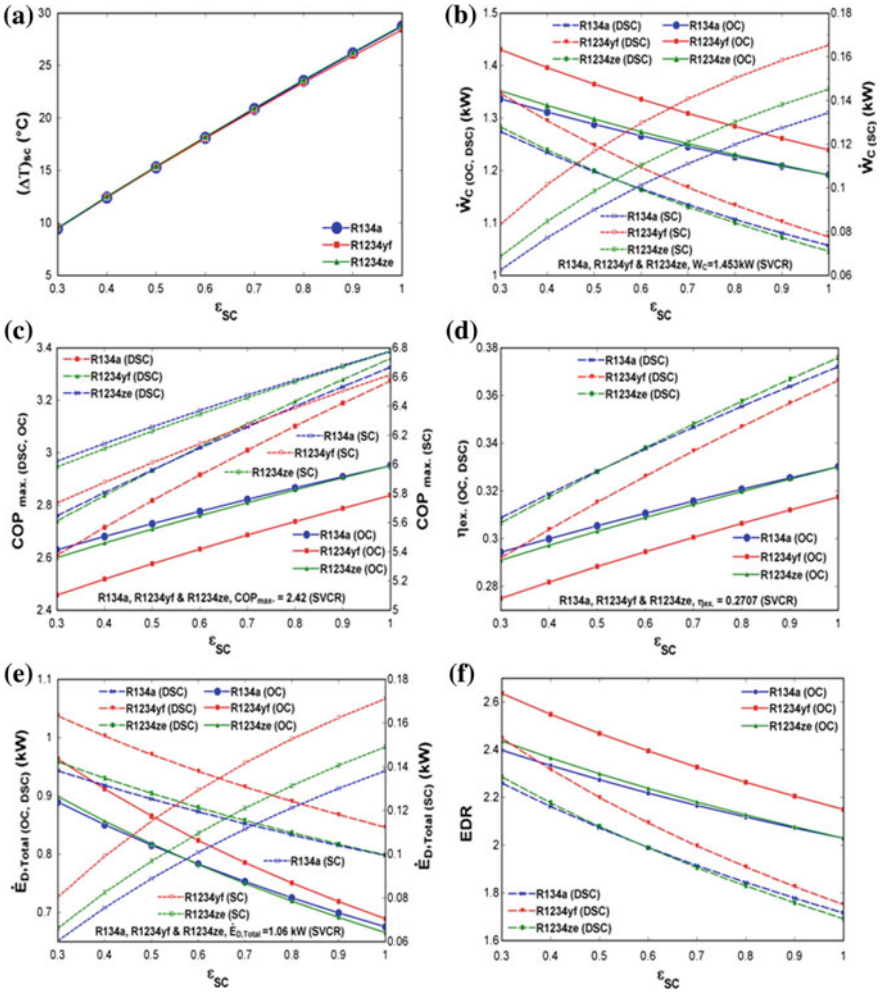

Fig. 3 **a** Effect of effectiveness of subcooler (ε_{SC}) on degree of subcooling $(\Delta T)_{sc.}$ **b** Variation in compressor work $\left(\dot{W}_C\right)$ with effectiveness of subcooler (ε_{SC}). **c** Variation in $COP_{max.}$ with effectiveness of subcooler (ε_{SC}). **d** Effect of effectiveness of subcooler (ε_{SC}) on exergetic efficiency (η_{ex}). **e** Effect of effectiveness of subcooler (ε_{SC}) on total exergy destruction rate $\left(\dot{E}_{D,Total}\right)$. **f** Variation in exergy destruction ratio (EDR) with effectiveness of subcooler (ε_{SC})

Figure 3c depicts the variation of maximum COP ($COP_{max.}$) with effectiveness of subcooler (ε_{SC}). The value of $COP_{max.}$ increases with increase in effectiveness of subcooler. For the constant refrigerant load $\dot{Q}_{e,DSC} = 3.5167$ kW (Table 1), the compressor work decreases with increase in ε_{SC} (Fig. 3a, b). Thus, the maximum value of COP increases with increase in ε_{SC} for DSC and OC. However, the cooling load of SC increases with increase in ε_{SC}. Thus, the value of $COP_{max.}$ of SC increases with increase in ε_{SC}. It is observed that the value of $COP_{max.}$ is higher for DSC, OC and SC than that of SVCR. The value of $COP_{max.}$ is maximum for R1234ze and minimum for R1234yf.

Figure 3d shows the effect of effectiveness of subcooler (ε_{SC}) on exergetic efficiency (η_{ex}). The value of η_{ex} increases with increase in ε_{SC} for DSC and OC and remains constant in SVCR for the refrigerants considered. The exergetic efficiency of OC and DSC is given by $\eta_{ex(DSC)} = \frac{\left|\dot{Q}_{e,DSC}\left(1-\frac{T_0}{T_{b,DSC}}\right)\right|}{\dot{W}_{comp1}}$ (Eq. 27) and $\eta_{ex(OC)} = \frac{\left|\dot{Q}_{e,DSC}\left(1-\frac{T_0}{T_{b,DSC}}\right)\right|}{\dot{W}_{comp1}+\dot{W}_{comp2}}$ (Eq. 29), in which the term $\left|\dot{Q}_{e,DSC}\left(1-\frac{T_0}{T_{b,DSC}}\right)\right|$ is constant and the compressor work $\dot{W}_{comp1}$ decreases and $\dot{W}_{comp2}$ increases with increase in effectiveness of subcooler (Fig. 3b). However, the increase in $\dot{W}_{comp2}$ is very less as compared to the values of $\dot{W}_{comp1}$. Thus, the exergetic efficiency of DSC and OC increases with increase in ε_{SC}. It is observed that the value of η_{ex} of DSC and OC is more than that of simple VCR cycle. The maximum and minimum values of η_{ex} are for R1234ze and R1234yf.

Figure 3e shows the effect of effectiveness of subcooler (ε_{SC}) on total exergy destruction rate $\left(\dot{E}_{D,Total}\right)$. The value of $\dot{E}_{D,Total}$ decreases with increase in ε_{SC} for DSC and OC. However, the value of $\dot{E}_{D,Total}$ increases with increase in ε_{SC} for SC. $\dot{E}_{D,Total}$ remains constant for simple VCR cycle. The exergy recovered from the system components increases with increase in ε_{SC} (Fig. 3d). Therefore, the exergy destruction in each system component decreases with increase in ε_{SC}, which results in decrease in $\dot{E}_{D,Total}$ with increase in ε_{SC}. However, the amount of heat transfer to the evaporator 2 increases with increase in ε_{SC} as the degree of subcooling increases with increase in ε_{SC} (Fig. 3a). It has been observed that the value of $\dot{E}_{D,Total}$ in DSC and OC is less than that of simple VCR cycle. The minimum and maximum values of $\dot{E}_{D,Total}$ are for R1234ze and R1234yf in DSC and OC. However, the minimum and maximum values of $\dot{E}_{D,Total}$ are for R134a and R1234yf in SC.

Figure 3f illustrates the variation in exergy destruction ratio (EDR) with effectiveness of subcooler (ε_{SC}). The value of EDR in DSC and OC decreases with increase in ε_{SC} for refrigerants considered. EDR of DSC and OC is given by $\frac{\sum(\dot{E}_D)_{DSC}}{\left|\dot{Q}_{e,DSC}\left(1-\frac{T_0}{T_{b,DSC}}\right)\right|}$ (Eq. 31) and $\frac{\sum(\dot{E}_D)_{OC}}{\left|\dot{Q}_{e,DSC}\left(1-\frac{T_0}{T_{b,DSC}}\right)\right|}$ (Eq. 33), which is directly proportional to the $\dot{E}_{D,Total}$ and inversely proportional to the $\left|\dot{Q}_{e,DSC}\left(1-\frac{T_0}{T_{b,DSC}}\right)\right|$, and the term $\left|\dot{Q}_{e,DSC}\left(1-\frac{T_0}{T_{b,DSC}}\right)\right|$ remains constant, and the value of $\dot{E}_{D,Total}$ decreases with increase in ε_{SC}. This results in decrease in EDR with increase in ε_{SC}. It can be observed that the minimum and maximum values of EDR are for R1234ze and R1234yf, respectively.

3.2 Effect of Compressor Efficiency

The effect of isentropic efficiency of compressor 1 and compressor 2 $(\eta_{comp.1}, \eta_{comp.2})$ on various performance parameters, viz. compressor work $(\dot{W}_C)$, $COP_{max.}$, exergetic efficiency (η_{ex}), total exergy destruction rate $(\dot{E}_{D,Total})$ and exergy destruction ratio (EDR), for the considered refrigerants R1234ze, R1234yf and R134a has been shown in Fig. 4a, e. It is observed that the optimum value of degree of subcooling for the maximum COP is 23.55, 23.39 and 23.65 for R134a, R1234yf and R1234ze, respectively.

Figure 4a shows the effect of isentropic efficiency of compressor 1 and compressor 2 $(\eta_{comp.1}$ & $\eta_{comp.2})$ on compressor work $(\dot{W}_C)$ of DSC, OC, SC and SVCR cycle for the refrigerants considered. The value of $\dot{W}_C$ decreases with increase in $\eta_{comp.1}$, $\eta_{comp.2}$ for DSC, OC, SC and SVCR cycle. It has been observed that the value of $\dot{W}_C$ is minimum for R1234ze and maximum for R1234yf.

Figure 4b shows the effect of isentropic efficiency of compressor 1 and compressor 2 $(\eta_{comp.1}, \eta_{comp.2})$ on maximum COP ($COP_{max.}$) for OC, DSC, SC and SVCR cycle. The value of $COP_{max.}$ increases with increase in $\eta_{comp.1}$, $\eta_{comp.2}$. For the constant refrigerating load $\dot{Q}_{e,DSC} = 3.5167$ kW (Table 1), the compressor work of compressor 1 and compressor 2 decreases with increase in $\eta_{comp.1}$, $\eta_{comp.2}$ (Fig. 4a). Hence, the value of $COP_{max.}$ increases with increase in $\eta_{comp.1}$, $\eta_{comp.2}$. It can also be observed that the value of $COP_{max.}$ for OC, DSC and SC is higher than that of SVCR cycle. The maximum and minimum values of $COP_{max.}$ are for R1234ze and R1234yf.

Figure 4c shows the effect of isentropic efficiency of compressor 1 and compressor 2 $(\eta_{comp.1}, \eta_{comp.2})$ on exergetic efficiency (η_{ex}) for OC, DSC and SVCR cycle. The exergetic efficiency increases with increase in $\eta_{comp.1}$, $\eta_{comp.2}$. The exergetic efficiency of OC and DSC is given by Eqs. (27) and (29), in which the term $\left|\dot{Q}_{e,DSC}\left(1 - \frac{T_0}{T_{b,DSC}}\right)\right|$ remains constant and the compressor work $\dot{W}_{comp1}$ and $\dot{W}_{comp2}$ decreases with increase in $\eta_{comp.1}$, $\eta_{comp.2}$. Thus, the value of η_{ex} increases with increase in $\eta_{comp.1}$, $\eta_{comp.2}$ for refrigerants considered. It can be observed that the exergetic efficiency of DSC and OC is higher than that of SVCR cycle. The maximum and minimum values of η_{ex} are for R1234ze and R1234yf, respectively.

Figure 4d illustrates the variation in total exergy destruction rate $(\dot{E}_{D,Total})$ with isentropic efficiency of compressor 1 and compressor 2 $(\eta_{comp.1}, \eta_{comp.2})$. The value of $\dot{E}_{D,Total}$ decreases with increase in $\eta_{comp.1}$, $\eta_{comp.2}$ for OC, DSC, SC and SVCR cycle. The exergy recovered from the system components increases with increase in $\eta_{comp.1}$, $\eta_{comp.2}$ (Fig. 4c). The exergy destruction rate of the system components decreases with increase in $\eta_{comp.1}$, $\eta_{comp.2}$. Therefore, the $\dot{E}_{D,Total}$ decreases with increase in $\eta_{comp.1}$, $\eta_{comp.2}$. It has been observed that the value of $\dot{E}_{D,Total}$ of OC and DSC is lower than that of SVCR cycle. The minimum and maximum values of $\dot{E}_{D,Total}$ are for R1234yf and R1234ze, respectively.

Figure 4e depicts the effect of isentropic efficiency of compressor 1 and compressor 2 $(\eta_{comp.1}, \eta_{comp.2})$ on exergy destruction ratio (EDR) for refrigerants considered.

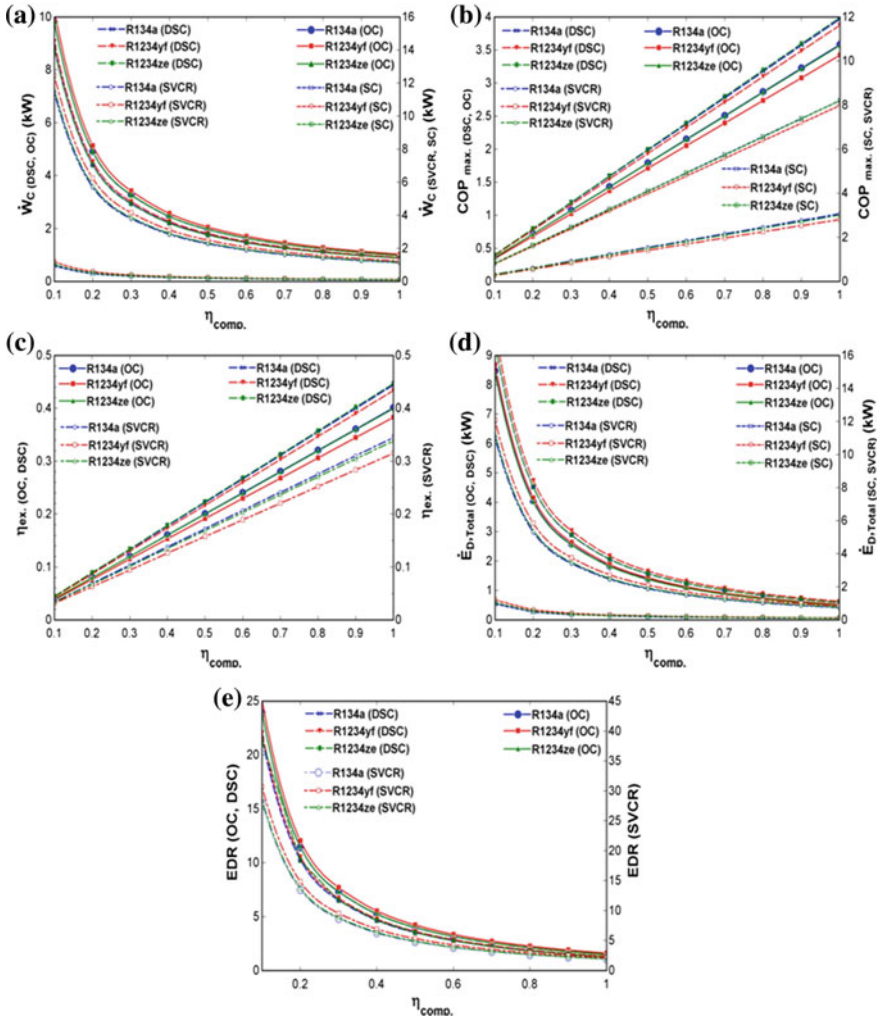

Fig. 4 **a** Variation in compressor work $\dot{W}_C$ with isentropic efficiency of compressor $(\eta_{comp.})$. **b** Effect of isentropic efficiency of compressor $(\eta_{comp.})$ on COP_{max}. **c** Variation in exergetic efficiency (η_{ex}) with isentropic efficiency of compressor $(\eta_{comp.})$. **d** Effect of isentropic efficiency of compressor $(\eta_{comp.})$ on total exergy destruction rate $(\dot{E}_{D,Total})$. **e** Effect of isentropic efficiency of compressor $(\eta_{comp.})$ on exergy destruction ratio (EDR)

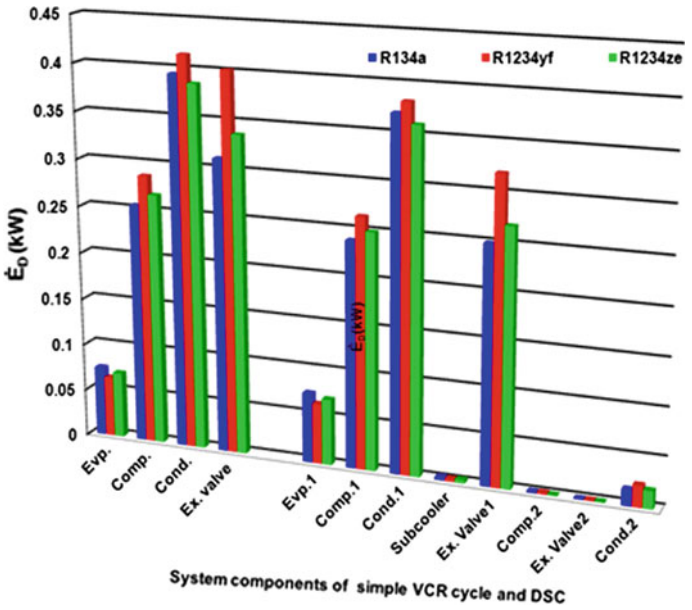

Fig. 5 Exergy destruction rate of system components in simple VCR cycle and DSC

The EDR of OC, DSC and SVCR cycle decreases with increase in $\eta_{\text{comp.1}}$, $\eta_{\text{comp.2}}$. EDR is given by $\frac{\sum(\dot{E}_D)_{OC}}{\left|\dot{Q}_{e,DSC}\left(1-\frac{T_0}{T_{b,DSC}}\right)\right|}$ (Eq. 33) which is proportional to $\dot{E}_{D,Total}$. The value of $\dot{E}_{D,Total}$ increases, and the term $\left|\dot{Q}_{e,DSC}\left(1-\frac{T_0}{T_{b,DSC}}\right)\right|$ remains constant with increase in $\eta_{\text{comp.1}}$, $\eta_{\text{comp.2}}$ (Fig. 4d). Hence, the value of EDR decreases with increase in $\eta_{\text{comp.1}}$, $\eta_{\text{comp.2}}$ for refrigerants considered. It is observed that the EDR of OC and DSC is lower than that of SVCR cycle. The minimum and maximum values of EDR are for R1234ze and R1234yf.

Figure 5 shows the exergy destruction rate in system components of simple VCR cycle and dedicated mechanically subcooled (DSC) VCR cycle. The condenser is the site of SVCR and DSC where the maximum exergy destruction takes place. However, the evaporator is the place where the minimum amount of exergy destruction occurs. In simple VCR cycle, the expansion valve is the site where more exergy destruction occurs in comparison with compressor and evaporator. Similarly, in DSC, expansion valve 1 is the second site of exergy destruction after condenser 1. However, subcooler, compressor 2 and expansion valve 2 are the sites where very less amount of exergy destruction takes place in comparison with other system components.

4 Conclusions

The present work analysed the dedicated mechanically subcooled vapour compression refrigeration cycle (DSC) exergetically. The performance of the overall cycle (OC), DSC, subcooler cycle (SC) and simple vapour compression refrigeration (SVCR) cycle has been compared for R1234ze, R1234yf and R134a. A computer software-based program in EES has been formulated for the theoretical performance analysis. It involves the variation of effectiveness of subcooler and isentropic efficiency of the compressor to check the performance parameters, viz. compressor work, COP, exergetic efficiency, total exergy destruction rate and exergy destruction ratio. The exergy destruction in each system component has also been shown. The main concluding points of the present work are as follows:

- The COP of dedicated mechanically subcooled (DSC) VCR cycle and overall cycle (OC) is higher than that of simple VCR cycle. However, the COP of SC is the highest.
- The exergy destruction rate of system components of simple VCR cycle is higher than that of the DSC.
- The performance (COP & η_{ex}) of DSC and OC improves with increase in subcooler effectiveness and isentropic efficiency of compressors.
- The higher value of subcooler effectiveness and isentropic efficiency of compressor reduces the total exergy destruction rate and EDR.
- R1234ze performs better than that of R1234yf and competes with R134a. It can be a good alternate to R134a.
- Condenser 1 is the site where the maximum amount of exergy destruction occurs in comparison with other system components.
- Expansion valve 2 and condenser 2 of the DSC are the sites where the maximum amount of exergy has been recovered.

It is inferred from the above concluding statements that the dedicated mechanically subcooled VCR cycle supersedes in its performance from the simple VCR cycle, and the HFO-R1234ze can be a good alternate to R134a. Condenser 1 is the sensitive system component of DSC.

References

1. Regulation (EU) No 517/2014 of the European Parliament and of the Council of Fluorinated Greenhouse Gases and Repealing Regulation (EC) (2014) No: 842/2006
2. Sarbu I (2014) A review on substitution strategy of non-ecological refrigerants from vapour compression-based refrigeration, air-conditioning and heat pump systems. Int J Refrig 46:123–141
3. Park C, Lee H, Hwang Y, Radermacher R (2015) Review recent advances in vapour compression cycle technologies. Int J Refrig 60:118–134

4. Qureshi BA, Zubair SM (2012) The effect of refrigerant combinations on performance of a vapour compression refrigeration system with dedicated mechanical sub-cooling. Int J Refrig 35:47–57
5. Qureshi BA, Zubair SM (2013) Mechanical sub-cooling vapour compression systems: current status and future directions. Int J Refrig 36:2097–2110
6. Qureshi BA, Inam M, Antar MA, Zubair SM (2013) Experimental energetic analysis of a vapour compression refrigeration system with dedicated mechanical sub-cooling. Appl Energy 102:1035–1041
7. Zubair SM (1990) Improvement of refrigeration/air conditioning performance with mechanical subcooling. Int J Refrig 15(5):427–433
8. Zubair SM (1994) Thermodynamics of vapour-compression refrigeration cycle with mechanical sub-cooling. Energy 19:707–715
9. Zubair SM, Yaqub M, Khan SH (1996) Second-law-based thermodynamic analysis of two-state and mechanical sub-cooling refrigeration cycles. Int J Refrig 19:506–516
10. Pottker G, Hrnjak P (2015) Experimental investigation of the effect of condenser subcooling in R134a and R1234yf air-conditioning systems with and without internal heat exchanger. Int J Refrig 50:104–113
11. Arora A (2009) Energy and exergy analysis of compression, absorption, and combined cycle cooling systems. PhD thesis, Centre for Energy Studies: IIT, Delhi
12. Arora A, Arora BB, Pathak BD, Sachdev HL (2007) Exergy analysis of a vapour compression refrigeration system with R-22, R-407C and R-410A. Int J Exergy 4:441–454
13. Arora A, Dixit M, Kaushik SC (2016) Computation of optimum parameters of a half effect water-lithium bromide vapour absorption refrigeration system. J Thermal Eng 2(2):683–692
14. Arora A, Dixit M, Kaushik SC (2016) Energy and exergy analysis of a double effect parallel flow LiBr/H_2O absorption refrigeration system. J Thermal Eng 2(2):541–549
15. Dixit M, Arora A, Kaushik SC (2016) Enery and exergy analysis of a waste heat driven cycle for triple effect refrigeration. J Thermal Eng 2(5):954–961
16. Dixit M, Kaushik SC, Arora A (2017) Energy and exergy analysis of absorption-compression cascade refrigeration system. J Thermal Eng 3(5):1466–1477
17. Kalla SK, Arora BB, Usmani JA (2018) Alternative refrigerants for HCFC- A review. J Thermal Engg 4(3):1998–2017
18. Bejan A, Tsatsaronis G, Moran MX (1996) Thermal design and optimization book. John Wiley & Sons, Inc., USA
19. Arora A, Kaushik SC (2008) T, heoretical analysis of a vapour compression refrigeration system with R502, R404A and R507A. Int J Refrig 31:998–1005
20. Dincer I, Kanoglu M (2010) Refrigeration systems and applications, 2nd edn. Wiley, UK
21. Klein SA, Alvarado F (2012) Engineering equation solver. F Chart Software, Middleton,WI. Version 9, 224-3D

The Effect of Eco-friendly Refrigerants on Performance of Vapor Compression Refrigeration System with Dedicated Mechanical Subcooling

Naushad Ahmad Ansari, Akhilesh Arora, Samsher and K. Manjunath

Abstract The demand for high-performance refrigeration systems with eco-friendly refrigerants is increasing due to global warming. In this article, the thermodynamic analysis of a vapor compression refrigeration system with dedicated mechanical subcooling using eco-friendly refrigerants R1243zf, R1233zd(E) is carried out and their performance is compared with refrigerant R134a. The parameters like COP and exergetic efficiency of the system is computed. The effects of subcooling temperature, condenser temperature, evaporator temperature, compressor efficiency, and effectiveness of heat exchanger are also investigated and discussed. The performance of the system can be directly related to subcooling temperature. There is an optimum value of subcooling temperature predicted for the system in this article. In the study, it is observed that low GWP refrigerant R1233zd(E) is a better-performing refrigerant than R134a, whereas R1243zf is also a low GWP refrigerant which has slightly lower COP and exergetic efficiency than R134a.

Keywords COP · Exergetic efficiency · Subcooling · Eco-friendly

Nomenclature

COP Coefficient of performance

N. A. Ansari (✉) · A. Arora · Samsher
Mechanical Engineering Department, Delhi Technological University,
Bawana Road, Delhi 110042, India
e-mail: naushad.nsr@gmail.com

A. Arora
e-mail: akhilesharora@dce.ac.in

Samsher
e-mail: samsher@dce.ac.in

K. Manjunath
Mechanical Engineering, Ch. B. P. Government Engineering College, Jaffarpur,
Delhi 110073, India
e-mail: manjukmys@gmail.com

G. Zhang et al. (eds.), *Advances in Energy and Built Environment*, Lecture Notes
in Civil Engineering 36, https://doi.org/10.1007/978-981-13-7557-6_4

GWP	Global warming potential
ODP	Ozone depletion level
Q	Heat transfer (kW)
W	Work transfer (kW)
h	Enthalpy (kJ/kg)
T	Temperature (°C)
P	Pressure (kPa)
η	Efficiency
$\dot{m}$	Mass flow rate (kg/s)
ε	Effectiveness
EP	Exergy in product (kW)

Subscripts

Comp	Compressor
r	Refrigerant
ex	Exergetic
0	Ambient states
scc	Subcooling refrigeration cycle

1 Introduction

A dedicated mechanical subcooling vapor compression refrigeration cycle consists of two vapor compression cycle where subcooling of refrigerant of main compression cycle at the exit of the condenser improves the performance of the system, thus saving the high-grade electrical energy which also contributes to a clean environment. It is accomplished by adding a small subcooler cycle with the main cycle and thus forming a system known as dedicated mechanical subcooling vapor compression refrigeration cycle. Apart from ozone depletion potential (ODP), the global warming potential has also become a very important criterion for the refrigerants to be used in the refrigeration and air-conditioning applications. Chlorofluorocarbons (CFCs) and hydrochlorofluorocarbons (HCFCs) were to be phased out due to their ODP and GWP problems when Montreal Protocol on January 1, 1989, came into force [1, 2]. Hydrofluorocarbons (HFCs) like R134a have zero ODP but due to significantly high GWP needs to be replaced by low GWP refrigerants [3]. All HFCs and other greenhouse gases have to be curbed under Kyoto Protocol agreement which was proposed in December, 1997, and enforced on February 16, 2005. The next-generation refrigerants, hydrochlorofluoroolefins (HCFOs) like R1233zd(E) and hydrofluoroolefins (HFOs) like R1243zf, can become a good alternative due to their very low GWP.

Thornton et al. [4] in their research predicted that the performance of overall dedicated subcooling cycle depended upon the optimum subcooling temperature and the

Table 1 Properties of refrigerants [12, 13]

Name	Atmospheric life	ODP	Solubility in water	Critical temperature	GWP	Boiling point
R-134a	14 years	0	0.11% by weight at 77 °F or 25 °C	252 °F or 122 °C	1200	−14.9 °F or −26.1 °C
R-1233zd(E)	26 days	0	0.19% by weight at 20 °C	439.6 K or 166.6 °C	1	66 °F or 19 °C
R-1243zf	11 days	0	0.33% by weight at 95 °C	222 °F or 105.5 °C	4	−13.3 °F or −25.2 °C

cycle extreme temperatures, i.e., condenser and evaporator temperature. She et al. [5] predicted a 67.67% higher COP of a subcooling system compared to the conventional refrigeration system under same operating conditions. Qureshi and Zubair [6] described exclusively different models of subcooling. Qureshi and Zubair [7] investigated the subcooling model using different refrigerants and showed that R134a is the best-performing refrigerant in main and subcooling cycle. Khan and Zubair [8] investigated an integrated subcooling refrigeration system and predicted that optimum subcooling temperature was approximately arithmetic mean temperature of evaporator and condenser temperature. Qureshi et al. [9] analyzed the mechanical subcooling system and predicted 21% increase in exergetic efficiency compared to the conventional compression refrigeration cycle. Pottker and Hrnjak [10] theoretically analyzed the subcooling system using different refrigerants. Dai et al. [11] analyzed a transcritical CO_2 refrigeration subcooling system and found that maximum rate of increase in COP is to be 43.8% and concluded that discharge pressure and subcooling temperature influenced the subcooling cycle more significantly than other parameters. Lai [12] predicted that R1243zf is a potential refrigerant to replace R134a in a refrigeration system. Miyoshi et al. [13] developed a centrifugal chiller using R1233zd(E) as a refrigerant and predicted it to be a good replacement of R134a as a better-performing refrigerant in chillers.

The objective of this article is to investigate the performance of low GWP refrigerants in a dedicated mechanical subcooling refrigeration cycle which is promising and energy efficient as recorded by the researchers. The properties of the refrigerants used for the analysis are provided in Table 1.

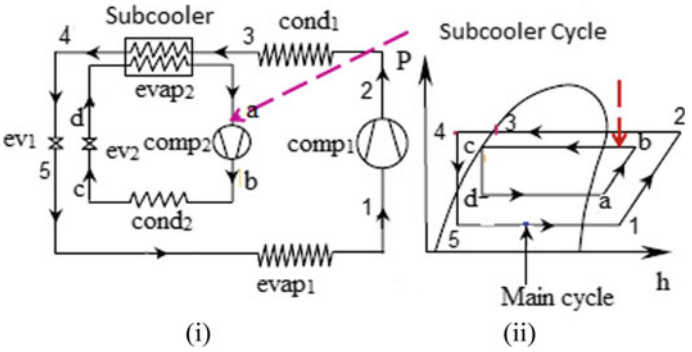

Fig. 1 (i) Schematic diagram of dedicated subcooling compression system and (ii) pressure enthalpy diagram of the system

2 Description of the Dedicated Subcooling Refrigeration System

Figure 1 shows the schematic diagram of the subcooling system where (i) represents the flow diagram and (ii) represents the pressure–enthalpy phase diagram. Points 1–2–3–4–5 is related to the main cycle of dedicated subcooling compression system, and points a–b–c–d is related to smaller cycle termed as subcooler cycle which is coupled with the main cycle at the exit of main cycle condenser (cond1). Compressed refrigerant (1–2) in the main cycle compressor (comp1) passes through cond1 (2–3) releasing heat to the atmosphere. It enters into the subcooler where heat is absorbed by the evaporator (evap2) of the subcooler cycle, or subcooling of the refrigerant takes place. It passes through the expansion valve (ev1) (4–5) of main cycle throttled to low pressure and then passes through the evaporator (evap1) of the main cycle attaining the desired objective of cooling by absorbing the heat from the space to be cooled before entering into comp1 and thus completing the cycle. In the subcooler cycle, which also functions like a conventional vapor compression cycle, the refrigerant is compressed to high pressure (a–b) in compressor (comp2) of the subcooler cycle enters into condenser (cond2) releasing heat to ambient (b–c) before throttling (c–d) to low pressure in expansion valve (ev2) and thereafter enters into the evaporator (evap2) (d–a) of the subcooler cycle where it absorbs heat of main cycle refrigerant acting as a heat exchanger. The refrigerant of the subcooler cycle then enters into comp2 thus completing the cycle.

3 Energy and Exergy Analysis of the System

The energy and exergy analysis is carried out by considering the principle of mass conservation, energy conservation, and exergy conservation.

$$W_{\text{comp1}} = \dot{m}_{\text{r}}(h_2 - h_1) \tag{1}$$

$$W_{\text{comp2}} = \dot{m}_{\text{r}}(h_b - h_a) \tag{2}$$

$$\text{COP}_{\text{s}} = Q_{\text{e}}/W_{\text{comp1}} \tag{3}$$

where COP_s is the simple compression cycle COP.

$$\Delta T_{\text{sub}} = T_3 - T_4 = \delta_{\text{sc}} \tag{4}$$

The effectiveness of the subcooler is defined as:

$$\in_{\text{subcooler}} = (T_3 - T_4)/(T_3 - T_d) \tag{5}$$

$$Q_{\text{e}} = \dot{m}_{\text{r}}(h_1 - h_5) \tag{6}$$

$$W_{\text{comp}} = W_{\text{comp1}} + W_{\text{comp2}} \tag{7}$$

$$\text{COP}_{\text{scc}} = Q_{\text{e}}/\left(W_{\text{comp1}} + W_{\text{comp2}}\right) \tag{8}$$

where COP_{scc} is subcooling compression refrigeration cycle COP.

The exergy in product is defined as:

$$\text{EP}_{\text{scc}} = Q_{\text{e}}(1 - (T_0/T_{\text{r}})) \tag{9}$$

Therefore, exergetic efficiency of the subcooling cycle is given by:

$$\eta_{\text{ex}} = \text{EP}_{\text{scc}}/W_{\text{comp}} \tag{10}$$

3.1 Model Validation

Yilmaz et al. [14] carried an analytical and numerical analysis of a subcooling cycle using R134a as refrigerant in main and subcooler cycle. They calculated the maximum increase of COP up to 30% at an optimum subcooling temperature of 35.5 °C (T_{c} = 60 °C, $T_{\text{e}} = -20$ °C, $\eta_{\text{comp}} = 0.80$) (assumed effectiveness of heat exchanger to be 5 °C less than maximum temperature). In the present study, the maximum increase of 32% in COP is calculated at an optimum temperature of 35.75 °C with the same input conditions. The small variation in result falls within the acceptable limit. Miyoshi et al. [13] calculated the theoretical COP of a simple vapor compression refrigeration system as 6.93 (T_{c} = 38 °C, $T_{\text{e}} = 6$ °C, $\eta_{\text{comp}} = 0.90$) with refrigerant R1233zd(E). In the present study, COP of the simple vapor compression

system is calculated as 6.922 using R1233zd(E) and the same input parameters. The calculated value is fit for validation of results.

4 Results and Discussion

The energy and exergy analysis of the subcooling refrigeration system is carried out by developing a computational model using engineering equation solver (EES) [15]. In the subcooling system, similar pairs of each refrigerant are considered to access the performance; e.g., R1233zd(E) is assumed in main cycle and subcooler cycle, and same is true for R134a and R1243zf. Compressor efficiency of main cycle and subcooler cycle are assumed to be same. Other assumptions for calculation are as follows:

Refrigeration capacity	50 kW
Isentropic efficiency of the compressor	0.65
Evaporator temperature	−35 to 10 °C
Condenser temperature	32 to 55 °C
Subcooling temperature	2 to 37 °C
Effectiveness of subcooler	0.8.

Further, dead state temperature and pressure are considered to be atmospheric, i.e., 25 °C and 1.01324 bar. Enthalpy and entropy reference for the refrigerants are calculated corresponding to dead state temperature. It is assumed that there is no heat loss or pressure drop in other components and connecting lines. The difference between evaporator temperature and space to be cooled is assumed as 5 °C.

4.1 Effect of Condenser Temperature

Figure 2 explores the effect of condenser temperature on coefficient of the performance of the system and also reveals the comparison of the performance of simple vapor compression refrigeration system (COP_s) with the performance of subcooling vapor compression refrigeration system (COP_{scc}). As the condenser temperature decreases, COP of both the system increases, while COP of subcooling system always remains greater than COP of simple compression system, but there is a distinct pattern of increase. COP of R1233zd(E) in subcooling compression cycle is 13.5% higher and 23.31% higher at condenser temperature of 32 and 55 °C, respectively, corresponding to simple compression cycle. Similarly, R134a shows a higher COP increase by 15.35 and 31% and R1243zf shows 15.9 and 33.13% increase for same condenser temperatures compared to simple compression system. Thus, R1233zd(E) is better-performing refrigerant followed by R134a and R1243zf. COP of R1243zf is slightly lower than R134a, but due to very low GWP of 4 and very small life cycle, it can offset the R134a as a preferred refrigerant. Also, the improvement in COP

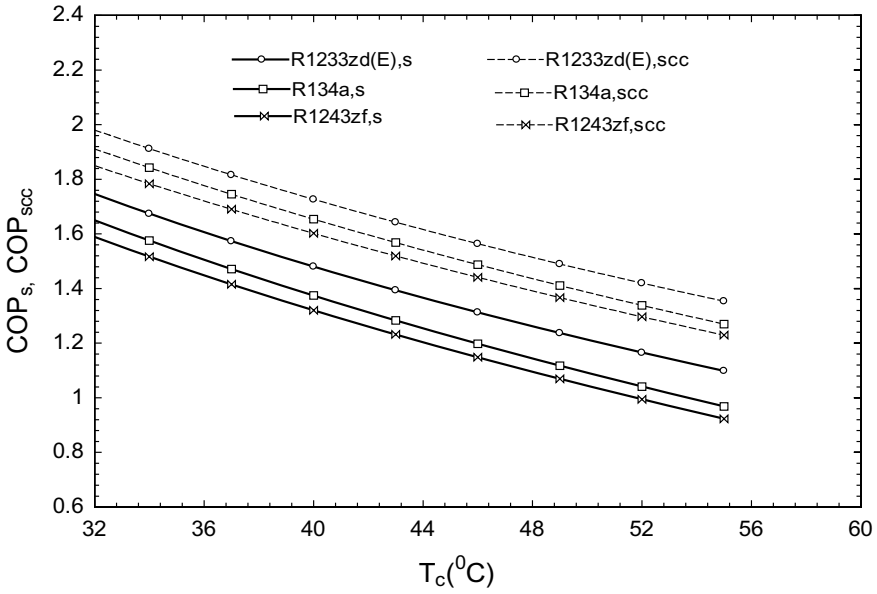

Fig. 2 Condenser temperature versus simple compression refrigeration cycle COP and subcooling compression cycle COP ($T_e = -35$ °C, $\delta_{sc} = 30$ °C)

of R1243zf is significantly better than the corresponding improvement of COP of other two refrigerants for high condenser temperature when it is used in subcooling compression cycle.

4.2 Effect of Evaporator Temperature

Figure 3 presents the effect of evaporator temperature on COP and exergetic efficiency of the subcooling cycle. COP increases with the increase in evaporator temperature, but it is observed that COP of subcooling cycle is improving compared to simple compression cycle. For 1233zd(E), COP improvement is recorded as 1.64% at 10 °C evaporator temperature, and it is 20.85% at −35 °C evaporator temperature. The similar pattern of improvement in COP and exergetic efficiency is observed for R1324a and R1243zf, where R1243zf shows the highest improvement of 28.64% in COP at −35 °C evaporator temperature. R1233zd(E) has the maximum COP of 3.948 and minimum COP of 1.466 at $T_e = 10$ °C and −35 °C, respectively. The corresponding COP of R134a is 3.677 (maximum) and 1.386 (minimum) and for R1243zf is 3.611 (maximum) and 1.343 (minimum) at same evaporator temperatures. The highest exergetic efficiency 33.28% is recorded for R1233zd(E) followed by 31.44% for R134a and 30.46% for R1243zf. At higher evaporator temperature,

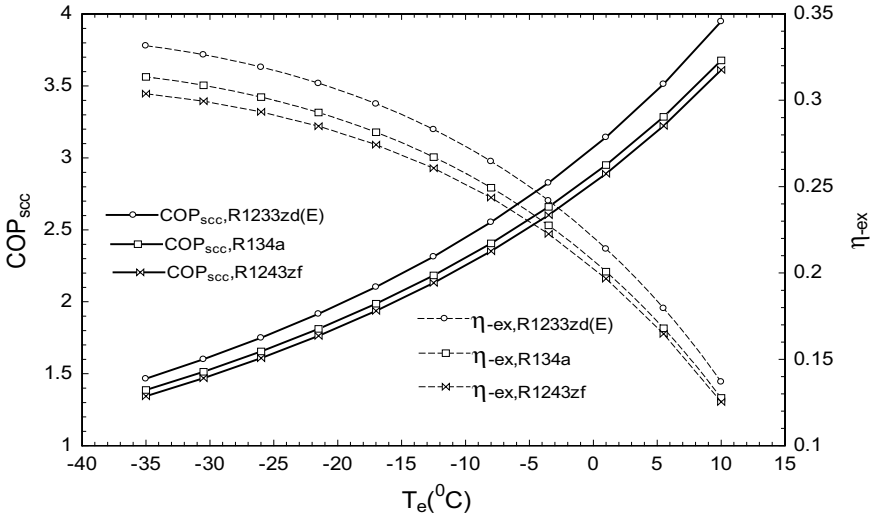

Fig. 3 Evaporator temperature versus COP and exergetic efficiency of subcooling compression refrigeration cycle (T_c = 50 °C, δ_{sc} = 30 °C)

exergetic efficiency curve for the three refrigerants converges, and at 10 °C evaporator temperature, R134a and R1243zf have the same exergetic efficiency.

4.3 Effect of Subcooling Temperature

Figures 4 and 5 explore the effect of subcooling temperature on COP and exergetic efficiency. It is observed that COP and exergetic efficiency are improving with the increase in subcooling temperature; it reaches to maximum at an optimum subcooling temperature which is recorded as approximately 31.5 °C for all the three refrigerants considered in the study, and after attaining this peak, COP and exergetic efficiency decrease with the increase in subcooling temperature. The trends of both the COP and exergetic efficiency curves are similar with respect to subcooling temperature. The optimum subcooling temperature is an important parameter to be considered for design conditions of dedicated subcooling system.

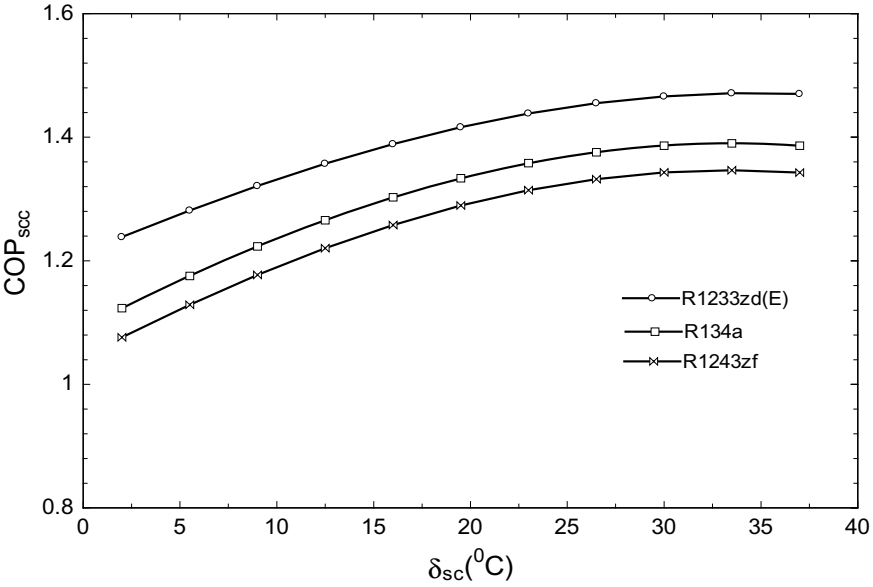

Fig. 4 Subcooling temperature versus subcooling compression refrigeration cycle COP (T_c = 50 °C, $T_e = -35$ °C)

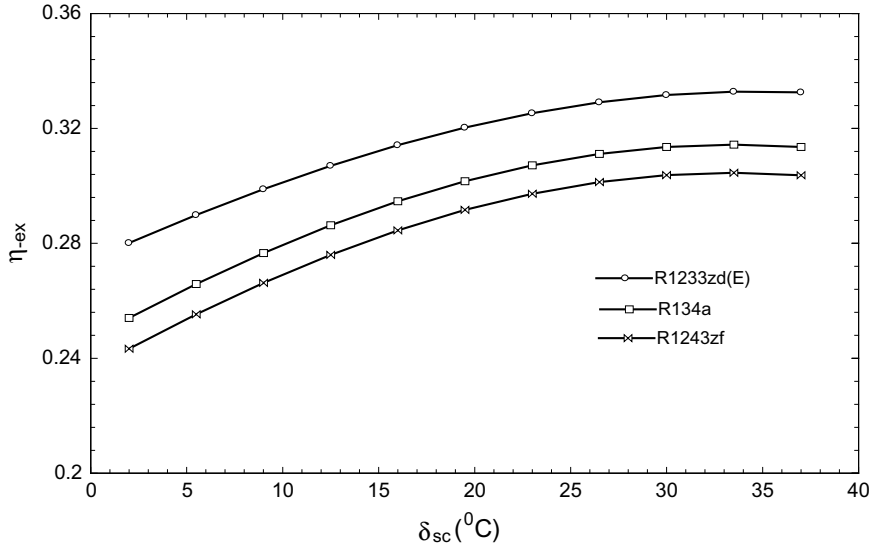

Fig. 5 Subcooling temperature versus exergetic efficiency of subcooling compression refrigeration cycle ($T_c = 50$ °C, $T_e = -35$ °C)

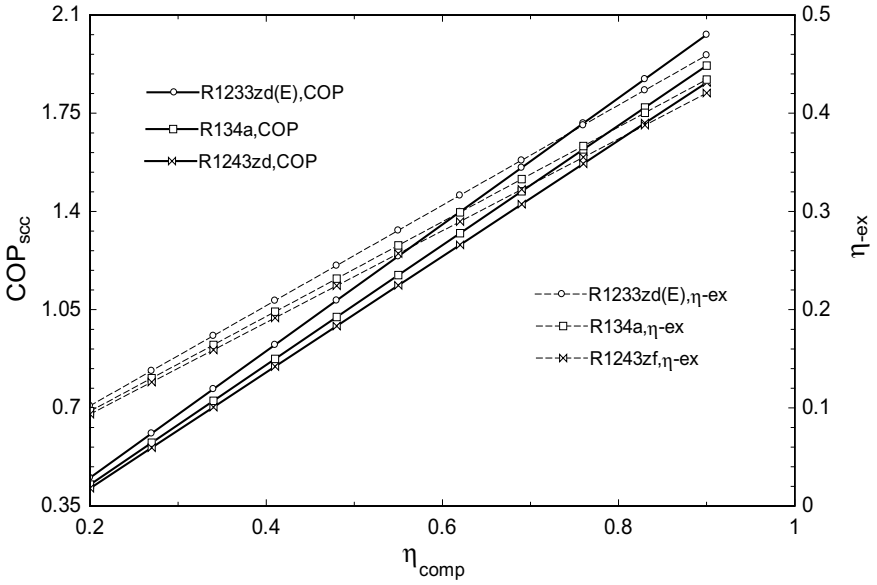

Fig. 6 Compressor efficiency versus COP and exergetic efficiency of subcooling compression refrigeration cycle ($T_c = 50$ °C, $T_e = -35$ °C, $\delta_{sc} = 30$ °C)

4.4 Effect of Compressor Efficiency

Figure 6 shows the effect of compressor efficiency on COP and exergetic efficiency of the system. It is observed that there is a sharp decline in the performance of system with the decrease in compressor efficiency. It is also observed that the COP and exergetic efficiency curves converge for all the three refrigerants with a decrease in compressor efficiency.

4.5 Effect of Subcooler Effectiveness

Figure 7 reveals the effect of subcooler effectiveness on system performance. It is observed that COP and exergetic efficiency decrease with the decrease in effectiveness where the trend of decrease is large at effectiveness values of 0.20–0.60, but thereafter, i.e., beyond 0.60, the effect of subcooler effectiveness is minimal in particular on exergetic efficiency as its curve becomes almost flat, whereas the COP curve smoothens and shows a small increase. The pattern is similar for all the three refrigerants in the study.

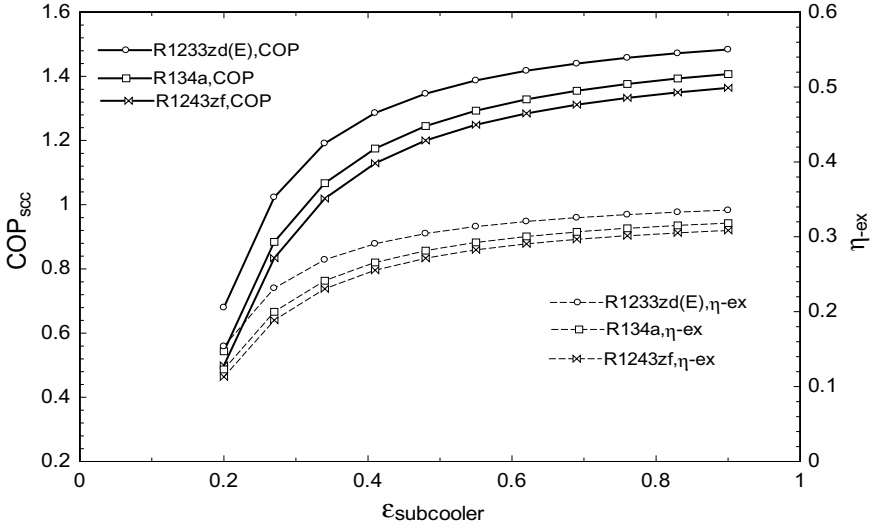

Fig. 7 Effectiveness of subcooler versus COP and exergetic efficiency of subcooling compression refrigeration cycle ($T_c = 50$ °C, $T_e = -35$ °C, $\delta_{sc} = 30$ °C)

5 Conclusion

The effect of evaporator temperature and condenser temperature is very significant on the dedicated mechanical subcooling compression refrigeration cycle compared to a simple vapor compression cycle. The performance of subcooling cycle shows more improvement at higher condenser temperature and lower evaporator temperature over the simple compression cycle. Compressor efficiency and effectiveness of subcooler also influence the performance of the system. COP and exergetic efficiency of R1233zd(E) are noticeably higher than R134a, whereas R1243zf has slightly lower COP and exergetic efficiency than R134a. But improvement in the performance of R1243zf at high condenser and low evaporator temperature is more compared to the corresponding improvement of R1233zd(E) and R134a when used in a subcooling compression refrigeration cycle. Therefore, R1233zd(E) and R1243zf are the potential refrigerants to replace R134a.

References

1. IPCC Climate Change (2015) The physical science basis, The working group I
2. United Nations Environmental Programme (1987) Montreal protocol on substances that deplete the ozone layer, Final Act, New York, United Nations
3. IPCC Fourth Assessment Report (2012)

4. Thornton JW, Klein SA, Mitchell JW (1992) Dedicated mechanical subcooling design strategies for supermarket applications. In: International refrigeration and air conditioning conference: paper-11
5. She X, Yin Y, Zhang X (2014) A proposed subcooling method for vapor compression refrigeration cycle based on expansion power recovery. Int J Refrig 43:50–61
6. Qureshi BA, Zubair SM (2013) Mechanical subcooling vapor compression systems: current status and future directions. Int J Refrig 36:2097–2110
7. Qureshi BA, Zubair SM (2012) The effect of refrigerant combinations on performance of a vapor compression refrigeration system with dedicated mechanical subcooling. Int J Refrig 35:47–57
8. Khan JR, Zubair SM (2000) Design and rating of an integrated mechanical subcooling vapor compression refrigeration system. Energy Conv Manage 41:1201–1222
9. Qureshi BA, Inam M, Antar MA, Zubair SM (2013) Experimental energetic analysis of a vapor compression refrigeration system with dedicated mechanical subcooling. Appl Energy 102:1035–1041
10. Pootker G, Hrnjak P (2015) Effect of the condenser subcooling on the performance of vapor compression systems. Int J Refrig 50:156–164
11. Dai B, Liu S, Sun Z, Ma Y (2017) Thermodynamic performance analysis of CO_2 transcritical refrigeration cycle assisted with dedicated mechanical subcooling. Energy Procedia 105:2033–2038
12. Lai NA (2014) Thermodynamic properties of HFO-1243zf and their application in study on a refrigeration cycle. Appl Therm Eng 70(1):1–6
13. Miyoshi N, Suemitsu R, Togano Y, Kanki Y, Hasegawa Y (2016) Centrifugal chiller using HFO-1233zd(E). In: Jraia international symposium: JRAIA2016
14. Yilmaz A, Aktas AE, Erdinc MT, Yilmaz T (2017) Analytical and numerical investigation of a refrigeration cycle integrated with another cycle for subcooling. In: International advanced research & engineering congress, pp 257–263
15. Klein SA, Alvarado F (2017) Engineering equation solver, V10.097. F Chart Software, Middleton, WI

Performance Analysis of ORC with Environment-Friendly Working Fluids Novec 649 and R1233zd[E] as Alternative to R245fa

Pradeep Kumar Jain, Akhilesh Arora and B. B. Arora

Abstract In the present work, two low GWP fluids, viz. Novec 649 and HFO1233zd[E], have been considered to replace R245fa in ORC with and without IHE. A computational model is developed in EES software for the evaluation of cycles. The cycles are studied on the basis of the first law of thermodynamics, and exergy analysis is also carried out. The results substantiate that the first law efficiency of Novec 649 is lower than R245fa, whereas R1233zd[E] shows better first law efficiency than R245fa. The first law efficiency increases with increase in evaporator temperature, whereas it decreases with increase in condenser temperature. The usage of IHE improves the first law efficiency. The exergetic efficiency for R1233zd[E] is higher than other fluids in comparison with R245fa and Novec 649. The effect of degree of superheat in both cycles on exergetic efficiency is to decrease it.

Keywords Energy analysis · Exergy analysis · ORC · Environment-friendly working fluids · Novec 649 · R1233zd[E]

Nomenclature

ExD	Exergy destroyed (kJ)
h	Enthalpy (kJ/kg)
$\dot{m}$	Mass flow rate (kg/s)
s	Entropy (kJ/kgK)
T	Temperature (°C)
W	Electric power (kW)
GWP	Global warming potential
IHE	Internal heat exchanger
ODP	Ozone depleting potential
ORC	Organic Rankine cycle

P. K. Jain (✉) · A. Arora · B. B. Arora
Department of Mechanical Engineering, Delhi Technological University, Bawana Road, New Delhi 110042, India
e-mail: pdcej@yahoo.co.in

G. Zhang et al. (eds.), *Advances in Energy and Built Environment*, Lecture Notes in Civil Engineering 36, https://doi.org/10.1007/978-981-13-7557-6_5

Greek Alphabets

ε IHE effectiveness
η Efficiency

Subscripts

c	Critical
cond	Condenser
e	Exit
em	Electromechanical
evp	Evaporator
exp	Expander
H	Heat source
i	Inlet
is	Isentropic
p	Pump
tot	Total
v	Volumetric

1 Introduction

Organic Rankine cycle is a power cycle which is operated using organic fluids. The traditional fluids used in it were R245fa, cyclohexane, benzene, etc. However, due to the environmental problems of ozone depletion and global warming related to use of traditional fluids, there has been a shift to use environmentally benign fluids. A number of studies have already been carried out on R245fa in past [1]; however, R245fa has a global warming potential of 1030 (refer Table 1); hence, it should be replaced with fluids which have low GWP. Tiwari et al. [2] performed the energy and exergy investigation of solar power recuperated organic Rankine cycle through glazed reverse absorber conventional compound parabolic concentrator (GRACCPC) system, and they concluded that overall thermal efficiency and exergetic efficiency improved through the use of internal heat exchanger. Wang et al. [4] experimentally studied a solar-driven ORC using pure fluid R245fa and zeotropic mixture R245fa/R152a. They reported that the efficiency of ORC improved when zeotropic mixture was used in comparison with pure fluid. Moles et al. [5] reported the various low GWP alternatives like HCFO-1233zd(E) and HFO-1336mzz(Z) for recovery of low-temperature heat. They analysed these working fluids on the basis of the first law of thermodynamics, over a broad range of evaporator and condenser temperatures and superheat values varying from 5 to 50 K. They computed the

Table 1 Thermophysical properties of HFC245fa, HCFO1233zd[E] (Moles et al. [5]) and Novec 649

Parameters	HFC-245fa	HCFO-1233zd-E	Novec 649
Chemical formula	$CF_3CH_2CHF_2$	$CF_3CH{=}CHCl$	$CF_3CF_2C(O)CF(CF_3)_2$
T_c (K)	427.16	438.75	442
P_c (MPa)	3.65	3.57	1.88
Mol. weight (kg/kmol)	134	130.5	316
Slope	Dry	Dry	Dry
Flammability	Non-flammable	Non-flammable	Non-flammable
ODP	0	0.000340	0
GWP	1030	7	1
Boiling point (K)	287.96	291.12	322
Latent heat at boiling point (kJ/kg)	196.23	195.52	88
Evaporating pressure at 400 K (MPa)	2.21	1.80	0.825
Condensing pressure at 300 K (MPa)	0.16	0.14	0.043
Vapour density at 300 K (kg/m^3)	9.31	7.65	5.734
Liquid density at 300 K (kg/m^3)	1333.5	1258.3	1600
Vapour specific heat at 300 K (kJ/kgK)	0.96	0.84	0.8725
Liquid specific heat at 300 K (kJ/kgK)	1.33	1.25	1.103

performance on the basis R245fa and concluded that the first law efficiency of both these fluids is greater than R245fa.

At present, the researchers are focussing on the substitute and environment-friendly refrigerants, especially since the Kyoto and the Montreal protocols. In recent time, the Novec 649 as alternative to R245fa has been developed. Novec 649 is an environment-friendly working fluid with low GWP = 1 and zero ODP value and is suitable for use in ORC (https://multimedia.3m.com/mws/media/5698650/3mtm-novectm-649-engineered-fluid.pdf assessed on 27 July 2018).

The new fluids as alternative to R245fa are Novec 649, HCFO-1233zd(E) and HFO-1336mzz(Z). In the study by Moles et al. [5], only energy investigation has been performed for superheated organic cycle with and without internal heat exchanger; however, the second law analysis has not been attempted. Performance analysis of ORC systems based on the first law of thermodynamics is of limited use as actual losses (irreversibility) are difficult to make out. To evaluate the real losses due to irreversibility in the procedure and system, exergy analysis based on the second law of thermodynamics is the apt tool. Exergy analysis is generally planned to calculate the

maximum effectiveness of the system and to find out the position of exergy destruction and to determine the path for potential enhancements. Hence, in the present communication, exergy analysis of ORC with environment-friendly working fluids Novec 649 and HFO1233zd[E] as alternative to R245fa has been carried out. The computation involves the variation of the first law efficiency and exergetic efficiency of the ORC through evaporator temperature, condenser temperature and degree of superheat.

1.1 ORC System Description

Figure 1a, b shows the schematic and T-s diagrams of organic Rankine cycle. The schematic and T-s diagrams of organic cycle with internal heat exchanger are shown in Fig. 2a, b, respectively. The simple ORC system as shown in Fig. 1 comprises four main components, viz. evaporator, turbine, condenser and a pump. The fluid is heated in evaporator with certain degree of superheat at constant pressure (as shown in constant pressure process 2–5 in Fig. 1b). It then enters into the expander where it expands polytropically (process 5–6). The used fluid then enters the condenser where it loses heat at constant pressure (process 6–1) and then is pumped back to evaporator (process 1–2). This completes the cycle. In basic cycle, the fluid which leaves the turbine is in superheated state. This superheated fluid is condensed in case of basic ORC in condenser, thereby wasting lot of energy available at turbine exit. In ORC with IHE, this heat available at the turbine exit is used for heating the fluid

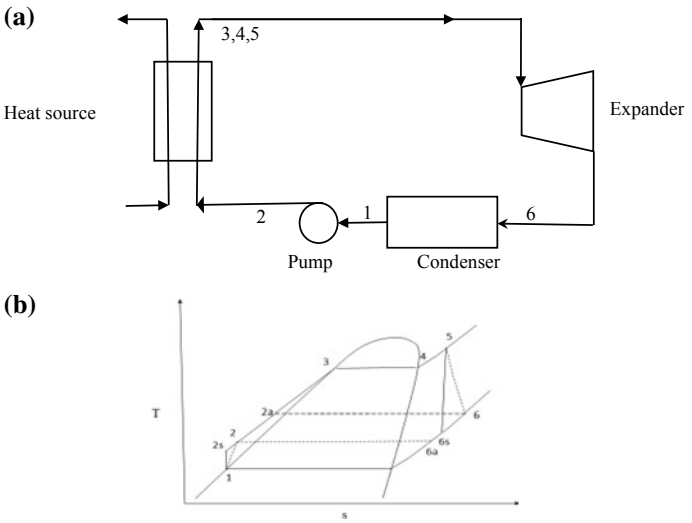

Fig. 1 **a** Schematic diagram of basic organic Rankine cycle. **b** T-s diagram of basic organic Rankine cycle

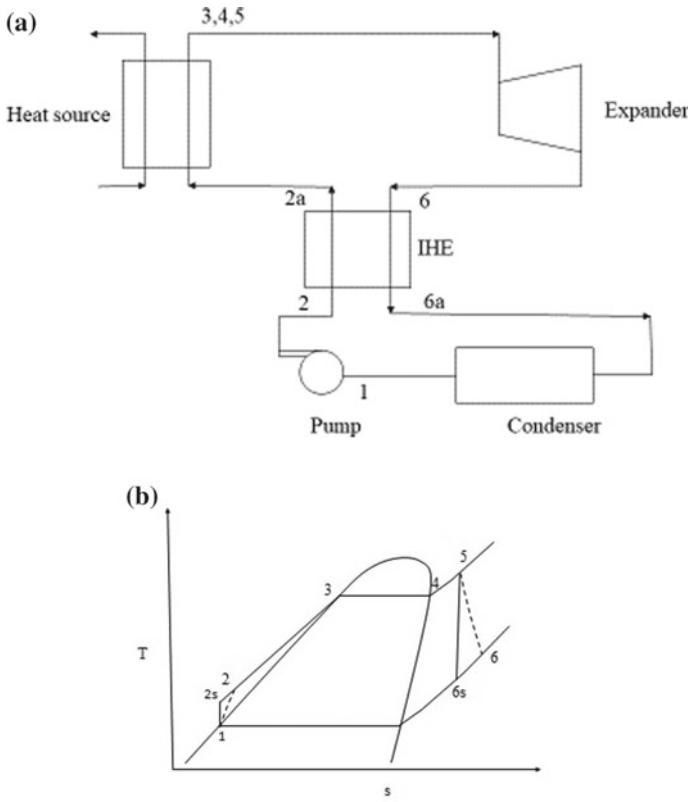

Fig. 2 **a** Schematic diagram for basic organic cycle with IHE. **b** T-s diagram for basic organic cycle with IHE

which leaves the pump in an IHE. This helps in reducing the energy input in the evaporator and improves the cycle efficiency.

2 Thermodynamic Modelling of ORC with and Without IHE

Thermodynamic modelling of the system requires the application of principles of conservation of mass, the first law of thermodynamics and the second law of thermodynamics. The second law of thermodynamics is required for exergy analysis of cycles. The following assumptions are made to develop the thermodynamic model

1. There are no heat losses in pipe lines.
2. Pressure drops in evaporator and condenser are neglected.
3. All components are assumed to be in steady state.

2.1 Energy and Exergy Balance Equations

$$\sum \dot{Q} - \sum \dot{W} = \sum \dot{m}_{\mathrm{e}} h_{\mathrm{e}} - \sum \dot{m}_{\mathrm{i}} h_{\mathrm{i}} \tag{1}$$

$$W_{\mathrm{p}} = \dot{m}(h_2 - h_1)/\eta_{\mathrm{em,p}} \tag{2}$$

$$W_{\mathrm{exp}} = \eta_{\mathrm{em,exp}} \eta_{\mathrm{v,exp}} \dot{m}(h_5 - h_{6a}) \tag{3}$$

$$\mathrm{Ex_{in}} - \mathrm{Ex_e} - \mathrm{ExD} = 0 \tag{4}$$

$$\mathrm{E_xD} = \sum (\dot{m}\mathrm{e_x})_{\mathrm{i}} - \sum (\dot{m}\mathrm{e_x})_{\mathrm{e}} + \left[\Sigma \left(\dot{Q}\left(1 - \frac{T_0}{T}\right)\right)_{\mathrm{i}} - \Sigma \left(\dot{Q}\left(1 - \frac{T_0}{T}\right)\right)_{\mathrm{e}} \right] \pm \dot{W} \tag{5}$$

Exergy destruction in evaporator

$$\begin{aligned} \dot{\mathrm{E}}_{\mathrm{x}}\mathrm{D}_{\mathrm{evp}} &= \dot{m}(h_{2a} - T_0 s_{2a}) - \dot{m}(h_5 - T_0 s_5) + \dot{Q}_{\mathrm{evp}} \left(1 - \frac{T_0}{(T_{\mathrm{H}} + 273)}\right) \\ &= \dot{m} T_0 [(s_5 - s_{2a}) - (h_5 - h_{2a})/(T_{\mathrm{H}} + 273)] \end{aligned} \tag{6}$$

Exergy destruction in pump

$$\dot{\mathrm{E}}_{\mathrm{x}}\mathrm{D_P} = \dot{m}[(h_1 - T_0 \mathrm{s}_1) - (h_2 - T_0 \mathrm{s}_2) + (h_2 - h_1)] = \dot{m} T_0 (\mathrm{s}_2 - \mathrm{s}_1) \tag{7}$$

Exergy destruction in expander

$$\dot{\mathrm{E}}_{\mathrm{x}}\mathrm{D_{exp}} = \dot{m}[(\mathrm{h}_5 - T_0 \mathrm{s}_5) - (h_6 - T_0 h_6) - (h_5 - h_6)] = \dot{m} \mathrm{T}_0 (\mathrm{s}_6 - \mathrm{s}_5) \tag{8}$$

Exergy destruction in condenser

$$\dot{\mathrm{E}}_{\mathrm{x}}\mathrm{D_{con}} = \dot{m}[(h_{6\mathrm{a}} - T_0 \mathrm{s}_{6\mathrm{a}}) - (h_1 - T_0 \mathrm{s}_1)] \tag{9}$$

Total exergy destruction

$$\dot{\mathrm{E}}_{\mathrm{x}}\mathrm{D_{tot}} = \dot{\mathrm{E}}_{\mathrm{x}}\mathrm{D_{con}} + \dot{\mathrm{E}}_{\mathrm{x}}\mathrm{D_P} + \dot{\mathrm{E}}_{\mathrm{x}}\mathrm{D_{evp}} + \dot{\mathrm{E}}_{\mathrm{x}}\mathrm{D_{exp}} + \dot{\mathrm{E}}_{\mathrm{x}}\mathrm{D_{IHE}} \tag{10}$$

Exergetic efficiency

$$\eta_{\mathrm{ex}} = (\dot{\mathrm{E}}_{\mathrm{x,in}} - \dot{\mathrm{E}}_{\mathrm{x}}\mathrm{D_{tot}})/\dot{\mathrm{E}}_{\mathrm{x,in}} \tag{11}$$

2.2 Model Validation

A computer program is developed in EES software for the computation of results. The results are calculated and compared with the results of Moles et al. [5]. The present results are within ±2% of the results of Moles et al. [5]. The following operating parameters are used for the computation of results of present work.

2.3 Cycle Operating Parameters

Condensing temperature (T_{cond}) = 27–77 °C (27 °C)
Evaporating temperature (T_{evp}) = 97–147 °C (127 °C)
Degree of superheat = 0–50 °C (5 °C)
IHE effectiveness (ε) = 80%
Isentropic efficiencies of expander and pump ($\eta_{is,exp}$, $\eta_{is,p}$) = 85%
Volumetric efficiency of expander ($\eta_{v,exp)}$ = 85%
Electromechanical efficiency of expander ($\eta_{em,exp}$) = 90%
Electromechanical efficiency of pump ($\eta_{em,p}$) = 35%.

3 Results and Discussion

3.1 Effect of Condenser Temperature on the First Law Efficiency for Basic ORC and ORC with IHE

Figure 3 refers the impact of condenser temperature on the first law efficiency of basic ORC and ORC with IHE. The first law efficiency reduces with improvement in condenser temperature in both the cases. It is noted that the first law efficiency for HFO1233zd(E) is highest followed by R245fa and Novec 649 for basic ORC cycle. It can also be observed that with incorporating IHE, the first law efficiencies are more for all the three fluids but highest and lowest values of the first law efficiencies were found to be differed by very slight amount.

The first law efficiency for R1233zd(E) varies between 11.09 and 5.23% for condenser temperature varying between 27 and 77 °C for basic ORC and 12.75% and 5.82% for ORC with IHE. The corresponding values vary from 10.54 to 4.72% for R245fa and from 8.86 to 4.56% for Novec 649 for basic ORC. For ORC with IHE, the corresponding values for R245fa and Novec 649 vary from 12.40 to 5.37% and 12.54 to 5.98%, respectively.

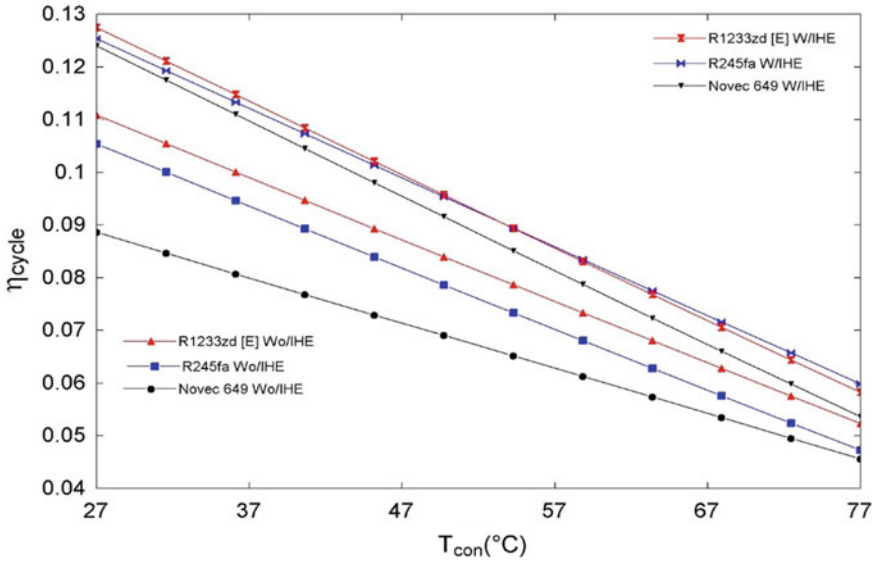

Fig. 3 Effect of condenser temperature on the first law efficiency

3.2 Effect of Condenser Temperature on Exergetic Efficiency for Basic ORC and ORC with IHE

Figure 4 shows the effect of condenser temperature on exergetic efficiency of basic ORC and ORC with IHE. The exergetic efficiency decreases with increase in condenser temperature in both the cases. It is observed that the exergetic efficiency for R1233zd[E] is highest followed by R245fa and Novec 649 for both the ORC cycles. It can also be observed that with incorporating IHE, the exergetic efficiencies are lower for all the three fluids compared to basic ORC.

The exergetic efficiency for R1233zd(E) varies between 59.73 and 34.83% for condenser temperature varying between 27 and 77 °C for basic ORC and 48.81% and 26.08% for ORC with IHE. The corresponding values for R245fa vary from 58.54 to 34.56% and from 45.93 to 27.76% for Novec 649 for basic ORC. For ORC with IHE, the corresponding values for R245fa and Novec 649 vary from 48.26 to 25.67% and 46.12 to 21.59%, respectively.

3.3 Effect of Evaporator Temperature on the First Law Efficiency for Basic ORC and ORC with IHE

Figure 5 shows the effect of evaporator temperature on the first law efficiency of basic ORC and ORC with IHE. The first law efficiency increases with increase in

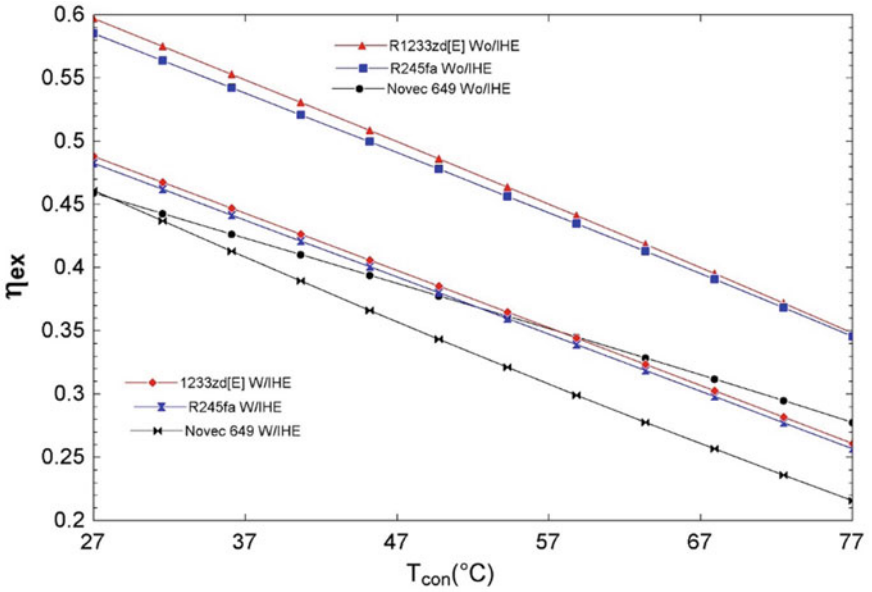

Fig. 4 Effect of condenser temperature on exergetic efficiency

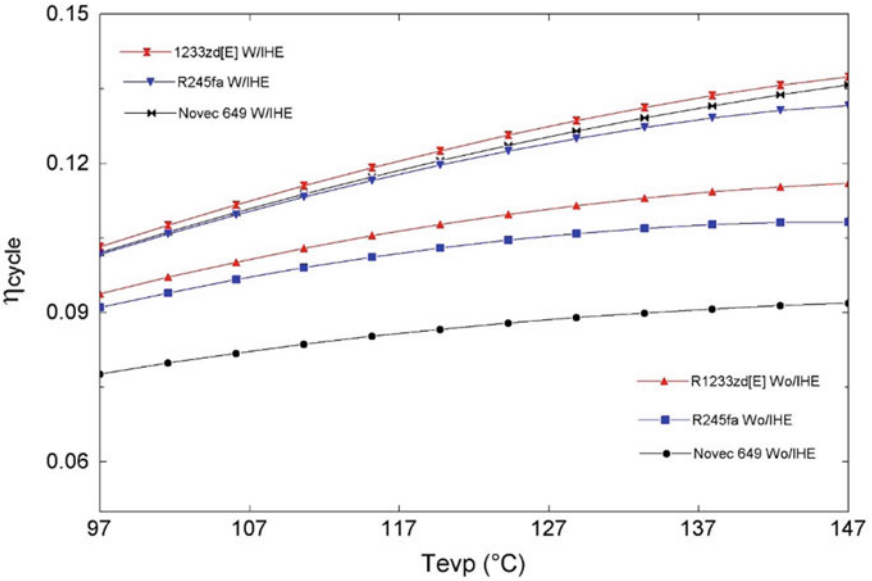

Fig. 5 Effect of evaporator temperature on the first law efficiency

evaporator temperature for both the cycles. It is observed that the first law efficiency for R1233zd(E) is highest followed by R245fa and Novec 649 for the basic ORC. However, for the ORC with IHE, the first law efficiency for R1233zd(E) is highest followed by Novec 649 and R245fa. The first law efficiency for R1233zd(E) varies between 9.38 and 11.60% for evaporator temperature varying between 97 and 147 °C for basic ORC and 10.32% and 13.74% for ORC with IHE. The corresponding values for R245fa and Novec 649 vary from 9.10 to 10.82% and 7.7 to 9.19%, respectively, for basic ORC. For ORC with IHE, the corresponding values for R245fa and Novec 649 vary from, respectively, 10.17 to 13.16% and 10.21 and 13.58%.

3.4 Effect of Evaporator Temperature on Exergetic Efficiency for Basic ORC and ORC with IHE

Figure 6 shows the effect of evaporator temperature on exergetic efficiency of basic ORC and ORC with IHE. In both the cases, a very little downward trend is observed in exergetic efficiencies of all the fluids as evaporator temperature rises. It is also noted that the exergetic efficiency for R1233zd(E) is highest followed by R245fa and Novec 649 for basic ORC. For ORC cycle with IHE, the exergetic efficiencies are found lower for all the three fluids compared to basic ORC except in case of Novec 649. In case of Novec 649, the exergetic efficiency for basic ORC is higher than ORC

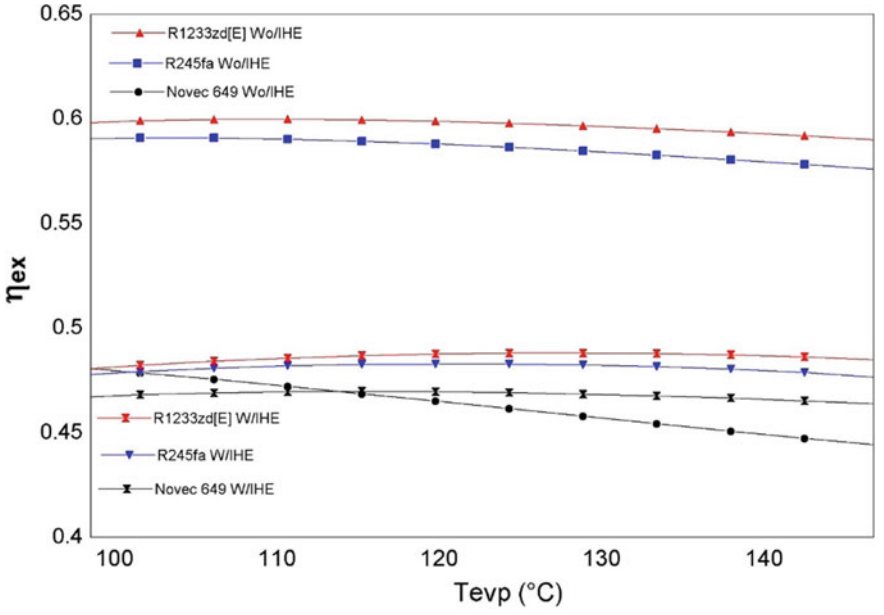

Fig. 6 Effect of evaporator temperature on exergetic efficiency

with IHE up to 114C, and above 114C, the exergetic efficiency for ORC with IHE is higher.

The exergetic efficiency for R1233zd(E) varies between 59.77 and 58.99% for evaporator temperature varying between 97 and 147 °C for basic ORC and 47.97% and 48.48% for ORC with IHE. The corresponding values for R245fa and Novec 649 vary from 59.02 to 57.59% and 46.66 to 46.37%, respectively, for basic ORC. For ORC with IHE, the corresponding values for R245fa and Novec 649 vary from 47.72 to 47.65% and 46.66 to 46.37%, respectively.

3.5 Effect of Degree of Superheat on the First Law Efficiency for Basic ORC and ORC with IHE

Figure 7 shows the effect of degree of superheat on the first law efficiency of basic ORC and ORC with IHE. The first law efficiency for basic ORC increases slightly with increase in degree of superheat for R245fa and R1233zd [E], but decreases slightly for the Novec 649 throughout the operating range of DOS. It is also noted that the first law efficiency for R1233zd[E] is highest followed by R245fa and Novec 649 for both the cycles. However, for the ORC with IHE, Novec 649 has little more first law of efficiency than R245fa for low degree of superheat, i.e. up to 10 °C The first law efficiency for R1233zd(E) varies between 11.01 and 11.38% for DOS

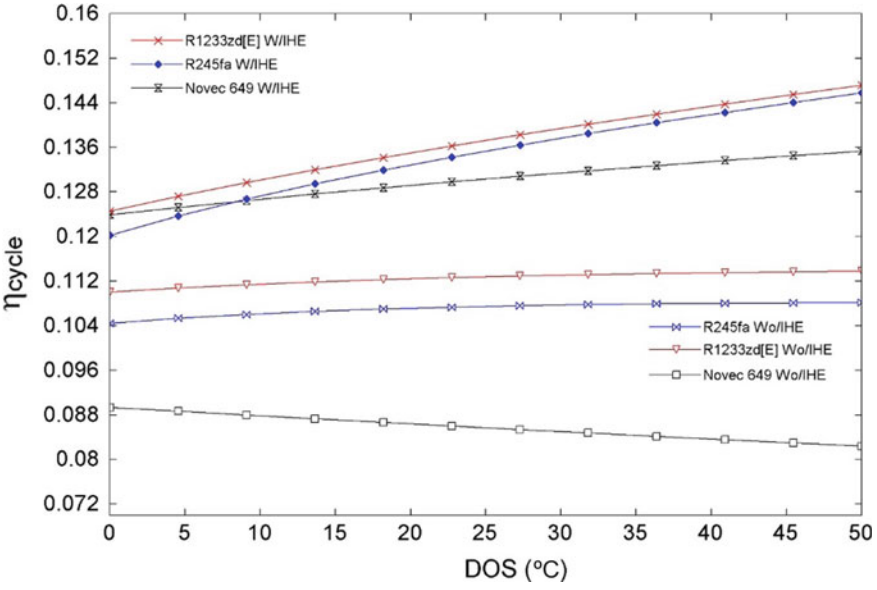

Fig. 7 Effect of degree of superheat on the first law efficiency

varying between 5 and 50 °C for basic ORC and 12.46% and 14.71% for ORC with IHE. The corresponding values for R245fa and Novec 649 very from 10.44 to 10.82% and 8.93 to 8.23%, respectively, for basic ORC. For ORC with IHE, the corresponding values for R245fa and Novec 649 vary from 12.02 to 14.58% and 12.39% and 13.53%, respectively.

3.6 Effect of Degree of Superheat on Exergetic Efficiency for Basic ORC and ORC with IHE

Figure 8 shows the impact of degree of superheat on exergetic efficiency of basic ORC and ORC with IHE. The exergetic efficiency for both the ORC systems reduces with rise in degree of superheat for all the three working fluids throughout the operating range of DOC, i.e. 5–50 °C. It is also observed that the exergetic efficiency for R1233zd[E] is highest followed by R245fa and Novec 649 for both the cycles. The exergetic efficiency for R1233zd(E) varies between 61.39 and 48.24% for DOS varying between 5 and 50 °C for basic ORC and 49.3% and 44.68% for ORC with IHE. The corresponding values for R245fa and Novec 649 vary from 60.14 to 46.91% and 47.86 to 33.89%, respectively, for basic ORC. For ORC with IHE, the corresponding values for R245fa and Novec 649 vary from 48.46 to 44.76% and 47.83% and

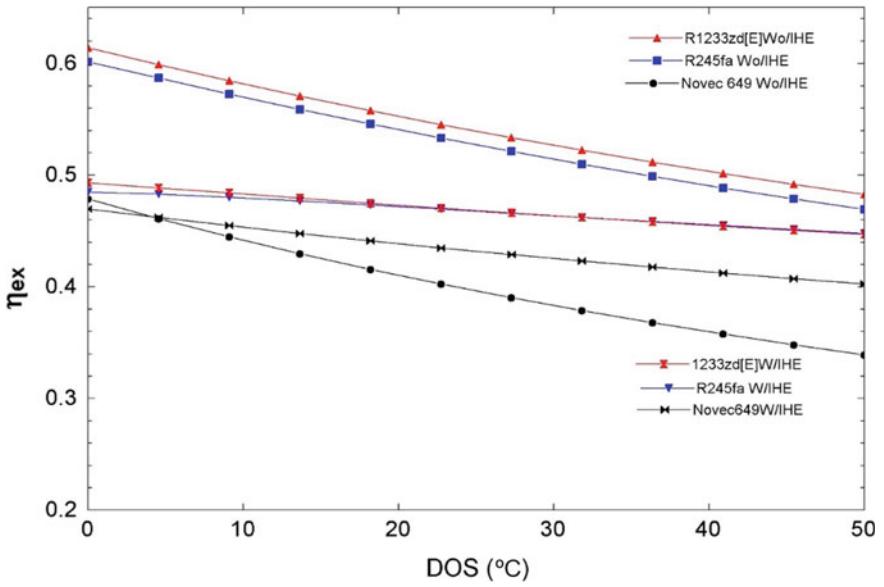

Fig. 8 Effect of degree of superheat on exergetic efficiency

40.42%, respectively. For ORC cycle with IHE, the exergetic efficiencies are found lower for all the three fluids compared to basic ORC.

4 Conclusions

In the present work, performance analysis of ORC using environment-friendly working fluids Novec 649 and HFO1233zd[E] as alternative to R245fa has been analysed. Following inferences can be found from the results obtained:

- With increase in condenser temperature, the first law efficiency decreases in both the cycles, i.e. basic ORC and ORC with IHE. The cycle efficiency is higher for the ORC with IHE, whereas the exergetic efficiency is lower for ORC with IHE in comparison with basic ORC.
- With increase in evaporator temperature, the first law efficiency increases in both the cycles. The exergetic efficiency is lower for the ORC with IHE in comparison with basic ORC for the fluids R245fa and R1233zd[E]; however, in case of Novec 649, the exergetic efficiency for basic ORC is higher than ORC with IHE up to 114 °C, and above 114 °C, the exergetic efficiency for ORC with IHE is higher.
- With increase in the DOS, the first law efficiency increases in both the cycles for R245fa and R1233zd[E]; however, in case of Novec 649, it decreases for the basic cycle and increases for the ORC with IHE. With all the fluids, ORC with IHE has higher first law efficiency compared to basic ORC. The exergetic efficiency for both the ORC cycles decreases with increase in degree of superheat for all the three working fluids throughout the operating range.
- Finally, it can be concluded that R1233zd[E] is a better long-term replacement of R245fa as it offers higher first law efficiency as well as exergetic efficiency.

References

1. Wang M, Wang J, Zhao Y, Zhao P, Dai Y (2013) Thermodynamic analysis and optimisation of solar driven regenerative organic Rankine cycle (ORC) based on flat plate solar collectors. Appl Therm Eng 50(1):816–825
2. Tiwari D, Sherwani AF, Atheaya D, Arora A (2017) Energy and exergy analysis of solar driven recuperated organic Rankine cycle using glazed reverse absorber conventional compound parabolic concentrator (GRACCPC) system. Sol Energy 155:1431–1442
3. https://multimedia.3m.com/mws/media/5698650/3mtm-novectm-649-engineered-fluid.pdf. Assessed on 27 July 2018
4. Wang JL, Zaho L, Wang XD (2010) A comparative study of pure and zeotropic mixtures in low temperature solar Rankine cycle. Appl Energy 87:3366–3373
5. Moles F, Esbri JN, Peris B, Babiloni AM, Cervera AB, Kontomaris K (2014) Low GWP alternative to HFC245fa in organic Rankine cycle for low temperature heat recovery: HCFO-1233zd-E and HFO-1336mzz-Z. Appl Therm Eng 71:204–212

Identifying Deterrents to Greening Existing Buildings

Devendra Pratap Singh and Ekta Singh

Abstract Green retrofitting of existing building stocks is inevitable as governments across the world are striving to formulate and implement relevant policy measures to achieve the sustainability goals. Green retrofitting or simply greening existing buildings is a very novel concept to reduce the impact of the existing building stock on the ecosystem through energy retrofits and technologies that in turn improve and enhance the overall energy efficiency of buildings, therefore reducing its carbon footprint. In this paper, various policies and processes of green retrofitting systems are investigated. The paper relies on qualitative techniques to capture the perception of different stakeholders to gain better understanding on the barriers and deterrents to greening existing building stocks. A framework of six indicators is derived based on the existing case studies to analyse the different components of Green retrofitting process. The subject of green retrofit and its practice is an under-researched area, mainly in Indian context. The paper attempts to bridge this gap, and the strength of the paper lies in the empirical nature of its investigation.

Keywords Energy efficiency · Green retrofitting · Barriers · Office building · India

1 Introduction

The origin of the much known—green building movement—can be traced back to the late twentieth century. During the 1970s, the deteriorating built environment, depleting level of natural fuels and growing global warming—forced scientist and engineers to invent mechanisms to reduce consumption of energy. According to the global statistics, the most polluting and energy-consuming sector is the building sector. 40% of the global energy consumption is building related while 50% of the global greenhouse emissions are due to buildings [31]. In the Indian context too, the annual energy consumption by the building sector is projected to increase at a

D. P. Singh (✉) · E. Singh
Amity University, Noida, Uttar Pradesh, India
e-mail: dpsingh@amity.edu

G. Zhang et al. (eds.), *Advances in Energy and Built Environment*, Lecture Notes in Civil Engineering 36, https://doi.org/10.1007/978-981-13-7557-6_6

9% growth rate by 2020, i.e. twice the consumption levels in 2010–2011 [18]. Consequentially, it is evident that the impact of building sector on the environment is detrimental. The term—green building—was coined by the National Association of Home Builders (NAHB), Washington, DC, i.e. the home building industry of USA in the late 1980s that transformed a movement of resource-efficient buildings into a revolution. Although it was initiated in USA, the green building movement was pioneered in Great Britain with a rating system called Building Research Establishment Environmental Assessment Method (BREEAM), launched in 1990 [14]. The Office of the Federal Environment Executive formerly defined green buildings as the practice of increasing the competence with which buildings and their sites consume energy, water and materials, and decreasing the negative building effects on human well-being and the environment, through efficient site planning, design and construction methods, building operation and maintenance techniques, and demolishing methods throughout the life cycle of the building [12]. Green buildings are therefore an effort to magnify the positive effects and diminish the negative effects of a built structure or built environment throughout the life cycle of the building.

1.1 Significance of Greening Existing Buildings

The rising cost of urban redevelopment has brought us on a precipice of sustainability and growth. Even if today countries decide to become sustainable, it is not possible to demolish all the constructions, to make space for new sustainable green buildings. Further, the opportunity cost of choosing to demolish an existing construction and building a new one is large [41]. There is a need to develop a new approach to sustainable building design that incorporates existing buildings into the mix and helps them achieve the goals of sustainability. The adverse impact of demolishing old building and constructing new one, on environment, is huge, knowingly it can take up to 80 years to make up for the ecological losses [29]. According to a study conducted by The Energy Resource Institute [37], the energy-saving potential (in MWh/Yr) of 100 old retrofitted buildings against the 16 new green buildings is approximately eight times (Fig. 1). It reinforces that the most suitable option for sustainable growth is to retrofit the existing buildings using green technologies; this is called ‘green retrofit’.

‘Green retrofit’ is a recent field of study, and interestingly, academic interest in understanding how existing building stock can be retrofitted is growing. Despite there exist several barriers which create obstacles in its adoption and implementation, several studies have been conducted to investigate about the suitability of existing buildings for retrofitting. However, there is a dearth of study that discusses the barriers and deterrents to greening existing buildings, especially in Indian context. The present manuscript aims to fill this gap and draws upon the findings of the existing case studies and perception of the various stakeholders to determine the impediments to green retrofitting in India. The first section of the manuscript provides a background on green retrofit, an overview of existing building stocks in India and a review and

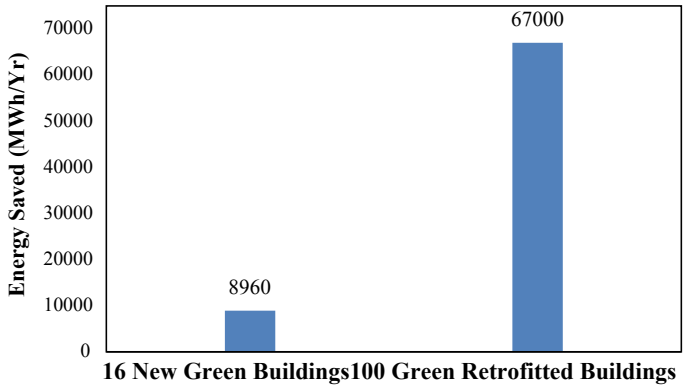

Fig. 1 Energy savings—New green buildings versus green retrofitted building. *Source* TERI [37]

synthesis of key published research into barriers to green retrofit of buildings in India and other economies. The next section explains the methodology to conduct this research, and the last section summarizes the key findings of the case studies and stakeholder's perception to uncover barriers to green retrofit.

2 Literature Review

2.1 Meaning Green Retrofit

The term Retrofit originated in USA in mid of twentieth century and is a combination of words retroactive, which means applying to the past, and ‗fit which refers to equipping [9]. Green retrofit refers to the gradual improvement in the existing building fabric and systems with the intent of achieving the energy efficiency and low-carbon emission objectives [33]. In the context of buildings, green retrofit could include processes such as adapting to newer sustainable technologies, modernization of an existing structure, renovation, refurbishment, upgradation and reuse [40]. According to US Green Building Council, green retrofit is defined as any kind of structural and technological advancement at an existing building that is wholly or partially intended to positively impact the energy and environmental performance, and the physiological quality of the space with respect to air quality, use of natural light and reduction in noise pollution—all conducted in a manner that strives to economically benefit the owner [4]. Apart from these benefits, it is imperative to conduct a clear analysis of the payback period of energy-efficient projects with respect to different components and their respective performance guarantees [24]. A further review of literature demonstrates that the most commonly implemented

strategies in green retrofit projects focus on either of the two aspects; thermal that includes improved heating, ventilation and cooling systems and lighting [3].

2.2 Building Stock in India and Green Retrofit

While discussing the various facets of greening existing buildings, it is imperative to understand certain statistics that are relevant to comprehend this concept, in both the Global and Indian contexts. According to a recent study, the expected growth percentage for greening existing buildings is 24% in the Indian context as compared to 37% in the global context [10]. This indicates that at both domestic and global fronts, the potential for green retrofit projects is very high. Further, India has a huge stock of relatively old and ageing buildings; mainly public and recently many state governments have proposed the mandatory adoption of green retrofit projects under Smart Cities initiatives. As per the US Green Building Council, a total of 11 States and 1 union territory (Delhi) from a total of 29 states and 7 union territories have successfully undertaken green retrofit projects (Illustration 1).

It is evident that major parts of Central and East India have been untouched. In total, there are approximately 120 green retrofit projects undertaken in the country and state of Karnataka is the leader in having maximum number of projects. Furthermore, according to a recent USGBC report on India, the operational savings of green retrofit buildings in India are slightly higher than the new green buildings over a period of 1–5 years (Table 1).

The payback time for green investments is marginally higher for green retrofits as compared to new green buildings in India. However, India reports greater decrease in operating costs for green retrofits than the global average, which may encourage more growth in the sector of greening existing buildings/green retrofitting.

Table 1 Expected operational savings of green retrofit buildings in India

Parameters	New green building	Green retrofit
Expected decrease in operating costs (in 1 year)	10%	11%
Expected decreased in operating costs (in 5 years)	15%	16%
Expected payback period (In Years)	4	5

Source IGBC [16]

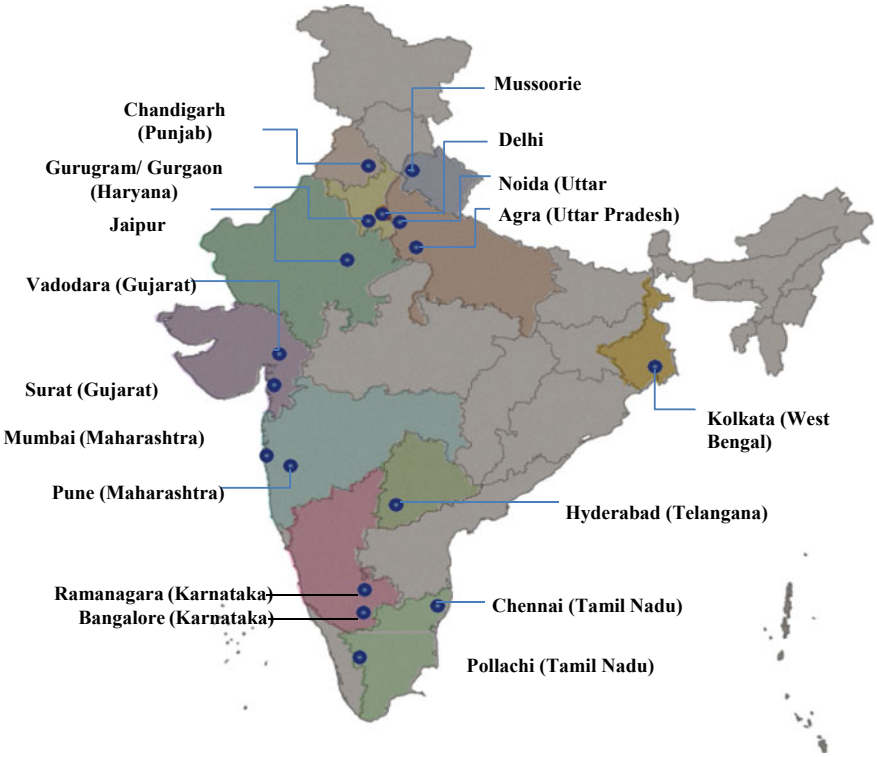

Illustration 1 India—distribution of green retrofit project. *Source* Author's compilation based IGBC Data

2.3 Barriers to Green Retrofitting

There are many factors that influence and encourage the green retrofitting of conventional buildings. Many a times, these factors are contextual and specific to the project type and its site as it has to cater to the project-specific issues. However, there exist a few dominant drivers of green retrofitting of the buildings which are independent of the site and project type or stakeholders. These are government policies, regulations, incentive programmes, substantial financial returns, enhanced performance ratings, reduced operational costs and improved rental rates and capital value [5, 7, 25, 22]. Regardless of these factors that give a positive push to the concept of greening existing buildings, there are many aspects that hamper the process and discourage the stakeholders to take up such projects [21]. There is a lack of awareness and knowledge on the real returns on energy efficiency and green retrofit measures [42]. Many a times a well informed and rational individual will characterize investment in energy efficient projects as –illiquid –risky and of—high transaction and will completely

dismiss the payoffs [36]. The ignorance of real benefits and advantages can foster resistance to change [6].

Certain studies highlight that incentives to promote adoption of policies are not in place which result in lack of knowledge and awareness [34]. Further, there are tenancy concerns. In studies conducted in UK, it is advocated that retrofitting is perceived to be risky and is seen to have a long payback period with interruptions to existing tenancies [25]. Further, though it is less costly to green retrofit than to rebuild, long payback period is a concern and has been cited by many studies as a barrier preventing stakeholders to invest [35].

In case of developing economies, though the policies and regulations are the most important drivers, the existing laws need to be enforced including strengthening of regulatory bodies. A study conducted by USGBC [38] on India highlighted certain barriers that discourage investment in green retrofit projects in the country. The main reason for them to be not effective is because of the difference at the state level in the adoption of policies for green retrofitting and no standards proposed for the green building materials and technologies. Lack of technical capacity for planning, design and construction of retrofitting buildings also creates a difficulty in making projects a success. With only 6% of employees having adequate training, the sector is already skill deficit. Similarly, there is shortage of contractors and lack of technical training capacity.

To summarize, the major problem faced by the industry in encouraging green retrofit practices is lack of awareness of benefits amongst the users of the building. These projects are considered to be prohibitively expensive making the public more concerned about the costs than the sustainability aspects. People are less aware of the longer-term savings. Further, authors analysed a few studies conducted specifically in Indian context to understand the existing deterrents to green retrofit projects. Table 2 provides a summary of same.

After reviewing the existing studies on the barriers in greening existing buildings in Indian context, authors identified the major barriers faced by the stakeholders. These are lack of information and awareness amongst the stakeholders about the new building retrofits and technologies available in the market. Following these barriers, the other significant barrier that affects the growth of this concept is the splitting of incentives—developers often rent their buildings to tenants who pay the utility bills. In these cases, the costs of the efficiency measures are incurred by the developer while the tenant benefits from the lower utility bills. Other than these, the other factors that hinder the process of green retrofitting are as follows: the new technology is perceived to be uncertain due to the greater uncertainties linked with the unproven performance, financial risk—the payback periods are largely determined by the construction costs and savings from operations, the other is the market risk as the market may have condensed to pay for unproven technologies, resulting into lower value of investment, lack of standardization of substitute materials and technologies which could help to reduce the costs of green construction, lack of requisite knowledge for designer and applicators creates a problem in carrying out green retrofit projects effectively, the incentives provided by the government are considered to be very small to bring any change in behaviour of the green building industry

Table 2 Barriers to green retrofit: in Indian context

Author	Description of study	Barriers
RBC's Corporate Environmental Affairs Group [32]	Moving into the mainstream green buildings and LEED	**Technology risk** New technologies can be perceived to be riskier because of the greater uncertainties associated with unproven performance. This can result in: **Financial risk** as payback periods are largely determined by construction costs and savings from operations **Market risk** as the market may have a reduced willingness to pay for unproven technologies, translating into a lower value of investment **Certification risk** Buildings that fail to achieve certification or do not perform as expected may be exposed to potential legal and financial risks if a party decides to litigate. This risk increases if there are financial incentives from government or other parties tied to certification or performance
Emily et al. [11]	Green building: a case study	Lack of awareness about the green retrofits. Weak unconvincing value proposition Efficiency is a luxury market—not affordable for masses. No strict definition for green construction/renovation. Poor implementation of bye-laws Lack of uniformity of bye-laws No standardization of alternate material and technologies Requisite knowledge for designers and applicators is missing
Kapure [20]	Parameters of upgrading existing building into a green building	Divergence between capital and operating costs Split incentives between tenants and owners Perceived high costs of greening Unproven future benefits Incentives too small to change behaviour Lack of financing for energy upgrades Wide variability of energy costs Organizational dynamics
Nair [28]	Improving energy efficiency in buildings	No mandates/govt. regulations High first costs-perception/reality Lack of awareness of commitment from building owners Lack of awareness of new technology amongst building professionals Setting a target for energy savings

(continued)

Table 2 (continued)

Author	Description of study	Barriers
Mahal [26]	Formulating guidelines for effective implementation of green building scheme of the urban local bodies	There is no uniformity and consensus in the definition of green construction practices There exist proper regulations and guidelines for conduct of green practices, however the implementation of these codes lack effectiveness The concept and benefits of Green buildings and Retrofit are not widely circulated amongst the industry and beneficiaries Green construction indulges in many alternative materials, however, in Indian context there is no centralized standardization guidelines for the use of the materials
ASCI and NRDC [2]	Building efficient cities: strengthening the Indian real estate market through codes and incentives	The study highlights three major barriers as **Upfront costs**: In any energy-efficient project, the main concern of developer is the reclamation of the direct cost. Nonetheless, there exists a lot of unawareness on the payback period of such projects. Traditionally, the payback period is moderately short **Split incentives**: Usually, energy-efficient projects are of large scale and occupied by multiple tenants responsible for paying the energy bills. This results in conflict of interest as the initial costs of energy retrofit measures are made by the developers while the benefits are experienced by the tenants in form of lower energy bills **Limited Incentives**: The government support programme for such projects lack wide publicity and stakeholders are mostly unaware of it

and its stakeholders. Experiences in other countries show that these barriers must be addressed comprehensively and holistically, simply solving one of these barriers will not achieve a meaningful improvement in scaling efficiency implementation [8]. Further, the authors reviewed a few existing case studies, 1 USA, 1 Australia and 4 India, to understand the existing deterrents to green retrofitting projects. The choice of buildings is corporate offices, as most of the retrofitting in Indian context is happening in corporate buildings [16]. The summary of the findings is listed in Table 3.

Based on above review of case studies and literature studies, it is inferred that the major barriers and problems faced in the process of greening existing buildings relate to

Financial aspect: The most significant of all risks. This is very crucial in making a decision of adopting green retrofitting projects. Long payback period, sunk illiquid

Table 3 Deterrents/barriers and risks of greening existing corporate buildings

Problems/barriers	Building/project					
	Empire State building (New York)	Szencorp building (Melbourne)	HUL building (Mumbai)	Express tower (Mumbai)	Godrej Bhawan (Mumbai)	Mahindra towers (Mumbai)
	Author					
	USGBC	Szencorp	IGBC	IGBC	Godrej	IGBC
Financial risks	✓	✓	✓	✓	✓	✓
Operational risks (retrofitting work going on while building is occupied)	✓	✗	✗	✓	✓	✓
Extensive task—time consuming	✓	✓	✓	✓	✗	✗
Difficulties, shortcomings due to location restrictions	✗	✗	✓	✓	✓	✗
Retaining the existing building structure	✗	✓	✓	✗	✗	✓
Limited availability of retrofitting products (procurement issues)	✗	✗	✗	✓	✓	✗
Lack of awareness/skill	✗	✓	✗	✓	✓	✓
Lack of govt. incentives and green retrofitting policies	✗	✗	✓	✓	✓	✓

Source Author's compilation

investment, high-transaction and upfront cost, and in a few instances split incentives between owner and tenant.

Operational aspect: These are the risks that creep in when the green retrofitting procedure is undertaken while the building is currently being occupied. This could include the risk of damage to retrofitting materials and systems due to the occupant activities as well as risk of injury/harm to occupants while assembly and installation of green retrofitting systems.

Extensive task—time consuming: Greening existing buildings tends to be a long, time-taking procedure, usually depending on the extent to which green retrofitting is being done, i.e. how green the existing building is being made.
Lack of Awareness on the Green Retrofit Processes and benefits: There is lack of awareness regarding issues around green construction and availability of green products amongst the general population of India. Even in the presence of knowledge, the people fail to understand the potential cost saving over the longer term. Moreover, assessment of the economic case for the people's uptake becomes more difficult due to lack of empirical evidence on the cost and savings associated with green buildings.
Lack of Govt. incentives and green retrofitting policies: Specifically, for the Indian case studies, it is evident that there is a barrier in terms of lack of government incentives and policies to encourage the formulation and execution of such projects. This has made it tough for architects, contractors and other stakeholders who may have an inclination and interest in undertaking such green retrofit projects.

3 Research Methodology

As mentioned earlier that there is lack of knowledge on the barriers that prevent uptake of green retrofitting of buildings. This leads to the research question of the present study: What restricts stakeholders to invest in these projects? In order to investigate about the barriers to green retrofitting, a qualitative approach has been implemented.

The methodology that was adopted to accomplish the purpose of the present study included extensive literature reviews, designing of the research tool, i.e. a survey questionnaire for the identified stakeholders, data collection and its analysis. The current perspective of greening existing buildings was investigated through a comprehensive critical literature review which also included a few case studies of the green retrofitted buildings in India. The data were collected from different sources, namely research papers, websites, articles, reports, term papers, etc. Based on the variables and factors obtained from the literature study, the primary survey was conducted. It is important here to understand the relevant stakeholders involved in any green retrofit projects. Table 4 provides the description of the stakeholders considered for this study; it is adapted from the findings of the study conducted by Liang et al. [23].

A list of certified green retrofit buildings was obtained from the GRIHA[1] and IGBC.[2] As already stated there are approximately over 100 buildings. A total of 133 stakeholders were identified from the entire above-listed category. This sample population in the present case is the various stakeholders of the green building industry involved in the project at various stages (Table 4). Around 100 questionnaires were randomly sent out to the identified sample population, and 30 responses

[1]GRIHA—Green Rating for Integrated Habitat Assessment.
[2]IGBC—Indian Green Building Council.

Table 4 Stakeholders' description

Stakeholder	Definition
Owner/client	Owns the existing building or the client of the project
Facilities manager	Manages the facilities in the existing building
Designer	Responsible for people involved in retrofit design, including architects, structural engineers, etc.
Contractor	Responsible for people involved in retrofit construction, including project manager, purchasing manager, and quantity surveyor
Government	Formulates policies and laws related to green retrofits
Industry institution	It has authority to define industrial standards and evaluate projects, e.g. World Green Building Council and LEED

Source Adapted from Liang et al. [23]

were received. The response rate was 30%, consistent with the norm of 20–30% as observed in questionnaire surveys in building research [1]. Although the sample size was not large, statistical analysis could still be performed because the central limit theorem holds true when the sample size is no less than 30 [30].

3.1 Questionnaire Description

The objective of the primary survey was to get a fresh perspective of the stakeholders on this subject of greening of existing buildings. The structured questionnaire was based on six identified indicators from literature study and was divided into three segments, as stated below.

1. *Respondents' Professional Background/Field of Expertise*

This covers the professional proficiency of the respondents since this is important in defining how respondents of various professional backgrounds and expertise react to the concepts of greening existing buildings. This section was mainly open-ended, except the professional experience question which is based on Likert scale (1–4; 1 = less than 5 years; 2 = 5–10 years; 3 = 10–15 years; 4 = Above 15 years).

2. *Green buildings and Greening of Existing Buildings—Concept Awareness*

This deals with analysis of the respondents' existing knowledge and awareness related to greening existing buildings. This section will help in extensively studying the knowledge gap and why it exists. This section is based on Likert scale from 1–4; 1—Highly Aware; 2—Aware; 3—Somewhat Aware; 4—Highly Unaware.

3. *Barriers, Deterrents and Risks in Greening Existing Buildings*

Understanding the perception of the different stakeholders with respect to the barriers, deterrents and risks in greening existing buildings is a critical aspect of the survey

Table 5 Description of indicators investigated

Variable name	Code	Description
Financial indicators	FA1	Long payback period is a major deterrent
	FA2	High-transaction cost of green retrofit projects is a deterrent
	FA3	Split incentives between the owner and tenant discourage the investment in these projects
Operational indicators	OA1	Building being occupied results in frequent interruptions to operations
	OA2	Material non-availability and lack of standardization in the industry is a big barrier
Time indicator	TI1	Highly time-consuming project
Technical/awareness indicator	LA1	Lack of awareness about the new technique
	LA2	Lack of technical expertise in the green retrofit technology
Government incentives	GI1	Lack of proper government incentives is a major barrier to uptake of green retrofit projects

as it helps analyse the problems that are being faced in the industry. It is based on six identified parameters from the review of existing case studies and literature studies. This section intents to capture the respondent's perception pertaining to their understanding on the relevancy of different identified barriers. Respondents are asked to provide the ranking of different variables depending on the severity of impact the indicators have on green retrofit projects uptaken by them. A few of the variables were further split to increase the accuracy of responses. The details of the indicators investigated are provided in Table 5.

4 Discussion

4.1 Data Analysis: Respondents Profile and Awareness Level

As stated above that 30 responses were received and analysed, it is impertinent here to understand the professional experience of the respondent. This is important to ensure that the respondents are highly specialized and experienced professionals. Majority of the respondents, around 69%, were in age group 35–50 years (Fig. 2) and about 53% had a professional experience of more than 10 years (Fig. 3).

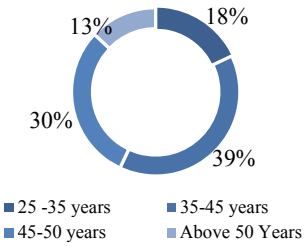

Fig. 2 Age composition of stakeholders. *Source* Author's data

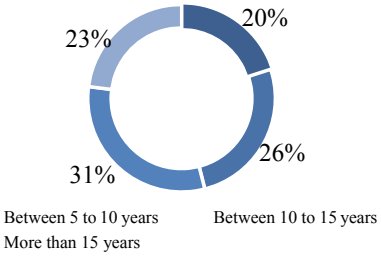

Fig. 3 Professional experience of stakeholders. *Source* Author's data

The respondents profile is suggestive that participants are well established and potentially have clear opinion process; this supports overcoming of any possible response bias. Further, respondents were asked about their understanding and awareness level of the green retrofit process. It is alarming that awareness level of respondents pertaining to green retrofitting process is very low, and this is consistent with the literature findings that the lack of awareness on various aspects of these projects makes an integrated implementation approach and acceptability difficult [42]. About 58% of the respondents claimed to have no good awareness on green retrofitting process while only 26% had high awareness level. The research further intends to understand whether any correlation exists between the awareness level and professional experience of the respondents. A correlation coefficient was conducted for the two items; correlation coefficient is a measure of the strength of relationship specifically linear between two variables. It enables the researchers to understand that how strongly the items under investigation are related to each other. Its value ranges from $+1$ to -1 and is represented by R; a value of 0 indicates that there is no relationship between the two items and a value closer to $+1$ is indicative that there exists a strong positive relation between two variables; it implies an increase in the value of one leads to increase in the other. The R value was -0.098, while significant P-value is 0.606 this implies there is no appreciable relationship between the two. It is not surprising that there is no statistical significance as green retrofit is a relatively new field of study. Furthermore, it can be concluded that most of the people are not aware either about concept of green buildings or the policies/incentive programmes that have been formulated by the government for the same. Subsequently, the real benefits of the government schemes fail to reach the end-users [6].

4.2 Data Analysis: Barriers to Green Retrofit Projects

An extensive statistical analysis of the collected data has been done in order to understand the perception of the stakeholders pertaining to perceived barriers. The data collected have been analysed using the SPSS statistical technique for ranking. Authors used the nonparametric technique of **Friedman's test**. The Friedman test is the nonparametric alternative to the one-way ANOVA with repeated measures [19]. Nonparametric statistical techniques are used to analyse data that are mainly ordinal, relying on ranking.

To conduct it, following null and alternative hypothesis is framed

HO—No statistically significant difference in the respondent's mean and
H1—There is statistically significant difference in the respondent's mean.

—Asym. Sig. is the significance level; it enables the researchers to understand the difference in the means of the sample when population distribution is normal. A value less than 0.05 signifies that the relationship between the variables in the data set is statistically significant and Friedman's test is acceptable and null hypothesis is rejected. For the present study, the significant *P-value* is 0.000; this concludes that there is statistically significant difference in the respondent's mean, and the ranking order as revealed by the Friedman test is acceptable and can be generalized. In the present investigation, researchers considered the first five important barriers as highlighted by the test. Based on the identified mean and median of the descriptive statistics result (Table 6) and Friedman test (Tables 7 and 8), the most significant barriers to green retrofit projects as identified in Indian context are as follows:

FA1 and FA2—Financial Concerns: As highlighted by the study findings, the most significant barrier to investments in green retrofit projects in India pertains to financial concerns. This includes long payback period and increased upfront cost. The

Table 6 Descriptive statistics

	N	Mean	Std. deviation	Minimum	Maximum	Percentiles		
						25th	50th (Median)	75th
FA1	30	2.83	2.479	1	11	1.00	2.00	3.00
FA2	30	3.13	1.456	1	5	2.00	3.50	4.00
FA3	30	6.67	1.953	3	9	5.00	7.00	8.25
OA1	30	5.20	2.091	1	9	4.00	5.50	7.00
OA2	30	6.97	1.450	3	9	6.00	7.00	8.00
TI1	30	7.13	1.814	1	9	6.00	8.00	8.25
LA1	30	7.73	1.112	5	9	7.00	8.00	9.00
LA2	30	2.90	1.626	1	8	2.00	2.00	4.00
GI1	30	3.23	1.591	1	7	2.00	3.00	4.00

Table 7 Friedman's test—ranks

	Mean rank
FA1	2.73
FA2	3.02
FA3	6.57
OA1	5.10
OA2	6.83
TI1	7.10
LA1	7.63
LA2	2.83
GI1	3.18

Table 8 Test statistics[a]

N	30
Chi-square	137.211
df	8
Asymp. Sig.	0.000

[a]Friedman's test

findings have been consistent with the literature. However, there exists significant financial, societal and intangible benefits to green retrofitting, but many of the benefits are not easily quantified or measured [39]. Further, it is experienced in many other countries that in lack of communication and absence of correct promotional strategies, the benefits are not conveyed to the stakeholders [15]. Also, findings of a study conducted in Singapore advocated that existing buildings that are green retrofitted can generate greater investment returns [43]. The study further highlighted that in terms of challenges, the most prevalent obstacle to greening existing buildings is to convince owners about the additional capital expenditures and to ensure that it will be recovered. It is imperative that stakeholders are able to comprehend the entire value chain in order to understand both the economic and social benefits associated with these projects. And, in India, lack of awareness and knowledge on the subject can be attributed as one major reason for resistance to adopt these new technologies. The present study also highlighted that about 58% of the respondents had no good information about green retrofit. Only, about 15% respondents had a good understanding of the subject.

LA2—Lack of Technical Expertise: The other important barrier as reported in the empirical analysis is the lack of technical experts in the area in India. Though there exist a handful of regulations and procedures as delineated by IGBC and GRIHA, which are the two leading institutions responsible for training green retrofit experts, there is still considerable scepticism pertaining to effective implementation and operation of such projects. Numerous reasons have been associated with it as highlighted by the study on India [16]—less number of trained professionals, a fewer realized projects, it is a new area and not much precedence exists to gain experience. Apart

from this, a comprehensive set of laws and codes are missing at the national level that can be followed.

GI1—Government Incentives: The findings of the study determined that **t**he incentives provided by the government are not enough to bring any acceptability within the building community on uptake of green retrofit projects in India. The present study was limited to rank the absence of proper incentives amongst the other perceived barrier. However, it is important to examine the various aspects of the incentives in detail to have the complete perspective on the associated benefits and shortcomings.

OA1—Operational Indicator: Building being occupied was the fifth most critical barrier perceived by the respondents. Th**e** risk was perceived as deterrent as the green retrofits work is usually conducted with the occupants' or tenants' operation continuing. The likelihood of non-cooperation and interruption is manifold in comparison to a new project [27]. And, in absence of standardized systems and lack of willingness, the perceived challenges are acute.

5 Conclusion

The existing research illustrates a few important themes related to barriers to green retrofit in India that are also highlighted by the other studies conducted overseas. However, as the present study is based on a closed set of survey conducted on a fewer category of stakeholders, further research is recommended to achieve a consensus and to examine each aspect in detail. Nonetheless, the study provides a basis to understand the deterrents and criticalities involved in any green retrofit projects in India for both practitioners and policy-makers. Furthermore, as a sector green retrofit is seen with scepticism and apprehension and in a complex, diverse and geographically varied country India, rolling out retrofit projects is a big challenge. It is understandable that India has a huge stock of existing buildings and a decision on demolishing or renovating or retrofitting is a complex process. However, with country's commitment to sustainability agenda sooner or later process of green retrofit would be mandatory and aligned with the regulatory aspects. The sector holds a lot of potential for growth as unavoidably all ageing buildings though maintained customarily will require alteration to accomplish sustainability objectives.

References

1. Akintoye A (2000) Analysis of factors influencing project cost estimating practice. Constr Managt Econ 18(1):77–89
2. ASCI and NRDC (2014) Greener construction saves money: incentives for energy efficient buildings across India
3. Benson A et al (2011) Retrofitting commercial real estate: current trends and challenges in building retrofitting in Australian cities. Build Environ 74:86–95

4. Bu S, Shen G, Anumba Chimay J, Wong Andy KD, Liang Xin (2015) Literature review of green retrofit design for commercial buildings with BIM implication. Smart Sustainable Built Environ 4(2):188–214. https://doi.org/10.1108/SASBE-08-2014-0043
5. Bullen P, Love P (2011) A new future for the past: a model for adaptive reuse decision-making. Built Environ Project Asset Manage 1(1):32–44
6. Dahle M, Neumayer E (2001) Overcoming barriers to campus greening: a survey among higher educational institutions in London, UK. Int J Sustain High Educ 2(2):139–160
7. Daly D, Cooper P, Ma Z (2014) Implications of global warming for commercial building retrofitting in Australian cities. Build Environ 74:86–95
8. Department of Energy and Climate Change (DECC) (2012) Energy efficiency statistical summary. Department of Energy and Climate Change, London
9. Dixon T (2014) Commercial property retrofitting: what does -retrofit‖ mean, and how can we scale up action in the UK sector? J Property Investment Financ 32(4):443–452. https://doi.org/10.1108/JPIF-02-2014-0016
10. DODG (2015) World green building trends 2016: developing markets accelerate global green growth smart market report. Retrieved from http://analyticsstore.construction.com/smartmarket-reports/2016WorldGreen.html?sourcekey=PRESREL. Accessed on 29th July 2018
11. Emily D, Kriti N, Niazi Z, Scott A, Varsha D, Lakshm KV (2013) Green buildings case study. Retrieved from http://basinsa.net/reportsAndPublications/20140709-11-12-07.pdf on 15th July 2018
12. EPA (2016) Green building: basic information. Available at https://archive.epa.gov/greenbuilding/web/html/about.html
13. Godrej & Boyce Mfg Ltd, n.d. [Online]. Available at http://www.godrejgreenbuilding.com/CaseStudies/OberoiMall_Mumbai.pdf. Accessed Aug 2018
14. Hopkins Erin A (2016) Barriers to adoption of campus green building policies. Smart Sustainable Built Environ 5(4):340–351
15. Horhota M, Asman J, Stratton JP, Halfacre AC (2014) Identifying behavioral barriers to campus sustainability: a multi-method approach. Int J Sustain High Educ 15. https://doi.org/10.1108/IJSHE-07-2012-0065
16. IGBC (2013) [Online]. Available at https://igbc.in/igbc/html_pdfs/abridged/IGBC%20Green%20EB%20O&M%20Rating%20System%20(Pilot%20Version).pdf
17. International Energy Agency (IEA) Energy policies beyond IEA Countries—Russia 2014. Executive sumnary. Available online http://www.iea.org/Textbase/npsum/russia2014sum.pdf
18. Jindal A (2016) TERI-UTC center of excellence (CoE) on energy efficient buildings in India. Retrieved from http://grihaindia.org/grihasummit/tgs2016/presentations/19feb/existing-buildings/Ashish_Jindal.pdf on 25th July 2018
19. Kamakura W, Wedel M, Agrawal J (1994) Concomitant variable latent class models for conjoint analysis. Int J Res Mark 11:451–464
20. Kapure R, Jain RK (2014) Parameters of upgrading existing building into a green building. Int J Eng Res Appl 4(2):19–23
21. Kok N, Jennen M (2012) The impact of energy labels and accessibility on office rents. Energy Policy 46:489–497
22. Kok N, Miller N, Morris P (2012) The economics of green retrofits. J Sustain Real Estate 4(1):4–22
23. Liang X, Shen G, Guo L (2015) Improving management of green retrofits from a stakeholder perspective: a case study in China. Int J Environ Res Public Health 12:13823–13842
24. Lockwood C (2009) Building the green way. Harvard Bus Rev 84(6):129–137
25. Ma Z, Cooper P, Daly D, Ledo L (2012) Existing building retrofits: methodology and state-of-the-art. Energy Build 55:889–902
26. Mahal NA (2016) Formulating guidelines for effective implementation of green building scheme of the urban local bodies. Available at https://issuu.com/www.ijera.com/docs/e0611061927. Accessed on 17 July 2018

27. Miller E, Buys L (2008) Retrofitting commercial office buildings for sustainability: tenants' perspectives. J Property Investment and Finan 26(6):552–561
28. NAIR S (2016) [Online]. Available at https://www.thebig5constructindia.com/media/2100/improving-energy-eff-in-bldgs-big5-sumesh-nair.pdf. Accessed July 2017
29. Omer A M (2008) Energy, environment and sustainable development. Renew Sustain Energ Rev Elsevier 12(9):2265–2300
30. Ott RL, Longnecker MT (2010) An introduction to statistical method & data analysis duxberry press
31. Pandey S (2015) Impact of green building rating systems on the sustainability and efficacy of green buildings: case analysis of green building index, malaysia. MIT-UTM Malaysia. Sustainable cities program. Retrieved from https://scienceimpact.mit.edu/sites/default/files/documents/Pandey.pdf on 23rd June 2018
32. RBC (2011) Moving into the Mainstream Green Buildings and LEED. Retrived from http://www.rbc.com/responsibility/environment/20111004-green-building-report.pdf on 25th June 2018
33. Rhoads J (2010) Low carbon retrofit toolkit—a roadmap to success, Better building partnership. Available at www.betterbuidlingspartnership.co.uk/download/bbp_low_carbon_retrofit_toolkit.pdf. Accessed 6 June 2012
34. Richardson GRA, Lynes JK (2007) Institutional motivations and barriers to the construction of green buildings on campus: a case study of the University of Waterloo, Ontario. Int J Sustain High Educ 8(3):339–354
35. Shipley R, Utz S, Parsons M (2006) Does adaptive reuse pay? A study of the business of building renovation in Ontario, Canada. Int J Heritage Stud 12(6):505–520
36. Sutherland RJ (1991) Market barriers to energy-efficiency investments. Energy J 12(3):15–34
37. TERI (2013) Roadmap for incorporating energy efficiency retrofits in existing buildings, the energy and resource institute (TERI), New Delhi
38. US Green Building Council (2015), LEED | US Green Building Council. Available at http://www.usgbc.org/leed
39. Weber CL, Kalidas SK (2004) Cost-benefit analysis of LEED silver certification for new house residence hall. Carnegie Mellon University, Pittsburgh, PA
40. Wilkinson S (2012) Analysing sustainable retrofit potential in premium office buildings. Struct Surv 30(5):398–410
41. World Economic Forum (WEF) (2011) A profitable and resource efficient future: catalysing retrofit finance and investing in real estate. WEF, Geneva
42. Wright TSA, Wilton H (2012) Facilities management directors' conceptualizations of sustainability in higher education. J Clean Prod 31:118–125
43. Yu S, Tu Y, Luo, C (2011) Green retrofitting costs and benefits: a new research Agenda. IRES working paper series No. 22. National University of Singapore, Institute of Real Estate Studies, Singapore

Field Investigation on the Orientation of 11.2 kWp Rooftop-Based PV System for Hot-Humid Location of India

Bibekananda Jena and Renu Sharma

Abstract Solar photovoltaic is becoming a major power generation means increasingly affordable and proving to be as reliable as the utilities. In fact, in recent years it has become a several billion dollar global sunrise industry growing well over 30% every year. In India, the rooftop-grid-connected solar PV systems are being subsidized to bridge the gap in demand and supply of power. At SOA University, Bhubaneswar, 11.2 kWp rooftop-grid-connected solar PV system has been installed and operated for over 3 years. This paper presents an outline of the setup, operational experiences, and limitations and highlights the measures to combat the limitations. It is concluded that seasonal adjustment of rooftop modular arrays will affect space conditioning in the building and significantly enhance the yield.

Keywords Solar photovoltaic · Tilt angle · Global solar radiation · Irradiance

1 Introduction

Development and harnessing of renewable energy sources using modern conversion technologies enhance the energy security and conserve fossil and nuclear fuels for futures generations. It also reduces the emission of greenhouse gases which otherwise are responsible for more disastrous consequences like climate change, etc. Of all the renewable and clean energy technologies, solar PV technologies have received comparatively more attention since it does not involve moving parts like the prime movers. In day-to-day life, the load demand increases rigorously. In India, 90% of the region receives 3.0–6.5 kWh per square meter per day, i.e., 10.8–23.4 megajoules per square meter per day during the months of summer. But, during May many parts of northern India receive average solar insolation up to 7.6 kWh meter square

B. Jena (✉) · R. Sharma
Department of Electrical Engineering, ITER, SOA Deemed to be University, Bhubaneswar, India
e-mail: masterbibekjena@gmail.com

R. Sharma
e-mail: renusharma@soa.ac.in

G. Zhang et al. (eds.), *Advances in Energy and Built Environment*, Lecture Notes in Civil Engineering 36, https://doi.org/10.1007/978-981-13-7557-6_7

per day, i.e., 27 megajoules per square meter per day [1]. The importance of solar irradiance has been seen in various applications such as solar cooker, solar thermal plants, solar water heating, day lighting, heating of the building, crop drying, and solar photovoltaic systems. In the past few years, many researches are going on to extract maximum insolation from the sun for the use of above applications. The most important source for the use of solar insolation is solar photovoltaic system in which the irradiance of the sun is directly converted into electricity by the principle of the photovoltaic effect.

The power output of the PV system strongly depends upon the solar irradiance received by it. However, the power output of PV system gets influenced by many factors such as installation technique, location, orientation, climatology, latitude, tilt angle, geographical region, azimuth angle, and proper positioning [2].

The output of a PV system largely depends upon its orientation. The orientation of PV system includes adjustment of the tilt angle so as to that the system can receive maximum insolation throughout the day. The trajectory path of the sun can be tracked by the employment of solar tracking equipment that could able to receive maximum solar insolation on the surface. This leads to performance enhancement of PV system [3, 4].

By using DC servo motors or stepper motors for manual adjustment of tilt angle, the solar tracking system can be done effectively. However, this can face various economic challenges as the tilt angle of the solar PV surface changes every hour, month, and seasons. From different studies [5], the land requirement for 1 MW_p power plant with static solar PV panels is 1.07 ha. While for the one-axis tracking power plant, it is 6.94 ha (550% more) and for two-axis tracking power plant, it is 4.81 ha (350% more). The servo motors used for automatic solar tracking system consume energy for its own operation that is near about 5–13% of the total energy generation of the PV system [6]. Also, the maintenance and replacement cost of the motor are the two implicit factors that can raise the total cost of the system. The system with solar trackers contains moving parts that may increase the capital cost of system that indirectly added in the cost of total energy generated from the PV systems [7]. It is found that adjusting azimuth angle of 10°, 20°, and placing the tilt angle equal to the latitude of the defined location, maximum solar isolation can be tracked [2]. However, these techniques are also not exact to actual values. Liu and Jordan's model is used to calculate the optimum tilt angle in India [8, 9].

2 System Setup

The complete layout plane of the system consisting of array network and balance of system, data acquisition, and monitoring system grid-system interface is shown in Fig. 1. System interface with the utility is achieved through the grid tie inverter, which is a power inverter that converts direct current (DC) electricity into alternating current (AC). The grid tie inverter has a fixed near-unity-power factor, which means its output voltage and current are perfectly lined up and its phase angle is within

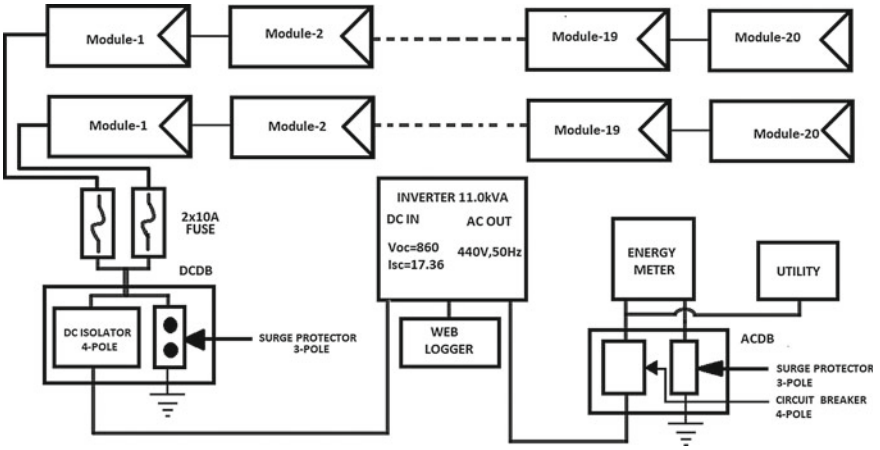

Fig. 1 Layout of rooftop-based 11.2 kW PV system at SOA Deemed to be University

one degree with the AC power grid. Built in the inverter is an onboard computer which senses the current, AC grid waveform and produces an output voltage in correspondence to grid. It will shut down automatically upon loss of utility supply for safety region. It does not provide backup power during utility outages.

The PV system consists of

- The PV array—Energy-generating unit
- The balance of System—Power conditioning unit
- Data acquisition and monitoring system
- Grid-system interface.

The PV array is the energy-generating unit. The array is a network of modules which are connected in series to obtain the desired voltage; the series arrangements of modules are known as a string. The strings are connected in parallel to obtain the desired current. Figure 2 shows the rooftop-based setup of 11.2 kW PV system at SOA Deemed to be University.

In our field experience, we investigated the series and parallel arrangements of modules with respect to fault tolerance of the array network and found that the parallel configuration of modules is less susceptible to the faults. We have therefore used two strings in parallel to obtain the desired electrical specification of the array network. The specification of PV module at STC 1000 w/m^2 and 25 °C has been given in Table 1. The dimension of the PV module and array to determine the appropriate spacing between them has been provided in Table 2. In Fig. 2, dimensions of PV modules and array are depicted.

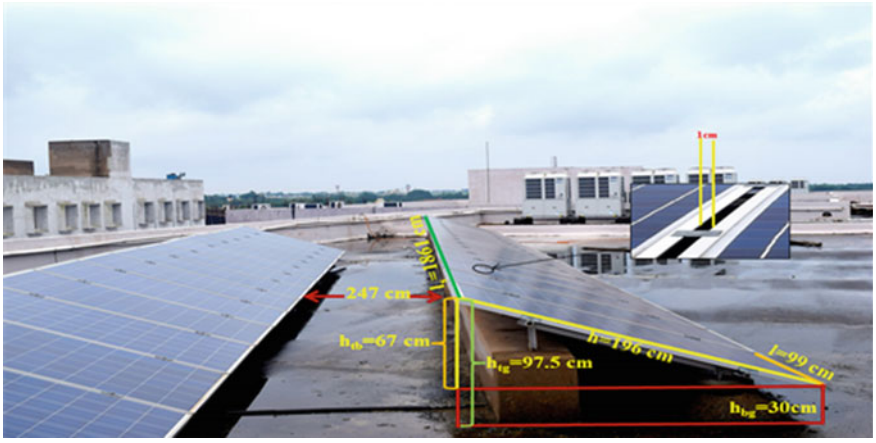

Fig. 2 Dimensions of PV modules and array

Table 1 Specification of PV module at STC (1000 W/m^2 and 25 °C)

Parameters	Rating
Rated peak power (P_{max})	280 W
Open-circuit voltage (V_{OC})	43 V
Short-circuit current (I_{SC})	8.68 A
Voltage at MPP (V_{MP})	35 V
Current at MPP (I_{MP})	8 A
Number of series connected PV modules	20
Number of parallel connected strings	2

Table 2 Dimensions of PV modules and array

Parameter	Dimension (cm)
Length of the PV module (l)	99
Height of the PV module (h)	196
Length of the PV string (l_s)	99
Height of the PV string (h_s)	196
Length of spacing/gap between PV modules (l_g)	1
Height of spacing/gap between PV modules (h_g)	196

Table 3 Energy yield in each month for 2015

Month	Jan	Feb	Mar	Apr	May	Jun
Energy yield in kwh	1339.281	1376.099	1644.539	1462.861	1491.995	1141.416
Month	Jul	Aug	Sept	Oct	Nov	Dec
Energy yield in kwh	1044.626	1202.049	1143.659	1336.38	1290.034	891.589

3 Operational Experience

The monthly power yield of the PV system during the year-round cycle of 2015 is shown in Fig. 3c and tabulated in Table 3. It was observed that the production of electricity during the winter and summer months is relatively less as compared to the theoretical expectations, whereas during equinox it coincides well with theoretical values of insolation. This is due to the fixed tilt angle which is sensitive to equinoxes (March, April, September, and October).

We have therefore investigated the effect of the seasonal adjustment of the array on GSR and shadow of modules on the rooftop. The optimum tilt angles for summer, winter, and equinoxes are determined and shown in Fig. 4.

4 Calculations

4.1 Solar Flux Gain Annually, on Monthly Tilted Plane and Seasonally Tilted Plane

Mean of global solar radiation (MGSR) is given by,

$$\text{MGSR}\ (F) = \sum_{i=1}^{n} X_i \tag{1}$$

where X_i refers to the global solar radiation (GSR) of months (January to December)/seasons (summer, winter, equinox) at the optimum tilt angle and fixed tilt angle.

Solar flux gain (SFG) in percentage is given by,

$$\text{SFG} = \frac{(F_{\text{OT}} - F_{\text{FT}})}{F_{\text{FT}}} \times 100 \tag{2}$$

where F_{OT} and F_{FT} stand for optimum tilt angle and fixed tilt.

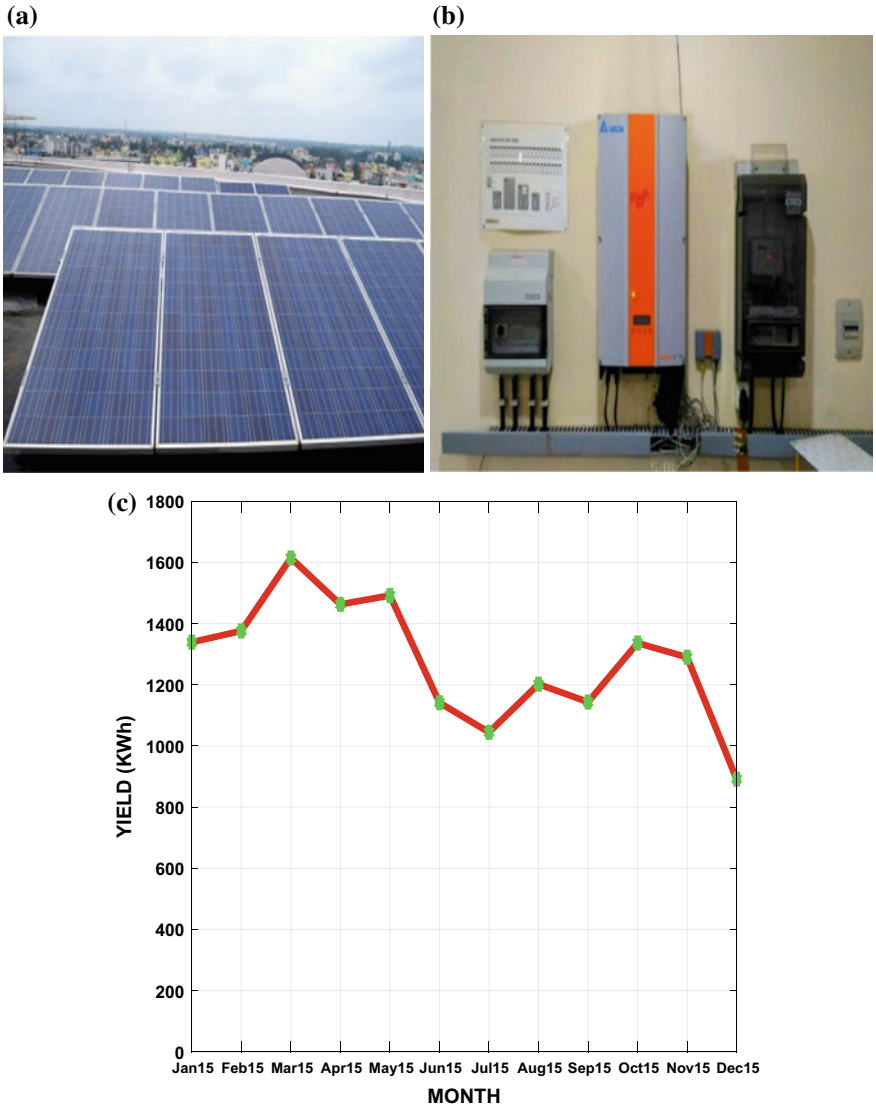

Fig. 3 **a** PV system, **b** PV system components, and **c** energy yield recorded by Watmon

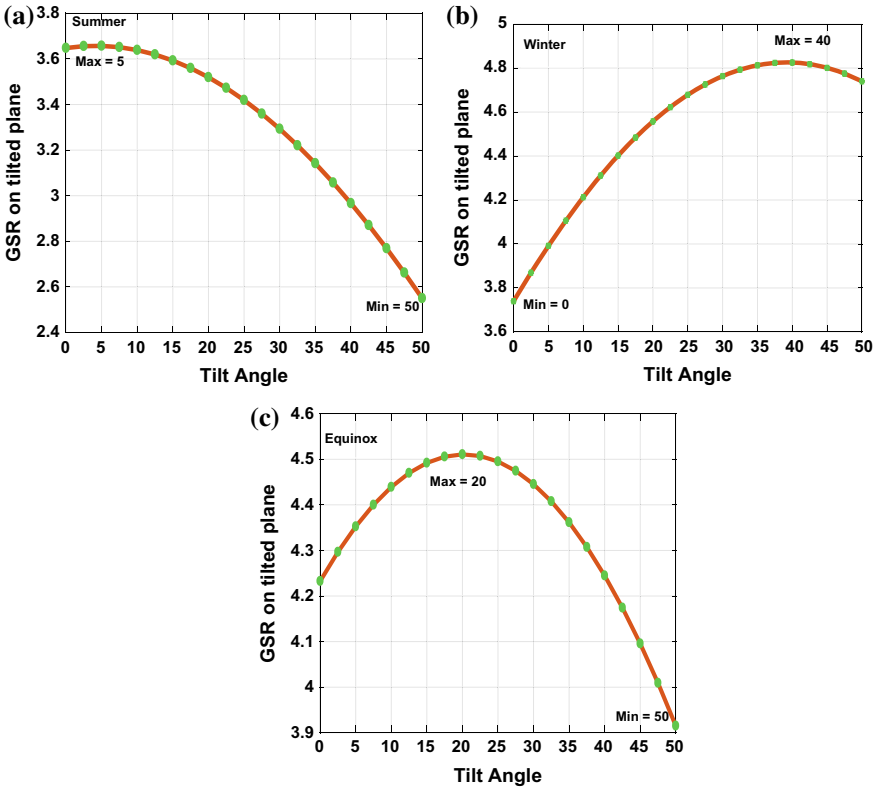

Fig. 4 Determination of modular tilt angle. **a** Summer, **b** winter, and **c** equinox

4.2 Shadow Formation Seasonal Adjustment of Array

The percentage of shadow found in seasonal (summer, winter, equinox) adjustment of arrays is given by

$$S = \left(\frac{S_i - S_j}{S_j} \right) \times 100 \tag{3}$$

where S is the percent of shading, S_i is shading due to the optimum tilt angle, and S_j is the shading due to the fixed tilt angle of SPV arrays.

5 Results and Discussions

The modules must be placed perpendicular to the sun rays to maximize the generation of electrical energy. We initially placed the modules at fixed tilt angle to maximize the generation of yearly average electrical energy. This tilt angle was determined from the consideration of GSR as shown in Fig. 5 and for Bhubaneswar, it was determined to be 22.5°, i.e., 20.2961° + 2.2039°.

According to the annual solar flux gain calculations, it was found the monthly, seasonally adjustment of SPV arrays is more effective at the optimum tilt as compared to annually fixed SPV arrays. The annual mean of global solar radiation (GSR) on monthly optimum tilt adjustment value is 4.3510 but in annually fixed tilt, it is 4.2006 as shown in Table 4 and Fig. 5.

So the annual solar flux gain between the annual mean of GSR on monthly optimum tilts and annually mean of GSR on monthly fixed tilt is 3–4% as shown in Table 4. But throughout the year due to seasonal adjusted, the solar flux gain in annually is 3–4% which is shown in Table 4. In the seasons like summer, winter, and equinox, the solar flux gain is estimated, i.e., 5–6, 4–5, and 1% which is on Table 5.

It is found that the performance of seasonal optimum tilt adjustment is more beneficial as compared to monthly optimum tilt, annual optimum tilt, and seasonal fixed tilt. We know that the shadow is formed by the SPV arrays when they are placed on the rooftop so it is required to adjust the tilt angle in such a manner that in the

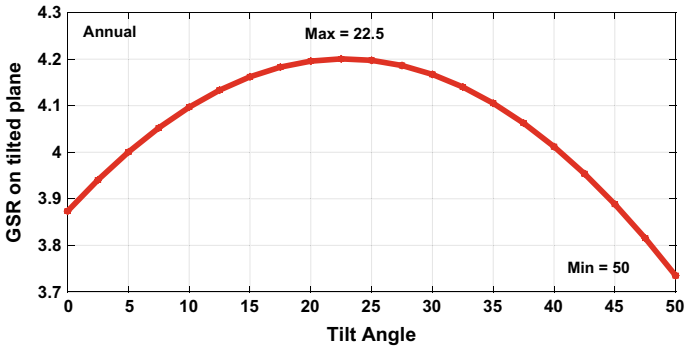

Fig. 5 Effect of variation of tilt angle on mean GSR annually

Table 4 Percentage of solar flux gain annually adjusted

Annual mean of GSR on monthly optimum tilt (F_{OT})	4.3510
Annual mean of GSR on monthly at fixed tilt (F_{FT})	4.2006
Annual SFG (%)	3.5804
Seasonally mean of GSR on optimum tilt (f_{ot})	4.3309
Seasonally mean of GSR on monthly at fixed at tilt (f_{ft})	4.2006
Annual SFG by seasonally adjusted in %	3.1019

Table 5 Percentage of solar flux gain annually by seasonally adjusted

Season	Optimum tilt angle of SPV module (β) in degree	GSR on optimum tilt angle (X_{OT})	GSR on fixed tilt (X_{FT}) (22.5°) tilt angle	SFG by seasonally adjusted in % $\left(\frac{X_{OT}-X_{FT}}{X_{FT}}\right) \times 100$
Summer	5	3.6571	3.4725	5.3160
Winter	40	4.8252	4.6223	4.3895
Equinox	20	4.5106	4.5071	0.0776

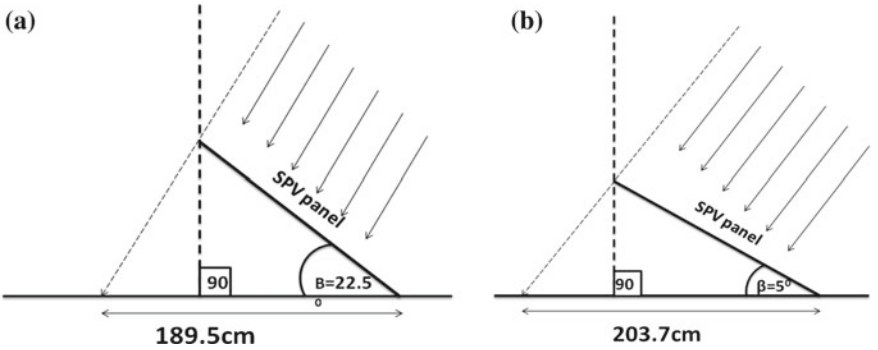

Fig. 6 Shadow formation at optimum tilt angle in summer (May, June, July, August) and at fixed tilt

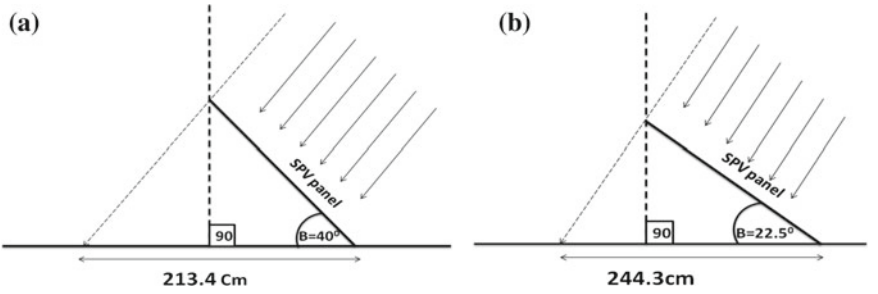

Fig. 7 Shadow formation at optimum tilt angle in winter (November, December, January, February) and at fixed tilt

summer the shadow should be more, i.e., the area exposed to sun is decreased, in the case of winter it should be less, i.e., area exposed to sun increases. The shadow formed at a seasonal fixed tilt and seasonal optimum tilt in summer, winter, and equinox are 189.5 and 203.7 cm, 244.3 and 213.4 cm, and 219.6 and 222.7 cm, respectively. The shadows formation due to seasonal adjustment and fixed tilt are shown in Figs. 6 and 7. It is estimated that the percentage of shading in summer, winter, and equinox is 7.5−12.7 and 1.14% as shown in Table 6, so at the equinox it is negligible.

Table 6 Shadow formation due to seasonal adjustment of solar SPV arrays

Season	β at optimum tilt	S_i, β at optimum tilt	S_j, β at fixed tilt, i.e., 22.5°	S in %
Summer	5	203.7	189.5	7.5
Winter	40	213.4	244.3	−12.7
Equinox	20	222.7	219.6	1.14

6 Conclusion

The seasonal adjustment of SPV arrays improves the global solar radiation (GSR) on the module surface, due to seasonal adjustment of SPV arrays the solar flux gain increased as compared to seasonal fixed tilt of SPV arrays in summer, winter, and equinox, it is about 5–6%, 4–5%, and 1%, respectively. It is estimated that the percentage of solar flux gain in seasonal adjustment with respect to seasonally fixed tilt is 3–4% annually. Besides that, the percentage of change in array shading in seasonal optimum tilt adjustment and seasonally fixed tilt adjustment is estimated. It is found that the change in shading in summer, winter, and equinox is 7–8%, −12 to 13%, and 1–2%, respectively. Due to the seasonal adjustment in summer, the shadow is increased by 7–8%, in winter the shadow is decreased by 12–13%, and in equinox it is negligible. So it is concluded that the seasonal adjustment of SPV arrays will work as space conditioner in the building and also yield more electrical energy as it is placed on the rooftop of a building. The proposed rooftop solar photovoltaic method can elucidate the additional purpose of building heating and cooling during different seasons of the year.

Acknowledgements The authors would like the thank Prof. (Dr.) N. D. Kaushika, Ex-Professor IIT Delhi and presently visiting SOA Deemed to be University, for giving his precious time and valuable ideas for completion of this study.

References

1. Ramachandra TV, Jain R, Krishnadas G (2011) Hotspots of solar potential in India. Renew Sustain Energy Rev 15(6):3178–3186
2. Yakup MH, Malik AQ (2001) Optimum tilt angle and orientation for solar collector in Brunei Darussalam. Renew Energy 24(2):223–234
3. Bahrami A, Okoye CO, Atikol U (2016) The effect of latitude on the performance of different solar trackers in Europe and Africa. Appl Energy 177:896–906
4. Okoye CO, Taylan O, Baker DK (2016) Solar energy potentials in strategically located cities in Nigeria: review, resource assessment and PV system design. Renew Sustain Energy Rev 55:550–566
5. Vermaak HJ (2014) Techno-economic analysis of solar tracking systems in South Africa. Energy Proc 61:2435–2438
6. Eldin SAS, Abd-Elhady MS, Kandil HA (2016) Feasibility of solar tracking systems for PV panels in hot and cold regions. Renew Energy 85:228–233

7. Sinha S, Chandel SS (2016) Analysis of fixed tilt and sun tracking photovoltaic–micro wind based hybrid power systems. Energy Convers Manage 115:265–275
8. Jamil Ahmad M, Tiwari GN (2009) Optimization of tilt angle for solar collector to receive maximum radiation. Open Renew Energy J 2(1):19
9. Ahmad MJ, Tiwari GN (2009) Optimum tilt angle for solar collectors used in India. Int J Ambient Energy 30(2):73–78

Rural Electrification Using Hybrid Solar and Biogas System in Phulwaria Village, Bihar: A Case Study

Sushmita Mohapatra, Saurabh Agrawal and Himanshu Ranjan

Abstract The economic development plans in the developing as well as developed countries have accelerated the consumption of electrical energy. Consequently, the gap between the demand and supply for power is widening around the world. In the present scenario, power generation by renewable energy sources has gained significant importance. In India, approximately 70% of the people live in rural parts where power from grid supply is scanty. This paper investigates and proposes a viable option for supplying power to Phulwaria village in Bihar by adopting hybrid energy systems (HESs) of solar photovoltaic (SPV) and biogas to produce electricity. Here, combined heat and power (CHP) model is used for biogas where the wasted heat is used to heat water and supply clean drinking water.

Keywords Anaerobic digestion · HES · CHP · Biogas · SPV

1 Introduction

In India, state electricity boards are in huge debts and therefore become incapable of buying power. At present, India is facing a power deficit of approximately 12% because of the reduction in the supply of fuel, especially coal. Also, the use of the conventional fuels has alarming adverse effect on the environment. Therefore, power generation using renewable sources like biomass, solar, wind, and mini–micro hydel has become very important. It is not possible for biogas and solar resources to separately meet the demands of electricity, drinking water, and clean cooking but can be accomplished by a hybrid system [1]. Hybrid energy systems use either completely different but complementary energy systems based on renewable energies or a combination of a renewable source with gasoline or diesel source.

S. Mohapatra · S. Agrawal (✉)
Department of Applied Science, Bharati Vidyapeeth's College of Engineering, New Delhi, India
e-mail: saurabh.goel9944@gmail.com

H. Ranjan
Department of Mathematics, Government Polytechnics Gopalganj, Gopalganj, Bihar, India

G. Zhang et al. (eds.), *Advances in Energy and Built Environment*, Lecture Notes in Civil Engineering 36, https://doi.org/10.1007/978-981-13-7557-6_8

The best feature of hybrid energy systems of the various renewable sources is captured, and then, a clean and good quality with power varying between 1 kW and several hundred kW can be achieved. Such type of hybrid models can give electrification to rural where grid power is not available and can be upgraded with grid connection in the future. Since the renewable energy systems are highly reliable with long-term performance, they can also be used as a backup solution even when the villages are connected with grid.

The village under consideration for the present investigation is a small village in Phulwaria, Siwan District of Bihar. This village has a very poor grid performance supplying power for 4–5 h in a day. This village has about 100 villages with approximately 2 bovine per house. Also, this village receives a good amount of sunlight (approximately on an average of 8 h per day). Thus, both biogas from bovine dung and solar energy through SPV can be used as the renewable energy source. Biogas gives AC loads, and SPV gives DC loads, so both the electricity-generating components are connected to both the sides of the master inverter which would control the supply of AC load.

2 Methodology

The village under study for the present paper is Phulwaria in Siwan District of Bihar. Agriculture is the main occupation of this village, but it lacks in good quality education, safe drinking water, roads, and electricity.

2.1 Energy Conversion

Among the various existing technologies, the technology under investigation is digester gas engine (DGE) and solar PV systems. In the following sections, the two technologies are described in detail.

2.1.1 Biomethane from Anaerobic Digesters

Anaerobic digestion of bovine dung is done in a controlled manner. The primary component of an anaerobic digester is a waste vessel containing bacteria that would convert organic waste (cattle dung) into biogas and slurry. The digestion is carried out in four phases. In the first phase, the hydrolytic bacteria break down the big complex molecules like carbohydrates, proteins, or fat into smaller molecules which are then subjected to the acidogenesis bacteria which break down the above formed molecules to acids. The third step is the action of acetogenesis bacteria which convert the acids into hydrogen, carbon dioxide, and acetic acid. In the last step, the methanogenesis bacteria convert hydrogen and acetic acid into methane and carbon dioxide. The

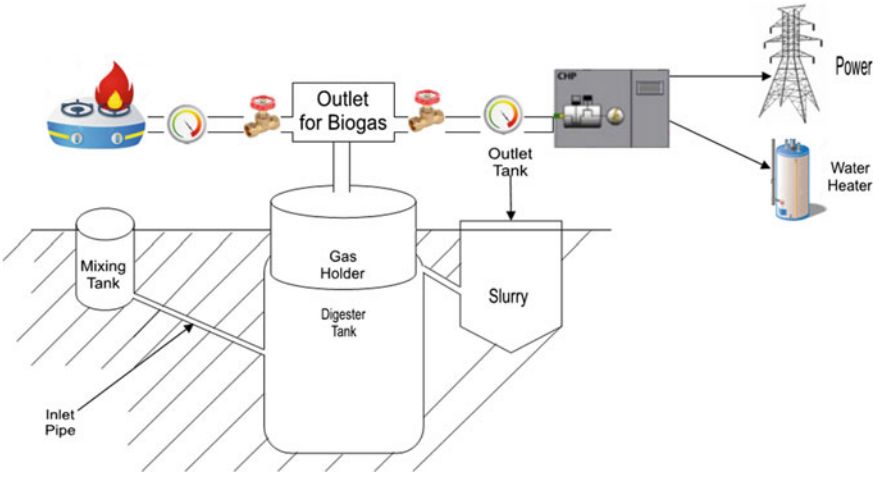

Fig. 1 Model of electricity generation from biogas

slurry which is obtained is rich in nitrogen and phosphorus and can be used in the fields for agriculture. Depending on the nature of feedstock, the biogas comprises of 55–75% methane, the rest being carbon dioxide and other gases.

2.1.2 Electricity Generation from Biogas

The electricity generation systems that use biogas consist of an internal combustion engine, a generator, and a control system. A typical biogas engine converts 35–40% of the calorific value into electricity; rest of the energy input goes as waste heat which would be utilized in heating water (Fig. 1). Although large-scale biogas plants are rare, many small-scale plants of 1.5–80 m^3 are common in many parts of Asia [2]. One kilogram of fresh cattle dung is capable of producing 0.04–0.05 m^3 of biogas [3].

2.2 Solar PV System

Solar PV system consists of a PV module, a charge controller, a rechargeable battery, and an inverter (Fig. 2).

The solar panel is placed in an open space or a rooftop, whereas the charge controller, battery, and the inverter are kept inside the room [4, 5]. The charge controller manages the flow of power in and out of battery and ensures that the battery is not overcharged and also prevents the battery from overdischarging [6]. The solar module does not require any maintenance during its life span of 20 years [7], but the battery

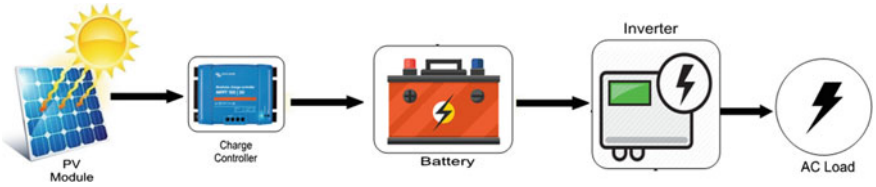

Fig. 2 Model of solar PV system

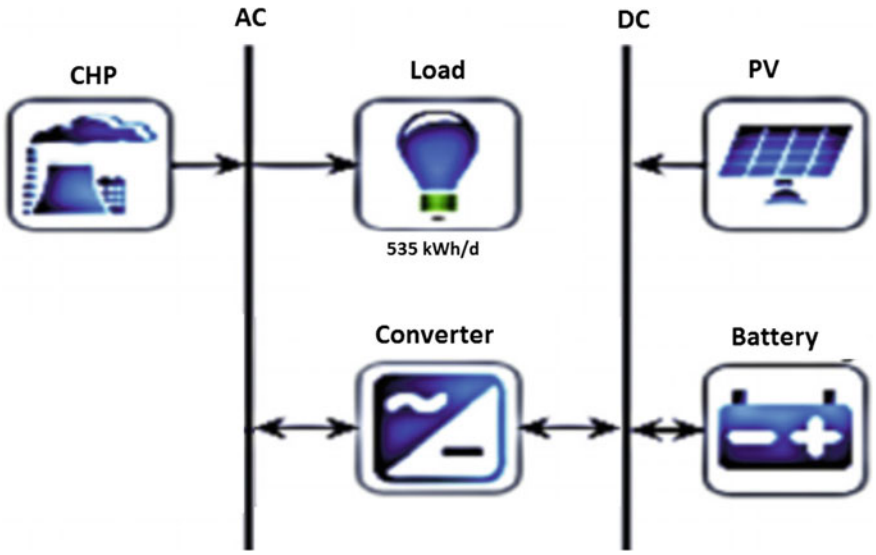

Fig. 3 Model of hybrid renewable energy system

requires periodic maintenance [8]. In the present case study, the hybrid renewable energy system with biogas generator is used which is shown in Fig. 3.

3 Household Survey

The data is based on the primary data collection by the authors. The survey was conducted in Phulwaria village in which 100 households were considered. The main aim of the survey was to count the total number of bovines and the amount of dung generated per day and to make the people aware of the advantages of renewable energy. Based on the survey, the load requirement on daily basis was also calculated and is given in Table 1.

Table 1 Load analysis estimation for a single house

Gadget/Hours	CFL (15 W/h)	Fan (120 W/h)	TV (60 W/h)	Computer (120 W/h)	Water pump (1000 W/h)	Refrigerator (60 W/h)	Others + Inverter (20 W/h)	Total per hour load (kWh)
00–01	1 * 1 = 15 W	2 * 1 = 120 W	–	–	–	1 * 1 = 60 W	1 * 1 = 20 W	0.215
01–02	1 * 1 = 15 W	2 * 1 = 120 W	–	–	–	1 * 1 = 60 W	1 * 1 = 20 W	0.215
02–03	1 * 1 = 15 W	2 * 1 = 120 W	–	–	–	1 * 1 = 60 W	1 * 1 = 20 W	0.215
03–04	1 * 1 = 15 W	2 * 1 = 120 W	–	–	–	1 * 1 = 60 W	1 * 1 = 20 W	0.215
04–05	1 * 1 = 15 W	2 * 1 = 120 W	–	–	–	1 * 1 = 60 W	1 * 1 = 20 W	0.215
05–06	1 * 3 = 45 W	2 * 1 = 120 W			1 * (1/4) = 250 W	1 * 1 = 60 W	1 * 1 = 20 W	0.495
06–07	1 * 1 = 15 W	1 * 1 = 60 W				1 * 1 = 60 W	1 * 1 = 20 W	0.405
07–08						1 * 1 = 60 W	1 * 1 = 20 W	0.080
08–09						1 * 1 = 60 W	1 * 1 = 20 W	0.080
09–10						1 * 1 = 60 W	1 * 1 = 20 W	0.080
10–11		1 * 1 = 60 W				1 * 1 = 60 W	1 * 1 = 20 W	0.140
11–12		1 * 1 = 60 W				1 * 1 = 60 W	1 * 1 = 20 W	0.140
12–13		1 * 1 = 60 W				1 * 1 = 60 W	1 * 1 = 20 W	0.140
13–14		1 * 1 = 60 W				1 * 1 = 60 W	1 * 1 = 20 W	0.140

(continued)

Table 1 (continued)

Gadget/Hours	CFL (15 W/h)	Fan (120 W/h)	TV (60 W/h)	Computer (120 W/h)	Water pump (1000 W/h)	Refrigerator (60 W/h)	Others + Inverter (20 W/h)	Total per hour load (kWh)
14–15		2 * 1 = 120 W	1 * 1 = 60 W			1 * 1 = 60 W	1 * 1 = 20 W	0.260
15–16		2 * 1 = 120 W	1 * 1 = 60 W			1 * 1 = 60 W	1 * 1 = 20 W	0.260
16–17		2 * 1 = 120 W	1 * 1 = 60 W			1 * 1 = 60 W	1 * 1 = 20 W	0.260
17–18						1 * 1 = 60 W	1 * 1 = 20 W	0.080
18–19					1 * (1/4) = 250 W	1 * 1 = 60 W	1 * 1 = 20 W	0.330
19–20	2 * 1 = 30 W	2 * 1 = 120 W	1 * 1 = 60 W			1 * 1 = 60 W	1 * 1 = 20 W	0.290
20–21	2 * 1 = 30 W	2 * 1 = 120 W	1 * 1 = 60 W			1 * 1 = 60 W	1 * 1 = 20 W	0.290
21–22	2 * 1 = 30 W	2 * 1 = 120 W		1 * 1 = 120 W		1 * 1 = 60 W	1 * 1 = 20 W	0.350
22–23	1 * 1 = 15 W	2 * 1 = 120 W				1 * 1 = 60 W	1 * 1 = 20 W	0.215
23–24	1 * 1 = 15 W	2 * 1 = 120 W				1 * 1 = 60 W	1 * 1 = 20 W	0.215
								Total = 5.325 kWh/Day

4 Analysis of Load Estimation for a Single House

The average domestic load with the number of gadgets and the duration for which the gadget is used was captured from the primary data to get an idea of the average load and the peak load per day.

Since there are 100 houses in this village, the total consumption of electricity becomes $100 \times 5.325 = 532.5 \approx 535$ kWh/Day.

5 Analysis and Design Result

5.1 Design of Biogas Power Plant

From the primary data, it was found that total of 200 animals (cow/Buffalo) are present in the proposed village and the average dung per animals is 18 kg. Maximum gas production per kg dung = 0.5 m^3 and 1 m^3 of gas is equivalent to 19 MJ of energy, and 3.6 MJ of energy is equivalent to 1 kWh. Thus, if in the production of electricity from gas, 65% of energy is lost as heat, the total production of electricity through animals dung is described in Table 2.

In cow dung, the total solid content is approximately of 20.5% weight in wet bases [9] which comprises of degraded compounds, i.e., protein, cellulose, starch, and hemicelluloses [10] and the minimum time for producing biogas is approximately of 10–15 days [11].

5.2 Design of PV Panel

Total load required through PV panel is 270 KW per day which is explained in Table 3.

The current of 60 A shown is the average current for 10 h in a day. The calculation in detail is given below:

(1) The current drawn between 8 AM to 10 AM = 5 A × 2 = 10 A
(2) The current drawn between 10 AM to 12 PM = 6 A × 2 = 12 A

Table 2 Analysis of electricity through animal's dung

No. of cow	Total dung per day	Total gas	Total energy per day	Total loss energy per day	Total useful energy for electricity per day is	CHP model of 12 KW energy generated per day
200	3600 kg	180 m^3	950 kWh/day	617.5 ≈ 618 kWh	≈332 kWh	288 kWh ≈ 265

(3) The current drawn between 12 PM to 3 PM = 8 A × 3 = 24 A
(4) The current drawn between 3 PM to 6 PM = 5 A × 3 = 15 A

Therefore, the total current drawn between 8 AM and 6 PM is (10 A + 12 A + 24 A + 15 A = 61 A) approximately 60 A. The maximum current drawn can be only 8.9 A (from the Literature). Hence, the current drawn from morning to evening varies approximately from 5 to 8 A according to weather conditions.

6 Cost of Power Through Renewable Energy Systems

Tables 2 and 3 indicate the capacity of power generated through biogas and SPV, respectively, whereas Tables 4 and 5 indicate the total cost of the systems with and without subsidy.

6.1 Cost of Biogas Plant

The cost of the plant 12-kW biogas plant with CHP is given in Table 4. The wasted heat, which is approximately 65% of the total heat generated from biogas, could be used for heating the water. This water could be used for drinking purpose by the villagers.

Table 3 Analysis of electricity production through PV panel

No. of PV 150 W/12 V	One PV generated current	Total current generated by 380 nos
380	60 A/12 V Daily	380 * 60 = 22800 A & 12 V = 273.6 kWh/Day ≈270 kWh/Day

Table 4 Cost analysis of biogas plant

CHP model (Rs.)	Digester capacity of 3 Ton (Rs.)	Water heating tank cost (Rs.)	Maintenance cost (Rs.)	Total cost (Rs.)
30,00,000 By Urja Bio System Pvt Ltd, Pune Maharashtra, Web site: http://www.urjabiosystems.com	100,000	100,000	5000/month 60,000/year Total 900,000 for 15 years	4,100,000 (without Gov. subsidy)

Table 5 Cost analysis of PV panel

Cost of PV (Rs.)	100 batteries cost (Rs.)	Cost of charge controller of 15,000 A (Rs.)	Batteries replacement cost after five years (Rs.)	Cost of 10-kV inverter (Rs.)	Maintenance cost (Rs.)	Total cost (Rs.)
380 * 6500 = 2,470,000 ≈ 2,500,000	100 * 10,000 = 1,000,000	500,000	8000 * 100 = 800,000 (2 times between 15 years of plant) = 1,600,000	200,000	15,000/year Total cost for 15 years = 225,000	6,025,000 (without subsidy)

Table 6 Total cost analysis of our proposed model

Biogas plant (without subsidy)	Biogas plant (with subsidy)	PV panel (without subsidy)	PV panel (with subsidy)	Total cost of model (without subsidy)	Total cost of model (with subsidy)
Rs. 4,100,000	with 40% subsidy total cost is Rs. 2,460,000	Rs. 6,025,000	Total cost with 40% subsidy only on PV and Batteries is Rs. 3,985,000	Rs. 10,125,000	Rs. ≈ 6,500,000

6.2 Cost of PV Setup

The total PV setup for 100 households is given in Table 5.

6.3 Cost Analysis

The result of cost analysis of the entire project is given in Table 6.

7 Results and Discussion

Total energy consumption of the proposed village of 100 houses for 15 years is calculated to be 535 * 365 * = 2,929,125 ≈ 3,000,000 unit. If the cost of per unit electricity is 4.5 in current scenario, the total cost of electricity for 15 years of the village is 3,000,000 * 4.5 = 13,500,000. However, the electricity cost per unit increase would approximately increase from Rs. 4.5 to Rs. 8–10 in the next 15 years; therefore, the total electricity cost of villagers will be varied from Rs. 13,500,000 to Rs. 20,000,000. If the battery cost is doubled in 15 years, then the total maintenance cost of battery replacement would vary from Rs. 1,600,000 to Rs. 2,500,000, so the total cost of PV model setup will vary from Rs. 6,025,000 to Rs. 7,000,000. Therefore, the total setup cost of the proposed model (Biogas + PV) is Rs. 10,125,000 to Rs. 11,000,000 without subsidy and with subsidy would be Rs. 6,500,000 to Rs. 7,500,000, respectively.

8 Conclusion

A hybrid biogas solar PV system would not only make the village independent of grid for the electrification but also provide clean drinking water to the villagers. Biogas plant alone would not fulfill this demand as the cow dung required would be very high. Also solar PV panel alone cannot provide electricity during the rainy season or when there is no bright sunshine. If proper monitoring is done, then the biogas produced from the cow dung will be sufficient both for providing electricity and for cooking purpose. Also in 15 years, the amount of money saved by the proposed villagers Rs. 3,375,000–9,000,000 without any subsidy, and with government subsidy, they can save Rs. 7,000,000–12,500,000 which is very high.

References

1. Kanase-Patil AB, Saini RP, Sharma MP (2010) Integrated renewable energy systems for off grid rural electrification of remote area. Renew Energy 35:1342–1349
2. Rahman MM, Paatero JV (2012) A methodological approach for assessing potential of sustainable agricultural residues for electricity generation: South Asian perspective. Biomass Bioenergy 47:153–163
3. Singh KJ, Sooch SS (2004) Comparative study of economics of different models of family size biogas plants for state of Punjab, India. Energy Convers Manag 45:1329–1341
4. Bala B, Siddique SA (2009) Optimal design of a PV-diesel hybrid system for electrification of an isolated island Sandwip in Bangladesh using genetic algorithm. Energy Sustain Dev 13:137–142
5. Mondal AH, Denich M (2010) Hybrid systems for decentralized power generation in Bangladesh. Energy Sustain Dev 14:48–55
6. Ganthia BP, Sasmita S, Routa K, Pradhan A, Nayak J (2018) An economic rural electrification study using combined hybrid solar and biomass-biogas system. Mater Today: Proc 5:220–225
7. Schleicher-Tappeser R (2012) How renewables will change electricity markets in the next five years. Energy Policy 48:64–75
8. Givler T, Lilienthal P (2005) Using HOMER software to explore the role of Gen-sets in small solar power systems: case study-Sri Lanka. National Renewable Energy Laboratory, Washington, DC
9. Syafruddin R (2011) Strategi Start-Up Produksi Biogas dari Campuran Sampah Buah, Tesis, Chemical Engineering, Gadjah Mada University, Yogyakarta
10. Burke DA (2001) Dairy waste anaerobic digestion handbook. Environmental Energy Company, Hill Street Olympia
11. Deublin D, Steinhauser A (2008) Biogas from waste and renewable resources. Wiley-VCH Verlag GmbH and Co. KgaA, Weinheim

Electricity Demand Forecasting Using Regression Techniques

Tanveer Ahmad Wani and Mohd Shiraz

Abstract Accurate demand forecasting is very important for electric utilities in a competitive environment created by the electric industry deregulation. By using regression analysis, we have analyzed the electricity demand forecast of all-India demand data. Forecast is compared with partial end-use technique. Multiple regression method has been used for forecasting electricity demand by selecting various combinations of independent variables such as Net State Domestic Product (NSDP), Sector-wise Domestic Savings Household sector, Consumers, Connected Load, etc. It was found that sector-wise Net Domestic Savings Household sector was very effective for ascertaining the future electricity demand in the domestic sector in the country.

Keywords Forecasting · Load · Electricity

1 Introduction

Electricity is a vital component for well-being of any society, and the electricity demand from an ever-expanding set of diverse needs is growing at an increasing rate. Forecasting of electricity demand has become an essential element of the planning exercise in the power sector. The precise projection of electricity demand has also become crucial for power planning of the country to cope-up with the energy crisis [1].

As per section 3(4) of the Electricity Act 2003, CEA has prepared a National Electricity Plan (NEP) in accordance with the National Electricity Policy, which serves as a road map toward optimum growth of the sector for 11th Five-Year Plan

T. A. Wani (✉)
Department of Physics, Noida International University,
Greater Noida, Uttar Pradesh, India
e-mail: tanveer.ahmad@niu.edu.in

M. Shiraz
Department of Mechanical Engineering, Noida International University,
Greater Noida, Uttar Pradesh, India

G. Zhang et al. (eds.), *Advances in Energy and Built Environment*, Lecture Notes in Civil Engineering 36, https://doi.org/10.1007/978-981-13-7557-6_9

(FYP: 2007–12) and includes a perspective plan for 12th Five-Year Plan (FYP: 2012–17). The Five-Year Plan is proposed by CEA using sophisticated software models which considers the optimal location of plants and the transportation of fuel to generation site or transmission of power at load center. The basic input is the load forecast to the National Electricity Plan, against which the infrastructure planning for capacity addition of a power plant is decided. Therefore, it is of great importance that the load forecasting is done judiciously. If the load forecast is erroneous for both infrastructure and finance, then it becomes imbalanced which could affect the economy of a country.

A variety of methods are existing for demand forecasting. An appropriate method is to be chosen on the basis of availability of the data like frequency, cross section, time series, panel data, and the desired nature of the forecasts [2–5]. Earlier linear extrapolations were commonly used for electrical demand forecasting but with development of new method/techniques, the forecasting become more accurate and precise [6–8]. Accurate system for electric energy demand forecasting is used by various electric utilities. The electric energy demand-forecasting period is based on the type of demand forecasting, i.e., long, medium, or short. However, this type of forecast does not consider segregation of electric loads on the technical/commercial grounds. Therefore, a methodology has to be evolved which can take care of following points.

The forecasting of electricity demand should be made in terms of peak electric load and electrical energy as well, so as to carry out realistic integrated planning exercises for addition of new electricity generation capacity, transmission and distribution systems, and fuel requirements [9–11].

Electricity consumers should be divided into various categories on technical/commercial basis giving due consideration to tariffs' structure prevailing in various states/union territories to assess the electricity demand using electrical energy consumption as base.

The methodology must be made sensitive to changes in electric power sector policies, technological improvements, compensation toward restrictions on electric power supply, and voltage and frequency corrections for abnormal conditions.

2 Case Study (All-India Demand Forecast Using Trend Method)

The historical year-wise data of all-India electricity demand for the period from 1970–71 to 2004–05 was taken (all-India electricity statistic-General review 2010 (annual publication of CEA) containing data from the years 1970–1971 to 2005–2006 published yearly in the month of June by Central Electricity Authority) and plotted in Fig. 1. The computation of demand has been done by considering two different sets of historical data.

$N = 35$ (number of observations)

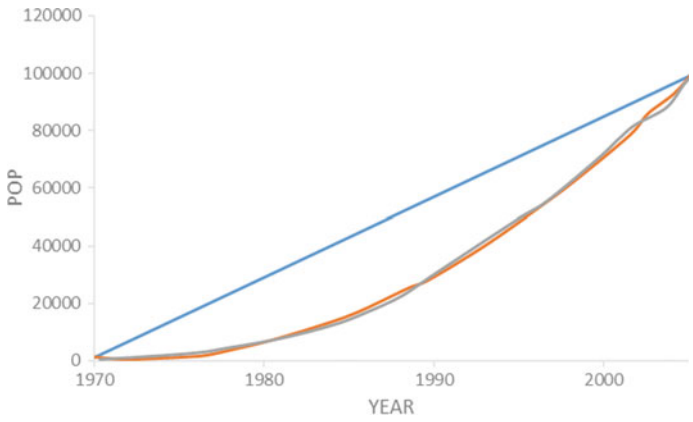

Fig. 1 Linear/parabolic fitting

$$(X \times Y) = 9{,}592{,}036$$

where Y represents the value of demand or energy, and X its index value.

$$X^2 \times Y = 145{,}443{,}386.5$$

The constants of the function c, a, and b are calculated as:
Calculation of parameter 'c':

$$c = \left(N \times \sum X^2 \times Y - \sum X^2 \times \sum Y\right)/N \times \sum X^4 - \left(\sum (X^2)^2\right) = 94.628$$

where

$$(N \times \sum X^2 \times Y = 5{,}090{,}518{,}528$$
$$\sum X^2 \times \sum Y) = 4{,}128{,}059{,}651$$
$$N \times \sum X^4 = 22{,}915{,}830$$
$$\left(\sum (X^2)^2\right) = 12{,}744{,}900$$

Calculation of parameter 'a':

$$a = \left(\sum Y - c \times \sum X^2\right)/N = 23{,}385.60$$

where

$$\sum Y = 156{,}319.23$$
$$c \times \sum X^2 = 337{,}823.404$$
$$N = 35$$

Calculation of parameter 'b':

$$b = \sum X \times Y / \sum X^2 = 2686.84$$

where

$$\sum X \times Y = 9{,}592{,}036$$
$$\sum X^2 = 3570$$

Therefore, the equation is given by

$$Yc = a + b \times X + c \times X^2$$

A. **Variables Used in Regression**

Sector-wise Domestic Savings Household sector would be used as an independent variable in the regression equation.

Sector-wise Domestic Savings Household sector = Financial savings + physical savings of assets

Apart from household savings, other savings like corporate savings in private and public sectors have been excluded from the independent variable as they do not account for energy consumption in household domestic sector. This is under the head of final private consumption expenditure which covers expenditures of households and non-profit institutions serving households under the domestic capital formation. The number of consumers in the domestic sector could be used as second independent variable. The third independent variable is the connected load in MW. The regression was done using EXCEL add-on tool "Data Analysis" under the subhead "Regression." Multiple regression was conducted on three independent variables for data from 1970–71 to 2004–05. The variables are:

(i) Net domestic saving in Rs. crore
(ii) Number of consumers in domestic category
(iii) Connected domestic load (MW)

Table 1 Results of regression with three independent variables

Regression statistics	
Multiple R	0.997697
R^2	0.9954
Adjusted R^2	0.99494
Standard error	2054.297
Observations	34

R^2 tends to unity indicating excellent corelation between variables

Table 2 Analysis of variance (ANOVA) with three independent variables

	df	SS	MS	F	Significance F
Regression	3	27,395,376,270	9,131,792,090	2163.862	3.90576E−35
Residual	30	126,604,091.4	4,220,136.379		
Total	33	27,521,980,361			

df degree of freedom, *SS* sum of squares, *MS* residue of sum of square

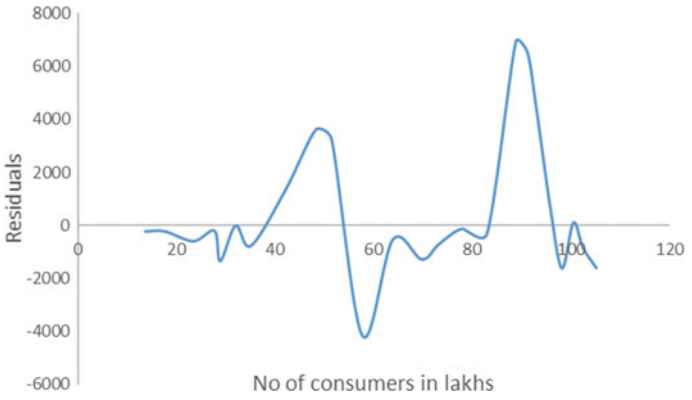

Fig. 2 No. of consumers' residual plot

The forecast was made up to 2020–21, but comparison with 17th EPS was made up to 2011–12 as the end use of EPS for domestic sector is available up to 2011–12 only (Table 1).

Colinearity with high R^2 has been studied separately, and its accountability is not significant (Table 2; Figs. 2, 3, 4, 5, 6 and 7).

The analysis of variance (ANOVA) table splits the sum of squares into its components.

$$\text{Total sum of squares} = \text{Residual (or error) sum of squares} + \text{Regression (or explained sum of squares)}$$

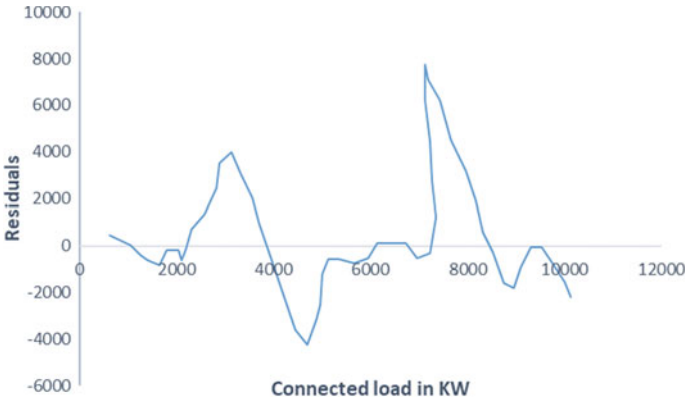

Fig. 3 No. of connected load residual plot

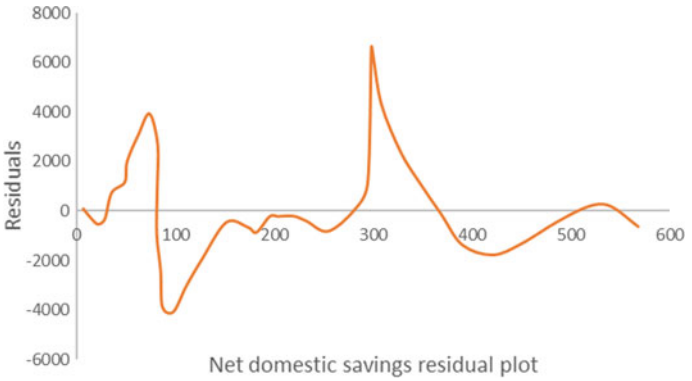

Fig. 4 Net domestic savings residual plot

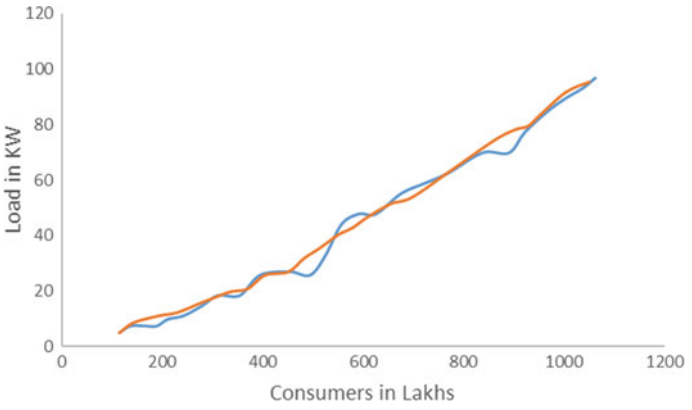

Fig. 5 No. of consumers' line fit plot

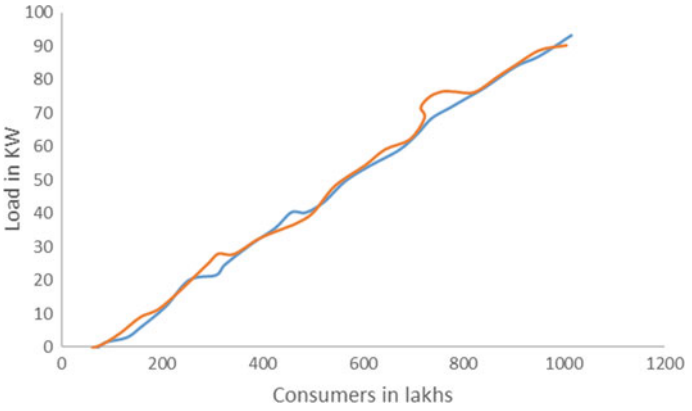

Fig. 6 Connected load line fit plot

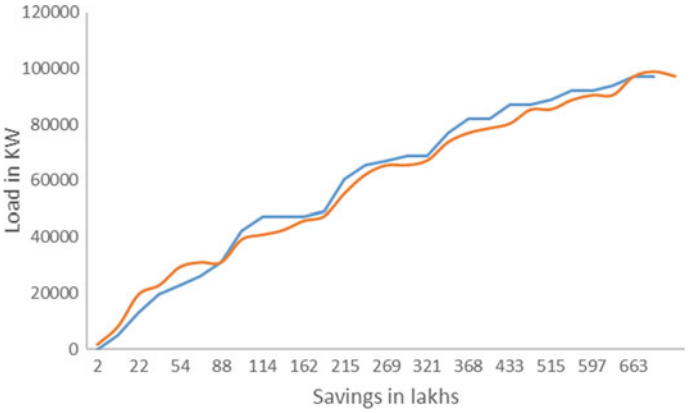

Fig. 7 Net domestic savings line fit plot

Table 3 Coefficients for forecast

	Coefficients
Intercept (a)	−6102.63914
No. of consumers (b)	0.000424144
Connected load (KW) (c)	0.000480563
Net domestic saving (d)	0.016833687

The column labeled F gives the overall F-test. The column labeled significance F has the associated p-value. Here F is significant as 2164 > 2.0 as per the tables (Tables 3 and 4).

All the three independent variables are significant as t-statistics >2.0 (Table 5).

Table 4 Significance of independent variables

	t-statistics
Intercept	−7.207848973
No. of consumers	4.496106778
Connected load (KW)	3.853348177
Net domestic saving	2.259378501

Table 5 Detailed parameters of regression

	Coefficients	Standard error	*t*-statistics	*P*-value	Lower 95%	Upper 95%
Coefficient of regression	−6102.64	846.6657887	−7.207848973	5.06E−08	−7831.761349	−4373.52
No. of consumers	0.000424	9.43358E−05	4.496106778	9.62E−05	0.000231484	0.000617
Connected load (KW)	0.000481	0.000124713	3.853348177	0.00057	0.000225865	0.000735
Net domestic saving	0.016834	0.007450583	2.259378501	0.031284	0.001617567	0.03205

t-statistics = coefficient of regression/std. error, *t*-statistics >2–2.5
Upper and lower bands are indicated as the deviations from mean

B. **Regression Equation**

$$\text{Energy Consumption } (E) = a + bx + cy + dz$$

x= Projection of Consumers @ 5.5%
y= Projection of Connected Load @ 7.0%
z= Projection of net domestic saving @ 16%
ED= Energy consumption in domestic sector
x, y, and z are projected using the above equation

1. Normal

$$\text{ED} = -6102.6 + 0.00042x + 0.0048y + 0.016z$$

2. 95% lower

$$\text{ED} = -7831.76 + 0.000231x + 0.000226y + 0.001618z$$

3. 95% Upper

Table 6 Contributing index of independent variables

	t-statistics at intercept =0
No. of consumers	−0.46467
Connected load (KW)	5.584729
Net domestic saving	1.013451

Table 7 Forecast details for domestic sector

Year	No. of consumers	Connected load (KW)	Net domestic saving	Consumption (GWh) ($\times 10^9$ Wh)
2004–05 (A)	106,228,737	102,293,088	687,079	100,090
Forecast	5.5%	7%	16%	
2005–06	112071318	109,453,604	797,012	107,448
2006–07	118,235,240	117,115,356	924,534	115,891
2007–08	124,738,178	125,313,431	1,072,459	125,079
2008–09	131,598,778	134,085,372	1,244,052	135,093
2009–10	138,836,711	143,471,348	1,443,101	146,024
2010–11	146,472,730	153,514,342	1,673,997	157,976
2011–12	154,528,730	164,260,346	1,941,836	171,066
2012–13	163,027,810	175,758,570	2,252,530	185,426
2013–14	171,994,340	188,061,670	2,612,935	201,209
2014–15	181,454,028	201,225,987	3,031,004	218,585
2015–16	191,434,000	215,311,806	3,515,965	237,751
2016–17	201,962,870	230,383,632	4,078,520	258,929
2017–18	213,070,828	246,510,487	4,731,083	282,375
2018–19	224,789,723	263,766,221	5,488,056	308,381
2021–22	263,957,394	323,124,962	8,566,284	405,337

$$\mathrm{ED} = -4373.52 + 0.000617x + 0.000735y + 0.03295z$$

The most important contribution is through the independent variable connected load (Tables 6, 7, 8; Fig. 8).

Table 8 Comparison of actual data with forecast of 17th EPS and normal regression

Year	Actual energy consumption	Consumption (GWH) as per normal regression	Consumption forecast as per 17th EPS (GWH)	% difference regression and 17th EPS
2005–06	100,093	107,448	106,659	+0.73
2006–07	111,002	115,891	119,688	−3.17
2007–08	120,918	125,079	134,962	−7.32
2008–09	130,056	135,093	152,653	−11.52
2009–10	141,845	146,024	172,443	−15.32
2010–11	153,193	157,976	194,937	−18.90
2011–12	163,341	171,066	220,372	−28.80

Source All-India electricity statistic-General review 2010 (annual publication of CEA) containing data from the years 2005 to 2010 published in June 2010 by Central Electricity Authority

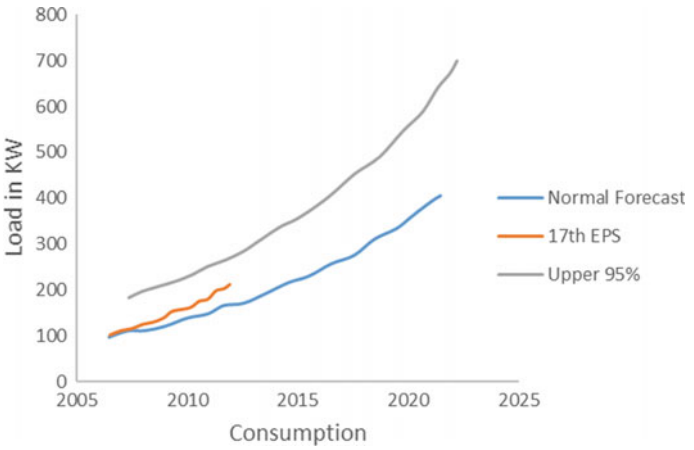

Fig. 8 Comparison of forecast

3 Conclusions

By using regression analysis, we have analyzed electricity demand forecast of all-India demand data. Forecast is compared with partial end-use technique. Multiple regression method has been used for forecasting electricity demand by selecting various combinations of independent variables such as Net State Domestic Product (NSDP), Sector-wise Domestic Savings Household sector, Consumers, Connected Load, etc.

The domestic sector accounts for 25% energy in overall composition of energy requirement. Therefore, it can be assumed that the forecast of domestic sector plays a predominant role in the overall forecast of energy.

Therefore, the analysis and forecast of domestic sector was studied using multiple regression technique taking household saving in private sector, domestic connected load and domestic number of consumers as independent variables. The energy consumption in domestic sector has been used as dependent variable. The forecast is made up to the year 2011–12 and compared with 17th Electric Power Survey (EPS).

References

1. Bowerman L, O'Connell RT, Koehler AB (2005) Forecasting, time series, and regression: an applied approach, vol 4, 4th edn. Thomson Brooks/Cole, Pacific Grove, CA, pp 391–392
2. Hyde O, Hodnett PF (1997) An adaptable automated procedure for short-term electricity load forecasting. IEEE Trans Power Syst 12:84–93
3. Haida T, Muto S (1994) Regression based peak load forecasting using a transformation technique. IEEE Trans Power Syst 9:1788–1794
4. Janacek G, Swift L (1993) Time series: forecasting, simulation, applications. Ellis Horwood Limited, West Sussex, p 331
5. Rahman S, Hazim O (1993) A generalized knowledge-based short-term load forecasting technique. IEEE Trans Power Syst 8:509–514
6. Gellings CW (1996) Demand forecasting for electric utilities. The Fairmont Press, Lilburn, GA, pp 490–539
7. Suganthi L, Samuel AA (2012) Energy models for demand forecasting—A review. Renew Sustain Energy Rev 16(2):1223–1240 (Elsevier)
8. Bianco V, Manca O, Nardini S (2009) Electricity consumption forecasting in Italy using linear regression models. Energy 34:1413–1421
9. Zadeh LA (1973) Outline of a new approach to the analysis of complex systems and decision processes. IEEE Trans Syst Man Cybern 3:28–44
10. Zadeh LA (1975) The concept of a linguistic variable and its application to approximate reasoning. Inform Sci 8:199–249
11. Engle RF, Mustafa C, Rice J (1992) Modeling peak electricity demand. J Forecast 11:241–251

Improvement of Energy Efficiency of Isolated Wind Power System Based on Voltage Indices Using ANFIS Tuned STATCOM

A. Gandhar, S. Gupta and S. Gandhar

Abstract Among renewable sources of energy, wind energy sources (WES) are the most demanded globally. Wind energy systems are usually facilitated with fixed velocity type induction machines that provide comparable lesser costly options for power generation. Although these asynchronous generators are used to consume reactive power, having numerous advantages over synchronous machines make them so popular. The shunt capacitors can be used to generate this consumable reactive power, but usually, these circuitries do not yield desired results during the contingencies or turbulent behavior of the system. Therefore, effective and continuous solutions such as flexible alternating current transmission systems (FACTS) are compulsory in such cases. In the presented paper, the stabilization of the voltage stability indices of energy system during the turbulent behavior of the integrated WES-based energy systems using the static compensator (STATCOM) is investigated. Furthermore, the proportional–integral controller of the control system is tuned by an adaptive technique, i.e., adaptive neuro-fuzzy inference system (ANFIS). The considered WES generators are the squirrel cage induction generators (SCIG). Simulation studies are performed on the IEEE-9 bus test system. Obtained results prove that the SCIG with ANFIS tuned STATCOM improves the performance of the designed power network during the turbulence.

Keywords Distributed generation · FACTS · STATCOM · ANFIS · MATLAB/Simulink

A. Gandhar (✉) · S. Gandhar
Department of Electrical and Electronics Engineering, Bharati Vidyapeeth College of Engineering, New Delhi, India
e-mail: abhishek.gandhar@gmail.com

S. Gupta
Department of Electrical and Electronics Engineering, Maharaja Surajmal Institute of Technology, New Delhi, India

G. Zhang et al. (eds.), *Advances in Energy and Built Environment*, Lecture Notes in Civil Engineering 36, https://doi.org/10.1007/978-981-13-7557-6_10

1 Introduction

The distributed generation is gaining very rapid popularity throughout the globe. The Government of India is also focusing these clean sources of energy sources for power generation. Wind energy is one of the best cost-effective renewable energy sources, gaining significant popularity throughout the globe. There have been currently millions of wind turbines in operation worldwide. More than 54 GW of clean renewable wind energy sources have been installed across the world energy market in 2016 which includes more than 90 countries altogether with some of the countries having more than 10,000 MW installed and many of them have crossed the barrier of 1000 MW installation. The annual growth rate is increasing by 12.6% to target a total of approx. 500 GW [1, 2]. There are numerous advantages of using asynchronous generators for a generation in renewable energy-based power systems. But these generators require reactive power for their normal operations. The shunt condensers can compensate for the requirement of reactive power in smooth operations but show very poor performance during the transient contingencies [3, 4]. Therefore, in such cases of dynamic compensation requirement, only power electronics-based controllers like flexible alternating current transmission systems (FACTS) can generate reactive power particularly for under voltage contingencies. A variety of valuable facilities can be availed with these FACTS in power systems such as dynamic voltage control, control of over-voltage phenomena in long, and lightly loaded transmission lines and cable lines, also protect heavily loaded lines or faulty lines from under voltage phenomena [5]. This application of FACTS devices also helps in the

- Reduction of the requirement of commissioning of new lines by increasing the loading capability and steady-state stability limit of lines. This is, in fact, a better solution as it saves a very big amount of expenditure and also has a healthy impact on the environment.
- Integration of non-conventional energy sources also increases the energy sourcing capability of existing energy systems [6].

This paper presents a transient performance of wind energy source-based micropower system. Investigations are performed on IEEE 9-bus system for evaluating the voltage stability performance. Simulation studies are also performed to improve the transient stability performance when the ANFIS tuned STACOM has been inserted in the system. All transient behavioral results with ANFIS tuned STATCOM and without STATCOM are presented.

2 Wind Generator Model

The constant speed, squirrel cage induction generator (SCIG) is associated with the grid with the help of a transformer. During the high-velocity windy condition, the gearbox matches the generator's velocity to the frequency of the grid, and the

generator stops the effect of high velocity of winds. This method saves the system from experiencing the large mechanical power generation because of high-speed winds. Generally, capacitor banks are connected in such type of cases, where reactive power compensation is really required. These capacitor banks minimize the quantity of reactive power that the generator consumes from the grid [7] (Fig. 1).

An approximate identical circuit for the induction machine is investigated for the state space modeling of the induction generator shown in Fig. 2. It is desirable that the model must have a minimum number of variables so that it can be easily extendable to a multi-machine system. In consideration of that, the power requirement is evaluated in terms of terminal voltage and induction generators' parameters. Receiving end voltage lags the generator's equivalent impedance, i.e., E (like voltage lags the synchronous reactance if there should arise an occurrence of the alternator) as appeared in Fig. 2.

From Fig. 2, the rated current I is given by

$$I = \frac{E - V}{R_{\text{eq}} + jX_{\text{eq}}} = \frac{E}{R_p} \tag{1}$$

Calculating for E in Eq. (1)

$$E = \frac{R_P}{R_Y - jX_{\text{eq}}} V \tag{2}$$

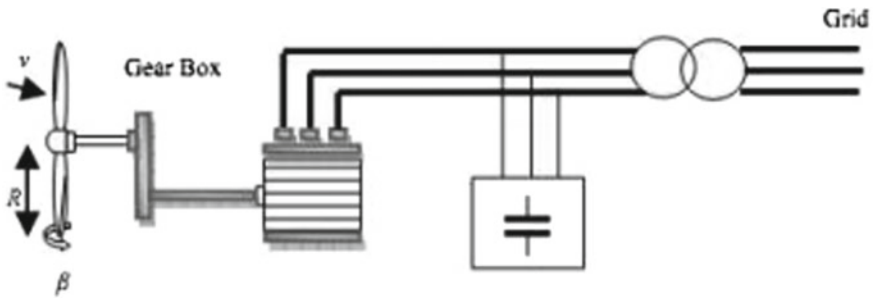

Fig. 1 Representation of the fixed speed induction generator

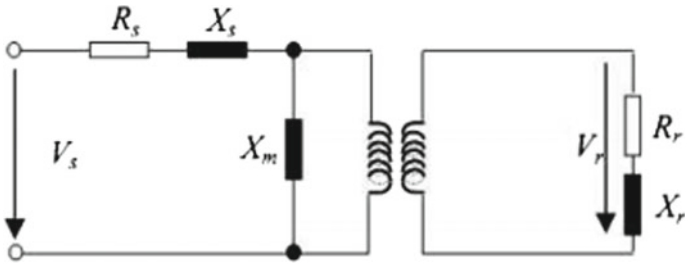

Fig. 2 An approximate equivalent circuit of the induction machine

Equation (2) can be rewritten as
where $R_Y = R_P - R_{\text{eq}}$

$$E = \left(\frac{R_P R_Y}{R_y^2 + X_{\text{eq}}^2} + j \frac{R_P X_{\text{eq}}}{R_y^2 + X_{\text{eq}}^2} \right) V \tag{3}$$

The total power provided by the induction generator is specified by

$$S_{\text{IG}} = P_{\text{IG}} + Q_{\text{IG}} = V \left(\frac{E - V}{R_{\text{eq}} + j X_{\text{eq}}} \right) - j \frac{V^2}{X_M} \tag{4}$$

Putting in the value of E from Eq. (2) in Eq. (3), the real and imaginary powers generated by the induction machine are given by

$$P_{\text{IG}} + \frac{R_Y}{R_y^2 + X_{\text{eq}}^2} V^2 \tag{5}$$

$$Q_{\text{IG}} = - \left[\frac{X_{\text{eq}}}{R_y^2 + X_{\text{eq}}^2} + \frac{1}{X_M} \right] V^2 \tag{6}$$

The −ve sign presents the lagging reactive power required by the induction machine.

3 The Static Synchronous Compensator (STATCOM)

The static compensator (STATCOM) is a shunt controller of the pedigree of flexible AC transmission systems (FACTS). These are power electronics-based circuitries which help power system to improve the transient stability and steady-state stability limit. It controls the voltage variations by injecting or captivating reactive power at its terminals. When the system voltage profile starts decreasing, the STATCOM injects reactive power like a dynamic capacitor and when the system voltage profile starts increasing, it captivates the reactive power like a dynamic inductor [8].

The modification of reactive power is attained with the help of a voltage-sourced converter (VSC). The VSC incorporated the forced-alternated power electronic devices (GTOs, IGBTs, or IGCTs) to produce a synchronous voltage V_2. The modes of operation of the STATCOM are described within Fig. 3 describing the flow of active and reactive powers between V_1 and V_2. Where V_1 shows the terminal voltage to be managed and V_2 is the voltage injected by the VSC.

$$P = (V_1 V_2) \sin \delta / X, \;\; Q = V_1 (V_1 - V_2 \cos \delta) / X \tag{7}$$

In unchanging condition, the voltage V_2 injected by the VSC is to some extent with V_1 ($\delta = 0$), so that only "Q" is transferred ($P = 0$). If V_2 is lesser than V_1, reactive power will flow from V_1 to V_2 (STATCOM is captivating). On the other

hand, if V_2 is greater than V_1, Reactive power will flow from V_2 to V_1 (STATCOM is injecting 'Q'). The total reactive power is specified by

$$Q = (V_1(V_1 - V_2))/X. \tag{8}$$

A condenser joined on the DC side of the VSC behaves as a DC voltage provider. In the turbulence-free environment, the voltage V_2 needs to be phase shifted slightly behind V_1. Therefore, to manage the losses incurred in the transformer and VSC, it also helps in the charging of condenser [9, 10] (Fig. 4).

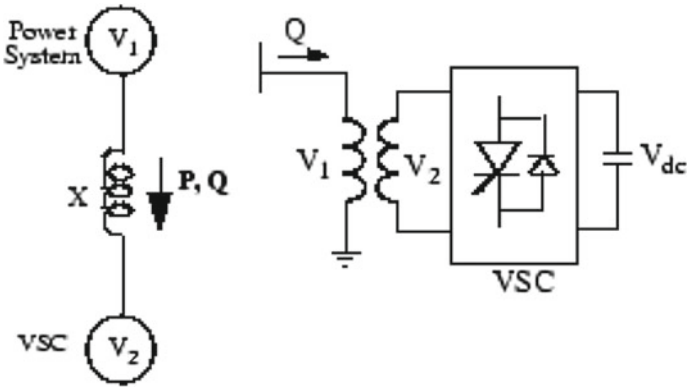

Fig. 3 Working mode of the STATCOM

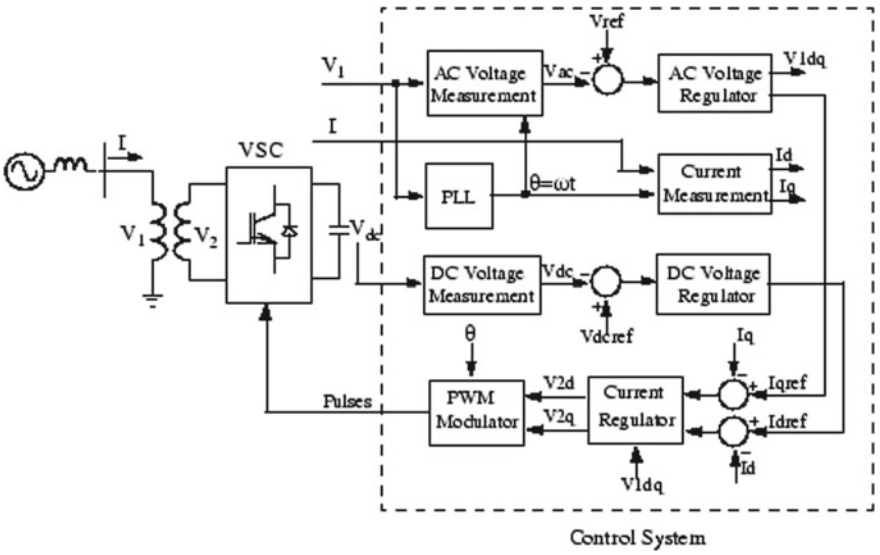

Fig. 4 Control system design of STATCOM

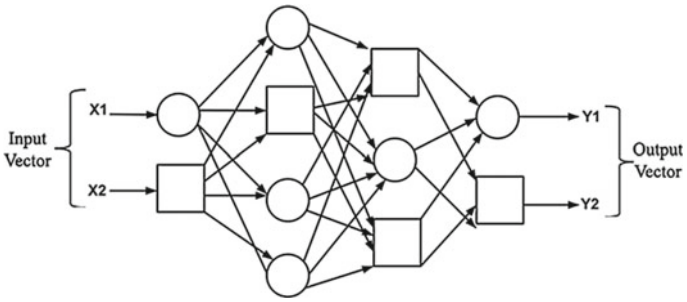

Fig. 5 Adaptive network

4 ANFIS Adaptive Network

In this section, a basic overview of ANFIS adaptive technique has been discussed. Here, Fig. 5 presented the rules for tuning of the ANFIS methodology. Additionally, online self-building neural fuzzy inference network technique is presented. An adaptive network is one of the cases of feed-forward neural system with many layers [11, 12]. In this learning procedure, these systems frequently utilize supervised learning algorithm. In addition, adaptive networks have the architecture characteristics that it comprises of various adaptive hubs interconnected straightforwardly with no weights in between them. In this system, every hub/node has different functions and task, and the output relies upon the incoming signals and parameters that are accessible in the hub. A learning rule used can influence the parameters in the hub, and it can lessen the event of errors at the output side of the adaptive network. The fundamental adaptive system utilizes gradient descent or back propagation, and therefore, the chain rule frequently such as the way over learning calculations had been proposed by Werbos in 1970.

5 Simulation Test System and Results

In this section, simulation studies are performed to demonstrate the transient effects of the power system with wind generation using the STATCOM and with ANFIS tuned STATCOM. IEEE 9-bus system is considered for test analysis, shown in Fig. 7 [11, 12]. It is connected with two wind energy systems. In this paper, the performances are analyzed on the presumption that the wind turbine is performing at a fixed velocity (9 m/s). The wind turbine generator of group 1 having rated the power of 1.5 KVA, connected at bus "1." The second generator having rated the power of 3 KVA, connected at bus "4." Different types of loads are connected with this "9" bus test system. The peak values of bus voltages are employed as indices to evaluated voltage stability and therefore the IEEE 9-bus test system shown in Fig. 6 is used

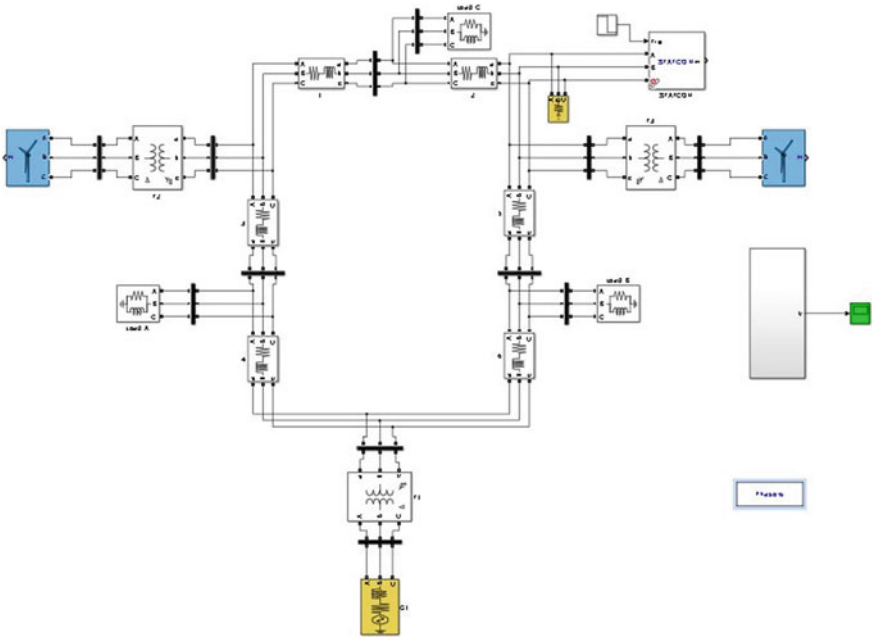

Fig. 6 Simulation test system

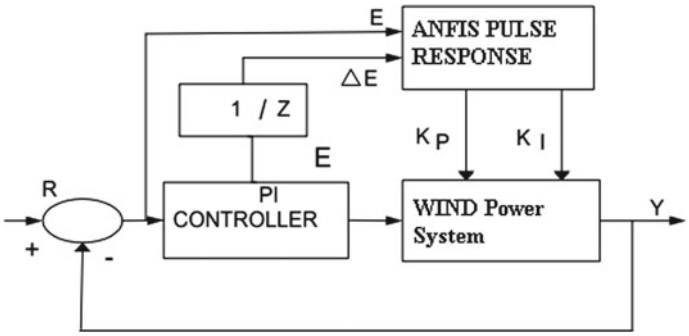

Fig. 7 ANFIS tuned PI controller block

to conduct the transient stability simulation A STATCOM is to be installed at the point of Common Coupling (PCC), wherever the wind energy facility is integrated with the utility system. Time Simulation studies are performed for 1 s on the test system. STATCOM has been inserted in these time simulations at 0.5 s and it is clearly shown in Fig. 10, it is stabilizing the turbulent energy system. The STACOM is also improving the voltage profiles of the buses in tests system presented in Fig. 9 whereas the Fig. 8 shows the transient behavior of the system without STATCOM Thus STATCOM is playing a pivotal role as a dynamic compensator of the

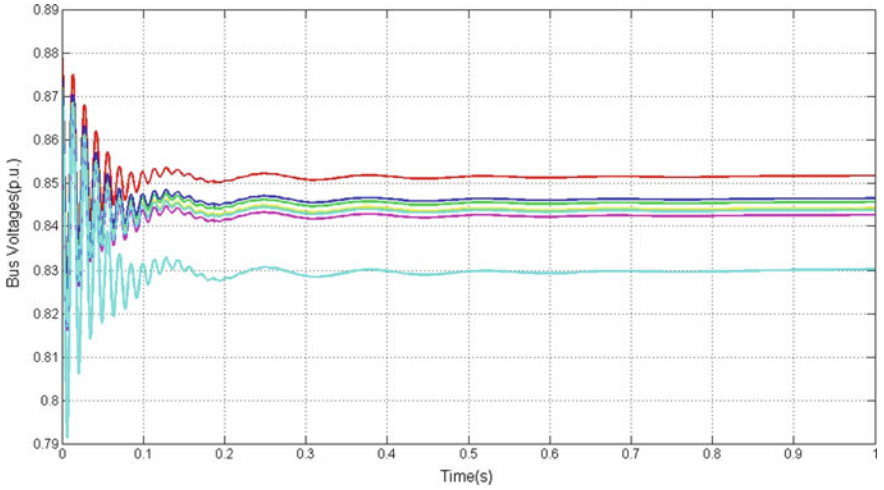

Fig. 8 Bus voltages (pu) of test design without STATCOM

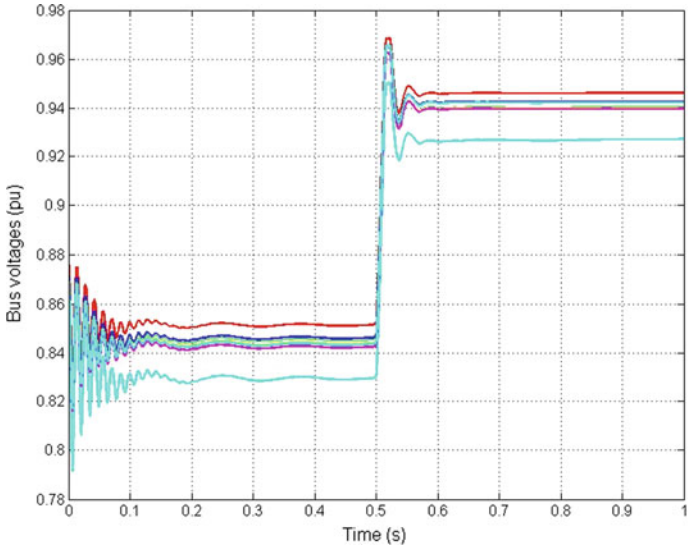

Fig. 9 Bus voltages (pu) of test design with STATCOM

test design and hence proved as important FACTS controller of the family. Whereas ANFIS tuned STATCOM is even producing better responses than the untuned STATCOM and the results shown in Fig. 10 clearly proves the fact that the system is stabilizing in a better manner with ANFIS tuned STATCOM. Table 1 has been used to compare the bus voltages responses of test system without STATCOM and with ANFIS tuned STATCOM.

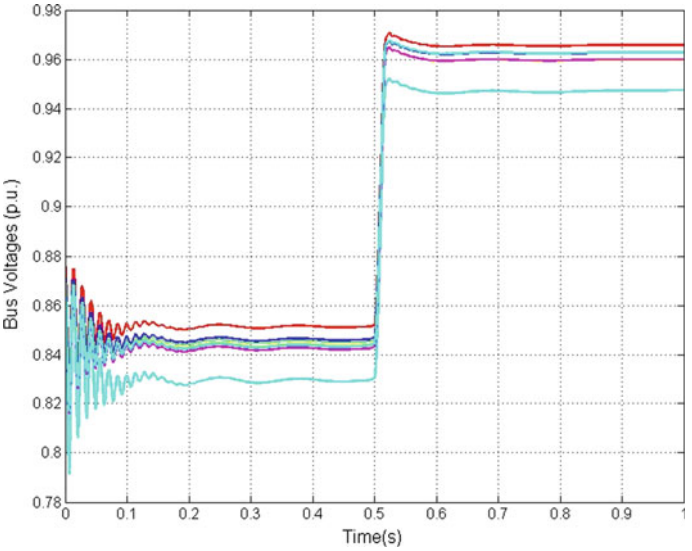

Fig. 10 Bus voltages (pu) of test design with ANFIS tuned STATCOM

Table 1 Bus voltages (pu) of test design with and without STATCOM

S. No.	Buses	Bus voltages without STATCOM (p.u.)	Bus voltages with STATCOM (p.u.)	Bus voltages with ANFIS tuned STATCOM (p.u.)
1	Bus '1'	0.8517	0.9462	0.9658
2	Bus '2'	0.8442	0.9338	0.9598
3	Bus '3'	0.8302	0.9262	0.9475
4	Bus '4'	0.8517	0.9461	0.9658
5	Bus '5'	0.8456	0.9405	0.9603
6	Bus '6'	0.8464	0.9426	0.9626
7	Bus '7'	0.8442	0.9399	0.9598
8	Bus '8'	0.8426	0.9396	0.9599
9	Bus '9'	0.8438	0.9422	0.9628

6 Conclusion

Increment in the popularity of wind generation globally needs powerful solutions for stability problems with the power system. Here, the voltage stability improvements of an existing wind energy system with the help of an ANFIS tuned STATCOM have been analyzed and presented. The wind generators considered are the induction machines with IEEE 9-bus system. A STATCOM is placed in a multi-machine power system with this test system. The results show the improvement in the voltage profiles

of buses of test power system using the ANFIS adaptive technique. The results reveal that, in such cases, deployment of the shunt capacitor banks are incapable, so adequate VAR compensation can only be obtained by the FACTS controllers like STACOM. Therefore, the need for compensating controller for the proposed wind energy sources-based power system has been discussed.

References

1. Aekcrmann T et al (2001) Distributed generation: a definition. Electr Power Syst Res 57:195–204
2. Ahilan T, Mohammed KP, Arumugham S (2009) A critical review of global wind power generation. Am J Appl Sci 6:204–213
3. Chaurasia GS, Singh AK, Agrawal S, Sharma NK (2017) A meta-heuristic firefly algorithm based smart control strategy and analysis of a grid connected hybrid photovoltaic/wind distributed generation system. Sol Energy 150:265–274
4. Chaurasia GS, Agrawal S, Sharma NK (2017) Comparative analysis of various MPPT-techniques for optimization of solar-PVEC system. Global J Enterprise Inf Syst 9(3):94–101
5. Al-Majed SI, Fujigaki T (2010) Wind power generation: an overview. In: Proceedings of the international symposium modern electric power systems (MEPS). IEEE Xplore Press, Wroclaw, Poland, 20–22 Sept 2010, pp 1–6
6. Kundur P (1994) Power system stability and control. McGraw-Hill, New York
7. Bansal RC, Bhatti TS, Kothari DP (2003) Automatic reactive power control of wind-diesel-micro hydro autonomous hybrid power systems using ANN tuned static VAR compensator. In: Proceedings of international conference on large engineering system conference on power engineering (LESCOPE), Montreal, Canada, 7–9 May 2003, pp 182–188
8. Gandhar S, Ohri J, Singh M (2014) Application of SSSC for compensation assessment of interconnected power system. In: 6th IEEE International conference on power electronics, NIT Kurukshetra, India, 8–10 Dec 2014
9. Grünbaum R (2010) FACTS for grid integration of wind power. In: Innovative smart grid technologies conference Europe), IEEEPES, 11–13 Oct 2010, pp 1–8
10. Madhavi Latha G, Kiranmayi R (2016) Transient stability improvement of hybrid power system by VR-FCL using PSO. Int J Sci Eng Technol Res (IJSETR) 5(11). ISSN: 2278–7798 (November)
11. Jang JSR (1993) ANFIS: adaptive-network-based fuzzy inference systems. IEEE Trans Power Syst 23(3):665–684
12. Ishibuchi H, Fujioka R, Tanaka H (1993) Neural networks that learn from fuzzy if-then rules. IEEE Trans Fuzzy Syst 1(2):85–97

Improvement of Voltage Stability of Renewable Energy Sources-Based Microgrid Using ANFIS-Tuned UPFC

S. Gandhar, Jyoti Ohri and Mukhtiar Singh

Abstract The paper proposed an impact strategy to stabilize the reactive power variations in islanded microgrid, which results in the control over voltage instability. The required voltage compensation is achieved by injection of an accurate synchronous voltage supply into the microgrid through the power electronics-based converters. This work is accomplished by using advanced flexible AC transmission (FACTS) device and unified power flow controller (UPFC) connected to the microgrid. This compensation reference is obtained through a synchronous voltage management, avoiding the load frequency control loop. In this paper, the improvement in the voltage stability of power system during the transient period in the integrated renewable energy sources (RES)-based microgrid using the unified power flow controller (UPFC) is investigated. Furthermore, the proportional–integral controller of the control system is tuned by adaptive neuro-fuzzy inference system (ANFIS) technique. The ANFIS-tuned UPFC yields the better control on the bus voltages of the test system. This strategy does not require any hardware modification. This strategy is simulated in MATLAB/Simulink to prove its effectiveness.

Keywords Microgrid · RES · FACTS · UPFC

1 Introduction

In India, the renewable energy sources-based industries are growing exponentially. In the coming years, there will be very significant growth in RES-based power systems. There are many locations in the world which are still deprived of electrical

S. Gandhar (✉)
Department of Electrical and Electronics Engineering, Bharati Vidyapeeth College of Engineering, New Delhi, India
e-mail: shashi.abhi@gmail.com

J. Ohri
Department of Electrical Engineering, National Institute of Technology, Kurukshetra, India

M. Singh
Department of Electrical Engineering, Delhi Technical University, New Delhi, India

G. Zhang et al. (eds.), *Advances in Energy and Built Environment*, Lecture Notes in Civil Engineering 36, https://doi.org/10.1007/978-981-13-7557-6_11

energy. The grid connection to those areas is not viable solution as it requires a hefty investment. So, the best solutions are isolated microgrids. This solution also becomes better when it is driven by renewable energy sources' microgrids that can provide continuous and cost-effective electric power to such areas. For such microgrids, the hybrid combination of nonconventional and conventional energy sources is advisable solution because it produces cost-effective and pollution reducing power. But power quality is the decisive concern in such types of microgrids, and a typical disadvantage is the voltage imbalance. Lots of analysis and research work have been done on this subject. Such microgrids feed a variety of constant loads, dynamic loads, and randomly variable loads. Thus, the currents transported by the dispersed generations are generally not balanced [1, 2]. Therefore, the voltages beyond the load impedances and thereupon different load voltages convert to unbalanced. Unbalanced voltages resulted in maloperation, especially for dynamic loads, and increase losses in connecting machines. Although every distributed generation (DG) unit among the microgrid is trying to enforce balanced voltages in the system, the presence of nonconventional energy sources brings a lot of voltage variations in the system. Therefore, power electronics-based converter management strategies are implemented in the power system to maintain the output voltage balance. The inverters equipped with high-rating thyristors will do balanced voltages; as a result, this plan of action controls the converter output voltage and frequency [3]. However, few unsteady and fluctuating sources such as random electrical contingencies can require rigorous power electronic converters' arrangement to deliver the required power. This paper proposes a technique to compensate reactive power to maintain the voltage variations within the system. Consequently, it enhances the power system quality despite connecting dynamic loads. The compensation is usually achieved for hybrid power system because the voltage imbalance is quite evitable in the islanding mode of microgrid caused by the increment in unbalanced load currents [4]. The compensation is required in islanding mode of microgrid, but this strategy also depends on the injection of synchronous voltage provide to supply locally, it requires the reactive power for maintaining the voltage imbalance [5]. In this paper a simulation model of the microgrid in islanded mode is presented to characterize the reactive power balance analysis to maintain the voltage stability of the system.

2 Unified Power Flow Controller

FACTS controller is a family of power electronics based on different devices. Among the group of these controllers, unified power flow controller (UPFC) is termed as the best FACTS controller. It acts like a multitasking controller, which can perform several functions at any instant, such as controlling the transmission voltage, impedance, and active and reactive power [6], providing benefit to the power system. It is an advanced power electronic device, which has two converters: One is connected in shunt, and other is connected with the transmission line. It is a combination of a static compensator (STATCOM) and static series synchronous compensator (SSSC). It can

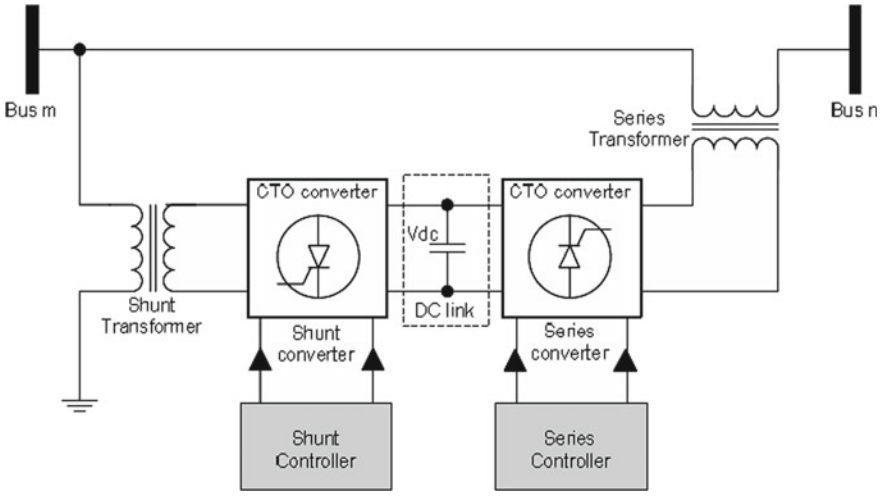

Fig. 1 Schematic diagram of the UPFC

be used for controlling many problems of the power system like managing power flow by enhancing transient stability and voltage (reactive power) control [7, 8]. The UPFC comprises of two voltage-source converters (VSCs), connected antiparallel and a DC electrical condenser is placed between those VSCs (Fig. 1). It feeds contemporary voltage supply of the needed amplitude into the system. The objective of series converter is to feed synchronous voltages, V series with the line, which leads to the flow of active power and the creation of the required reactive power into the system. The reactive power is created by the series converter, while the active power is carried to or from the line over the DC electrical condenser. Meanwhile, the shunt converter creates the need of this DC terminal power to or from the line, thereby maintaining the flow of active power of system. The total real power consumed by UPFC is account of losses of the converters and the coupling transformers. The creation of reactive power is directly done by series and shunt converters like a STATCOM. Therefore, reactive power compensation methodology of the shunt converter is similar to standard STATCOM.

An approximate identical circuit of the induction machine is examined for the state-space modeling of the induction generator as shown in Fig. 2. It is desirable that the model must have the least number of factors, and furthermore, it can be easily remodeled into multi-machine control framework. In perspective of this, the power conditions are expressed in terms of bus voltage and induction machine parameters, steady voltage lagging the equivalent impedance is E (like voltage behind the synchronous reactance if there should arise an occurrence of alternator) as shown in Fig. 2.

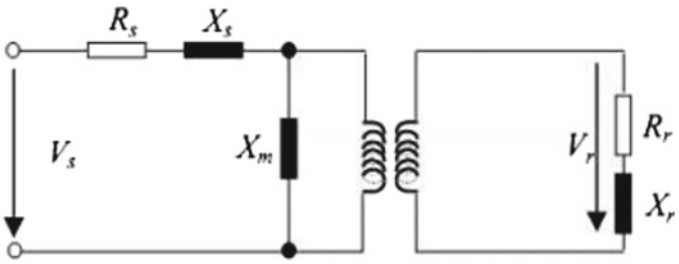

Fig. 2 An approximate equivalent circuit of the induction machine

3 Modeling of the Test System

The proposed test system shown in Fig. 3 comprises of 14 buses (six 22 kV buses, six 230 kV buses, and two 345 kV buses). The designed system is divided into three specific regions. Area 1 is termed as generation area, which is modeled by a three-phase generating source and a doubly-fed induction generator (DFIG) representing the renewable energy source in the system. Area 2 is placed between generation area (Area 1) and load center area (Area 3). It has the most advanced FACTS controller, i.e., UPFC. Area 3 consists of different types of loads, which are connected to different bus locations in the circuit as shown in Fig. 3, i.e., resistive–inductive, resistive–capacitive, purely capacitive loads, and a combination of both inductive and capacitive loads [9]. Power balance equations are considered for the simulation studies. Because of the presence of many inductive loads and the reactive power demand of DFIG, it is highly desirable to connect the condensers in the system. But after observing the transient responses of the system, it is really impossible to balance the reactive powers of the system with these fixed capacitors, and this results in the drop in bus voltages' profiles. Therefore, a very powerful FACTS controller is connected in between the Bus-7 and Bus-8 and responses are collected and presented in the next section.

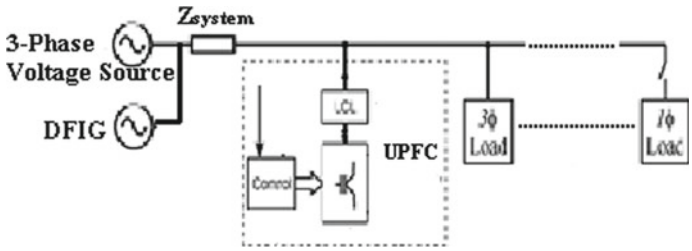

Fig. 3 Simulation set up

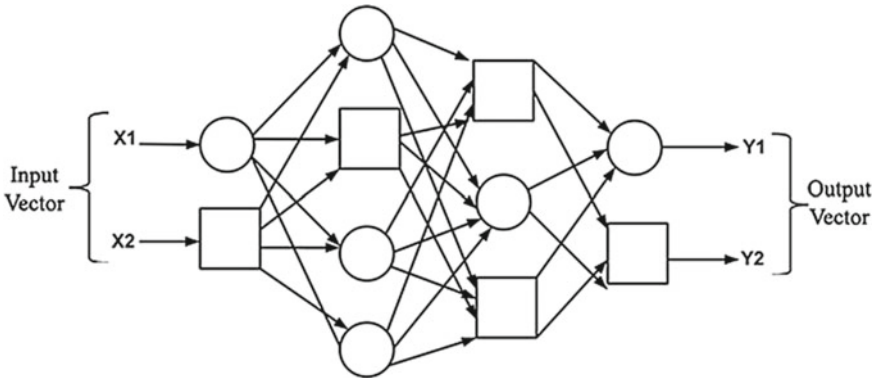

Fig. 4 Adaptive network

4 ANFIS Adaptive Network

In this section, a basic overview of ANFIS adaptive technique has been discussed. Here, Fig. 4 shows the rules for tuning of the ANFIS methodology additionally, which presented the online self-building neural fuzzy inference network technique. Adaptive network is one of the cases of feed-forward neural system with many layers [10, 11]. In this learning procedure, these systems frequently utilize supervised learning algorithm. In addition, adaptive networks have the architecture characteristics that it comprises of various adaptive hubs interconnected straightforwardly with no weights in between them. This system describes that every hub/node has different functions and tasks, and the output relies upon the incoming signals and parameters that are accessible in the hub. A learning rule that was used can influence the parameters in the hub, and it can lessen the event of errors at the output side of the adaptive network. The fundamental adaptive system utilizes gradient descent or backpropagation, and therefore, the chain rule frequently such as the way over learning calculations had been proposed by Werbos in 1970.

5 Simulation Test System and Results

Simulation studies are carried out in this section to demonstrate the transient performance of the test system with renewable energy sources using the UPFC and with ANFIS-tuned UPFC. IEEE 14-bus system is examined for the test analysis. It is attached with two generating systems as shown in Fig. 5. In this paper, the examination is studied on the supposition that renewable energy sources are controlling at a constant speed. The DFIG of Area 1 is of rating 1.5 KVA nominal power and jointed at bus ‘1’. The second source is having nominal power of 3 KVA and connected at bus ‘4’. Different types of loads are connected with this 14-bus test system. The

crest values of bus voltages are reviewed as indices to evaluated to assessed voltage stability and therefore the IEEE 14-bus test system shown in Fig. 5 is used to conduct the transient stability simulation. A UPFC is to be installed at the point of common coupling (PCC), wherever the wind energy facility is integrated with the utility system. Time simulation studies are carried out for 10 s on the test system. The UPFC has been inserted in these time simulations at 05 s. The voltage profiles of the most affected buses are presented in Figs. 7, 8, 9, 10, and 11. It is clearly presented that the UPFC is helping the turbulent energy system for the stabilization. The UPFC is also improving the voltage profiles of the buses in test system as presented in Figs. 7, 8, 9, 10, and 11, whereas the time simulation before 5 s shows the transient behavior of the system without the UPFC. Thus, the UPFC is playing a pivotal role of a dynamic compensator of the given test system and to be proved as an important FACTS controller of the family. The ANFIS-tuned UPFC is even producing better responses than the untuned UPFC, and the results shown in Figs. 7, 8, 9, 10, and 11 clearly prove the fact that the system is stabilizing in better manner with ANFIS-tuned UPFC (Fig. 6). Table 1 has been used to compare the bus voltages responses of test system without the UPFC and with the ANFIS-tuned UPFC.

Table 1 Bus voltages (pu) of IEEE 14-bus test system

S. No.	Buses	Bus voltages without UPFC (p.u.)	Bus voltages with UPFC (p.u.)	Bus voltages with ANFIS-tuned UPFC (p.u.)
1	Bus '1'	0.9217	0.9462	0.9658
2	Bus '2'	0.9042	0.9338	0.9598
3	Bus '3'	0.9102	0.9262	0.9475
4	Bus '4'	0.8517	0.9461	0.9658
5	Bus '5'	0.8456	0.9405	0.9603
6	Bus '6'	0.8464	0.9426	0.9626
7	Bus '7'	0.9042	0.9399	0.9598
8	Bus '8'	0.8426	0.9396	0.9599
9	Bus '9'	0.8438	0.9422	0.9628
10	Bus '10'	0.9137	0.9261	0.9247
11	Bus '11'	0.9134	0.9338	0.9438
12	Bus '12'	0.9011	0.9039	0.9339
13	Bus '13'	0.9197	0.9309	0.9397
14	Bus '14'	0.9093	0.9150	0.9153

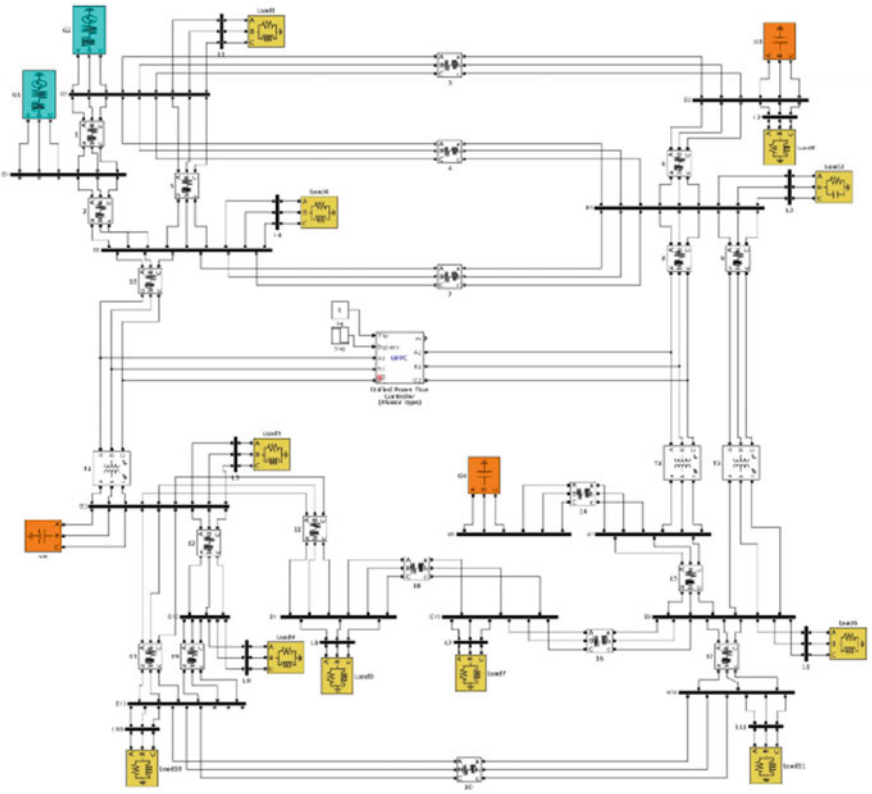

Fig. 5 Simulation test system

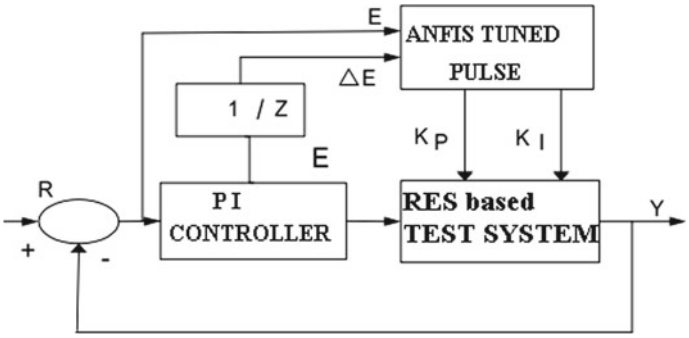

Fig. 6 ANFIS-tuned PI controller of the UPFC

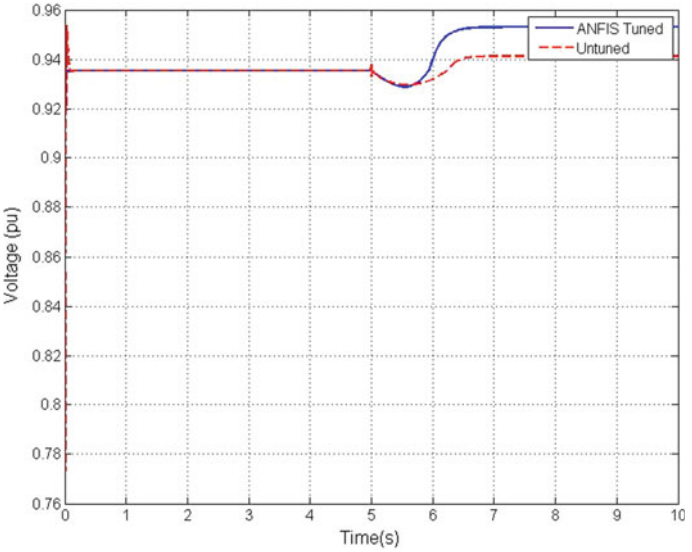

Fig. 7 Bus-5 voltage (pu) of test system with ANFIS-tuned UPFC

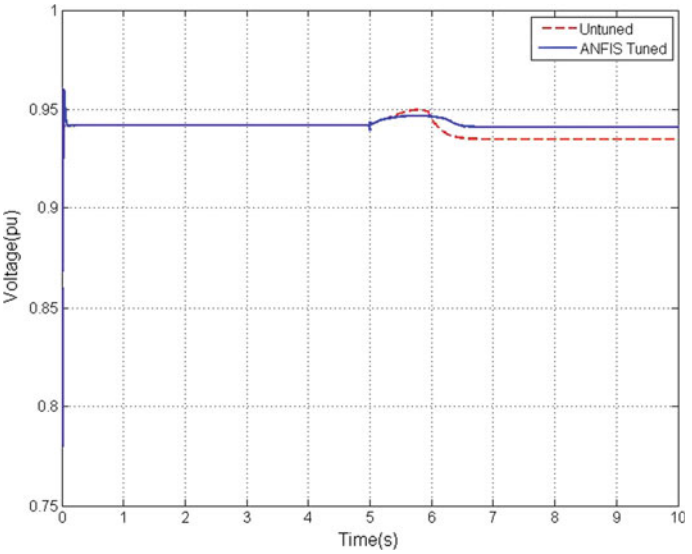

Fig. 8 Bus-8 voltage (pu) of test system with ANFIS-tuned UPFC

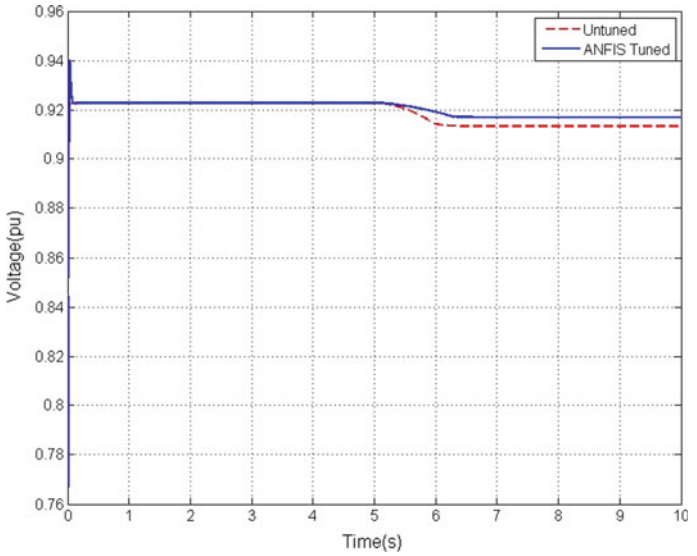

Fig. 9 Bus-10 voltage (pu) of test system with ANFIS-tuned UPFC

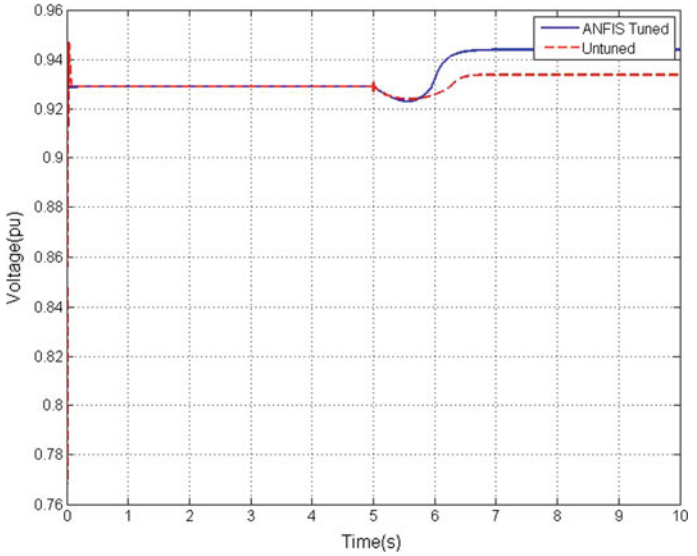

Fig. 10 Bus-11 voltage (pu) of test system with ANFIS-tuned UPFC

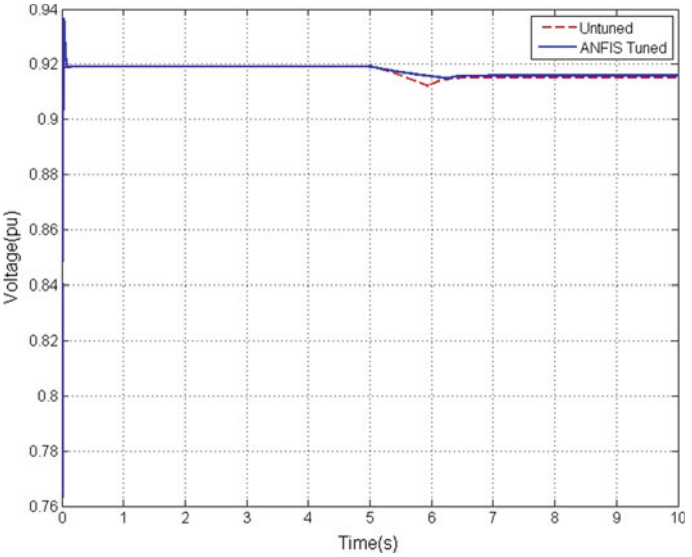

Fig. 11 Bus-14 voltage (pu) of test system with ANFIS-tuned UPFC

6 Conclusion

Renewable energy sources are gaining popularity around the globe, but it brings power and voltage instability in the system. Herein, the voltage stability improvements of a renewable energy sources-based system with the help of an ANFIS-tuned UPFC have been analyzed and presented. The nonconventional generators considered are the doubly-fed induction generators (DFIGs) with IEEE 14-bus system. A UPFC is placed in multi-machine power system with this test system. The obtained results show the improvement in voltage profiles of buses of the test power system using the ANFIS adaptive technique. The results reveal that, in such cases, the deployment of the shunt capacitor banks is incapable, so adequate VAR compensation may be attained by using the FACTS controllers, viz. UPFC only. Therefore, the need of compensating controller for the proposed wind energy sources-based power system has been discussed.

References

1. Aekcrmann T et al (2001) Distributed generation: a definition. Electr Power Syst Res 57:195–204
2. Hingorani NG, Gyugi L (2000) Understanding FACTS: concepts and technology of flexible AC transmission systems. IEEE Press, New York

3. Al-Majed SI, Fujigaki T (2010) Wind power generation: an overview. In: Proceedings of the international symposium modern electric power systems (MEPS). IEEE Xplore Press, Wroclaw, Poland, 20–22 Sept 2010, pp 1–6
4. Kundur P (1994) Power system stability and control. McGraw-Hill, New York
5. Bansal RC, Bhatti TS, Kothari DP (2003) Automatic reactive power control of wind-diesel-micro hydro autonomous hybrid power systems using ANN tuned static VAR compensator. In: Proceedings of international conference on large engineering system conference on power engineering (LESCOPE), Montreal, Canada, 7–9 May 2003, pp 182–188
6. Mohaghehi S, Venayagamourthy GK, Rajagopalan S, Harley RG (2009) Hardware implementation of mamdani fuzzy logic controller for a static compensator in multimachine power system. IEEE Trans Ind Appl 45(4):1535–1544
7. Grünbaum R (2010) FACTS for grid integration of wind power. In: Innovative smart grid technologies conference Europe), IEEEPES, 11–13 Oct 2010, pp 1–8
8. Madhavi Latha G, Kiranmayi R (2016) Transient stability improvement of hybrid power system by VR-FCL using PSO. Int J Sci Eng Technol Res (IJSETR) 5(11). ISSN: 2278–7798 (November)
9. Mohammad A, Mina S (2014) Transient stability improvement of grid connected wind generator using UPFC and STATCOM. In: Proceeding of international conference on innovative engineering technologies (ICIET), Bangkok, 28–29 Dec 2014, pp 136–140
10. Jang JSR (1993) ANFIS: adaptive-network-based fuzzy inference systems. IEEE Trans Power Syst 23(3):665–684
11. Ishibuchi H, Fujioka R, Tanaka H (1993) Neural networks that learn from fuzzy if-then rules. IEEE Trans Fuzzy Syst 1(2):85–97

Analysis, Design, and Comparison of Different Building-Integrated Photovoltaic Thermal (BIPVT) System for Indian Meteorological Condition

Amit Kumar Dash, Sanjay Agrawal, Sanjay Gairola and Shweta Shukla

Abstract Analysis of BIPVT system has been carried out in this paper based on arrays named as solar cell tile array and semitransparent array. Previously, comparisons and performance analysis were carried out for opaque and semitransparent system in a non-optimized way, but in the present case, optimization has been done to get better results. As far as energy effectiveness and exergy are concerned, semitransparent PVT has an edge as compared to others in all respects. Semitransparent PVT has relatively higher useful energy gain by 2.5 kWh as compared to SCT. Further, the electrical and thermal effectiveness has been derived, and a conclusion has been made that semitransparent PV cell has an edge in all respects as compared to SCT. The electrical effectiveness has been enhanced to 17.17% from the previous 16% and overall exergy to 18.4% from the previous 17.1%, i.e., an overall growth of 6.8 and 7.6%, respectively.

Keywords SCT and semitransparent PVT array · Building-integrated photovoltaic system (BIPVT) · Photovoltaic (PV) · Exergy

Nomenclature

A_{roof}	Area of roof, m^2
C_{air}	Specific heat of air, J/kg K
dt	Elemental time, s
dx	Elemental length, m
h_{air}	Heat transfer coefficient from tedlar to flowing air, W/m^2K

A. K. Dash (✉) · S. Gairola
Noida Institute of Engineering and Technology, Greater Noida, UP, India
e-mail: amitkudash@rediffmail.com

S. Agrawal
School of Engineering and Technology, IGNOU, New Delhi, India

S. Shukla
Meerut Institute of Engineering and Technology, Meerut, UP, India

G. Zhang et al. (eds.), *Advances in Energy and Built Environment*, Lecture Notes in Civil Engineering 36, https://doi.org/10.1007/978-981-13-7557-6_12

h_t Heat transfer coefficient from solar cell to tedlar in W/m^{2}K
$I(t)$ Incident solar intensity, W/m^2
K Thermal conductivity, W/mK
M_{f} Mass flow rate of air in PVT array, kg/s
M_{air} Mass of air in the room, kg
n Number of solar cell tiles
n_{pv} Number of rows of PVT array
N Number of PVT air collectors
N_0 Number of air changes
Q_u Useful heat, W
t Time, s
T Temperature, K
$\bar{T}$ Average temperature, K
U_L Overall heat transfer coefficient for the system, W/m^2 °C
v Velocity of air, m/s
V Volume of air in the room, m^3

Subscripts

a ambient
eff effective
f fluid (air)
f_i inlet fluid
f_{air} outgoing fluid
g glass
ins insulation
ar room
T tedlar

Greek letters

α Absorptivity
β_e Packing factor
τ Transmissivity
ρ Density, kg/m^3

1 Introduction

In recent times, solar thermal systems are widely used, but PVTs are not used extensively. Greater than 80% of the inward solar energy is either absorbed or reflected as heat energy. Agrawal et al. [1] concluded that in terms of energy saving, glazed hybrid gives better result as compared to normal PV module. Kim and Kim [2] studied simulation of air-type building-integrated photovoltaic thermal system.

In 1998, Loferski et al. [3] studied and obtained few results related to the system with air circulation in housing. Raman and Tiwari [4] analyzed PVT air collector, single and double pass, for varying Indian meteorological surroundings of Srinagar, Mumbai, Jodhpur, and Bangalore. Singh et al. [5] described the modeling and optimization of single-channel system by genetic algorithm. The scheme proposed by Singh [6] made a comparative study of exergy of different cities and concluded that there is an increment of 5.8–14.7% of exergy as compared to proposed by Agrawal and Tiwari by soft computing technique. Vats et al. [7] provided various data of the effectiveness of different types of material out of which one can select. Wickeret al. [8] have shown various outcomes from a building-integrated photovoltaic thermal (BIPVT) technique for various operations in different meteorological zones. The BIPVT system designed by Agrawal and Tiwari [9] have shown that the rooftop placed in an area of 65 m^2, generating the net electrical and thermal exercise of 16,300 and 1550 kWh, respectively, at an overall thermal effectiveness of 54.2% (Fig. 1).

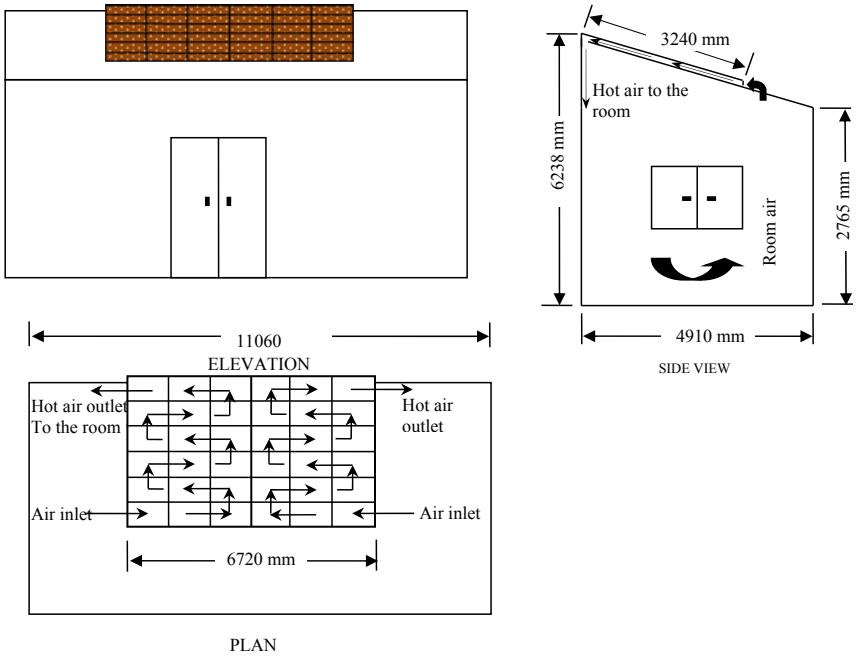

Fig. 1 Design of BIPVT system with alignment

2 Thermal Modeling of BIPVT System

In the current paper, research has been made on cold meteorological condition of India by placing the designed model on the rooftop of the building. As Srinagar is located at 34° 1′N, 74° 51′E due to which the propose systems is fitted in the south direction inclined at an angle of the latitude of that city i.e. 35° to the horizontal. With proposed area of 65 m^2, the model proposed by Agrawal and Tiwari (2010) is able to produce the electrical and thermal energy of 16,300 and 1550 kWh, respectively, with overall thermal effectiveness of 54.6% (Tables 1 and 2).

2.1 Thermal Modeling of the Proposed Design

To calculate electrical effectiveness of any PV cell, [9] designed a theory given by,

$$\eta_{ca} = \eta_{\text{ref}}[1 - \phi_{\text{ref}}(T_c - T_a)] \tag{1}$$

Quantities η_{ref}, T_a, and φ_{ref} are generally references to what the researcher has to set accordingly.

$$E_{\text{out}} = \eta_{ca} * I(t) * bL * n_{\text{pv}} \tag{2}$$

The equivalent thermal energy of electrical is given by

$$E_{\text{eth}} = \frac{E_{\text{out}}}{C_f} \tag{3}$$

Adding thermal gain of the proposed method to the equivalent thermal energy of electrical energy, the overall thermal energy of the proposed method may be evaluated as,

$$Q_{\text{hourly}} = \frac{E_{\text{out}}}{C_f} + Q_u \tag{4}$$

Table 1 Specification of proposed model

V_{max}	425 V
η	17.1%
Size of room	5580 mm × 4910 mm
Side wall height	2765 * 6238 mm
Roof area	11,060 mm × 6144 mm
Roof inclination	35°
η_{ref}	16%

Table 2 Design parameters of proposed model

Design parameters	Corresponding values
Length of proposed system	1650 mm
Width of propose dv system	800 mm
Net output	155 W
Depth of proposed duct	255 mm
Channel	Single-pass channel
C_{air} (J/kg K)	1005
C_r	0.38
A (ambient)	25°
h_0 (W/m^2)	$5.70 + 3.8V_a$
h_i (W/m^2)	2.8
h_T (W/m^2)	$2.80 + 3 \times V_{air}$
K_c (W/m^2)	0.040
K_G (W/m^2)	0.80
K_i (W/m^2)	0.0350
K_T (W/m^2 K)	0.380
L_c (mm)	0.3
L_G (mm)	34
L_i (mm)	11
L_T (mm)	3
α_c	0.7
α_t	0.7
β_c	0.9
η_c	0.16
$\acute{\iota}_g$	0.85
ρ_a (kg/m^3)	1.29

The thermal energy of the proposed system can be derived from

$$Q_{\text{daily}} = \sum_{j=1}^{n} \frac{(\eta_{ca})_j * [I(t)]_j * bL * \eta_{\text{pv}}}{C_f} + \sum_{j=1}^{n} (Q_u)_j \tag{5}$$

Overall thermal effectiveness can be derived as (Figs. 2 and 3),

$$\eta_{\text{TH}} = \frac{\sum_{j=1}^{n} \frac{(\eta_{ca})_j * [I(t)]_j * bL * \eta_{\text{pv}}}{C_f} + \sum_{j=1}^{n} (Q_u)_j}{\sum_{j=1}^{n} [I(t)]_j * bL * \eta_{\text{pv}}} \tag{6}$$

$$\text{Thermal Exergy} = Q_u \left(1 - \frac{T_a}{T_{\text{airout}}}\right) \tag{7}$$

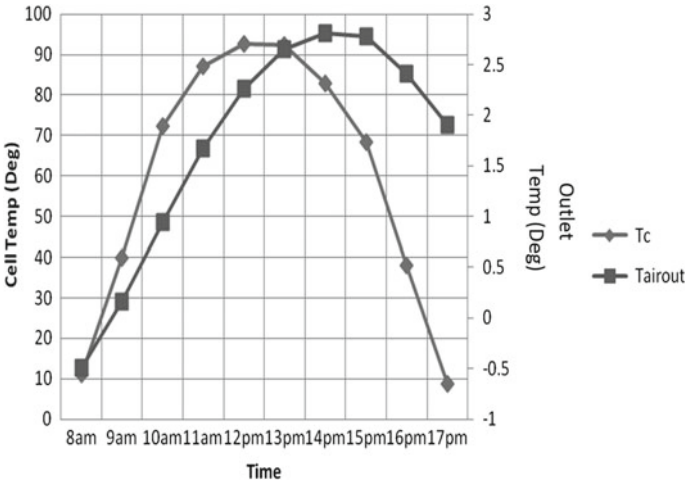

Fig. 2 Comparative study of temperature between cell and duct outlet

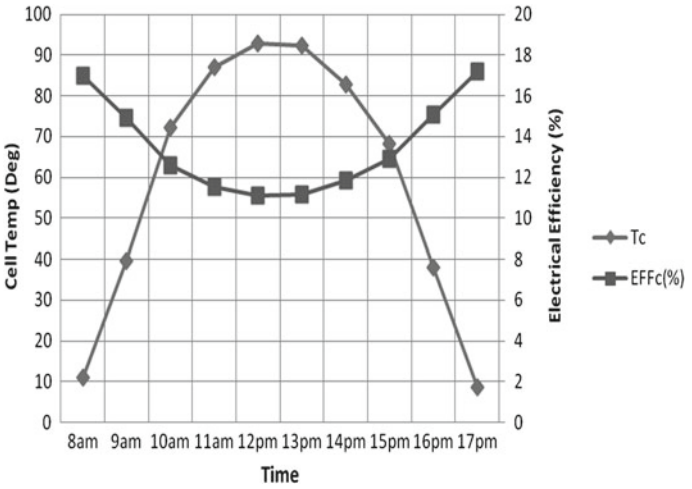

Fig. 3 Comparison between cell temperature and electrical effectiveness w.r.t time

$$\text{Net Exergy Gain} = E_{\text{out}} + Q_u\left(1 - \frac{T_a}{T_{\text{airout}}}\right) \tag{8}$$

Energy balance equation of the proposed model is given by:

$$\begin{bmatrix}\text{Rate of heat}\\ \text{received by}\\ \text{solar cell}\end{bmatrix}+\begin{bmatrix}\text{Rate of heat}\\ \text{received by}\\ \text{non packing area}\end{bmatrix}=\begin{bmatrix}\text{Rate of heat loss}\\ \text{from PV module to}\\ \text{air as the toploss}\end{bmatrix}+\begin{bmatrix}\text{Rate of heat loss from}\\ \text{pv module to}\\ \text{back surface/tedlar}\end{bmatrix}+\begin{bmatrix}\text{rate of Electricity}\\ \text{produced}\end{bmatrix}$$

$$\tau_g[\alpha_c\beta_c+(1-\beta_c)\alpha_T]I(t)b\mathrm{d}x=[U_T(T_c-T_a)+h_T(T_c-T_{bs})]b\mathrm{d}x+\eta_{ca}I(t)b\mathrm{d}x \tag{9}$$

Simplifying

$$T_c=\frac{h_TT_{bs}+U_TT_a+I(t)(\alpha\tau)_{\text{eff}}}{U_T+h_T} \tag{10}$$

For proposed model, the energy balance can be derived as,

$$\begin{bmatrix}\text{Rate of heat gain from}\\ \text{PV module to tedlar}\end{bmatrix}=\begin{bmatrix}\text{Rate of heat loss from tedlar to}\\ \text{air side in the duct}\end{bmatrix}$$

$$h_T(T_c-T_{bs})b\mathrm{d}x=h_{\text{air}}(T_{bs}-T_{\text{air}})b\mathrm{d}x \tag{11}$$

Substituting T_c in Eq. (11)

$$T_{bs}=\frac{h_{\text{air}}T_{\text{air}}+U_{tT}T_a+h_{\rho1}I(t)(\alpha\tau)_{\text{eff}}}{U_{tT}+h_{\text{air}}} \tag{12}$$

Energy balance of air flowing in the duct of the BIPVT system is given by,

$$\begin{bmatrix}\text{Rate of heat received from tedlar}\\ \text{to air side in the duct}\end{bmatrix}=\begin{bmatrix}\text{Rate of heat gain by air}\\ \text{flowing in duct}\end{bmatrix}+\begin{bmatrix}\text{Rate of heat loss from air}\\ \text{through insulation}\end{bmatrix}$$

$$h_{\text{air}}(T_{bs}-T_{\text{air}})b\mathrm{d}x=M_{\text{air}}C_{\text{air}}\left(\frac{\mathrm{d}T_{\text{air}}}{\mathrm{d}x}\right)\mathrm{d}x+U_{bb}(T_{\text{air}}-T_{\text{ar}})b\mathrm{d}x \tag{13}$$

On substituting T_{bs} from Eqs. (12) to (13), we have

$$h_{\text{air}}\left[\frac{h_{\rho1}h_{\rho2}I(t)(\alpha\tau)_{\text{eff}}-U_{tT}(T_{\text{air}}-T_c)}{U_{tT}h_{\text{air}}}\right]b\mathrm{d}x=M_{\text{air}}C_{\text{air}}\left(\frac{\mathrm{d}T_{\text{air}}}{\mathrm{d}x}\right)\mathrm{d}x+U_{bb}(T_{\text{air}}-T_{\text{ar}})b\mathrm{d}x \tag{14}$$

By $T_{\text{air}}=T_{\text{ar}}$; $T_{\text{air}}=T_{\text{airout}}$
The warmth at the output of duct for length L can be derived as,

$$T_{\text{airout}} = \left[\frac{U_{bb}T_{\text{ar}} + U_{t\text{air}}T_a + h_{\rho 1}h_{\rho 2}I(t)(\alpha\tau)_{\text{eff}}}{U_{ti}}\right]\left(1 - \text{e}^{-\frac{bU_{ti}L}{M_{\text{air}}C_{\text{air}}}}\right) + T_{\text{ar}}\text{e}^{-\frac{bU_{ti}L}{M_{\text{air}}C_{\text{air}}}} \tag{15}$$

$$T_{\text{air}} = \left[\frac{U_{bb}T_{\text{ar}} + U_{t\text{air}}T_a + h_{\rho 1}h_{\rho 2}I(t)(\alpha\tau)_{\text{eff}}}{U_{ti}}\right]\left(1 - \frac{1 - \text{e}^{-\frac{bU_{ti}L}{M_{\text{air}}C_{\text{air}}}}}{\frac{bU_{ti}L}{M_{\text{air}}C_{\text{air}}}}\right) + T_{ar}\frac{1 - \text{e}^{-\frac{bU_{ti}L}{M_{\text{air}}C_{\text{air}}}}}{\frac{bU_{ti}L}{M_{\text{air}}C_{\text{air}}}} \tag{16}$$

For η_{pv} row of the system, the overall thermal energy can be derived as,

$$Q_u = n_{\text{pv}} * M_{\text{air}}C_{\text{air}}(T_{\text{airout}} - T_{\text{ar}}) \tag{17}$$

For heating of space of the building, the energy balance equation can be derived as,

$$n_{\text{pv}} * M_{\text{air}}C_{\text{air}}\left[\frac{U_{bb}T_r + U_{t\text{air}}T_a + h_{\rho 1}h_{\rho 2}I(t)(\alpha\tau)_{\text{eff}}}{U_{ti}} - T_{ar}\right] * \left(1 - \text{e}^{-\frac{bU_{ti}L}{M_{air}C_{air}}}\right)$$
$$+ U_{bb}(T_{\text{air}} + T_{\text{ar}})A_{\text{roof}} = M_rC_{\text{air}}\left(\frac{\text{d}T_r}{\text{d}t}\right) + (UA)_t(T_{\text{ar}} - T_a) + 0.33N_oV(T_{\text{ar}} - T_a) \tag{18}$$

Temperature of air inside the room can be derived as

$$T_{\text{ar}} = \frac{f(t)}{a}\left(1 - \text{e}^{-at}\right) + T_{ri}\text{e}^{-at} \tag{19}$$

$$f(t) = \frac{1}{M_rC_{\text{air}}}\left[\left\{(UA)_t 0.33N_oV\right\}T_a + \left\{\eta_{\text{pv}}M_{\text{air}}C_{\text{air}}\left[\frac{U_{t\text{air}}T_a + h_{\rho 1}h_{\rho 2}I(t)(\alpha\tau)_{\text{eff}}}{U_{ti}}\right]\right.\right.$$
$$\left.\left.\left(1 - \text{e}^{\frac{-bU_{ti}L}{M_{\text{air}}C_{\text{air}}}}\right)\right\} + U_{bb}\left\{\frac{U_{t\text{air}}T_a + h_{\rho 1}h_{\rho 2}I(t)(\alpha\tau)_{\text{eff}}}{U_{ti}}\right\}\left(1 - \frac{1 - e^{\frac{-bU_{ti}L}{M_{\text{air}}C_{\text{air}}}}}{\frac{bU_{ti}L}{M_{\text{air}}C_{\text{air}}}}\right)A_{\text{roof}}\right] \tag{20}$$

The effectiveness, exergy, and thermal and electrical gain have been calculated after changing the parameters related to the system. The values have been compared with the previous one, and percentage change is calculated with the use of "MATLAB-13." The air is blown at a pace of 1.5 kg/s inside the duct to get maximum effectiveness (Figs. 4, 5, and 6).

3 Results and Discussion

Based on the above discussions and plots, the following summarization has been made:

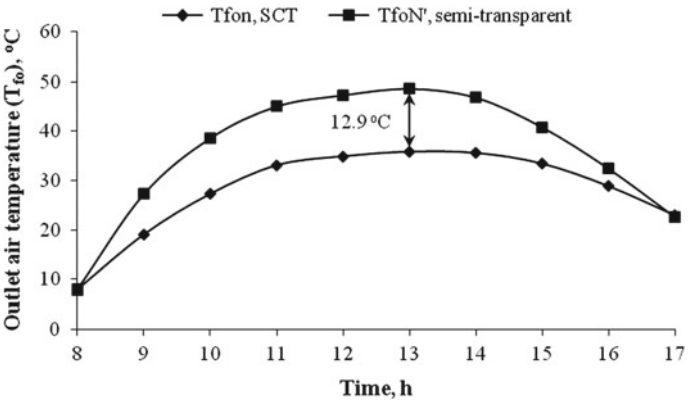

Fig. 4 Variations of room air temperature w.r.t time

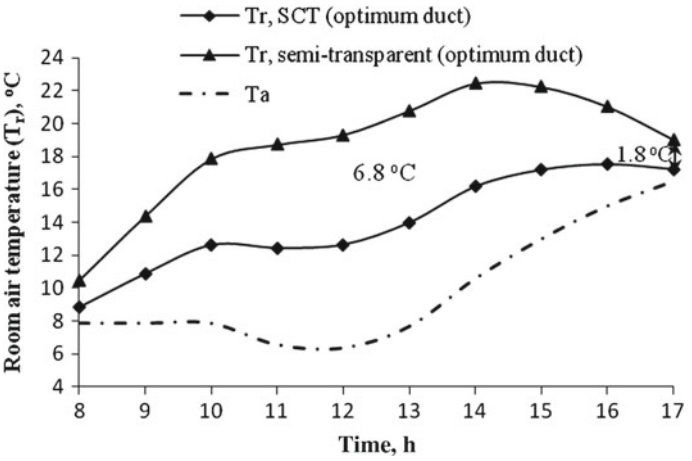

Fig. 5 Variation of thermal energy w.r.t number of air changes

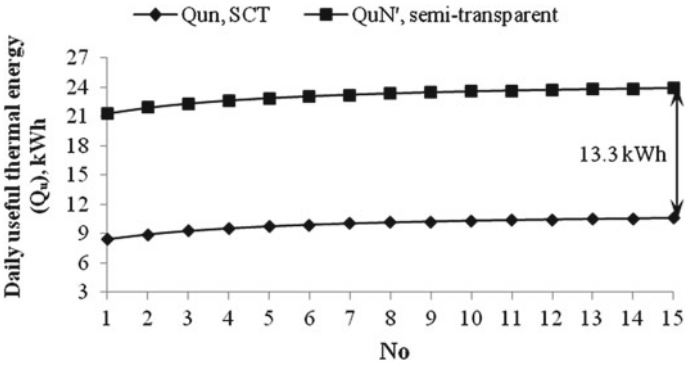

Fig. 6 Variation of thermal energy w.r.t number of air changes

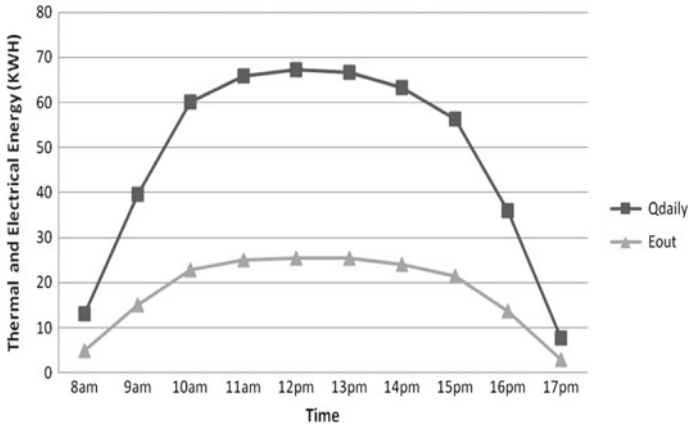

Fig. 7 Variation of electrical and thermal energy gain w.r.t time

- A comparison has been made between electrical effectiveness and exergy effectiveness which shows that after combining the electrical and thermal energy, the net electrical effectiveness increases from 17.1 to 18.4% which can be shown in Fig. 3.
- Figure 2 shows that even if the cell temp dies out at 5 pm, there is a presence of duct temperature which indicates the effectiveness of the module.
- At 12.9% more outlet temperature of semitransparent PVT, it has an edge as compared to other system.
- At 13.3 kWh, semitransparent system has more daily useful heat gain as compared to SCT roof.
- Figure 7 shows the overall thermal electrical gain in kWh.
- Figure 8 shows better idea that present system is best suited for Srinagar meteorological condition as compared to Delhi.

4 Conclusion

Depending upon the above investigations, the paper can be summarized as follows:

- Data show that the solar intensity is maximum in Srinagar at 1 pm in the month of January. If for the same system a comparison is made, then it has been concluded that Srinagar gives better result as compared to Delhi, i.e., almost 2% more. Comparison has also been made to know about the room temperature, the duct, and the outlet in Table 3.
- The present system produces approximately 67 kWh thermal energy per day as compared to 51 kWh of the previous system (Fig. 7).

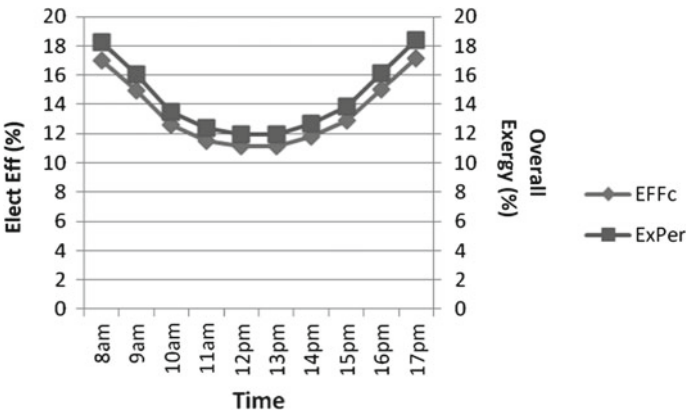

Fig. 8 Variation of electrical and exergy effectiveness w.r.t time

Table 3 Variation of temperature at different places

T_c	T_{air} (duct)	T_{airout} (duct outlet)	T_{ar} (room)
11.0321	−0.5437	−0.4915	−0.5959
39.742	−0.0194	0.1598	−0.1986
72.298	0.6211	0.9442	0.298
87.1728	1.281	1.6682	0.8939
92.7663	1.8499	2.2598	1.4401
92.2978	2.2433	2.6493	1.8374
82.8908	2.448	2.8109	2.0857
68.2848	2.4816	2.7782	2.185
38.0957	2.2473	2.4089	2.0857
8.664	1.868	1.8986	1.8374

Time	T_c (degree) cell temp	Electrical effectiveness (%)
8 am	11.0321	17.0057
9 am	39.742	14.9386
10 am	72.298	12.5945
11 am	87.1728	11.5236
12 pm	92.7663	11.1208
13 pm	92.2978	11.1546
14 pm	82.8908	11.8319
15 pm	68.2848	12.8835
16 pm	38.0957	15.0571
17 pm	8.664	17.1764

- As far as the total electrical energy is concerned, it produces 25 kWh per day from 8 am to 5 pm as compared to 23 kWh of the previous system.
- As far as the effectiveness is concerned, this system produces 17.1% of electrical effectiveness and overall exergy of 18.4% as compared to 16 and 17% of the previous system.

Acknowledgements The authors are really thankful for the support from Basant Agarwal and C. S. Rajoria whose papers provided lots of information regarding design and made the proposed system possible. The Indian Meteorology Department (IMD), Pune, has a major role in providing data related to temperature of different cities.

Appendix

$$(\alpha\tau)_{\text{eff}} = \tau_g[\alpha_c\beta_c + (1-\beta_c)\alpha_T] - \eta_c$$

$$U_T = \left(\frac{\text{Lg}}{\text{Kg}} + \frac{1}{\text{ho}}\right)^{-1}$$

$$h_T = \left(\frac{L_T}{K_T}\right)^{-1}$$

$$h_{\rho 1} = \frac{h_T}{U_{T+h_T}}$$

$$U_{tT} = \frac{U_T * h_T}{U_{T+h_T}} = \left(\frac{1}{h_T} + \frac{1}{U_T}\right)^{-1}$$

$$U_{bb} = \left(\frac{1}{h_{\text{air}}} + \frac{\text{Li}}{K_i} + \frac{1}{h_r}\right)^{-1}$$

$$h_{\rho 2} = \frac{h_{\text{air}}}{U_{tT+h_{\text{air}}}}$$

$$U_{t\text{air}} = \left(\frac{1}{h_{\text{air}}} + \frac{1}{U_{tT}}\right)^{-1}$$

$$U_L = (U_{bb} + U_{t\text{air}})$$

$$(\text{UA})_t = (\text{UA})_{t\_\text{wall}} + (\text{UA})_{t\_\text{win}} + (\text{UA})_{t\_\text{dr}}$$

$$(\text{UA})_{t\_\text{dr}} = \frac{A_d}{\left(\frac{1}{h_0} + \frac{1}{h_r} + \frac{L_d}{K_d}\right)}$$

$$(\text{UA})_{t\_\text{win}} = \frac{A_{\text{win}}}{\left(\frac{1}{h_0} + \frac{1}{h_r} + \frac{L_{\text{win}}}{K_{\text{win}}}\right)}$$

$$(\mathrm{UA})_{t\_\mathrm{wall}} = \frac{A_{\mathrm{wall}}}{\left(\frac{1}{h_0} + \frac{1}{h_r} + \frac{L_{\mathrm{wall}}}{K_{\mathrm{wall}}}\right)}$$

References

1. Agarwal B, Tiwari GN (2009) Performance evaluation of building integrated photovoltaic thermal (BIPVT) systems. Int J Green Energy
2. Kim Jin-Hee, Jun-Tae Kim (2012) A simulation study of air-type building-integrated photovoltaic-thermal system. Energy Procedia 30:1016–1024. https://doi.org/10.1016/j.egypro.2012.11.114
3. Loferski JJ, Ahmad JM, Pandey A (1998) Performance of photovoltaic cells incorporated into unique hybrid photovoltaic/thermal panels of a 2.8 KW residential solar energy conversion system. In: Proceedings of the 1988 annual meeting, American solar energy society, Cambridge, Massachusetts, pp 427–432
4. Raman V, Tiwari GN (2008) Life cycle cost analysis of HPVT air collector under different Indian meteorological surroundings. Energy Policy 36:603–611. https://doi.org/10.1016/j.enpol.2007.08.031
5. Singh S, Agrawal S (2015) Modelling and parameter optimization of hybrid single channel photovoltaic thermal module using GA. Sol Energy 113:78–87. https://doi.org/10.1016/j.solener.2014.12.031
6. Singh S, Agrawal S (2016) Parameter extraction and performance evaluation of glazed PVT module for Indian meteorological condition based on soft computing technique. In: IEEE conference, 17–19 Nov, pp 1–8. https://doi.org/10.1109/ictfcen.2016.8052712
7. Sathe T, Dhoble AS (2017) A review on recent advancements in photovoltaic thermal techniques. Renew Sustain Energy Rev 76:645–672
8. Vats K, Tiwari GN (2012) Energy and exergy analysis of a building integrated semitransparent photovoltaic thermal (BISPVT) system. Appl Energy 96:409–416
9. Zondag HA, De Vries DW, Van Helden WGJ, Van Zolingen RJC, Van Steenhoven AA (2002) The thermal and electrical yield of a PV thermal collector. Sol Energy 72(2):113–128

Nonlinear Coupled Ion Acoustic Wave (IAW) with Inertial Alfvén Wave (AW): An Application to Solar Coronal Heating

B. K. Das, R. Prasad and Tanveer Ahmad Wani

Abstract This paper mainly represents the analytical nonlinear coupling of ion acoustic wave (IAW) with inertial Alfvén wave (AW) in the low-β plasmas. The pump IAW is perturbed by the inertial AW. Under the consideration of ponderomotive force in the IAWs and inertial AW dynamics, the governing equations come out to form a modified Zakharov system of equations (MZSE). Through this, the growth of modulational instability has to be evaluated. It has been also presented that the growth also depends on the perturbation in their wave number. From this investigation, it is obvious that the IAW becomes unstable as it interacts by the inertial AW nonlinearly and modulational instabilities appeared. The importance of these analyses for solar coronal plasma is to be described.

Keywords Solar corona · Ponderomotive force · Inertial Alfvén wave · Ion acoustic wave

1 Introduction

The nonlinear instabilities (like modulational and filamentation instabilities) have been a topic of great attention for many researchers from the last few decades, and it has been investigated by the wave–wave interactions in plasmas. The general characteristic in space plasma is mainly the production of active particles in the solar wind, moreover heating of solar corona. However, the observations from the Freja spacecraft gave a significant contribution to the study of inertial AW in the auroral acceleration. As per recent simulations and its results, Alfvén waves (AWs) turbulence may be a direct energization mechanism of plasmas in the corona [1]. These waves have been detected by some special spacecraft like FAST, Freja and Cluster in

B. K. Das (✉) · T. A. Wani
Department of Physics, Noida International University, Greater Noida, India
e-mail: drbkdas.iitd@gmail.com

R. Prasad
Department of Applied Sciences, Galgotias College of Engineering and Technology, Greater Noida, India

G. Zhang et al. (eds.), *Advances in Energy and Built Environment*, Lecture Notes in Civil Engineering 36, https://doi.org/10.1007/978-981-13-7557-6_13

the space plasmas [2–4]; also, it has been shown that these waves are responsible for the energization of particle in the Aurora [5, 6]. The nonlinear interaction between kinetic AWs and ion acoustic waves (IAW) has been studied by several authors [7–9]. Tam and Chang [10] have observed the heating of corona and the motion of particles in the solar wind plasma due to the action of wave–particle interaction.

Although a large number of mechanisms have been suggested for the mechanism of coronal heating and acceleration of the solar wind, the recent study shows that ion acoustic wave can energize the particles by the nonlinear method. Hence, ion acoustic wave turbulence may play a significant role for the energization of particles in the space as well as coronal plasma and also explains the spectra obtained from the solar wind plasma. Most recently, Malik et al. [11] examined parallel travelling two kinetic AWs when they intermingle and also it gets filamented. Frycz et al. [12] have studied analytically and numerically the nonlinearity between derived kinetic AWs resonances with field line and IAW. They found that kinetic AW resonances with field lines radiate an ion acoustic solitons for the duration of its temporal nonlinear evolution. The observed data from *Freja* satellite and other resources by Wahlund et al. [13] confirmed that the IAWs and the kinetic AWs turbulence have a close link within auroral regions. An analytical study has been done by Ghosh and Das [14], and the coupling of kinetic AWs and IAWs, including nonlinear effects in higher order, produces solitary structures.

In this paper, the nonlinearity between IAW and inertial AWs has been discussed. For investigating the nonlinear coupled mechanism, the governing equations for IAW and the inertial AW have been obtained. The governing equations represented are believed to be the generalized Zakharov system of equations (ZSE). Therefore, it can be said here as modified MZSE. Through this, the growth of instability can be computed and applied to study the solar coronal heating.

This paper can be organized as follows: the governing equations for IAW and inertial AW are put in Sects. 2 and 3, respectively.

2 Ion Acoustic Wave (IAW) Dynamics

We assume an IAW is travelling in the direction of z-axis with ambient B-field (magnetic field) B_0, i.e. $\vec{B}_0 = B_0\hat{z}$

The equations used for the derivation of the dispersion relation are as follows:

(i) Equation used the for particle motion:

$$\frac{\partial \vec{\upsilon}_j}{\partial t} = \frac{q_j}{m_j}\phi + \frac{q_j}{cm_j}\left(\vec{\upsilon} \times \vec{B}_0\right) - \frac{\gamma_j k T_j}{m_j}\vec{\nabla}\frac{n_j}{n_0} + \frac{\vec{F}_j}{m_j} \tag{1}$$

(ii) Equation of continuity for fluid:

$$\frac{\partial n}{\partial t} + \vec{\nabla}.(n\vec{\upsilon}) = 0 \tag{2}$$

(iii) Maxwell's equation (Faraday law):

$$\text{Curl}\,\vec{E} = -\frac{\partial \vec{B}}{\partial t} \tag{3}$$

Here, υ_j, m_j and T_j represent the velocity, mass and temperature for both species $j = i, e$; where i stands for ions, e stands for electrons. c, n_0 and B_0 represents the speed of light in vacuum, unperturbed plasma number density and background magnetic field respectively. The quantity $\vec{F}_j = \left[m_j\left(\vec{\upsilon}_j.\vec{\nabla}\right)\vec{\upsilon}_j - \left(\frac{q_j}{c}\right)\left(\vec{\upsilon}_j \times \vec{B}_0\right)\right]$ defines ponderomotive force, and $\phi = (\gamma_e k_B T_e/n_0 e)n_e - F_{ez}/eik_z$, scalar potential, where V_{Te}, V_{Ti}, γ_e, k_B, T_e and F_{ez} are electron and ion thermal speeds, electron specific heat ratio, Boltzmann constant and electron temperature and parallel electron ponderomotive force, respectively. We obtained an equation for IAW as follows:

$$\frac{\partial \upsilon_{ix}}{\partial t} = \frac{\omega^2}{n_0}\frac{\partial n_e}{\partial x}\rho_s^2 - \frac{\omega^2}{\omega_{ci}^2}\frac{ik_x}{ik_z}\frac{F_{ez}}{m_i}, \tag{4}$$

and

$$\frac{\partial \upsilon_{iz}}{\partial t} = -\frac{1}{n_0}\frac{\partial n_e}{\partial z}c_s^2 + \frac{(F_{ez} + F_{iz})}{m_i}, \tag{5}$$

where $c_s = \left(\frac{\gamma_e k_B T_e + \gamma_i k_B T_i}{m_i}\right)^{1/2}$ defines acoustic speed, and here, it is assumed that the electrons along with ions are to be isothermal, i.e. $\gamma_e = \gamma_i = 1$, $\rho_s(= c_s/\omega_{ci})$ defines ion acoustic gyroradius. We obtained a parallel components of ponderomotive forces for both electron and ion, which is given by

$$F_{ez} = \frac{m_e e^2 \omega_0^2}{4k_B^2 T_e^2 k_{0z}^4}\frac{\partial}{\partial z}|E_z|^2 \text{ and } F_{\text{iz}} \approx \text{negligible}$$

Now differentiating Eq. (2) with respect to time and putting the values from Eqs. (4) and (5), we find

$$\left(\frac{\partial^2}{\partial t^2} - c_s^2\frac{\partial^2}{\partial z^2}\right)\frac{n_e}{n_0} = -\frac{\partial}{\partial z}\frac{(F_{ez})}{m_i} \tag{6}$$

Putting the expressions for F_{ez} in Eq. (6), we have

$$\frac{\partial^2 n}{\partial t^2} - c_s^2\frac{\partial^2 n}{\partial z^2} = -\xi\frac{\partial^2}{\partial z^2}|B_y|^2 \tag{7}$$

$n = n_{\text{e}} \approx n_0$ and $\xi = \left[\frac{c^2 k_x k_z\left(\omega^2 - k_z V_{\text{th}}^2\right)}{\omega_{pe}^2 \omega^2}\right]^2\left(\frac{\omega^2}{k_z^2 c^2}\right)\left(\frac{m_e e^2 \omega_0^2}{m_i k_B^2 T_e^2 k_z^2}\right)$

Here, V_A represents Alfvén speed, k_z, a wave vector component which is parallel ($\|$) to $\hat{z}B_0$, ω and B_y denote normal frequency and the perpendicularly acting B-field ($B_\perp$) respectively. Hence, we obtained Eq. (7) which represents ion acoustic wave (IAW) under the consideration of ponderomotive force.

3 Inertial Alfvén Wave

The nonlinear dynamical equation for the inertial AW travelling in the $x - z$ plane along positive x-direction under ambient magnetic field B_0 is given by [15–21]

$$\frac{\partial^2 \tilde{B}_y}{\partial t^2} = \lambda_e^2 \frac{\partial^4 \tilde{B}_y}{\partial x^2 \partial t^2} + v_A^2 \left(1 - \frac{\delta n_s}{n_0}\right) \frac{\partial^2 \tilde{B}_y}{\partial z^2}, \tag{8}$$

where $\lambda_e = \left(\sqrt{c^2 m_e / 4\pi n_0 e^2}\right)$, $v_{Te} = \left(\sqrt{T_e / m_e}\right)$, T_e $\delta n = n_e - n_0$ are representing the skin depth for collisionless electron, thermal speed, temperature, change in number density, respectively.

The general solution for Eq. (8) is given by

$$\tilde{B}_y = B_y(x, z) e^{i(k_{0x}x + k_{0z}z - \omega t)}. \tag{9}$$

From Eqs. (8) and (9), one can get the dynamical equation:

$$\begin{aligned} &- 2i\omega\left(1 + k_{0x}^2 \lambda_e^2\right) \frac{\partial B_y}{\partial t} - 2ik_{0z} v_A^2 \frac{\partial B_y}{\partial z} - v_A^2 \frac{\partial^2 B_y}{\partial z^2} \\ &+ \lambda_e^2 \omega^2 \frac{\partial^2 B_y}{\partial x^2} + 2ik_{0x} \lambda_e^2 \omega^2 \frac{\partial B_y}{\partial x} - k_{0z}^2 v_A^2 n B_y = 0. \end{aligned} \tag{10}$$

The above inertial AW dynamical equation has been deliberated by several authors numerically [18, 21], moreover analytically [11, 22, 23], for the following conditions $\frac{\partial B_y}{\partial x} \gg k_{0x} B_y$ and $\frac{\partial B_y}{\partial z} \ll k_{0z} B_y$, where k_{0x} (k_{0z}) is the wave vector $\perp$ (or $\|$) to $\hat{z}B_0$, but no other author has considered the inertial AW as a pump wave to produce the filamentation of IAW as we discussed in our manuscript.

The Eqs. (7) and (10) subsequently its normalisation, is to be obtained as MZSE in its dimensionless form:

$$\left[\frac{\partial^2}{\partial t^2} - \xi_1 \frac{\partial^2}{\partial z^2}\right] n_e = -\frac{\partial^2}{\partial z^2} \left| B_{0y} \right|^2 \tag{11}$$

and

$$-i\frac{\partial B_y}{\partial t} + i\frac{\partial B_y}{\partial x} - i\frac{\partial B_y}{\partial z} - \xi_2 \frac{\partial^2 B_y}{\partial z^2} - n B_y = 0 \tag{12}$$

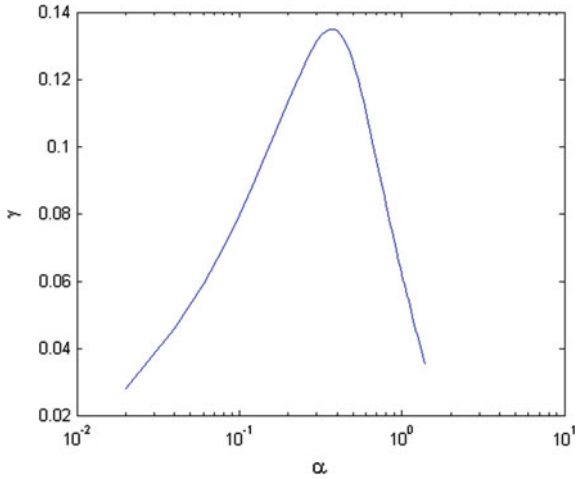

Fig. 1 Variation in growth rate γ with α for low-β plasma

where $\xi_1 = \frac{c_s^2 k_z^2}{\omega^2}$, $\xi_2 = k_{0x}^2 \lambda_e^2$ and normalizing parameters are $z_n = 1/2k_{0z}k_{0x}^2\lambda_e^2$, $t_n = \left(1 + k_{0x}^2\lambda_e^2\right)/2\omega k_{0x}^2\lambda_e^2$, $n_n = 4n_0 k_{0x}^2\lambda_e^2$ and $B_n = \left[\left\{c^2k_x^2\left(\omega^2 - k_z^2V_{\text{th}}^2\right)^2/\omega_{pe}^4\omega^2\right\}\left(m_e e^2\omega_0^2/4m_i k_B^2 T_e^2 k_z^4\right)\right]^{-1}$.

Using a general solution with time variable as $\sim \exp[i(k_x x + \alpha z - \omega t)]$ and following the model methods [24], we get dispersion relation as

$$\omega^4 + 2(k_x - \alpha)\omega^3 + \left(2k_x\alpha - k_x^2 - \alpha^2 - \xi_2\alpha^2 + \xi_1\alpha^4\right)\omega^2 + 2(k_x - \alpha)\omega + 2\xi_2 k_x\alpha^3 - \xi_2 k_x^2\alpha^2 - \xi_2\alpha^4 + \xi_1^2\xi_2\alpha^6 - 2\xi_1\alpha^4 B_{0y}^2 = 0 \quad (13)$$

where $\alpha(k_z)$ is parallel (||) perturbed wave number. The value of ξ can be approximated from the plasmas limitations. As the above fourth-order equation is in terms ω, analytically, it is difficult to solve. However, it has been solved in MATLAB with the help of root finding algorithm. Also, four roots of ω have been obtained for a given k_x, α and B_{0y}. A curve has been plotted for growth rate γ with respect to perturbed wave number α, keeping B_{0y} and k_x fixed (Fig. 1). From the figure, it has been observed that as we increase the value of α, the growth in the filament gradually increases and then decreases gradually. For the solar coronal parameters, the growth time ($\tau = \gamma^{-1}$) is of the order of seconds (i.e. 2.15 s). This calculated value is smaller than the observed timescales for coronal heating (images taken by *Yohkoh* and SOHO).

For low-β plasma, the characteristic values for coronal plasma [25] are $B_0 = 0.3$ G, $n_0 = 5 \times 10^3$ cm^{-3}, $T = 1$ eV, $c_s = 9.8 \times 10^5$ cm/s, $V_A = 9.3 \times 10^8$ cm/s, $\beta = 2.2 \times 10^{-6}$, $V_{\text{th}} = 4.2 \times 10^7$ cm/s, $\omega_{ci} = 2.9 \times 10^3$ Hz, $\lambda_e = 7.5 \times 10^3$ cm and $\omega_{pe} = 6.35 \times 10^5$ Hz. For these parameters at $k_{0x}\lambda_e = 0.1$ and $\omega/\omega_{ci} = 0.02$, we have $k_{0x} = 1.3 \times 10^{-5}$ cm^{-1}, $\omega = 58$ Hz and $k_{0z} = 6.2 \times 10^{-8}$cm^{-1} and we have

normalizing values $\xi = 0.369$, $z_n \simeq 8 \times 10^8$ cm, $t_n \simeq 0.87$ s, $n_N = 2 \times 10^2$ cm^{-3}, $x_n = 3.8 \times 10^4$ cm and $B_n = 0.28$ G.

4 Conclusion

The nonlinear coupling of ion acoustic waves with inertial AWs, when pump inertial AW is perturbed by the IAW, has been investigated. As in our mathematical formulation, the derived equations of IAW and inertial AW turn into modified Zakharov system of equations (modified ZSE) because the ponderomotive force is taken into account in the dynamics of IAW. We have also presented for growth rate γ with respect to perturbed wave number α on the basis of pump wave values. Following the coronal parameters, the growth time ($\tau = \gamma^{-1}$) is found in the order of seconds which is smaller than the observed timescales for coronal heating (images taken by *Yohkoh* and SOHO). Therefore, this investigation will be a key in the study of the solar coronal heating as well as the ejection of particles from the solar wind.

References

1. Chaston CC, Salem C, Bonnell JW, Carlson CW, Ergun RE, Strangeway RJ, McFadden JP (2008) Phys Rev Lett 100:175003
2. Seyler CE, Liu K (2007) J Geophys Res 112:302
3. Louarn P, Wahlund JE, Chust T, de F´eraudy H, Roux A (1994) Geophys Res Lett 21:1847
4. Chaston CC, Carlson CW, Peria W, Ergun RE, McFadden JP (1999) Geophys Res Lett 26:647
5. Wygant JR, Keiling A, Cattell CA, Lysak RL, Temerin M, Mozer FS, Kletzing CA, Scudder JD, Streltsov V, Lotko W, Russell CT (2002) J Geophys Res 107:1201
6. Chaston CC, Peticolas LM, Carlson CW, McFadden JP, Mozer F, Wilber M, Parks GK, Hull A, Ergun RE, Strangeway RJ, Andre M, Khotyaintsev Y, Goldstein ML, Acu˜na, M, Lund EJ, Reme H, Dandouras I, Fazakerley AN, Balogh A (2005) J Geophys Res 110: A02 211
7. Wu DJ, Wang DY, Carl GF (1996) Phys Lett 13:594
8. Wu DJ, Wang DY (1996) Phys Plasma 3:4304
9. Brodin G, Stenflo L, Shukla PK (2006) Sol Phys 236:285
10. Tam SWY, Chang T (1999) Geophys Res Lett 26:3189
11. Sharma RP, Malik M, Singh HD (2007) Solar Phys 241:317
12. Frycz P, Rankin R, Samson JC (1998) Phys Plasmas 5:3565
13. Wahlund JE et al (1994) Geophys Res Lett 21:1831
14. Ghosh G, Das KP (1995) Phys Scr 52:80
15. Bellan PM, Stasiewicz KL (1998) Phys Rev Lett 76:3534
16. Shukla PK, Stenflo L (1999) Phys Plasmas 6:4120
17. Shukla PK, Stenflo L (2000) Phys Plasmas 7:2738
18. Shukla A, Sharma RP (2001) Phys Plasmas 8:3759
19. Shukla A, Sharma RP (2000) J Geophys Res 107:1338
20. Shukla A, Sharma RP, Malik M (2004) Phys Plasmas 7:2738
21. Singh HD, Sharma RP (2006) Phys Plasmas 13:012902
22. Sharma RP, Singh HD, Malik M (2006) J Geophys Res 111:A12108

23. Singh HD, Sharma RP (2007) Phys Plasmas 14:102304
24. Shen MM, Nicholson DR (1987) Phys Fluids 30:1096
25. Wu DJ, Huang GL, Wang DY (1996) Phys Rev Lett 77:4346

Embodied Energy and Carbon Emissions of Pavements: A Review

Sharon T. Abey and Sreevalsa Kolathayar

Abstract Energy consumption takes place at each stage of pavement construction, right from extraction of raw materials to finished products like roads. Carbon emission is an undesirable product that materializes simultaneously with energy consumption that is indispensable right through the construction activities. Reusability is another important feature that we should consider when we speak about sustainability. Though pavements made of bitumen have a higher embodied energy, it readily yields to recycling, when compared to concrete pavements, thereby reducing the energy consumed. Reducing consumed energy helps to save the resource for the future. Many situations warrant compromised sustainability when a particular type of pavement is preferred to serve a special function. In such cases, alternative materials with low embodied energy and low carbon emission may be used for the pavement design. Designs using waste materials and recycled materials would help to make energy-efficient pavements with lesser carbon emissions. This paper presents a review on various studies that have been conducted, and focuses on embodied energy and carbon emission of different types of pavements. Alternate options are suggested considering best-suited pavement types that consume minimal energy and ensure reduced carbon emissions.

Keywords Energy · Carbon emission · Pavement · Sustainability · Environment

1 Introduction

Construction activities are indispensable for any nation. They are an integral part of development and civilization. The industry deals mainly with the construction of residential and commercial buildings and pavements. For most of the countries, road transport is still the major mode of travel and goods movement. This disposes road construction to hold a vital part in the construction sector. We know that construction

S. T. Abey · S. Kolathayar (✉)
Department of Civil Engineering, Amrita School of Engineering,
Amrita Vishwa Vidyapeetham, Coimbatore, India
e-mail: sreevalsakolathayar@gmail.com

G. Zhang et al. (eds.), *Advances in Energy and Built Environment*, Lecture Notes in Civil Engineering 36, https://doi.org/10.1007/978-981-13-7557-6_14

activities lead to serious environmental issues and wide-ranging pollution levels that cause global warming. Today, environmental impact and sustainability have become a major concern in the construction sector. Several studies on this subject provide compelling evidence against the construction industry as the second largest contributor to pollution. This pollution is a direct result of consuming large quantities of energy that in turn raises carbon emissions to alarming levels correspondingly. This is the prime source that gives rise to global warming. Therefore, it is evident that pavement construction that utilizes energy massively also leads to a large amount of carbon emissions. Due considerations were not paid to these ill effects in the past thus causing the current concern of chaotic climactic changes, global warming, and other environmental issues that can prove detrimental to the biosphere. Increased pollution rate of air, water, and soil upsets the ecology and can potentially endanger the existence of humankind, animals, and plants. The concept of sustainability was put forward some while ago in the past in order to overcome the predicaments associated with this situation. The idea is to preserve the globe safe and secure for the future generations by optimizing the use of resources in such logical ways that least impact is meted out to environment and ecology. In this context, it is crucial to reduce the amount of energy consumption, find alternative materials that have less embodied energy, materials that can be easily recycled with phenomenally low energy consumption rates.

Of all, carbon dioxide is the most prolific gas contributing to the greenhouse effect, the precursor to global warming. That makes control of carbon dioxide a priority for us in all our activities. Construction processes make abundant use of energy and this translates to the release of huge proportions of carbon dioxide into the atmosphere. Therefore, the trick is to put a check on energy consumption and control it judiciously so that emissions are brought to the acceptable levels in order that the damage potentials are forestalled.

We know pavement constructions are of two types: flexible pavement with asphalt and rigid pavement with reinforced concrete. The most widely used one is asphalt pavement, and due to numerous advantages, it has over reinforced concrete pavement. To name a few, cost, the speed of construction and durability. Usually, when we decide on the type of pavement to construct, stress would be due to technical and economic considerations. There would be occasions where a particular type of pavement is opted to serve a special purpose, where all the other considerations are simply ignored.

When we consider sustainability in the pavement construction, it is crucial to know which type of pavement consumes less energy, has less emission rates, and subsequently causes less environmental damage and would still maintain the ecological balance. The scope of recyclability is also an important factor. There have been case studies to calculate embodied energy of these two types of pavements and to observe the environmental implication they posed in bids to compare, evaluate, and establish which of these is high on energy efficiency and low on environmental penalties.

1.1 Embodied Energy

Embodied energy is the total energy consumption associated with a product or a system. This includes energy consumed for extraction, processing, transportation, placement, maintenance, and disposal. As of now, procedures and processes are not standardized and many cases are subject to improvisation. Such a scenario makes it difficult to follow any standard guidelines to calculate embodied energy. Thus, the embodied energy values found for similar products and systems would vary widely depending on a number of factors such as system boundary, methods adopted, completeness of data, how old the available data is, and geographic location where a study conducted.

1.2 Carbon Dioxide Emission

Emissions are obvious with energy consumption. Colossal proportions of energy consumed at different stages of pavement construction result in gross emissions primarily of carbon dioxide gas. So, energy consumption and carbon dioxide emission go hand in hand. Embodied CO_2 analysis helps us get a better picture of the environmental impact of construction activities.

2 Life Cycle Assessment (LCA)

LCA is a method that systematically approaches environmental impact at various stages of the entire life cycle of a product or a process: the material extraction stage, the manufacturing or production stage, the use phase, and the ultimate disposal phase. This includes inventory analysis, impact analysis, and improvement analysis which are: quantification of environmental burden, estimation of the impact of these burdens on humans and nature, and identification of areas where improvements are possible, respectively.

Studies conducted in the USA used two methods to fix the boundary of the analysis. They are SETAC-EPA and EIO-LCA. These approaches were developed by the Society of Environmental Toxicology and Chemistry and the US Environmental Protection Agency. This is a process-based method that considers all necessary processes or activities to create a product or a system. EIO-LCA is economic input–output-based LCA. This was developed for the Green Design Initiative in Carnegie Mellon Univ. The model uses 498 $\times$ 498 economic input–output matrixes (commodity-by-commodity) of the US economy to identify the entire chain suppliers (both direct and indirect) to a commodity, thus setting the boundary of the materials extraction and the manufacturing stage assessment at the level of the national economy [1].

Studies show that the results of these two methods for a similar study varied sometimes even to the extent of turning contradictory. One of the main reasons for this is the system boundaries that are considered for these methods. SETAC-EPA model is used in many countries, unlike the other method. Use of this model is widely accepted since it is recognized as a standard procedure by the International Organization for Standardization. However, the method is typically limited by data availability, time, and cost (Zapata et al. 2005).

3 Asphalt Pavements

Asphalt pavement is the most widely used type of pavement because of its numerous advantages over the concrete pavement. Firstly, asphalt pavement is economic, laying, and maintenance of asphalt pavement is easier and it takes lesser landfill area due to its outstanding properties of recyclability. Flexibility is another important reason for its increased use. Not until recently, studies were conducted to determine the type of pavement that is more sustainable. Crucial need to save energy for the future and a growing concern for environment and ecology have made it necessary to conduct such studies and spread awareness.

Asphalt production is an energy-intensive process, which includes extraction, transportation, storage, heating, distillation, cooling, and final processing (Zapata et al. 2005). Distillation of petroleum is done at high pressure and temperature which requires an enormous amount of energy. In the asphalt concrete production plant, asphalt is stored in large containers which are constantly heated to ensure fluidity (Zapata et al. 2005). Aggregate made of this is also heated to higher temperatures before mixed with bitumen. The mixture is then stored in hot storage bins prior to transportation to construction sites.

4 Cement Concrete Pavements

Cement concrete pavements and reinforced cement concrete pavements are rigid pavement systems. Concrete being mixture of cement aggregate and water becomes energy-intensive mainly because of the use of cement which consumes a huge amount of energy during its manufacture. There are two methods of cement manufacture—wet process and dry process. The wet process was commonly used in the long past, but due to a high rate of fuel consumption, it has been replaced by the dry process. However, in some old cement manufacturing plants in developing countries, the wet process is still in use. As more amount of fuel is burnt in the wet process, emission rates are exorbitantly high compared to dry process. Reinforced concrete pavements require steel which is another energy-intensive material.

Table 1 Embodied energy and CO2 emission from ingredients of concrete

Ingredient	Embodied Energy (MJ/kg)	Carbon dioxide (CO_2/kg)
Cement	4.6	0.83
Aggregate	0.1	0.005
Water	0.20	0

According to the Inventory of Carbon and Energy (ICE-2008 University of Bath), the embodied energy and CO_2 emission from the primary ingredients used in concrete are shown in Table 1.

5 Discussion–Comparison of Asphalt and Reinforced Concrete Pavements

5.1 Embodied Energy

As mentioned earlier, assessment of the embodied energy lacks standard guidelines consequently projecting wide variations in the results obtained for similar studies. This makes comparison difficult. Although there exist only a handful of studies on this area, the majority of them conclude cement concrete pavement consumed more energy than asphalt pavements when same service life is assumed, yet in reality, the service life cannot be same for different types of pavements. In cement concrete pavement, the major energy consumption is due to cement. The other major factor that hits energy efficiency is steel used to reinforce concrete pavements, which is an energy-intensive material.

Energy consumed for the manufacture of bitumen is less compared to cement. In the asphalt pavement, the only energy-intensive material is bitumen. Asphalt pavement consumes a huge amount of energy during the mixing of asphalt concrete as it needs very high temperature. Preheating of its ingredients like aggregate before mixing is also an energy-intensive process. Unlike asphalt pavement, cement concrete pavement does not consume much energy in mixing. No significant energy is spent on its storage or other processes such as drying of aggregate prior to mixing. Energy requirement to transport raw materials of cement concrete pavement is also minimal when compared to fuel consumed by oil tankers to transport the crude oil. In spite of all these advantages of cement concrete pavement, it still accounts for high embodied energy because of its energy-intensive raw materials.

There are a few studies that suggest reinforced concrete pavement register lower energy consumption than asphalt pavement; however, the majority of the studies arrive at the contrary standpoint.

5.2 Carbon Dioxide Emission

Many of the studies support a finding that carbon dioxide emission associated with reinforced concrete pavement is higher than that of asphalt pavement. That is again because cement and steel, during their manufacture, release high volumes of outputs, undesirable on the perspective of environmental conservation, of which the carbon dioxide majors.

5.3 Service Life of Pavements

When we compare the types of pavements, one major factor that we would consider is their service life. It was found that continuously reinforced concrete has a longer service life in comparison with asphalt pavement, although some papers conclude conversely. Estimating the average service life of pavements is tedious as pavements solicit continuous maintenance activities and overlays. The average service life of asphalt pavement is 13–15 years and of reinforced concrete pavement is 20–25 years. Service life will exclusively depend on factors such as its use as national highway, state highway or rural roads, the material used for pavement, traffic, the temperature to which it is subjected to, rainfall, etc. So, using national averages for service life estimation is often problematic [1]. State and regional data on the expected design life of pavement would be more helpful than national data [1].

The energy consumption and carbon dioxide emission of these types of pavements become comparable when we consider the service life. Overall, environmental implication among the types of pavement will also depend on the average repair works that are needed for one pavement in comparison to the other.

5.4 Recyclability

Recyclability of pavements has a great impact on sustainability. Both asphalt and concrete pavements are recyclable but recycling of asphalt is simpler and economical. The popular methods of asphalt recycling are plant (hot-mix asphalt) recycling, cold in-place recycling, and hot in-place recycling. The most common method adopted is hot-mix plant recycling; the other method is used for low traffic roads. Asphalt pavement can be recycled many times over and reused. Long-term strength and durability statistical data of recycled asphalt pavement is yet to be explored. The high amount of moisture content in recycled aggregate would cause stability problems.

Concrete pavements also can be recycled, but not as economically as asphalt pavement. Concrete with reinforcement steel is difficult to recycle as removing the steel reinforcement requires a backhoe and manual labor. This increases the cost involved and would render it costlier than the virgin aggregate.

6 Conclusion

Only a handful of studies have ventured into this area which makes the comparison a whole bit difficult. A few papers are available to review and record diverse values for embodied energy and CO_2 releases. Their calculations have wide variation due to many reasons. One major reason for this irreconcilable variation is system boundary chosen for different studies. Another important factor is the methodology adopted. Similar studies with different methodology have yielded contrasting results. This highlights the need for standard guidelines for the calculation. As many attempts were not made in this area, for a more reliable comparison, the area necessitates further exploration. Use of recycled asphalt contributes to sustainability. Recycling of reinforced concrete pavement is a difficult process and would incur higher costs than asphalt pavement.

References

1. Horvath A (1998) Estimation of environmental implications of construction materials and designs using life cycle assessment techniques
2. Horvath A, Hendrickson CT, Lave LB, McMichael FC, Wu TS (1995) Toxic emissions indices for green design and inventory. Environ Sci Technol 29(2):86A–90A
3. Berthiaume R, Bouchard C (1999) Exergy analysis of the environmental impact of paving material manufacture. Trans Can Soc Mech Eng 23(1):187–196
4. Bloomquist D, Diamond G, Oden M, Ruth B, Tia M (1993) Engineering and environmental aspects of recycled materials for highway construction. Appendix 1. Final report, (No. PB-94–140977/XAB), Western Research Inst., Laramie, WY (United States), September 1992–June 1993
5. DOT U (1993) A study of the use of recycled paving material: report to congress. US Department of Transportation (US DOT) and Federal Highway Administration (FHWA), Report No. FHWA-RD-93–147
6. Love RM (1987) State DOT experiments with concrete pavement recycling. Public Works 118(6):83–85
7. Hendrickson C, Horvath A, Lave L, McMichael F (1996) Recycled materials markets for the transportation infrastructure. TR News
8. Valdés G, Pérez-Jiménez F, Miró R, Martínez A, Botella R (2011) Experimental study of recycled asphalt mixtures with high percentages of reclaimed asphalt pavement (RAP). Constr Build Mater 25(3):1289–1297
9. Ang BW, Fwa TF, Ng TT (1993) Analysis of process energy use of asphalt-mixing plants. Energy 18(7):769–777
10. Portland Cement Association and National Asphalt Pavement Association (PCA/NAPA) (1986) Asphalt vs concrete. American City Country 101(7): 30–38
11. Unruh B (2002) Delivered energy consumption projections by industry in the annual energy outlook 2002. Energy Information Administration, Washington, DC www.eia.doe.gov/oiaf/analysispaper/industry/consumption.html 31 March 2003

Life Cycle Energy Analysis of a 3.4 kWp Stand-Alone Rooftop Solar Photovoltaic System in Eastern India

Sonali Goel, Bibekananda Jena and Renu Sharma

Abstract Life cycle energy analysis is important for the estimation of greenhouse gas emission and global warming parameters. This paper presents the assessment of energy payback time (EPBT) and energy return on energy investment (EROI) of a 3.4 kWp solar photovoltaic (PV) system installed in the rooftop of ITER, Siksha "O" Anusandhan, Bhubaneswar, India. The photovoltaic system is analyzed to find its viability aspect to its cost economics and energy and to compare its performance with some previous work available in the literature. The energy analysis was carried out by embodied energy basis and the results of the installed stand-alone PV system were compared with an equivalent grid-connected PV system. The EPBT was found to be 4.61 and 3.78 years while the EROI was found to be 5.42 and 6.62 for stand-alone system and grid-connected system, respectively.

Keywords Solar · Energy payback time · Energy return on investment · Embodied energy

1 Introduction

Access to electricity is highly essential for economic and social development of a nation. Fossil fuel-based energy generation causes the release of harmful pollutants to the atmosphere that causes global warming. Planners and policy makers from all over the world are thinking seriously to reduce the causes of global warming

S. Goel (✉) · R. Sharma
Department of Electrical Engineering, Institute of Technical Education and Research, Siksha 'O' Anusandhan (Deemed to be University), Bhubaneswar, India
e-mail: sonali19881@gmail.com

R. Sharma
e-mail: renusharma@soa.ac.in

B. Jena
Department of Electrical and Electronics Engineering, Institute of Technical Education and Research, Siksha 'O' Anusandhan (Deemed to be University), Bhubaneswar, India
e-mail: masterbibekjena@gmail.com

G. Zhang et al. (eds.), *Advances in Energy and Built Environment*, Lecture Notes in Civil Engineering 36, https://doi.org/10.1007/978-981-13-7557-6_15

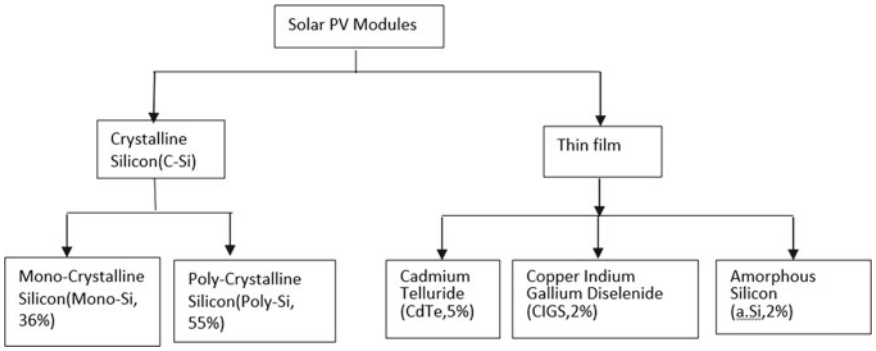

Fig. 1 Market share of module with various cell technology

to save humanity. Researchers are working all over the world to find alternative sources of energy that are cleaner and safer. Renewable energy sources such as solar photovoltaic, wind, biogas, hydro energy, and concentrating solar power are the safer and cleaner sources of energy and are the best alternatives nowadays adopted by different nations around the globe. These renewable energy sources can be harnessed to generate electricity in areas where grid connectivity is not possible due to their inaccessibility. The significant fall in the cost of solar modules since 2012 (i.e., 26% reduction of price in 2016) and an increase in solar cell efficiency encouraged entrepreneurs and individuals to set up solar PV system both for commercial and personal use [1, 2]. As the PV installations are growing around the globe, their performance studies in terms of energy production, energy payback time and life cycle energy analysis that are required to find its feasibility for the location. Energy analysis of any solar PV system is carried out to find its feasibility in terms of energy payback time (EPBT) and energy return on energy investment (ERoEI or simply EROI). EROI is the ratio of energy required to produce the components of the PV system including installation to the lifetime energy generation by the system. Hence, EROI has no unit. If the EROI value is lower than 1:1, then the energy system is considered as unsuitable and not viable. The minimum EROI should be 3:1 for a project to be viable one [3].

One 3.4 kWp stand-alone PV system has been installed on the rooftop of E-block, Electrical Engineering department of ITER, SOA, Bhubaneswar (Latitude: 20.24N, Longitude: 85.80E). Twelve number of polycrystalline silicon modules (Waree 280 Wp) having 14% efficiency are installed during February 2014. It is equipped with 24 numbers of VRLA batteries (2 V, 340 Ah) and one 3.5 kW inverter. The EPBT and EROI of this PV system have been computed to assess its feasibility in terms of energy. The embedded energy in PV modules is different for different types of modules. Most widely used PV modules are of polycrystalline silicon (55%) followed by monocrystalline silicon (36%) [4]. The market share of modules with various type of cell technologies are shown in Fig. 1.

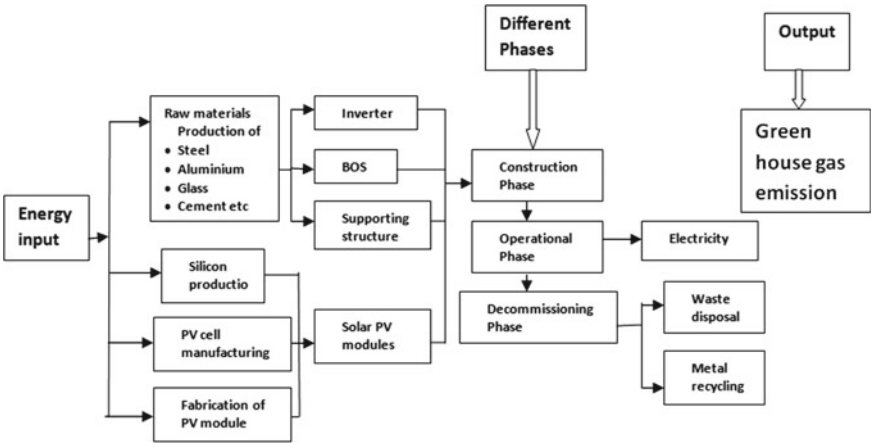

Fig. 2 Energy input in PV modules in various stages of its life cycle

In solar PV systems, the energy is consumed during the process of manufacturing of various components of PV system including solar modules, inverters, batteries, charge controller, and also for structural units required for installation and commissioning. The energy utilized for the manufacturing of all these units is called embedded energy. The energy inflow during the life cycle of a PV system is shown in Fig. 2.

2 Energy Payback Time

The energy payback time of a PV system is the ratio of the energy requirements for the manufacturing of PV modules including the balance of the system (BOS) components to its annual energy output. It is calculated by Peng et al. [5]

$$\text{EPBT} = \frac{E_{\text{input}} + E_{\text{BOS.}}}{E_{\text{output}}} \tag{1}$$

It is also given by Evans and Florschuetz [6]

$$\text{EPBT} = \frac{\text{Embedded energy}}{\text{Annual Energy output}} \tag{2}$$

where E_{input} = primary energy input in the PV module during its life cycle. It includes the energy requirements (MJ) during manufacturing of module, its transportation to the site of installation, its operation and maintenance, and lastly dismantling and disposing of the module and other garbage or scrap materials after the expiry of its life period. E_{BOS} is the energy requirement(MJ) for the balance of the system com-

ponents that includes a support structure, cables, electrical components, inverters, and batteries.

3 Embodied Energy

The embodied energy is the energy expenditure made during the course of the manufacturing of PV modules, BOS, structure components, transportation from production to installation site, and commissioning the structure. These are the inherent energy in the system. The time required by a system to repay this amount of spent energy is called EPBT and expressed in years. EPBT is considered as an indicator to measure the sustainability of a PV system [5]. The embodied energy for BOS is considered as 300 MJ/m^2 and aluminum frame installation as 400 MJ/m^2 while it is taken as 2300 MJ/m^2 for polycrystalline silicon PV module. Considering annual efficiency improvement of 1% for battery and inverters, the embodied energy decreases for subsequent replacement of these items [3]. The energy requirement of battery and inverters were calculated by using the following equation.

$$\text{Embodied energy of replaced component(battery, inverter etc)} = E(1-r)^n$$

where

E initial embodied energy in the component
r yearly rate of decrease in energy due to the enhancement of efficiency (decimal value)
n replacement year.

4 Energy Analysis

The embedded energy of PV module, BOS, frame structure, battery, and converter were estimated as per the previous literature [3] and are presented in Table 1. Though many literature are available on embedded energy of PV modules, BOS etc., these previous data may not be suitable for determining embedded energy in recent years because energy expenditure in manufacturing process is gradually decreasing over the years due to technological advancements. The material requirement for manufacturing of silicon cells has been reduced significantly during the last 12 years from 16 g/Wp to less than 6 g/Wp due to use of thinner wafers and increased inefficiencies [7]. So, energy spent in manufacturing solar modules in earlier days is gradually reducing due to the requirement of lesser quantity of materials and advanced manufacturing process. The data taken in this study are as per the latest available literature [3].

Table 1 Energy requirement of components of solar PV systems (Taken as per 2014 data)

PV module (Poly crystalline silicon modules)			
Process	Energy requirement (MJ/m^2 module)	Energy requirement (kWh/m^2)	Energy requirement for 3.4 kWp system (23.52 m^2) (kWh)
Frameless PV module	2300	638.88	15,026.4
Aluminum frame	400	111.11	2613.3
Additional components (BOS)	300	83.33	1959.9
Total module (installed)	3000	833.33	19,599.6
Inverter			
State	**Energy requirement (MJ/W power)**	**Energy requirement (kWh/W Power)**	**Energy requirement for 3.5 kW inverter (kWh)**
Inverter (initial)	1	0.278	973
Inverter (after 15 years)	0.86	0.239	836.78
Total inverter	1.86	0.517	1809.78
Batteries			
State	**Energy requirement (MJ/Ah storage)**	**Energy requirement (kWh/Ah storage)**	**Energy requirement for 340 Ah (kWh)**
Battery (initial)	11	3.058	1039.72
Battery (after 5 years)	10.46	2.91	989.4
Battery (after 10 years)	9.95	2.77	941.8
Battery (after 15 years)	9.46	2.62	890.8
Battery (after 20 years)	8.99	2.50	850.0
Total battery			4711.72

1 kWh = 3.6 MJ or 1 MJ = 0.278 kWh
Replacement period of battery: 5 years and replacement period of inverter: 15 years

Hence, total embodied energy for stand-alone system (with battery system)
= Energy requirement for PV system + energy requirement for inverter + energy requirement for battery system
= 19,599.6 + 1809.78 + 4711.72
= 26,121.1 kWh
Total embodied energy for grid-connected PV system(without battery system)
= Energy requirement for PV system + energy requirement for inverter
= 19,599.6 + 1809.78
= 21,409.38 kWh

A. **Total energy generation**

The measured annual average solar irradiance is 4.62 kWh/m^2/d. Considering the project life span of 25 years, the energy generation has been computed.

Annual energy generation by 3.4 kWp (actual 3.36 kWp) rooftop PV system is 3.36 kWp × 4.62 kWh/m^2/day × 365 days/year × 25 years = 141,650 kWh and energy generation per year is 5666 kWh.

B. **Estimation of energy payback time**

The energy payback time (EPBT) of an energy source is calculated by first determining the embedded energy (energy spent during the manufacturing process) of PV module, BOS, frame structure, battery, and converter. The embedded energy of various components of PV systems was estimated as per the previous literature [3] and is presented in Table 1

$$\text{Total embodied energy} = 26{,}121.1\ \text{kWh(with battery)for standalone system}$$
$$= 21{,}409.38\ \text{kWh(without battery)for grid connected system}$$

Hence,

$$\text{EPBT} = \text{Embodied energy}/\text{Annual generation}$$
$$= 26{,}121.1/5666 = 4.61\ \text{years(standalone system with battery storage)}$$
$$\text{and EPBT} = 21{,}409.38/5666 = 3.78\ \text{years for grid connected system}$$

The EPBT of the system was found to be 4.61 and 3.78 years for stand-alone and hypothetical equivalent grid-connected system, respectively. The EPBT of the present study for stand-alone system is lower than the EPBT found by earlier studies conducted in India by Nawaz and Tiwari [8] and Lamba et al. [9]. The EPBT, embedded energy, and type of cell technologies used by some researchers are presented in Table 2.

C. **Energy return on energy investment**

Energy return on energy investment (ERoEI) or simply energy return on investment (EROI) is the ratio of lifetime energy output to the embedded energy of the system and is given by Bhandari et al. [4]

Table 2 Embedded energy and EPBT of PV systems

Author	Location of study	System size (kWp)	Solar cell type	Embedded energy (MJ/m^2)				Life (years)	EPBT (years)
				Module	Frame	BOS	Total		
Nawaz and Tiwari 2006 [8]	IIT Delhi, India	1.2	c–Si	–	–	–	4968	–	13–26
Lamba et al. 2014 [9]	IIT, New Delhi, India	1	a–Si	–	–	–	3400	20	11.38
Kannan et al. 2006 [10]	Singapore	2.7	mc–Si	–	–	–	2.2 MJ/kWh	25	6.74
Alsema et al. 2000 [11]	Nether land	–	pc–Si	3700	400	500	4600	–	2.5–3.0
		–	a–Si	800	400	400	1600	–	
Abbes et al. 2014 [3]		–	pc–Si	2300	400	300	3000	–	
Kato et al. 1997 [12]	Japan	–	c–Si	–	–	–	4160–15,520	–	15.5

$$\text{EROI} = \frac{\text{Life time energy output}}{\text{Embedded energy}}$$
$$= \frac{\text{Annual energy output}(\text{MJ/m}^2/\text{year}) \times \text{lifetime}(\text{years})}{\text{Annual energy generated by the system}(\text{MJ/m}^2) \times \text{EPBT}(\text{Years})}$$
$$= \frac{\text{Lifetime}(\text{years})}{\text{EPBT}}$$

EROI is an important parameter to represent the energy performance of any power generating system. For long-term viability study of any energy source, EROI is a better term to consider than EPBT.

D. **Determination of EROI**

The EROI of the stand-alone system = 141,650 kWh/26,121.1kWh = 5.42:1 and EROI for grid-connected system = 141,650 kWh/21,409.38 kWh = 6.62:1.

As the EROI of the systems are greater than 3:1, both the stand-alone system and hypothetical grid-connected PV system are viable on energy point of view.

5 Conclusion

Energy analysis of a 3.4 kWp stand-alone rooftop PV system installed in SOA, Bhubaneswar, India was carried out. The salient findings are summarized below

- The energy payback time of the PV system was found to be 4.61 years and 3.78 years for stand-alone and hypothetical grid-connected PV system, respectively.
- EROI was found to be 5.42:1 and 6.62:1 for the stand-alone system and grid-connected system, respectively.
- As the EROI of the systems are greater than 3:1, both the stand-alone systems and grid-connected PV system are viable on energy point of view.

Acknowledgements The authors are highly indebted to Dr. N. D. Kaushika, Research Professor, ITER for his valuable suggestions and guidance for preparation of the manuscript.

References

1. Padmanathan K, Govindarajan U, Ramachandaramurthy VK, Selvi TSO (2017) Multiple criteria decision making (MCDM) based economic analysis of solar PV system with respect to performance investigation for Indian market. Sustainability 9(5):820
2. Padmanathan K, Govindarajan U, Ramachandaramurthy VK, Selvi TSO (2017) Multiple criteria decision making (MCDM) based economic analysis of solar PV system with respect to performance investigation for Indian market. Sustainability 9(5):820 (Supplementary material)

3. Abbes D, Martinez A, Champenois G (2014) Life cycle cost, embodied energy and loss of power supply probability for the optimal design of hybrid power systems. Math Comput Simul 98:46–62
4. Bhandari KP, Collier JM, Ellingson RJ, Apul DS (2015) Energy payback time (EPBT) and energy return on energy invested (EROI) of solar photovoltaic systems: a systematic review and meta-analysis. Renew Sustain Energy Rev 47:133–141
5. Peng J, Lu L, Yang H (2013) Review on life cycle assessment of energy payback and greenhouse gas emission of solar photovoltaic systems. Renew Sustain Energy Rev 19:255–274
6. Evans DL, Florschuetz LW (1977) Cost studies on terrestrial photovoltaic power systems with sunlight concentration. Sol Energy 19(3):255–262
7. Photovoltaics Report (2017) Fruanhofer ISE (https://community.innoenergy.com/docs/DOC-3458-photovoltaics-report-2017-fruanhofer-isepdf)
8. Nawaz I, Tiwari GN (2006) Embodied energy analysis of photovoltaic (PV) system based on macro-and micro-level. Energy Policy 34(17):3144–3152
9. Lamba R, Gour A, Tiwari GR (2014) Life cycle cost assessment and enviro-economic analysis of thin film amorphous silicon photovoltaic system. Fundam Renew Energy Appl 4(2)
10. Kannan R, Leong KC, Osman R, Ho HK, Tso CP (2006) Life cycle assessment study of solar PV systems: an example of a 2.7 kWp distributed solar PV system in Singapore. Solar energy 80(5):555–563
11. Alsema EA, Nieuwlaar E (2000) Energy viability of photovoltaic systems. Energy policy 28(14):999–1010
12. Kato K, Murata A, Sakuta K (1997) An evaluation on the life cycle of photovoltaic energy system considering production energy of off-grade silicon. Sol Energy Mater Sol Cells 47(1–4):95–100

Carbon Balance and Emission Factor for the Cookstoves

Harshika Kumari

Abstract The main upshots from the fuel are heat and emissions. The aim is to get high thermal energy with low emission factors. The carbon balance and CO_2 mitigation study have an important decision to play in energy planning. In this context, it is necessary to understand how the bioenergy can help in mitigation by considering its potential for carbon emission reduction and sequestration.

Keywords Biomass · Cookstoves · Carbon balance · Greenhouse gas · PIC

1 Introduction

Biomass is a carbon-neutral-renewable fuel. We can recapture the amount of carbon emitted from the biomass fuel during combustion by proper harvesting of the biomass. Therefore, carbon emission from the combustion of biomass does not result in net increment of global carbon built up. Nevertheless, there is a new problem associated with the combustion of biomass fuels. Apart from emission of carbon dioxide (CO_2) which is captured during the photosynthesis process of the plants, the products of incomplete combustion (PIC) are also released into the atmosphere during the combustion of the biomass fuels [1, 2]. PICs are harmful to human health and results in further decrease in the efficiency and wastage of the fuels [3, 4]. The PICs are even more powerful GHGs than CO_2 in terms of per gram carbon emitted by them [5]. According to Smith et al. [6], an estimate of the global warming potential (GWP) of non-CO_2 greenhouse gases (GHGs), such as CO, CH_4, and non-methane hydrocarbons, could be in the range of 20–110% of as much as that of CO_2 itself, depending on the time perspective [6]. This means that when a large million tons of biomass fuel is combusted then there will be no net emission of CO_2 as it comes from sustainable harvesting but PICs will still account for a significant contribution to the GWP. At the global level, the overall contribution of CO_2 emissions from biomass

H. Kumari (✉)
Northern India Engineering College, New Delhi, India
e-mail: harshikaiitd@yahoo.co.in; harshika@niecdelhi.ac.in

G. Zhang et al. (eds.), *Advances in Energy and Built Environment*, Lecture Notes in Civil Engineering 36, https://doi.org/10.1007/978-981-13-7557-6_16

cookstoves to global warming was estimated to be about 2% [7]. Thus, it can be seen that the combustion of biomass fuels plays an important role in the global carbon cycle [8, 9].

2 Carbon Balances and Absolute Emission Factors of the Cookstoves

Due to above-said issues, it is important to evaluate the emission factors from the various biomass cookstoves. The number of studies has been carried out for both developed and developing countries to understand the linkage between the energy efficiency of the cookstoves, health exposure to the emissions from the cookstoves, and global warming effect. There has been fewer research on the small-scale burning of biomass fuels, and most of the literature available is on the studies of large-scale combustion of biomass like Savannah burning and forest fires [10]. However, some researchers have studied the emissions from the cookstoves by monitoring the burning of biomass fuels [11, 12].

The carbon balance equations were constructed for various fuels and cookstoves. The emission ratios required for LPG, kerosene, acacia, mustard, and cowdung cakes for constructing the carbon balance equations were obtained experimentally from the standard international method called water boiling test (WBT). WBT was performed systematically for the different fuels and cookstoves in a simulated kitchen [13, 14]. The emission from solid biomass fuels was not constant but vary with time during the burning process. Therefore, integrated sampling was required to obtain the data that can cover the complete burn cycle from the first start of fuel combustion to the last fire extinction. This represented the real burning situation of fuels and cookstoves [15]. The emission ratios obtained by WBT are summarized in Table 1.

Table 1 Emission from different fuels and cookstoves

Fuels	CO_2 (ppm)	CO_2 (mg/m^3)	CO (ppm)	CO (mg/m^3)	N_2O (ppm)	N_2O (mg/m^3)	TSP (mg/m^3)
LPG stove	2300	4139.06	9	10.30	0.362	0.592	0.21
Kerosene wick stove	2800	5038.85	42	48.10	0.354	0.579	0.54
Acacia/traditional cookstove	4300	7738.24	145	166.05	0.02	0.033	0.71
Mustard/traditional cookstove	6100	10,977.50	225	257.67	0.02	0.033	5.27
Cowdung cake/traditional cookstove	2100	3779.14	374	428.30	0.03	0.049	6.64

Table 2 Carbon content and emission ratios for various fuels and cookstoves

Fuels	Carbon content in fuel (%)	CO_2 (mg/m^3)	CO (mg/m^3)	N_2O (mg/m^3)	TSP (mg/m^3)	$E = CO + N_2O + TSP$	$K = \frac{E}{CO_2}$
LPG stove	86.0	4139.06	10.30	0.592	0.21	11.102	0.002
Kerosene wick stove	85.0	5038.85	48.10	0.579	0.54	49.219	0.009
Acacia/traditional cookstove	50.0	7738.24	166.05	0.033	0.71	166.793	0.021
Mustard/traditional cookstove	43.0	10,977.50	257.67	0.033	5.27	262.973	0.024
Cowdung cake/traditional cookstove	33.0	3779.14		0.049	6.64	434.989	0.115

The emission ratios obtained in Table 1 were used to construct carbon balance equation with the following assumptions:

- The samples took for the calculations were the real representations of the emission ratios of the WBT.
- The carbon source in the experiment was the cooking fuel only.
- The fraction of carbon that was not monitored during the experiment was less than 1% and was considered negligible in the study.
- The carbon content of the cooking fuels obtained by ultimate analysis was in close approximation with the reported literature. There was 50% carbon in wood, 86% carbon in kerosene, and 87% carbon in LPG [16, 17].

Therefore, the carbon content was taken as negligible in the unmeasured flows of the experiment that includes aerosol (TSP) and char. This assumption has been proved correct, as the aerosol emission factor is less than 5 g/kg [16]. The ash obtained from the solid fuels was a common source of error in the experiment. The previous experiments and reported data said that there was approximately 2% of fuel carbon present in the char of the fuelwood. LPG and kerosene produce no ash or char [18, 19]. The fuels and cookstoves emission factors under the above assumption were calculated for which ash-to-CO_2 carbon ratio was assumed as zero. Based on Table 2 the carbon balance equation has been designed [20].

$$CB = CO_2 + CO + N_2O + TSP \tag{1}$$

where CB is fuel carbon

CO is carbon monoxide
N_2O is nitrogen dioxide
TSP is total suspended particulates

Table 3 Emission factors for different fuels and cookstoves

Fuels	CO_2 (gm/kg fuel)	CO (gm/kg fuel)	N_2O (gm/kg fuel)
LPG stove	3147.049	4.984	0.410
Kerosene wick stove	3088.870	18.764	0.323
Acacia/traditional cookstove	1795.625	24.519	0.006
Mustard/traditional cookstove	1539.713	22.997	0.004
Cowdung cake/traditional cookstove	1085.201	78.265	0.015

or

$$1 = \mathrm{CB}/\mathrm{CO}_2 - K \tag{2}$$

where

$$K = (\mathrm{CO} + \mathrm{N}_2\mathrm{O} + \mathrm{TSP})/\mathrm{CO}_2 \tag{3}$$

K is known as the absolute CO_2 emission factor, shown in Table 2.

The emission factors can now be calculated using Eq. 3 and Table 2. The solved emission factors for all fuels and pollutants are shown in Table 3. The CO emission factor for dung cake is highest followed by acacia and mustard. The CO emission factor is minimum for LPG. It is well within the range (100 g/kg) as reported for CO emissions measured by Smith [16]. Smith reported the CO emission within the range of 17–130 g/kg for wood-fired cookstove. Crutzen and Andreae [8] and Ward and Hardy [21] have carried out the similar study. The CO emission factor from kerosene stove is found to be 18 g/kg, which is approximately same as that measured by TERI [22] for wick stoves, and it is much higher than kerosene-radiant-heating stoves and CO emission factor as 2.8 g/kg.

Table 3 has been further used to derive carbon cycle which is shown in next Figs. 1, 2, 3, 4, and 5. The fate of one kilogram of fuel with its fixed carbon content is evaluated. In addition, the global warming potentials (GWPs) are taken into consideration for the calculation of CO_2 equivalent. Ultimately all the products of incomplete combustion convert into carbon dioxide in the atmosphere. Ash and aerosol have not been measured in this study.

2.1 Energy

For the analysis of energy content of the fuel in the carbon cycle, PICs released during the experiment has to be put in the terms of its CO_2 equivalent. We can conclude from Fig. 3 that 4% of fuelwood energy is released as PICs and they have

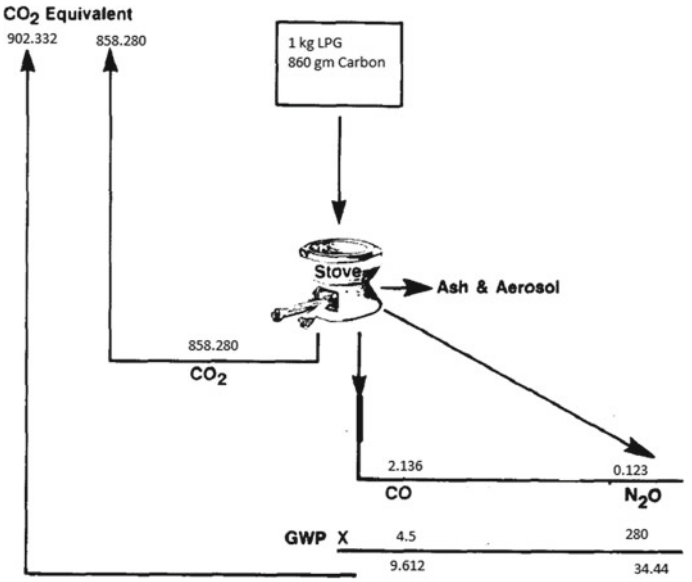

Fig. 1 Carbon balance cycle for LPG cookstove

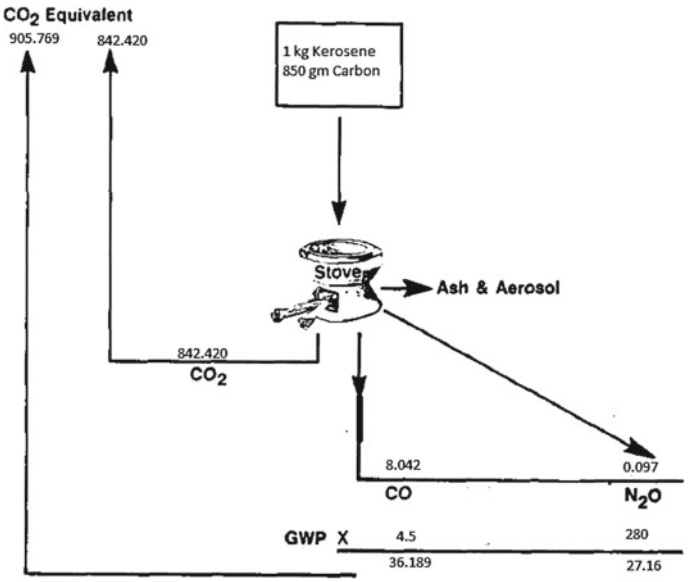

Fig. 2 Carbon balance cycle for Kerosene cookstove

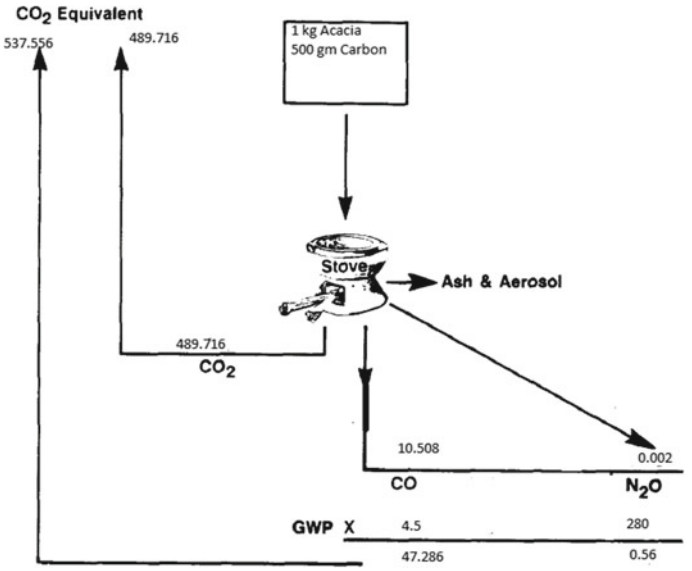

Fig. 3 Carbon balance cycle for Acacia in traditional cookstove

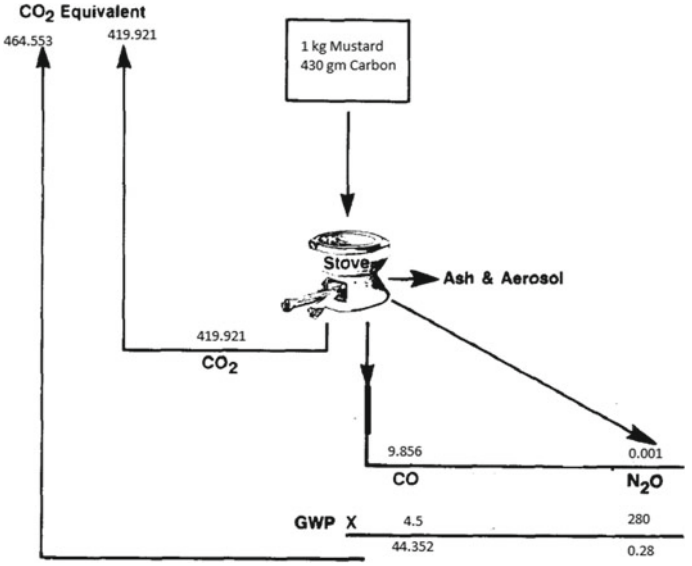

Fig. 4 Carbon balance cycle for Mustard in traditional cookstove

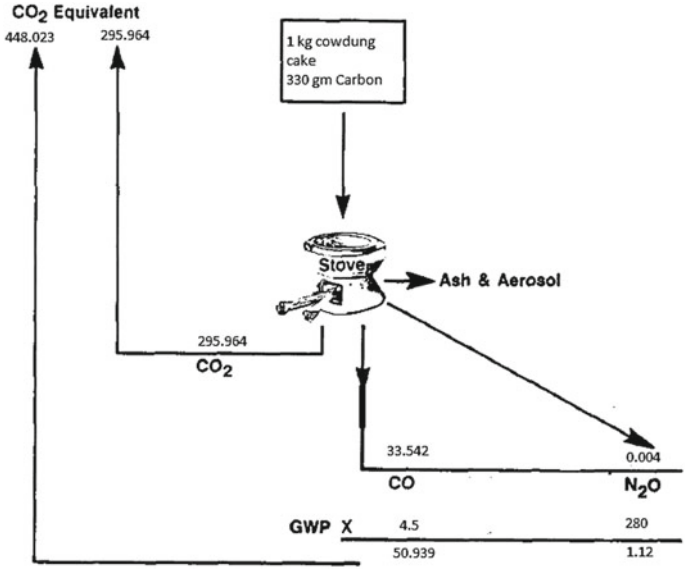

Fig. 5 Carbon balance cycle for Cowdung cake in traditional cookstove

a combustion efficiency of 96%. In comparison with cookstove of approximately 100% combustion efficiency, the traditional cookstove will require about 10% more fuel. Similar result has been acquired from Figs. 4 and 5. The PICs contain about 10% of the energy originally in the mustard and dungcake fuels resulting in about 11% more fuel consumption. The combustion efficiency is about 90% for the mustard and cowdung cakes in the traditional cookstove in comparison with an ideal cookstove of 100% combustion efficiency. Therefore, inefficient traditional cookstove requires more fuel for the same task. The other technical reason for low efficiency of the cookstove is its low heat transfer efficiency.

2.2 Global Warming

The PICs in terms of GHG potential have been shown from Figs. 1, 2, 3, 4, and 5. Since the greenhouse gases have different atmospheric lifetimes, the GWP depends on the time horizon. The CO_2 equivalent has been calculated for all the GHGs. Since the GWP is drawn based on the CO_2 equivalent, the emissions from the cookstoves gives only a rough picture of their global warming implications and improvements. The combustion efficiency seems to be in larger reductions in total GWP.

For all the biomass cookstoves, carbon monoxide emission factors are in the same range as estimated by Ahuja [7], and it was estimated that the overall contribution of biomass cookstoves to the global warming is 2%. Around 1/8th of the deforestation

and 1.5% of net human CO_2 addition to the atmosphere that is equivalent to 1.1% of total global warming are reported to be from inefficient biomass cookstoves and PICs released from them.

2.3 Control Measures

To reduce the PICs emitted from the biomass cookstoves, we have to reduce the fraction of carbon present in the PICs and reduce the amount of fuel consumed during the burn cycle. With the reduction in the use of fuel, the amount of fuel combusted will be less and the amount of carbon dioxide equivalent released to the atmosphere will also be less. To obtain a decrease in PICs, the quality of fuel has to be improved along with the design of more efficient cookstove.

For reducing the GHG's emission from the cookstoves into the atmosphere, there is a need for a strong and encouraging energy policy to make people switch to cleaner fuels and efficient cookstoves. This will make them move up in the energy ladder and reduce the health-damaging pollutants emission into the atmosphere [23, 24]. Switching from biomass to cleaner fuels like kerosene and LPG will also reduce the GWP and PICs into the environment as the energy content per carbon atom is high in them. Therefore, kerosene and LPG cookstoves which are more efficient and whose combustion lead to less PICs should be promoted and provided with more incentives.

3 Conclusions

Biomass, which is renewably harvested and considers as net zero carbon balance cycle, does not give net zero GHG. The greenhouse impact is high as the PICs released during the combustion of biomass fuel have high GWP. Therefore, to get a real picture of GHGs emitted from the cookstoves, we need to add two factors to our analysis, that is, we need to add the renewability factor along with the combustion efficiency or PICs. When the combustion efficiency of the biomass cookstove is low, it emits high PICs and that makes the biomass a dirty fuel with low position in the energy ladder. Improving combustion efficiency should be the main target of the researchers and policy makers. In addition, more measurements and analysis are needed to understand the various combustion devices available in the market. The improvement in the combustion efficiency of the biomass cookstoves will ultimately result in reduction in fuel consumption, reduction in the time and exposure to the health-damaging indoor air pollutants and finally reduction in the GHGs.

References

1. Li XH, Duan L, Wang SX et al (2007) Emission characteristics of particle matter from rural household biofuel combustion in China. Energy Fuels 21:845–851
2. Liu Y, Shao M, Fu LL, Lu SH, Zeng LM, Tang DG (2008) Source profiles of volatile organic compounds (VOCs) measured in China: part 1. Atmos Environ 42:6247–6260
3. Baldwin S (1987) Biomass stoves. Volunteers in Technical Assistance, with Princeton University, Arlington, VA
4. Baldwin SF (1987) Biomass stoves: engineering design, development, and dissemination. Volunteers in Technical Assistance (VITA), Virginia, USA, p 287
5. WHO (2006) Fuel for life: household energy and health. Oxford University Press, Geneva
6. Smith KR, Rasmussen RA, Manegdeg F, Apte M (1992) Greenhouse gases from small-scale combustion in developing countries, EPA-600-R-92-005. Office, Washington, DC
7. Ahuja DR (1990) Research needs for improving biofuel burning cookstove technologies. Nat Resour Forum 14:125–134
8. Crutzen RJ, Andreae MO (1990) Biomass burning in the tropics: impact on atmospheric chemistry and biochemical cycles. Science 250:1169–1178
9. Lee CM, Chandler C, Lazarus M, Johnson FX (2012) Assessing the climate impacts of cookstove projects: issues in emissions accounting. In: Working paper 2013-01. Stockholm Environment Institute, Stockholm, Sweden
10. Venkataraman C, Habib G, Eiguren-Fernandez A, Miguel AH, Friedlander SK (2005) Residential biofuels in South Asia: carbonaceous aerosol emissions and climate impacts. Science 307:1454–1456
11. Smith KR, Uma R, Kishore VVN, Lata K, Madne S, Rao G, Zhang J, Rasmussen RA, Khalil MAK, Thorneloe SA (2003) Greenhouse gases from small-scale combustion devices in developing countries. Phase IIa: household stoves in India. U.S. EPA, Office of Research and Development, Washington, DC
12. Smith KR, Ahuja DR (1990) Toward a greenhouse equivalence index: the total exposure analogy. Clim Change 17:1–7
13. Bailis R, Ogle D, MacCarty N, Still D, Smith KR, Edwards R (2007) The water boiling test (WBT) version 3.0. Shell Foundation, Household Energy and Health Programme 2003, revised, London
14. Smith KR, Uma R, Kishore VVN, Zhang J, Joshi V, Khalil MAK (2000) Greenhouse implications of household stoves: an analysis for India. Annu Rev Energy Environ 25:741–763
15. VITA (1985) Testing the efficiency of wood burning cookstoves. 1815N. Lynn Street, Suite 200, Arlington 22209 USA
16. Smith KR (1987) Biofuels, air pollution, and health. Plenum, New York
17. Zhu SL (2004) Study on emission factors of GHG and pollutants from rural stoves in developing countries. Renew Energy 2:16–19
18. Kumari H, Chandra A, Kaushik SC (2014) Comparative study on emissions from traditional and improved biomass cookstoves used in India. IJRASET 2:249–257
19. Kandpal JB, Maheshwari RC, Kandpal TC (1994) Air pollution from biomass combustion in domestic cookstove. Renew Energy 4:545–549
20. Ward DE, Nelson RM, Adams DF (1979) Forest fire smoke plume documentation. In: 72nd Annual meeting of the air pollution control association, Cincinnati, Ohio
21. Ward DE, Hardy CC (1991) Smoke emissions from wildlife fires. Environ Int 17:117–134
22. TERI (1995) Environmental considerations and options in managing India's long term energy strategy. Submitted to the United Nations Environment Programme, RISO Centre, Denmark. Tata Energy Research Institute, New Delhi
23. Smith KR, Khalil A, Rasmussen RA et al (1993) Greenhouse gases from biomass and fossil fuel stoves in developing countries: a Manila pilot study. Chemosphere 26:479–505
24. Smith KR, Dutta K (2011) Cooking with gas, editorial. Energy Sustainable Dev 15:115–116

Greywater Recycle and Reuse for Domestic and Irrigation Purposes

Rosysmita Bikram Singh, J. Sai Priya, K. Amrutha Varshini and S. Praneeth Kumar

Abstract Water scarcity has been regarded as an emerging issue since years around the world. According to the reports, it is found that India may end up with 50% water deficiency by the year 2030. This issue has motivated the treatment of grey water, which can be an alternative source for different purposes such as irrigation and toilet flushing. The paper presents the typical characteristics, the finest design of laboratory scale grey water treatment which comprises of natural and physical operation such as primary settling of heavy particles with the help of vermicompost, charcoal, coarse aggregates and fine aggregates (sand) and existing regulations for grey water treatment and reuse. The overall performance of the treatment plant produced a very improved quality of grey water, whose values found to be in the limits recommended for domestic and irrigation purposes. The treatment plant was found to be cost-effective and easily operated manually. The treated water can be used for gardening, flushing toilets, car washing, fire fighting, industrial purposes, etc.

Keywords Grey water · Vermicompost · Treatment · Primary settling

1 Introduction

Water is proceeding to be ranked as the 'limited resource' around the globe. It has become very much essential to minimize the use of groundwater and surface water in all sectors of consumption and choose an alternative source for the reuse of domestic

R. B. Singh (✉) · J. Sai Priya · K. Amrutha Varshini · S. Praneeth Kumar
Department of Civil Engineering, MGIT, Hyderabad, India
e-mail: puja00003@gmail.com

J. Sai Priya
e-mail: saipriya32542@gmail.com

K. Amrutha Varshini
e-mail: amruthakav97@gmail.com

S. Praneeth Kumar
e-mail: praneeth12kumar@gmail.com

G. Zhang et al. (eds.), *Advances in Energy and Built Environment*, Lecture Notes in Civil Engineering 36, https://doi.org/10.1007/978-981-13-7557-6_17

water. These alternative sources comprised of rainwater and grey water. Grey water is generally defined as the water generated from laundry, kitchen and bathroom. The increased urbanization and industrialization have raised the opportunity of reusing the grey water. It is observed on daily basis that our paramount need for water for our domestic activity is for 'gardening' and 'toilet flushing'. Mostly about 65% of the total water need is to be used to satisfy these activities. The water quality for these activities is not to be essentially potable, so it can be recycled upto some extent. If the grey water is recycled properly, we can save approximately 70:1 of potable water per person per day in the domestic household.

Grey water generally contains some traces of excreta, which is not free from pathogens and it also depend upon the living standard of people (personal hygiene, detergents used, kitchen waste, water from floor cleaning).

2 Methodology

A very major part of grey water is always allowed to flow into the stream without prior treatment in many of the urban and rural residential areas. Direct discharge of grey water is generally extracted from bathroom, kitchen, laundry, etc. which has caused environment concern in recent decades. The grey water should be treated in a environmentally friendly method to save the public environment and health pollution. The treatment was carried out using closed container and the set up was kept unexposed to sunlight.

2.1 Materials and Samples

1. Vermicompost
2. Charcoal
3. Coase aggregate
4. Fine aggregate (sand)
5. Wire mesh.

2.2 Grey water Sampling

Grey water samples were collected from the pipes of a single house in Hyderabad. Sampling of grey water was done in the morning. The following parameters were analysed for the samples taken:

1. Total dissolved solids (TDS)
2. Chemical oxygen demand (COD)

3. Ammonia nitrogen (AN)
4. pH
5. Turbidity
6. Total phosphorous
7. Nitrogen
8. Dissolved oxygen
9. Sulphates
10. Residual chlorine.

All the above parameters were measured by using the SMART spectrophotometer, a USEPA approved method.

2.3 Filter Media Establishment

The filter media was established in a 20 l container. The gravity concept was used for the set up of the filter. The filter consists of two parts: (i) pre-treatment and (ii) vermicompost + charcoal filter process.

2.4 Pre-treatment Process

It is a combination of gravel and sand layer. The screening process is the primary treatment, which is covered by layers of gravel at the top (helps in removing the suspended solids and particles). The second layer is covered in the bottom of the filter media by sand (sand imparts holding back the coagulum) (Fig. 1).

2.5 Secondary Treatment Process

Vermifilters consist of three layers which are vermicompost, charcoal and gravel. The vermicompost is filled up to 5 kg, charcoal 2 kg and gravel up to 5 kg. Charcoal is used to remove the colour and odour of grey water. Charcoal filters can also remove the micropollutants. Gravel acts as a basement to support the overall filter system. The vermifilter is allowed to reach up to the saturation level, in order to allow grey water passage. Wire mesh is used for separation of layers and to avoid vermicompost taking down during the filtration process. The vermicompost layer helps in the removal of BOD, COD, phosphates nitrates, etc. (Fig. 2).

Fig. 1 Screening filter

2.6 Equipments Used to Test the Samples

2.6.1 SMART Spectro 2 Spectrophotometer

The spectrophotometer is used for the quantitative analysis of molecules. The following instrument is used for the experiment (Fig. 3).

2.7 Sample Collection

Three number of samples were collected from one household are floor cleaned water sample, kitchen waste sample, laundry sample of one litre each and the fourth sample is a uniform mixture of the above three samples.

2.7.1 Sampling

- Floor cleaned water
- Kitchen waste water

Fig. 2 Secondary filter

- Laundry waste water
- Mixed water (a mixture of floor, kitchen and laundry water).

2.8 Sample Data Before Treatment

See Table 1.

3 Results and Discussion

The samples after treatment when tested for its characteristics are within the standard limits prescribed by WHO, FAO and EPA. The total period of treatment is 15 min for the primary phase and another 15 min for the secondary phase (Table 2).

Fig. 3 Smart spectrophotometer

Table 1 Sample data before treatment

Sl. No.	Parameter	Unit	Before treatment			
			Sample 1	Sample 2	Sample 3	Sample 4
1	TDS	mg/l	200	637	640	526.5
2	Turbidity	NTU	32	59	62	74
3	Ammonia nitrogen	mg/l	0.45	0.88	0.9	1.01
4	COD	mg/l	266	380	344	320
5	BOD_5	mg/l	51	96	63	54
6	Nitrogen	mg/l	12	25	24	18
7	Phosphorous	mg/l	0.35	0.4	0.59	0.94
8	Residual chlorine	mg/l	0.36	0.71	0.8	1.03
9	pH	–	6.5	6.7	6.8	6.1
10	Hardness	mg/l	18	–	49	65
11	Sulphate	mg/l	13	19	18	22

3.1 Characteristics of Treated Grey Water

See Table 3.

Table 2 Guidelines for treated greywater quality—for recycling of grey water for toilet flushing, general washing and irrigation

Sl. No.	Parameters	Unit	Permissible limit
1	Odour	–	Non-offensive
2	Total dissolved solids	mg/l	<450
3	Turbidity	NTU	≤10
4	pH	–	6–9
5	Residual chlorine	mg/l	≤1
6	Biological oxygen demand (BOD_5) at 20 °C	mg/l	<30
7	Chemical oxygen demand (COD)	mg/l	<250
8	Nitrogen	mg/l	≤5
9	Ammonia nitrogen	mg/l	≤1
10	Total phosphorous	mg/l	≤0.05
11	Sulphates	mg/l	10
12	Hardness	mg/l	<50

Table 3 Characteristics of treated grey water

Sl. No.	Parameter	After treatment				Removal efficiency
		1	2	3	4	
1	TDS	154 mg/l	10.15 mg/l	587 mg/l	331 mg/l	37.132
2	Turbidity	14 NTU	15 NTU	18 NTU	10 NTU	86.48
3	Ammonia nitrogen	0.19 ppm	0.09 ppm	0.25 ppm	0.18 ppm	82.178
4	COD	161 mg/l	37 mg/l	117 mg/l	105 mg/l	67.2
5	BOD_5	27 mg/l	33 mg/l	21 mg/l	15 mg/l	72.22
6	Nitrogen	5 mg/l	3 mg/l	6 mg/l	5 mg/l	72.22
7	Phosphorous	0.15 mg/l	0.27 mg/l	0.12 mg/l	0.02 mg/l	97.87
8	Residual chlorine	0.25 ppm	0.14 ppm	0.24 ppm	0.23 ppm	77.66
9	pH	6.4	6.3	6.4	6.4	
10	Hardness	9 ppm	42 ppm	5 ppm	11 ppm	83.077
11	Sulphate	8 ppm	6 ppm	9 ppm	6 ppm	72.72

4 Conclusion

The treatment plant overall produced very good results with improved quality, whose values lie between permissible limits. The treatment system found to be very much cost-effective and can be handled manually. The treated water can be used for flushing and gardening purpose. The mixture sample can be used for car washing. The samples other than kitchen sample can be used for gardening. The laundry sample can be used for industrial use. All the samples can also be used for dampening of dusty roads. From the review of past records, it is also concluded that the Vermifilters are also effective and an eco-friendly technology, which consists of the activities of earthworms and adsorption of materials like sand, soil and gravel particles.

Bibliography

1. Ghrair AM (2011) grey water filtration systems for a sustainable water culture
2. Suman K, Bharat R, Harish P (2013) Intelligent grey water management system—new approach to use grey water efficiently
3. Albalawneh A, Chang T-K (2012) Review of the grey water and proposed grey water recycling scheme for agricultural irrigation reuses. Int J Res Granthaalayah 3(12):16–35
4. Sahu P, Raut S, Mane S (2015) Treatment of grey and small scale industry waste water with the help of Vermi-filter. Civ Eng Urban Plann: Int J (CiVEJ) 2(1):29–35
5. Shegokar VV, Ramteke DS, Meshram PU (2015) Design and treatability studies of low cost grey water treatment with respect to recycle and reuse in rural areas. Int J Curr Microbiol Appl Sci 4(8):113–124. ISSN: 2319-7706
6. Singh SP, Ali N, Dr. Ahmad S, Singh JK, Kumar M (2015) A study on grey water treatment processes: a review. Int J for Sci Res Dev 3(8). ISSN: 2321-0613

Evaluation of Natural Ventilation Potential for Indoor Thermal Comfort in a Low-Rise Building in Arid and Semi-arid Climates of India

K. N. Patil, S. C. Kaushik and Ayush Aggarwal

Abstract Natural ventilation potential (NVP) has been evaluated for two climate-specific Indian cities New Delhi and Jodhpur in terms of pressure difference Pascal hour (PDPH), under various indoor conditions. Indoor temperature, indoor heat gain, and natural ventilation rate because of both buoyancy and wind effect have been evaluated for a conceptualized low-rise building using an analytical model for NVP. Thermal comfort in these stations has been evaluated in terms of percentage of time the indoor temperature falls within the thermal comfort zone. Qualitative assessment of NVP has been carried out through the cumulative frequency curves for adequate pressure variation throughout the indoor and outdoor environment of the building. The thermal comfort assessment shows that New Delhi and Jodhpur have indoor thermal comfort for 40% of the time in a typical year. Thermal comfort is found to exist for 45–90% of the time during the months of July, August, and September, whereas least thermal comfort period of 20–40% is observed during winter months of December, January, and February and PDPH curves confirms the fact that natural ventilation alone does not provide indoor thermal comfort. To achieve thermal comfort in the building during the rest of the time, an active system or complex passive systems are required to be employed.

Keywords Climatic potential · Natural ventilation potential · Pressure difference—Pascal hours · Thermal comfort assessment

K. N. Patil (✉)
SDM College of Engineering and Technology, Dharwad 580002, Karnataka State, India
e-mail: kalmeshnp@gmail.com

S. C. Kaushik
Centre for Energy Studies, Indian Institute of Technology Delhi,
Hauz Khas, New Delhi 110016, India
e-mail: kaushik@ces.iitd.ac.in

A. Aggarwal
Department of Computer Science, Vellore Institute of Technology, Vellore,
Tamilnadu State, India

G. Zhang et al. (eds.), *Advances in Energy and Built Environment*, Lecture Notes in Civil Engineering 36, https://doi.org/10.1007/978-981-13-7557-6_18

Nomenclature

A_f	Floor area (m^2)
A_n	Area of north wall (m^2)
A_s	Area of south wall (m^2)
A_t	Total wall area (m^2)
A_w	Area of wall (m^2)
C_d	Coefficient of discharge
C_{pn}	Coefficient of wind pressure on north wall
C_{ps}	Coefficient of wind pressure on south wall
E_d	Direct heat gain due to windows (W)
E_i	Internal heat gain (W)
g	Acceleration due to gravity (m/s^2)
H	Height of building (m)
H	Heat transfer coefficient between building envelop surface and ambient air
I	Solar global irradiance (W/m^2)
K, a	Terrain constants
N_p	No. of persons living in building
PDPH	Pressure difference Pascal hours (Pa h)
$T_{Sol.air}$	Sol-air temperature (°C)
T_{IC}	Indoor thermal comfort temperature
T_{AO}	Monthly average outdoor temperature
T_i	Indoor temperature (K)
T_o	Outdoor temperature (K)
V	Total ventilation (m^3/s)
V_S	Ventilation due to stack effect (m^3/s)
V_w	Ventilation due to wind effect (m^3/s)
V_r	Required ventilation (m^3/s)
v	Wind velocity measured in weather station (m/s)
v_o	Wind velocity calculated at buildings height (m/s)
ΔP	Pressure difference due to wind effect on building (Pa)
ΔP_r	Required pressure difference to meet indoor air quality in building (Pa)
ΔP_e	Effective pressure difference (Pa)
η	Wall porosity
λ	Absorption coefficient of exterior surface
ρ_o	Outdoor Air density (kg/m^3)

1 Introduction and Literature Review

In Indian building sector, heating ventilation and air condition (HVAC) is the largest energy consuming sector, hence, employment of passive approach and energy efficient systems in the HAVC is inevitable to conserve energy in the building sector.

Natural ventilation has been in use in the building since time immemorial and it has been neglected due to the advent of forced circulation machines. The interest toward natural ventilation has been reinstated due to its sustainable and energy saving benefits.

It is very essential to study the regional climate for its suitability to assist pure ventilation. The temperature in outdoor and indoor, wind pattern and its velocity, indoor heat gain and specification of the building are the important parameters to be considered for the evaluation of pure ventilation in the structure. Very few literature are found related to this area of research in Indian climates.

Natural ventilation potential is evaluated by indoor and outdoor pressure difference per hour, known as pressure difference Pascal hour (PDPH). In presented work, a natural ventilation potential (NVP) model is used for evaluation for Indian stations. Two typical stations, New Delhi and Jodhpur, are considered for NVP evaluation related to low-rise residential buildings. PDPH is evaluated considering complete thermal comfort (temperature and RH).

Natural ventilation phenomenon is a well-understood and well-established subject. Substantial numbers of research articles on broad areas of natural ventilation may be found in the literature, but very less references in relation to the natural ventilation potential of climates are found in the literature. Axley and Emmerich [1] recommended a technique to evaluate the climatic potential for natural ventilation of commercial buildings, using hourly weather data for a typical meteorological year (TMY). Yang et al. [2] investigated the prospect of the crude driving forces for ventilation in four major cities of China; PDPH concept was used to assess the natural ventilation potential of the local climate. Evaluation of PDPH was carried out considering indoor temperature to be constant (22 °C), which may not reflect the actual natural ventilation potential. Luo et al. [3] extended the study of Yang et al., and the revised model for NVP was developed. Indoor temperatures were evaluated using the heat balance equation for the building. NVP in terms of PDPH was evaluated, taking thermal comfort as well as indoor air quality into account. Haase and Amato [4] assessed the climates of Hong Kong and Singapore and few cities of China and Thailand, for their prospect for natural ventilation. The Study found tropical and temperate climates provide higher potential as compared to subtropical climates. Yao et al. [5] assessed the natural ventilation cooling potential (NVCP) of office buildings in varying climatic zones of China, using a new analytical model called thermal resistance ventilation (TRV) model which was validated by a case study of the low-energy office building.

This article caters with the study of six typical Indian cities for the evaluation of NVP and thermal comfort. NVP is evaluated in terms of PDPH with and without thermal comfort. A detailed assessment of thermal comfort, indoor heat gain, and natural ventilation hours are discussed in this paper.

2 Theoretical Basis and Methodology

2.1 Evaluation of Heat Gained by Building

Concept and theoretical basis have been referred from the work of Luo et al. We consider a structure with an opening across north and south walls only as shown in Fig. 1. Inhabitants of the building are examined as heat sources (E_i), solar radiation acts on the structure through a sol-air temperature through the walls, and direct heat gain is from the openings (E_d). There is no thermal mass assumed in the structure because, if thermal mass is involved, the analysis becomes too complex and it is impossible to obtain an analytical solution to the governing equations as pointed out by Li and Delsante [6]. The model is based on principles of energy conservation.

Following are the assumptions made in the NVP model,

1. Conceptual building is assumed to be at the city outskirts and in an open area.
2. Building is south oriented with the same opening area on both south and north walls as illustrated in Fig. 1.
3. Indoor air distribution in the building is uniform.
4. Relative humidity (RH) of outdoor air and indoor air is the same.

North wall area (A_n), south wall area (A_s), and other parameters required for the evaluation can be easily calculated from the building details given in Table 1 and Fig. 2.

Applying energy balance Eq. (3) on the conceptualized building (Fig. 1)

$$\rho\, C_p V(T_i - T_o) + \sum U_j A_j (T_i - T_{Sol.air}) = E_i + E_d \tag{1}$$

where $T_{Sol.air}$ is defined as [7]

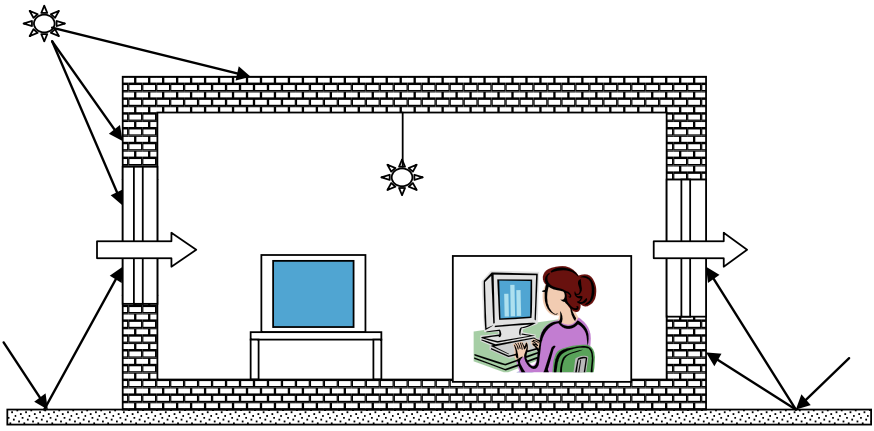

Fig. 1 Conceptual building

Table 1 Details of conceptual building

Particulars	Dimensions	Particulars	Dimensions
Length (L)	20 m	$Z = H$	8 m
Width (W)	10 m	η	0.35
Height (H)	8 m	N_p	10
C_d	0.61	ρ	1.2 kg/m^2
K	0.68	a	0.17

Fig. 2 Building orientation

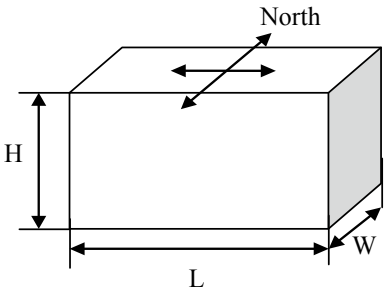

$$T_{\text{Sol.air}} = T_o + \frac{\lambda I}{h} \tag{2}$$

Substituting $T_{\text{Sol.air}}$ from Eq. 2 into Eq. 1, we get

$$\rho\, C_p V (T_i - T_o) + \sum U_j A_j (T_i - T_o) = E \tag{3}$$

The overall heat transfer coefficient for the jth wall is represented by U_j, and its value for cold zone stations (Shillong and Leh station) is recommended as $U_j = 0.352$ W/m^2 °C and for other stations, it is 0.44 W/m^2 °C [8].

Where total heat gain (E) in the building is given as

$$E = E_i + E_d + \sum U_j A_j \cdot \frac{\lambda I}{h} \tag{4}$$

where E_i and E_d are internal and direct heat gain in the building. The E_i is evaluated taking into account of heat release by home appliances, electric lamps, and occupants of the building as shown in Fig. 3; it is computed to an average of 1100 W/h. Each occupant releases heat of 100 W [7]. It is assumed that ten persons live in the building during night hours and three persons during day hours. Heat release by various home appliances and their daily use hours are suitably assumed for a typical residential building in India.

Direct heat gain through the windows is given as

$$E_d = F \cdot I.A_{\text{window}} \tag{5}$$

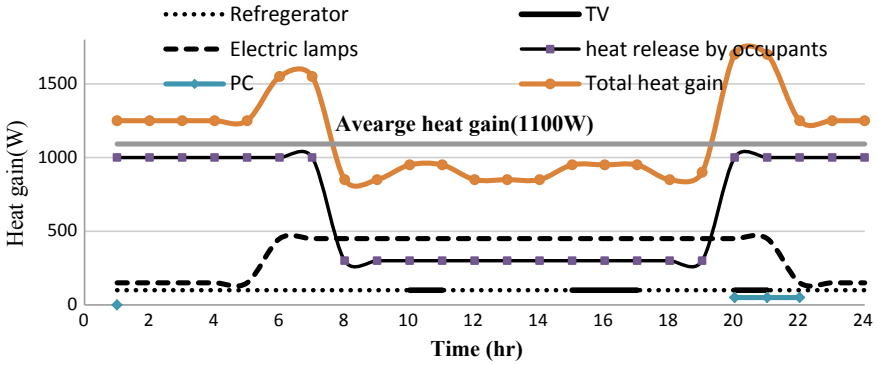

Fig. 3 Details of internal heat gain in the building

where F is a solar heat gain factor. The relation between solar heat gain factor and shading coefficient (SC) of the window with 3 mm plain glass is given by

$$F = \frac{\text{SC}}{1.15} \tag{6}$$

where SC = 1 for 3 mm glass [7]

Considering the heat gained from various internal sources leads to positive indoor temperature. From Eq. (3), we get a temperature variation across indoor and outdoor in terms of ventilation rate and total heat gain as,

$$(T_\text{i} - T_\text{o}) = \frac{E}{\rho\, C_\text{p} V + \sum U_j A_j} \text{ for } T_\text{i} \geq T_\text{o} \tag{7}$$

2.2 *Natural Ventilation Due to Combined Thermal Buoyancy and Wind Effect*

Natural ventilation due to thermal buoyancy [9] is given as

$$V_\text{s} = \frac{1}{3} C_\text{d} A_\text{t} \sqrt{g H \left(\frac{T_\text{i} - T_\text{o}}{T_\text{o}} \right)} \tag{8}$$

where A_t is total opening area and it is given as follows

$$A_\text{t} = (A_\text{n} + A_\text{s}) \cdot \eta$$

where η is wall porosity which is defined as

$$\eta = \frac{A_{\text{window}}}{A_{\text{wall}}}$$

Natural ventilation rate by wind effect is given as [10]

$$V_{\text{w}} = C_{\text{d}} \cdot A^* \cdot \eta \sqrt{\frac{2|\Delta P_{\text{w}}|}{\rho}} \tag{9}$$

where A^* is an effective wall area which is given as

$$A^{*2} = \frac{A_{\text{n}}^2 \cdot A_{\text{s}}^2}{A_{\text{n}}^2 + A_{\text{s}}^2}$$

Indoor and outdoor wind pressure difference is given by

$$\Delta P_{\text{w}} = \frac{1}{2}\rho \cdot C_{\text{pn}} \cdot v^2 - \frac{1}{2}\rho \cdot C_{\text{ps}} \cdot v^2 \tag{10}$$

where C_{pn} and C_{ps} are pressure coefficients for north and south wall, respectively, and their values vary with wind direction. The pressure coefficient data for various wind directions have been obtained from Ref. [10]. The wind velocity at building height [11] can be evaluated as follows.

$$v = k \cdot v_{\text{o}} \cdot H^a \tag{11}$$

From Eqs. (9)–(11), the natural ventilation rate due to wind effect is given as

$$V_{\text{w}} = C_{\text{d}} \cdot \frac{A_{\text{s}} \cdot A_{\text{n}} \cdot \eta \cdot k \cdot H^a \cdot v_{\text{o}}}{\sqrt{A_{\text{n}}^2 + A_{\text{s}}^2}} \cdot \sqrt{C_{\text{pn}} - C_{\text{ps}}} \tag{12}$$

Natural ventilation rate due to the combined effect of wind and thermal buoyancy assuming both are in step with each other.

$$V = \sqrt{V_{\text{s}}^2 + V_{\text{w}}^2}$$

$$V = \sqrt{\frac{1}{9}C_{\text{d}}^2 A_{\text{t}}^2 g \cdot H\left(\frac{T_{\text{i}} - T_{\text{o}}}{T_{\text{o}}}\right) + C_{\text{d}}^2 \cdot \frac{A_{\text{s}}^2 \cdot A_{\text{n}}^2 \cdot \eta^2 \cdot k^2 \cdot H^{2a} \cdot v_{\text{o}}^2}{A_{\text{n}}^2 + A_{\text{s}}^2} \cdot \left(C_{\text{pn}} - C_{\text{ps}}\right)}$$

$$V^2 = \frac{1}{9}C_{\text{d}}^2 A_{\text{t}}^2 g \cdot H \frac{E}{T_{\text{o}}\left(\rho\, C_{\text{p}} V + \sum U_j A_j\right)} + C_{\text{d}}^2 \cdot \frac{A_{\text{s}}^2 \cdot A_{\text{n}}^2 \cdot \eta^2 \cdot k^2 \cdot H^{2a} \cdot v_{\text{o}}^2}{A_{\text{n}}^2 + A_{\text{s}}^2} \cdot \left(C_{\text{pn}} - C_{\text{ps}}\right)$$

Further rearranging the terms, we get cubic equation as:

$$V^3 + V^2\left(\frac{\sum U_j A_j}{\rho_o\, C_p}\right) - V \cdot C_d^2 \cdot \frac{A_s^2 \cdot A_n^2 \cdot \eta^2 \cdot k^2 \cdot H^{2a} \cdot v_o^2}{A_n^2 + A_s^2} \cdot \left(C_{pn} - C_{ps}\right) - \left(\frac{\sum U_j A_j}{\rho_o\, C_p}\right)\left(C_d^2 \cdot \frac{A_s^2 \cdot A_n^2 \cdot \eta^2 \cdot k^2 \cdot H^{2a} \cdot v_o^2}{A_n^2 + A_s^2} \cdot \left(C_{pn} - C_{ps}\right)\right) - \frac{C_d^2 A_t^2 g \cdot H \cdot E}{9 T_o \rho_o\, C_p} = 0 \tag{13}$$

Equation (13) can be expressed as

$$V^3 + A_o \cdot V^2 - B_o \cdot V - A_o \cdot B_o - C_o = 0 \tag{14}$$

where

$$A_o = \frac{\sum U_j A_j}{\rho_o\, C_p}$$

$$B_o = C_d^2 \cdot \frac{A_s^2 \cdot A_n^2 \cdot \eta^2 \cdot k^2 \cdot H^{2a} \cdot v_o^2}{A_n^2 + A_s^2} \cdot \left(C_{pn} - C_{ps}\right)$$

$$C_o = \frac{C_d^2 A_t^2 g \cdot H \cdot E}{9 T_o \rho_o\, C_p}$$

Equation (14) has three solutions with negligible complex parts and only positive solution without the complex part is taken as a solution to Eq. (14). It is given as:

$$V = \left(\frac{C_o}{2} + \frac{A_o B_o}{3} + \left(\left(-\frac{A_o^3}{27} + \frac{A_o B_o}{3} + \frac{C_o}{2}\right)^2 - \left(\frac{A_o^2}{9} + \frac{B_o}{3}\right)^3\right)^{\frac{1}{2}} - \frac{A_o^3}{27}\right)^{\frac{1}{3}} - \frac{A_o}{3} + \frac{\left(\frac{A_o^2}{9} + \frac{B_o}{3}\right)}{\left(\frac{C_o}{2} + \frac{A_o B_o}{3} + \left(\left(-\frac{A_o^3}{27} + \frac{A_o B_o}{3} + \frac{C_o}{2}\right)^2 - \left(\frac{A_o^2}{9} + \frac{B_o}{3}\right)^3\right)^{\frac{1}{2}} - \frac{A_o^3}{27}\right)^{\frac{1}{3}}} \tag{15}$$

2.3 Pressure Difference Pascal Hours (PDPH)

The difference of effective pressure difference and the required pressure difference is given as

$$\Delta P = \Delta P_e - \Delta P_r \tag{16}$$

The effective pressure difference across indoor space and outdoor environment is given by Yang et al. [2]

$$\Delta P_{\mathrm{e}} = \frac{\rho_{\mathrm{o}} \cdot V^2}{2C_{\mathrm{d}}^2 \cdot A_{\mathrm{t}}^2} \tag{17}$$

Pressure difference required to meet the indoor air quality [2] given by

$$\Delta P_{\mathrm{r}} = \frac{\rho_{\mathrm{o}} \cdot V_{\mathrm{r}}^2}{2C_{\mathrm{d}}^2 \cdot A_{\mathrm{t}}^2} \tag{18}$$

The ventilation rate needed to lessen background sources is suggested by ASHRAE standard, 2002 [12] as: 7.5 l per person and 10 l per 100 m^2 of the floor area of the complete building per second. Thus, ventilation rate in building is given as

$$V_{\mathrm{r}} = 0.0075 \cdot N_{\mathrm{p}} + 0.0001 \cdot A_{\mathrm{f}} \tag{19}$$

The variation in actual effective pressure difference and needed pressure difference (ΔP) is a measure of the potential of a local climate to provide natural ventilation in buildings. Pressure difference Pascal hours (PDPH) to meet the requirement of indoor air quality (IAQ) through natural ventilation only is the addition of the positive differences between the hourly effective pressure difference and the hourly required pressure difference as mentioned by Eq. (20); hourly positive values of ΔP are added for daily, monthly, or yearly basis to evaluate the corresponding PDPH.

$$\mathrm{PDPH} = 1\,\mathrm{hr} \cdot \sum_{\mathrm{hr}} \Delta P^{+} \tag{20}$$

2.3.1 PDPH with IAQ and Thermal Comfort

Assessment of NVP based on IAQ and thermal comfort not only helps in quantitative assessment of natural ventilation indirectly, but also harnessing the environmental driving forces for natural ventilation through proper strategies of passive ventilation systems in buildings. PDPH to meet the requirement of indoor air quality as well as thermal comfort based on indoor comfort temperature, through natural ventilation only, is the sum of the positive differences between hourly effective pressure difference and hourly required pressure difference as given by Eq. (21), and only those hours with positive value of PDPH with indoor temperature falling within the acceptable limit are added to evaluate PDPH for daily, monthly, or a yearly as given by Eq. (21).

$$\mathrm{PDPH_{TC}} = 1\,\mathrm{hr} \cdot \sum_{\mathrm{hr}} \Delta P_{\mathrm{TC}}^{+} \tag{21}$$

2.3.2 Indoor Temperature Limits for Thermal Comfort in Naturally Ventilated Buildings

Widely accepted thermal comfort evaluation index in the building is through predicted mean vote of the people (PMV). PMV for thermal comfort is entirely different in a naturally ventilated building as compared to PMV for air-conditioned building. People living in naturally ventilated buildings tend to accept higher limits of temperature for thermal comfort and are less sensitive and more tolerant to the changes in both indoor and outdoor climatic conditions as compared to those living in an air-conditioned building. An evaluation model for thermal comfort in naturally ventilated buildings called adapted comfort standard (ACS) was proposed by de Dear [13] and optimum comfort temperature for natural ventilation is in tune with monthly outdoor air temperature. It is given by Eq. (22)

$$T_{IC} = 0.31 \cdot T_{AO} + 17.8 \tag{22}$$

where T_{AO} is monthly mean outdoor temperature.

Considering 80% of acceptability for Indian people, the adoptive standards for naturally ventilated buildings the upper and lower limits of acceptable indoor temperatures are given as [14].

The upper limit of acceptable indoor temperature (T_{up}) is:

$$\left.\begin{aligned} T_{up} &= 22.85 \quad \text{for} \quad 0 < T_{AO} < 5 \\ T_{up} &= 0.31 T_{AO} + 21.3 \quad \text{for} \quad 5 < T_{AO} < 33 \\ T_{up} &= 31.53 \quad \text{for} \quad 33 < T_{AO} < 40 \end{aligned}\right\} \tag{23}$$

The lower limit of acceptable indoor Temperature (T_{lo}) is:

$$\left.\begin{aligned} T_{lo} &= 15.85 \quad \text{for} \quad 0 < T_{AO} < 5 \\ T_{lo} &= 0.31 \mathrm{T}_{AO} + 14.3 \quad \text{for} \quad 5 < T_{AO} < 33 \\ T_{lo} &= 24.53 \quad \text{for} \quad 33 < T_{AO} < 40 \end{aligned}\right\} \tag{24}$$

the thermal comfort limits of indoor air temperatures are computed for monthly average outdoor temperatures given by Eqs. (23) and (24) as shown in Fig. 4. Thermal comfort zone (Fig. 4) is limited within the monthly mean outdoor temperature in the range 0-40 °C because, it is known that thermal comfort cannot be achieved when the outdoor temperatures are below 0 °C and above 40 °C.

2.4 Methodology

Hourly weather data on vertical surfaces and horizontal surface in a typical meteorological year (TMY) were obtained using Transys software. Hourly weather data

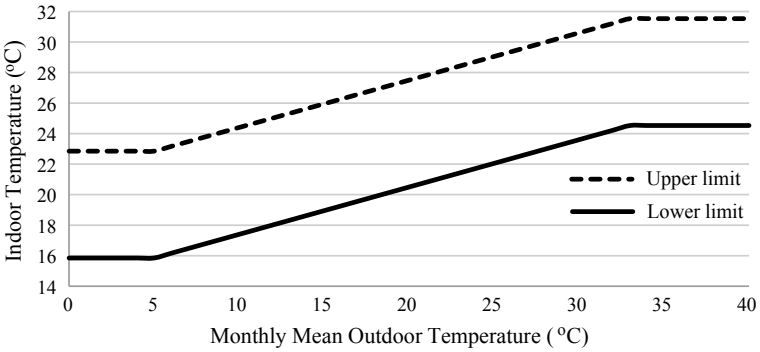

Fig. 4 Thermal comfort limits in naturally ventilated building

were used to evaluate monthly average outdoor temperature, hourly indoor temperature, and monthly PDPH, using MATLAB and MS Excel program. Details of the evaluation steps are presented in Fig. 5.

2.5 Meteorological Data for India

India, being in the northern hemisphere under tropical region between the longitudes 60° E–100° E and latitude between 5° and 20° N, is subjected to extremely sunny climates. A clear difference of temperatures in entire regions of India is found in summer and winter months. Indian climates are driven by monsoon winds from the southwest direction at the beginning of the rainy season and reversal of these winds in northeast direction at the end of the rainy season [15]. Indian climate is divided into six zones based on Koppen–Geiger climate classification system: high land, humid subtropical, tropical wet and dry, arid, semi-arid, and tropical wet. These zones are shown in Fig. 6. Two cities, New Delhi from semi-arid climate, Jodhpur from arid climate, are referenced for the study.

3 Results and Discussion

3.1 Thermal Comfort Assessment in the Building

Hourly indoor temperatures have been evaluated from the NVP model. Thermal comfort based on indoor temperature has been assessed for two stations. From Figs. 7 and 8, it is found that New Delhi and Jodhpur cities obtain thermal comfort in the range, 45–85% of the time during the end of the summer months and at the beginning

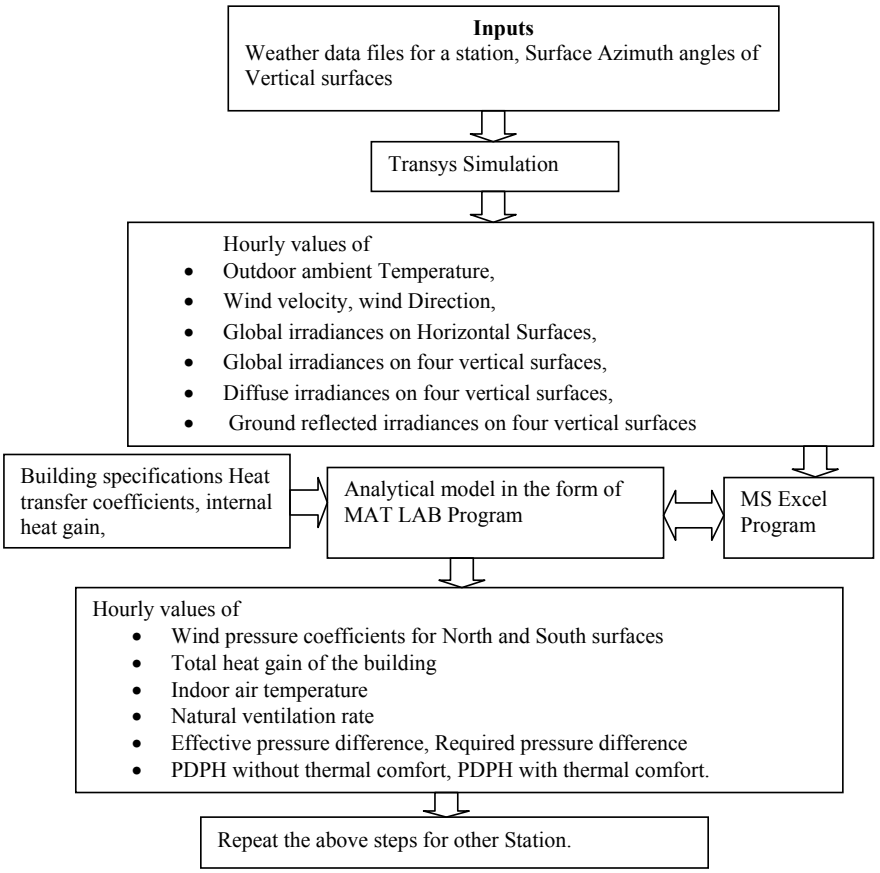

Fig. 5 Evaluation steps of the natural ventilation model

of the monsoon months (July, August, and September). Whereas the least thermal comfort period (20–40%) is found in the winter months of December, January, and February. To achieve thermal comfort in the rest of the time, active systems or a complex passive system have to be integrated into the building.

Figure 7 shows indoor air temperatures at different months for corresponding monthly mean outdoor air temperatures in New Delhi. From the study of the hourly indoor temperatures and their occurrences in the band of thermal comfort, it is found that thermal comfort prevails for 40% of the time in New Delhi station in a TMY. The highest thermal comfort period is found to be in the months of July, August, and September (55–60% of the time), whereas least thermal comfort exists during the winter months of December, January, and February (20–30% of the time). The duration of thermal comfort varies in the range 35–40% in the rest of the month.

Figure 8 shows indoor air temperatures and comfort indoor temperature zone in Jodhpur. It is seen that the monthly average outdoor temperature is the same for the

Fig. 6 Climatic zones of India

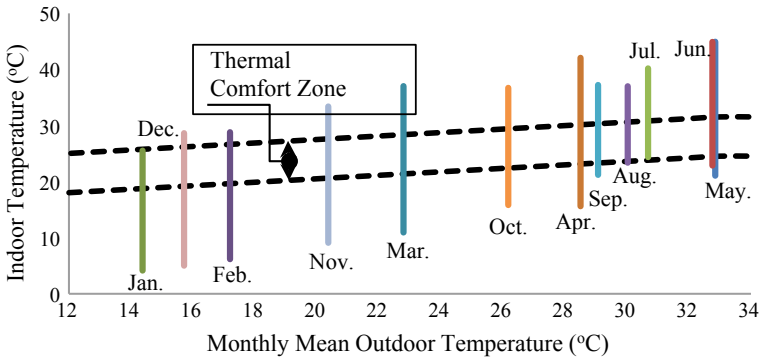

Fig. 7 Thermal comfort assessment at New Delhi

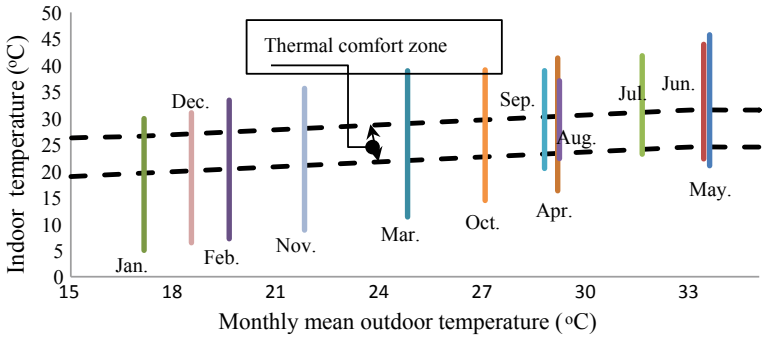

Fig. 8 Thermal comfort assessment at Jodhpur

months of January and December. From a study of the hourly indoor temperatures and their occurrence in the band of thermal comfort, it is found that thermal comfort is prevailed in 40% of the time in a TMY. The highest thermal comfort period is found to be in the months of July, August, and September (45–55% of the time), whereas least thermal comfort period exists during the winter months of Dec. Jan. and Feb. (30–35% of the time). Thermal comfort varies in the range 35–40% during of the rest of the months in a year.

3.2 Cumulative Frequency of Effective Pressure Difference

The hourly effective pressure difference of ambient air across the indoor space of the building and the surrounding atmosphere is a climatic resource that can be harnessed to achieve natural ventilation. Figure 9 shows the cumulative frequency curves of an effective pressure difference across indoor space and outdoor space of the conceptual building in Indian cities. For effective pressure difference of 0.2 Pa or above, the cumulated frequency for the stations is: New Delhi 30% and Jodhpur (20%), whereas for an effective pressure difference of 1.0 Pa or above, the cumulative frequency values for the stations Jodhpur and New Delhi are 2–4%. Cumulative frequency is 1% for a pressure difference of 1–2 Pa from the study of cumulative frequency curves.

3.3 Heat Gained by Building

Total heat gain due to internal heat sources and external solar irradiance for the building is shown in Fig. 10. The highest heat gain is observed in the range of 9–9.5 kW, during summer months. New Delhi and Jodhpur station bear the highest

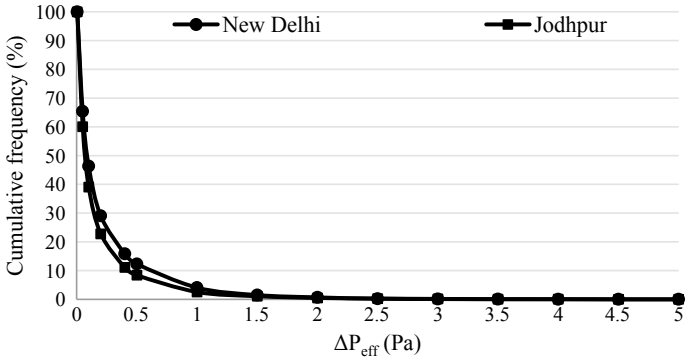

Fig. 9 Cumulated frequency of effective pressure difference at Indian stations

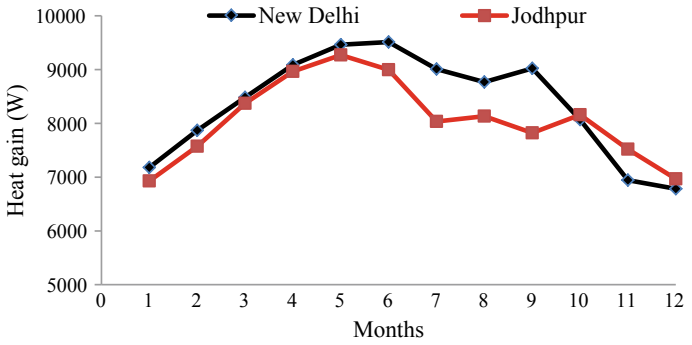

Fig. 10 Total heat gain in the building at different stations

heat gain, 9.5 kW, whereas during winter months, the total heat gain varies between 6 and 7 kW for these stations.

3.4 Monthly Hours of Natural Ventilation with Thermal Comfort

Monthly hours of natural ventilation with thermal comfort were evaluated by adding hours with positive PDPH and indoor temperature within the comfort zone (Fig. 11). it is observed that New Delhi and Jodhpur stations experience natural ventilation with thermal comfort, for 40% of the time in a year. High ventilation hours are observed at the end of the summer months and at the beginning of the monsoon months. Highest monthly ventilations hours are found to be 421 and 413 for Jodhpur and New Delhi, respectively.

Fig. 11 .

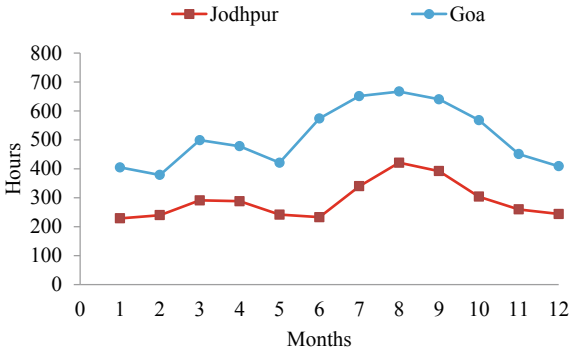

Fig. 12 Monthly PDPH

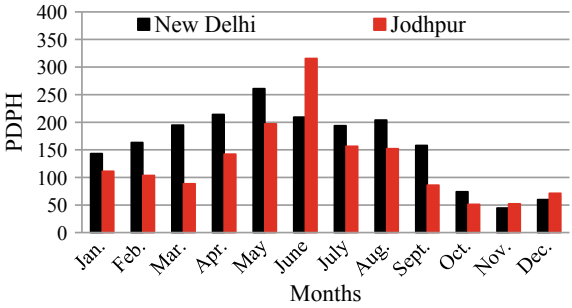

Fig. 13 Monthly PDPH with indoor temperatures are in thermal comfort

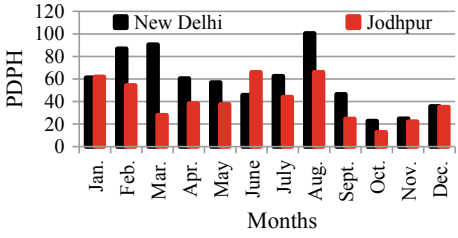

3.5 PDPH Under Various Indoor Conditions

Figures 12, 13 and 14 show the monthly pressure difference Pascal hours in a TMY under different indoor conditions for these stations. PDPH follows the decreasing trend when it is evaluated considering those hours where indoor temperatures are within the thermal comfort range. PDPH values further fallow drastic downturn trend, when it is evaluated for those hours where both indoor temperature and relative humidity within the thermal comfort are considered. For thermal comfort, 30–60% of RH is considered (ASHRAE 55 [16, 17]) for the estimation.

Monthly PDPH is evaluated by adding the hourly values of the positive difference between effective pressure difference, and required pressure difference as shown in

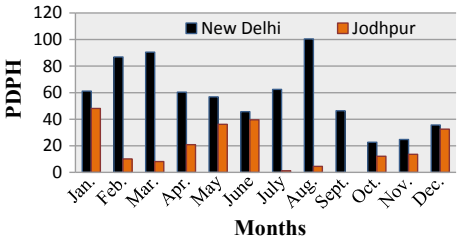

Fig. 14 Monthly PDPH with thermal comfort of indoor temperature and RH

Fig. 12. Higher PDPH indicates higher natural ventilation potential of the climate. High PDPH is observed during summer months and lower value of PDPH is seen during winter months where PDPH values fall in the range of 60–300 Pa h.

Monthly PDPH with indoor temperature within the thermal comfort is evaluated by adding the only positive difference between effective pressure difference and required pressure difference for those hours, where hourly indoor temperatures are in the comfort zone. PDPH values fall drastically as shown in Fig. 13. PDPH scenario shows that for New Delhi and Jodhpur stations, PDPH are 100 and 66 Pa h, respectively. Lower values of PDPH are found in winter months the values are in the range, 30–100 Pa h. Shilling station shows lower range due to low ambient temperatures,

Further, monthly PDPH is evaluated for complete thermal comfort hours, viz. indoor temperature and relative humidity. It is irrelevant to consider RH in the evaluation of natural ventilation potential in terms of PDPH, as RH does not contribute for natural ventilation or PDPH. But to know its effect on thermal comfort, it is necessary to assess the PDPH scenario with both indoor temperature and RH. Now, PDPH falls exponentially as presented in Fig. 14. An entirely different scenario of PDPH emerges. New Delhi shows the highest PDPH (100 Pa h) followed by Jodhpur (48 Pa h). The occurrence of high PDPH is during winter because RH is out of the comfort zone during the summer period.

4 Conclusions

An analytical model for NVP was used to assess the climatic potential of two typical cities of India, for natural ventilation to ensure indoor air quality and thermal comfort in the low-rise residential building. From the analysis of the results, following conclusions came into view.

- New Delhi and Jodhpur stations are greatly appropriate for natural ventilation during summer and monsoon periods, as the study showed that 40–45% of the time, there could be a thermal comfort achievable through natural ventilation, provided RH is controlled.
- Cumulative frequency of effective pressure difference across indoor and surrounding shows that pressure difference of 2.0 Pa exists for 20–30% of the time of the

year in these cities. Overall thermal comfort due to natural ventilation prevails for 35–40% of the time in a year.

- Natural ventilation alone could not provide thermal comfort throughout the year. PDPH assessment shows different scenarios when it is evaluated for different thermal conditions in the building. High PDPH is observed during the summer months and lower value of PDPH is seen during the winter months. PDPH values vary between 60 and 300 Pa h when considering IAQ and neglecting indoor thermal comfort, it falls drastically into the range of 10–100 Pa h, when both IAQ and indoor temperatures within the comfort range only are taken into account, while PDPH further drops substantially in the range of 0–100 Pa h, when indoor temperatures as well as RH within the comfort limits are taken into account.
- This study provides the guidelines for the township planners, real estate engineers at different levels of public and private firms, to assess the natural ventilation potential and hence energy conservation potential in an early stages of strategic planning of the real estate projects. Such study can be extended to other stations also.

References

1. Axley JW, Emmerich SJ (2002) A method to assess the suitability of a climate for natural ventilation of commercial buildings. In: Proceedings of indoor air, Monterey, CA. pp 854–863
2. Yang L, Zhang G, Li Y, Chen Y (2005) Investigating potential of natural driving forces for ventilation in four major cities in China. Build Environ 40:738–746
3. Luo Z, Zhao J, Gao J, He L (2007) Estimating natural ventilation potential considering both thermal comfort and IAQ issues. Build Environ 42:2289–2298
4. Haase M, Amato A (2009) An investigation of the potential for natural ventilation and building orientation to achieve thermal comfort in warm and humid climates. Sol Energy 83:389–399
5. Yao R, Li B, Steemers K, Short A (2009) Assessing the natural ventilation cooling potential of office buildings in different climate zones in China. Renew Energy 34:2697–2705
6. Li Y, Delsante A (2001) Natural ventilation induced by combined wind and thermal forces. Build Environ 36:59–67
7. Kreider JF, Curtiss PS, Rable A (2002) Heating cooling of buildings. Mc Graw Hill, New York
8. Bureau of Energy Efficiency (2007) Energy conservation building code 2007. Ministry of Power, Government of India, New Delhi
9. Awbi HB (1996) Air movement in naturally-ventilated building. Renew Energy 8:241–247
10. Orme M, Liddament MW, Wilson (1998) A numerical data for infiltration and natural ventilation calculations. Technical note AIVC 44. The International Energy Agency, The Air Infiltration and Ventilation Centre
11. British Standards Institution (BS5925-1991) Code of practice for design of buildings: ventilation principles and designing for natural ventilation. London
12. ASHRAE Standard 62.2P (2002) Ventilation and acceptable indoor air quality in low rise residential building. American Society of Heating and Ventilation Engineers
13. de Dear R, Brager GS (2002) Thermal comfort in naturally ventilated buildings: revision to ASHRAE standard 55. Energy Buil 34:549–561
14. Brager GS, De DR (2000) A standard for natural ventilation. ASHRAE J 21–8
15. Atri SD, Tyagi A (2010) Climate profile of India, Met monograph No 01. Environment Meteorology—Government of India, Ministry of Earth Sciences, Indian Meteorological Department

16. Balaras CA, Dascalaki E, Gaglia A (2007) HVAC and indoor thermal conditions in hospital operating rooms. Energy Build 39:454–470
17. Peder W, Kjaergaard SK (2007) The dichotomy of relative humidity on indoor air quality. Environ Int 33:850–857

Hybrid Absorption Cycles for Solar Cooling

S. C. Kaushik, Akhilesh Arora and Manoj Dixit

Abstract In this paper, a comprehensive review of vapour absorption refrigeration systems and hybrid absorption refrigeration systems is carried out for solar cooling application. The review shows that a lot of research work has been done on vapour absorption refrigeration systems which include single-effect, double-effect and triple-effect configurations. However, studies pertaining to hybridization of vapour absorption refrigeration systems with vapour compression refrigeration system, ejector refrigeration system or other types of refrigeration systems are quite scant. Also, most of the available studies on hybrid absorption refrigeration system are based on first law of thermodynamics and only a few studies are there which analyse them from the viewpoint of exergy and exergoeconomics. Hence, there is a need to carry out exergy and exergoeconomic analyses of hybrid absorption refrigeration systems together with energy analysis.

Keywords Hybrid · Absorption · Refrigeration · Exergy · Exergoeconomics

1 Introduction

Refrigeration and air-conditioning industry has seen significant growth during the past few decades. It is playing a vital role in the advancement of society. It is traditionally used in commercial, residential and industrial sectors. The traditional vapour compression refrigeration (VCR) machine used for air-conditioning and refrigera-

S. C. Kaushik (✉)
Centre for Energy Studies, Indian Institute of Technology Delhi,
Hauz Khas, New Delhi 110016, India
e-mail: kaushik@ces.iitd.ac.in

A. Arora
Mechanical Engineering Department, Delhi Technological University,
Bawana Road, New Delhi 110042, Delhi, India

M. Dixit
Mechanical Engineering Department, Faculty of Engineering,
Dayalbagh Educational Institute, Agra 282005, India

G. Zhang et al. (eds.), *Advances in Energy and Built Environment*, Lecture Notes in Civil Engineering 36, https://doi.org/10.1007/978-981-13-7557-6_19

tion operates on electrically driven compressors. As per the report of International Institute of Refrigeration, the consumption of electricity by air-conditioning and refrigeration systems is around 15% of the global generation [1].

The conventional vapour compression refrigeration systems employ CFCs and HCFCs as refrigerants because of their favourable thermodynamic and thermophysical properties. Both HCFCs and CFCs maintained their dominion in the cooling industry for about 70 years. The Montreal Protocol slapped a ban on their use to contain the ozone depletion triggered by their use. HFCs emerged as their substitute as they have nil potential for ozone depletion. However, HFCs may not be permanent solution due to their high global warming potential (GWP). The GWP of HFC refrigerants is 500–3000 times greater than CO_2 [2]. Also, VCR systems contribute indirectly to global warming as majority of global electricity generation comes through fossil fuels, which causes a significant amount of emissions of greenhouse gases. The issue of global warming led to the signing of Kyoto Protocol in 1997 which aims at reducing the emission HFCs and other greenhouse gases (GHGs).

The twin problems of energy crisis and environmental damage can be solved to some extent by the use of alternate cooling technologies that can utilize renewable sources of energy. Absorption refrigeration and heat pump methodology is powered by low-grade heat, and requirement of electricity is negligible. It utilizes eco-friendly refrigerants or 'green refrigerants' with zero ODP and low GWP. Many working pairs have been studied, but H_2O–LiBr and NH_3–H_2O are the most preferred working pairs for VAR systems.

The VAR system, however, has its own limitations too. For NH_3–H_2O systems, the presence of various regulations regarding usage of NH_3 in residences and buildings is the major hurdle. Secondly, such systems also require rectification. The H_2O–LiBr VAR system cannot achieve evaporator temperature lower than 5 °C as water is the refrigerant. As far as the performance of VAR systems are considered, the COP of such systems is far less than that of conventional VCR systems. Therefore, it is necessary to combine VAR systems with other systems to overcome these limitations.

Among all the environmentally benign and renewable energy sources, solar energy lies on top of the chart owing to its natural availability, cleanliness and coincidence of its highest availability with the maximum need of cooling. Solar-driven air-conditioning and refrigeration systems offer environment-friendly and sustainable alternatives to conventional cooling systems.

Another issue which needs attention is the method of analysis of refrigeration systems for computing their energy efficiency. Energy analysis is the conventional way of judging the refrigeration systems. The first law of thermodynamics is implicated only with energy preservation, and it provides null knowledge on where, how and how much system performance is debased. The concept of quality of energy is neglected by energy analysis. Thus, the limitations of energy analysis are overcome by exergy analysis depending upon the second law of thermodynamics. Exergy analysis is an important tool in the design, maximization and effectiveness evaluation of energy systems. It is usually focused at determining the best effectiveness of the model and recognizing the locations, reasons and real amounts of available energy losses which can lead to improvement in its operation [3].

2 Vapour Absorption Refrigeration (VAR) Systems

2.1 Single-Effect and Double-Effect VAR Systems

Single-effect (Fig. 1) and double-effect (Fig. 2) systems are the most studied configurations of VAR systems. Many studies are available in the literature regarding the first-law-based analysis of single- and double-effect VAR systems. These studies involve the work of Vliet et al. [4], Kaushik and Chandra [5], Kumar and Devotta [6], Gommed and Grossman [7], Xu et al. [8], Xu and Dai [9], Sun [10] and Arun et al. [11, 12].

Lee and Sherif [13] carried out the second law analysis of a single-effect water–lithium bromide absorption refrigeration method. Lee and Sherif [14] gave the second law analysis of single-effect and various configurations of double-effect water–lithium bromide absorptions systems. Gomri and Hakimi [15] gave the exergy analysis of double-effect lithium bromide–water absorption refrigeration model. Kaushik and Arora [16] carried out energy-based and exergy-based evaluation of both single-effect and double-effect (series flow) VAR systems. The study involved the parametric analysis to determine the effects of absorber, generator and evaporator temperatures on the energy and exergy performance of these systems. Arora and

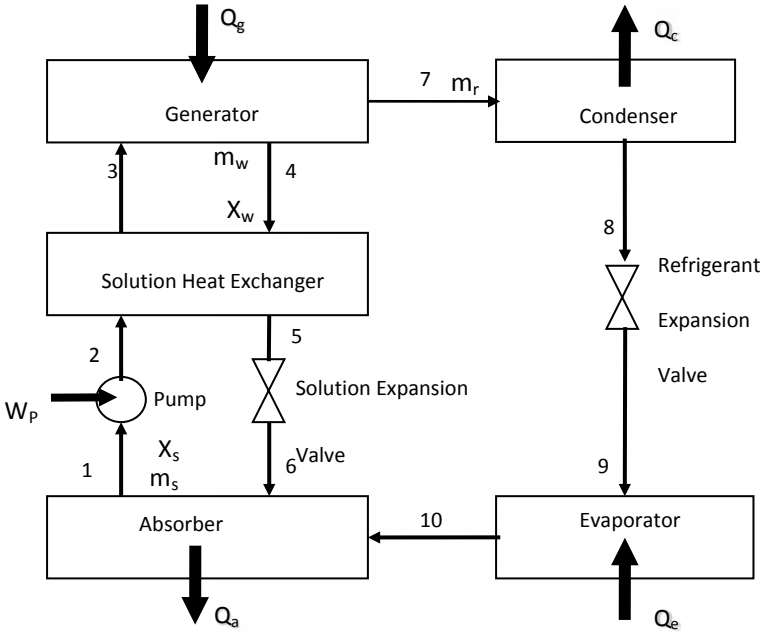

Fig. 1 *S*ingle-effect VAR system [16]

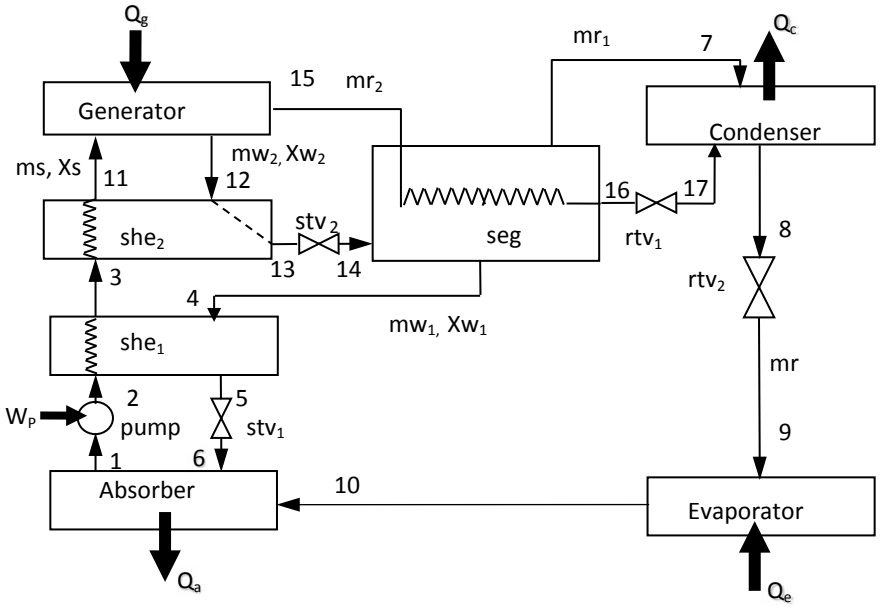

Fig. 2 Series-flow double-effect VAR system [16]

Kaushik [17] matured a computational model for theoretical analysis of H_2O–LiBr absorption refrigeration systems.

Li et al. [18] performed investigation of solar air-cooled double-effect H_2O–LiBr absorption refrigeration system. Bellos et al. [19] carried out the steady-state analysis of a 100-kW single-effect H_2O–LiBr solar-driven absorption chiller using Energy Equation Solver (EES). The concept of exergoeconomics has been applied by a number of analysts in order to evaluate and optimize energy conversion systems, specifically, refrigeration systems. Misra et al. [20, 21] used exergoeconomic principles to optimize single-effect and double-effect (series flow) VAR systems. The concept of exergoeconomics was also used by Farshi et al. [22] for analysing various configurations of double-effect absorption refrigeration systems.

2.2 Triple-Effect VAR System

Grossman et al. [23] accomplished simulation and performance investigation of triple-effect VAR systems (Fig. 3) on the basis of the first law of thermodynamics. They found that COP ranging from 1.272 for the series flow to 1.729 for the parallel flow was achievable at the design point. Lee and Sherif [24] examined COP and exergetic efficiency of multi-effect absorption refrigeration systems using water–lithium bromide. It was concluded that triple-effect system has a better cooling COP over

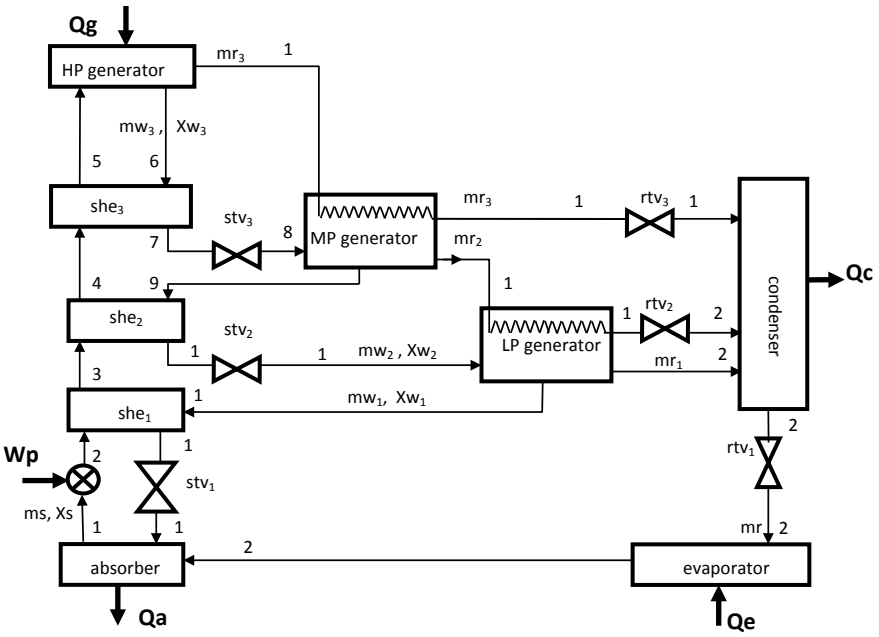

Fig. 3 Series-flow triple-effect water–lithium bromide VAR system [23]

the single- and double-effect systems, whereas exergetic efficiencies of all the three systems are similar. Kaita [25] carried out the simulation analysis for three kinds of triple-effect vapour absorption cycles including parallel flow, series flow and reverse flow using a newly developed computer simulation program. For each configuration, a number of parameters like COP, maximum temperature and maximum pressure were calculated. It was concluded in the comparative study that parallel-flow configuration was the best as it offered highest COP.

2.3 Two-Stage (Half Effect) VAR System

Herold et al. [26] has shown that the two-stage (half effect) cycle, shown in Fig. 4, is possible with heat input temperatures below that of a single-effect cycle. Ma and Deng [27] performed the theoretical study of low-temperature heat origin operated two-stage H_2O–LiBr vapour absorption cooling system. They examined the impact of hot water temperature and chilled water temperature on COP. The COP of two-stage system was found to be lower than the COP of single-stage single-effect system.

Sumathy et al. [28] matured a thermodynamic model of two-stage H_2O–LiBr solar VAR system and found in their study that it could be operated by any low-temperature heat source having temperature in the range of 60–75 °C.

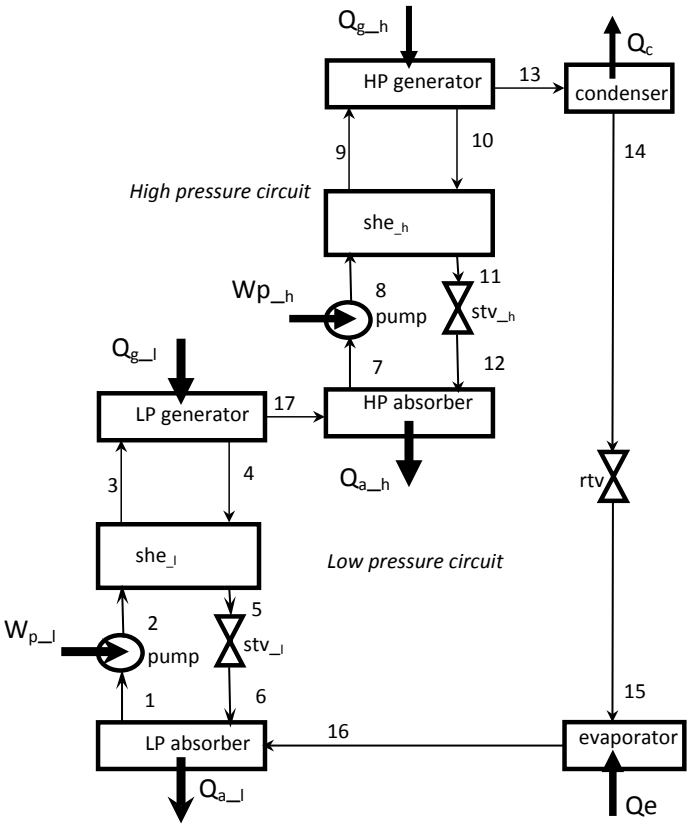

Fig. 4 Half-effect water–lithium bromide VAR system [26]

Izquierdo et al. [29] modelled a solar refrigeration plant consisting of double-stage absorption machine fed by flat plate collectors and compared it with single-stage absorption cycle. They reported that single-stage cycle cannot be operated by flat plate collectors for condensation temperature greater than 40 °C, whereas two-stage cycle can be driven by flat plate collectors up to condensation temperature of 53 °C for the evaporator warmth of 5 °C. Crepinsek et al. [30] evaluated the effectiveness of single-stage and double-stage vapour absorption refrigeration system for obtaining evaporator warmth below 0 °C depending on of solution circulation ratio and COP.

Arivazhagan et al. [31, 32] accomplished simulation study and experimental investigation of two-stage vapour absorption refrigeration system using R134a-DMAC working pair. The COP of this cycle was found to be varying between 0.35 and 0.46 with heat input in the generator at 70 °C, absorber temperatures of 25 °C, evaporator and condenser temperatures varying in the zone −5 to 5 °C and 20 to 30 °C, respectively. The most favourable generator temperature was found to be in the range of 65–70 °C. The second law efficiency was found to be fluctuating between 28 and 44%

for the sink temperature of 30 °C. Izquierdo et al. [33] executed the exergy analysis of solar thermal energy-driven half-effect H_2O–LiBr vapour absorption refrigeration cycle. For the generator temperature of 80 °C and condenser temperature of 50 °C, it attained the COP of 0.37. Gebreslassie et al. [34] carried out exergy-based analysis of various configurations of water–lithium bromide vapour absorption refrigeration cycles, considering only unavoidable part of exergy destruction. Similarly, principles of energy and exergy were applied by Gomri [35] for performing thermodynamic analysis of solar thermal energy-driven two-stage vapour absorption cooling system of 10 kW cooling capacity.

Lin et al. [36] carried out the numerical investigation of air-cooled two-stage ammonia-water vapour absorption refrigeration system and reported the thermal COP of 0.34 and electrical COP of 26 with 85 °C hot water supply from solar collector for 5 kW cooling capacity. They selected circular finned tubes for air-cooled condenser and absorbers and concluded that such systems are technically feasible for practical solar cooling application. Du et al. [37] built a prototype of 2 kW cooling capacity air-cooled two-stage ammonia-water vapour absorption refrigeration system driven by solar-energy-heated hot water. The prototype yielded a COP of 0.21 for hot water, and evaporator and ambient air temperatures of 85, 8 and 29 °C, respectively. Domínguez-Inzunza et al. [38] compared the thermodynamic effectiveness of single-effect, double-effect, triple-effect and half-effect VAR cycles employing ammonia–lithium nitrate as working pair. For half-effect cycle, the COP obtained for lowest generator and evaporator temperatures was 0.3.

3 Absorption–Compression Hybrid Systems

The VAR systems can be combined with VCR systems either in series or in parallel [39]. The series combination is often referred to as cascade refrigeration system, in which condenser of VCR system acts as evaporator for VAR system. This allows the condensing temperature of VCR system to be reduced, thereby reducing the utilization of electricity in the compressor of the VCR system. So, for low-temperature applications (below 5 °C), LiBr–H_2O absorption refrigeration systems are often cascaded with VCR systems. In parallel configuration, the cooling is achieved jointly by both VAR and VCR systems and thus reducing required compressor power. The basic absorption–compression cascade and parallel refrigeration cycles are shown in Figs. 5 and 6, respectively.

Chinnappa et al. [40] analysed solar-assisted vapour compression absorption cascaded air-conditioning systems using refrigerant R22 in compression section and NH_3–H_2O in absorption section. Fernandez-Seara et al. [41] studied a refrigeration system with vapour compression refrigeration system at low-temperature circuit and a vapour absorption refrigeration system at high warmth circuit. The cascaded system was powered by co-generation system and could provide low-temperature cooling. The ammonia and carbon dioxide were the refrigerants used in the low-temperature circuit, and ammonia water was used in high-temperature circuit. For evaporator tem-

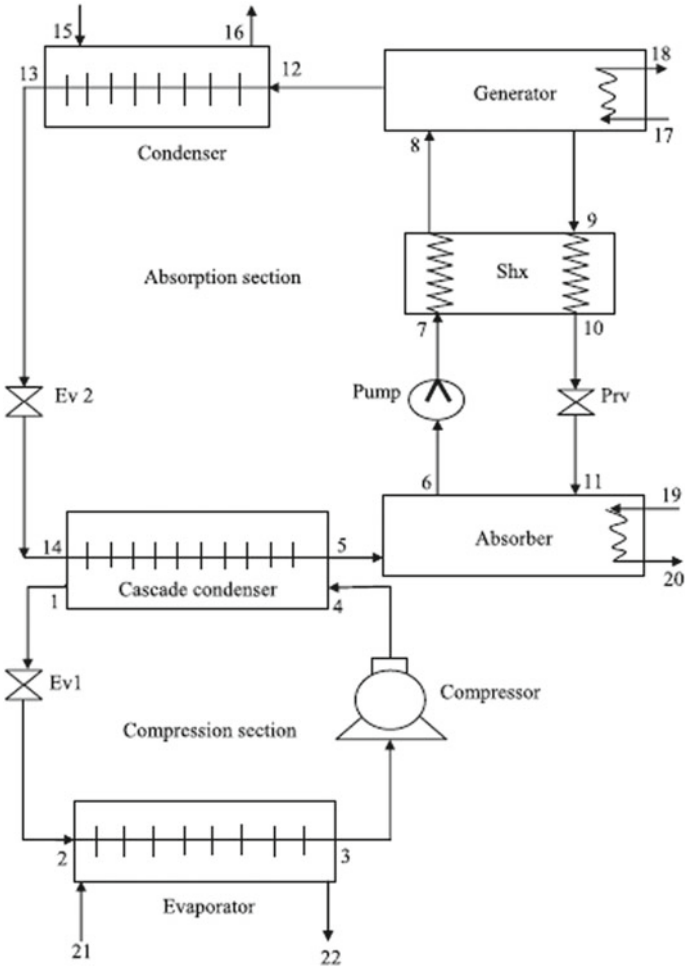

Fig. 5 Absorption–compression cascade refrigeration system [39]

perature of −45 °C, the COP of compression stage was found to be 2.463 and 2.602 with NH_3 and CO_2, respectively. Kairouani and Nehdi [42] analysed the geothermal energy-based compression–absorption cascade refrigeration system. The refrigerants used in compression section were R22, R134A and R717, while working pair used in absorption section was NH_3–H_2O. The COP of the cascaded system was found to be 37–54% than the equivalent VCR system.

Garimella et al. [43] developed a thought and investigated a novel cascaded absorption–vapour-compression cycle with a high warmth lift for a naval ship application, shown in Fig. 7. A single-effect water–lithium bromide vapour absorption cycle and a subcritical carbon dioxide vapour compression cycle were combined in order to provide −40 and 5 °C for electronic applications and space condition-

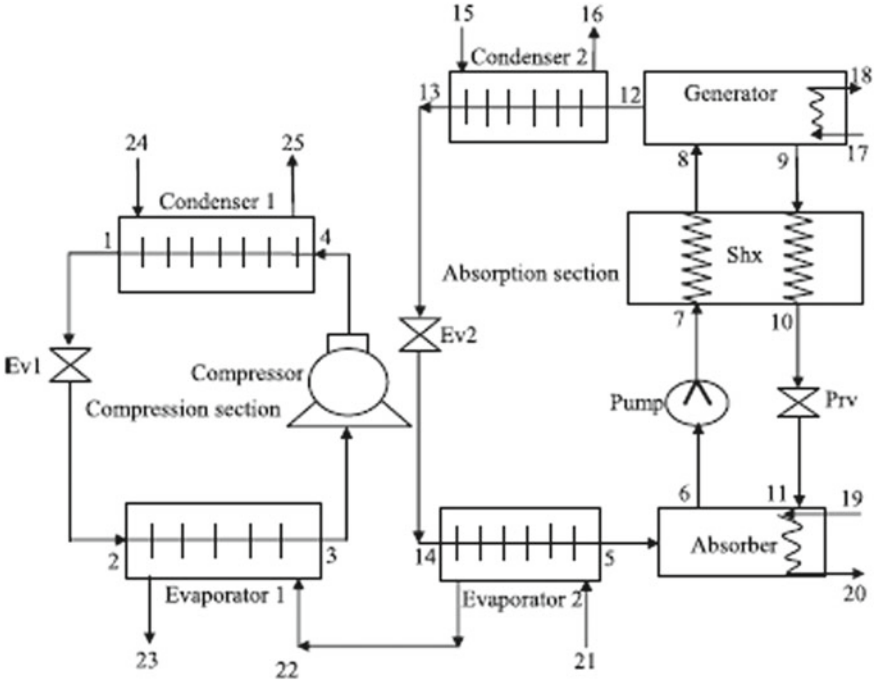

Fig. 6 Absorption–compression refrigeration cycle in parallel [45]

ing, respectively. The VAR cycle received its thermal power from the waste heat of onboard gas turbine power plants. On the view of total energy input, the COP of the system was reported to be 0.594, whereas on the basis of electrical energy input, it was 5.685. With the use of only 23 MW compressor power, 51 MW cooling at −40 °C and 82 MW cooling at 5 °C were obtained. The waste heat of the order of 200 MW was converted to useful entity during this process.

Cimsit and Ozturk [39] in their study used H_2O–LiBr and NH_3–H_2O as fluid partner in absorption section, while R134a, R410A and NH_3 fluids were used as refrigerants in the vapour compression section of the absorption–compression cascade refrigeration cycle. It was found in the study that the absorption–compression cascade refrigeration cycle consumed 48–51% lesser electrical energy than conventional VCR cycle for same conditions of operation. The COP of the cycle with H_2O–LiBr was found to be greater by 33% than with NH_3–H_2O. Wang et al. [44] studied the solar thermal energy-assisted cascade cooling system which incorporates the solar-driven vapour absorption refrigeration unit and electric energy-powered vapour compression refrigeration system. Solar heat is stored in solution reservoirs and refrigerant water. The stored energy allows the system to run even in the absence of sun.

Jain et al. [45] compared a 66.67-kW VCR system with cascaded vapour compression–absorption system (CVCAS) theoretically on the basis of energy and exergy

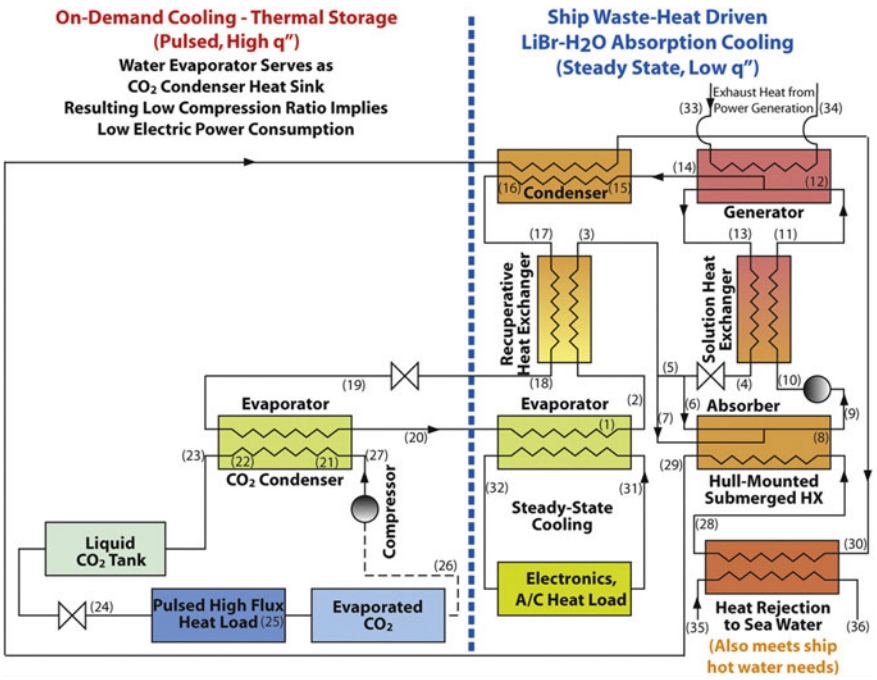

Fig. 7 Cascade absorption–vapour-compression cycle [43]

principles. They reported 61% reduction in power consumption and 155% increment in COP of compression section in case of CVCAS. Moreover, the environmentally benign refrigerants like R407C, R410A and R134A were found to perform almost at par with refrigerant R22.

Riffat and Shankland [46] have investigated the first law performance of various configurations of vapour absorption-and-compressor-integrated vapour absorption refrigeration systems using H_2O–LiBr as working pair. The schematic diagram of single-effect, series-flow double-effect and parallel-flow double-effect absorption–recompression refrigeration systems are shown in Figs. 8, 9 and 10, respectively. Their results indicated that integrated compression absorption systems could provide higher COP than individual system.

Kim et al. [47] advocated four compressor-assisted water–lithium bromide cooling cycles so as to resolve the issue of corrosion. The reduction in the generator temperature for simple triple-effect cycle can greatly minimize the problem of corrosion. Each cycle consisted of one compressor at a varying state point to raise the pressure of the refrigerant vapour till a level corresponding to helpful condensation temperature. In view to achieve 40 K of generator temperature fall (from 475.95 K) for all cycles, 3–5% of cooling ability equivalent mechanical energies were needed to operate the compressor. Pratihar et al. [48] performed simulation studies on a 400-kW ammonia-water compression absorption refrigeration system for water chilling

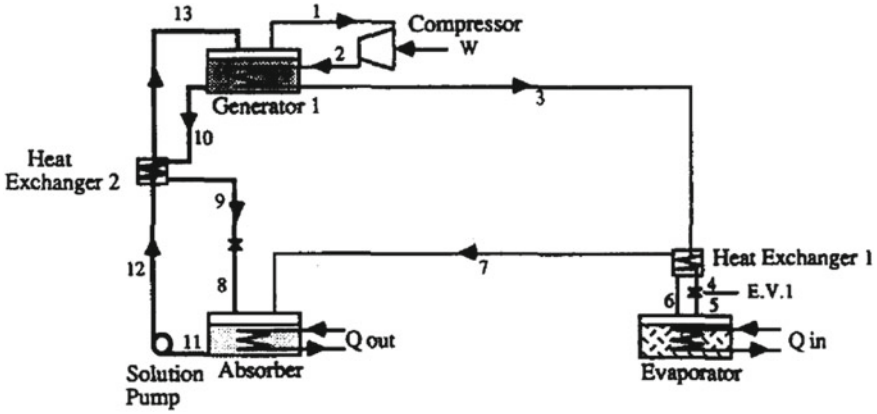

Fig. 8 Single-effect absorption–recompression system [46]

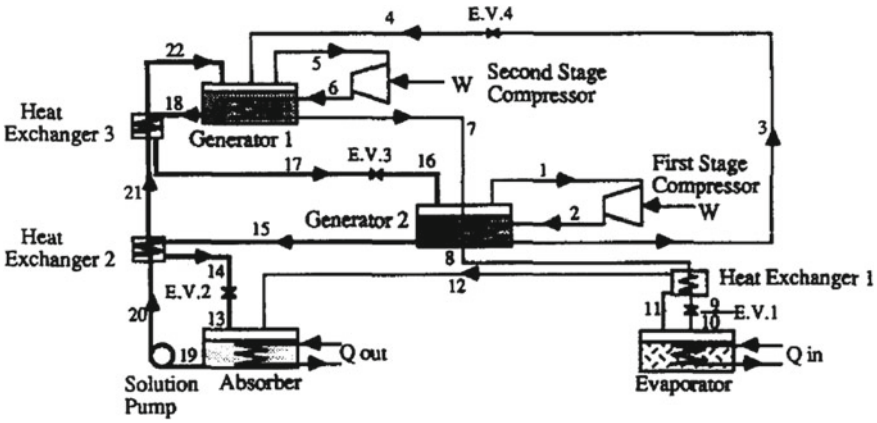

Fig. 9 Series-flow double-effect absorption–recompression system [46]

application. They studied the effect of relative area distribution, desorber pressure and mass flow rate of weak solution on COP, absorber heat load and cooling capacity.

Kang et al. [49] matured four different innovative hybrid GAX cycles with help of ammonia water through combination of vapour absorption and vapour compression cycles. Four different cycles are as follows: Type A was proposed for the improvement of coefficient of performance, Type B for low-temperature purposes, Type C for depletion of required desorption temperature and Type D for hot water applications. In Type A and Type B, a compressor is placed among the evaporator and the absorber as shown in Fig. 11, while in Type C and Type D compressor is positioned between the desorber and the condenser. The COP of Type A was observed to be 24% greater than the standard GAX cycle. In Type B, temperature of −80 °C could be achieved in the evaporator. The COP of HGAX–Type C increases as high as 1.19, which is

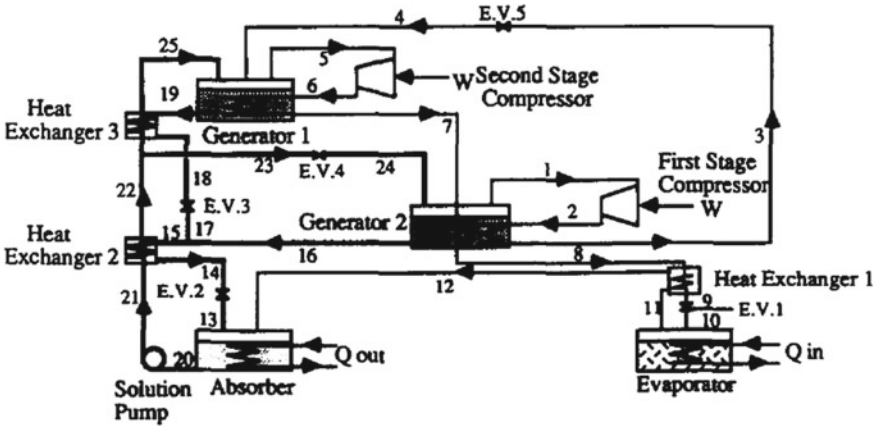

Fig. 10 Parallel-flow double-effect absorption–recompression system [46]

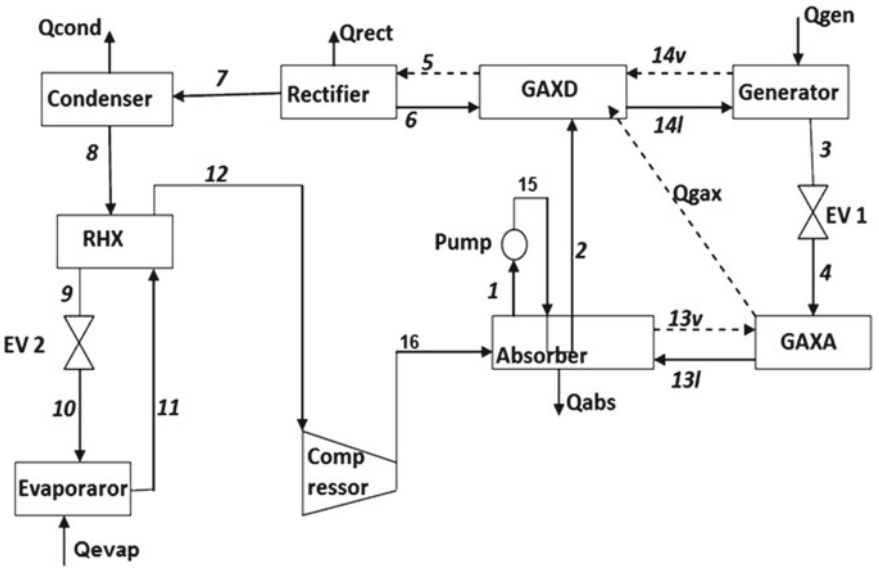

Fig. 11 Hybrid GAX refrigeration system [51]

19% greater than the COP of standard GAX, by controlling the desorber pressure. In Type D, the hot water at temperature as high as 106 °C could be attained. Thus, HGAX–Type D can be adapted for floor heating and space heating utilization.

Rameshkumar and Udayakumar [50] theoretically analysed an ammonia-water hybrid GAX absorption cycle for air-conditioning system. They found that the maximum coefficient of performance occurs at the average value of the degassing ratio of 0.4 with the variation of ±0.05. Yari et al. [51] analysed hybrid GAX and standard

GAX vapour absorption cycle for air-conditioning application. The investigation involved the application of both the first law of thermodynamics and the second law of thermodynamics. They concluded that generator temperature affects the second law efficiency much more than the first-law-based COP. They reported that rise in generator temperature from 400 to 440 K results in improvement in COP by merely 5% but improvement in the second law efficiency was 75%.

4 Ejector-Coupled VAR Systems

VAR systems utilize low- and medium-temperature heat sources like solar energy, geothermal energy, waste heat and exhaust heat. Nonetheless, due to complex configuration and lower COP, than VCR systems, they are less favoured as compared to vapour compression refrigeration systems. The addition of ejector to most studied single-effect vapour absorption refrigeration system enhances the absorption system's performance to a great extent. The utilization of ejector with single-effect absorption cycle allows us to get the performance of multi-effect VAR machine with less complexity. Furthermore, the initial capital investment of ejector-integrated single-effect absorption refrigeration system is comparatively far more less than other multi-effect VAR systems.

Many studies are available in the literature on combined vapour absorption and ejector refrigeration (ER) systems. The combined system consists of VAR system integrated with one or more ejectors. Sun et al. [52] proposed a combined absorption and ejector refrigeration cycles suitable for waste heat utilization. It entails the advantages of both the refrigeration technologies. The main component of the combined cycle, the ejector, was designed on the basis of constant pressure mixing theory and assuming the diffuser efficiency and nozzle efficiency of 85% each. They concluded that combined absorption ejector refrigeration cycle could provide higher COP than conventional single-effect VAR cycle. Hong et al. [53] suggested novel absorption ejector combined cycle (Fig. 12) to efficiently use high-temperature heat. The ejector was incorporated between the generator and the condenser of H_2O–LiBr parallel-flow double-effect VAR system.

Ejector-integrated absorption refrigeration system was studied by Sozen et al. [54] to evaluate the prospects of utilizing solar energy in 17 cities of Turkey for cooling applications. The working fluid selected for VAR cycle was ammonia water. The ejector was situated at the exit of the evaporator and at the inlet of the absorber; thus, higher pressure can be maintained in absorber as compared to evaporator. The higher pressure, due to ejector, in absorber upgrades mixing process and pre-absorption of ammonia by weak solution apart from helping in pressure recovery. This triple pressure cycle could achieve the maximum COP of 0.739 at evaporator, generator, condenser and absorber temperatures of 5, 90, 40 and 30 °C, respectively.

Wang et al. [55] combined a power cycle to an ejector-integrated vapour absorption refrigeration cycle as shown in Fig. 13. The joined system could produce cooling as well as power simultaneously. An ejector is used between the rectifier and the con-

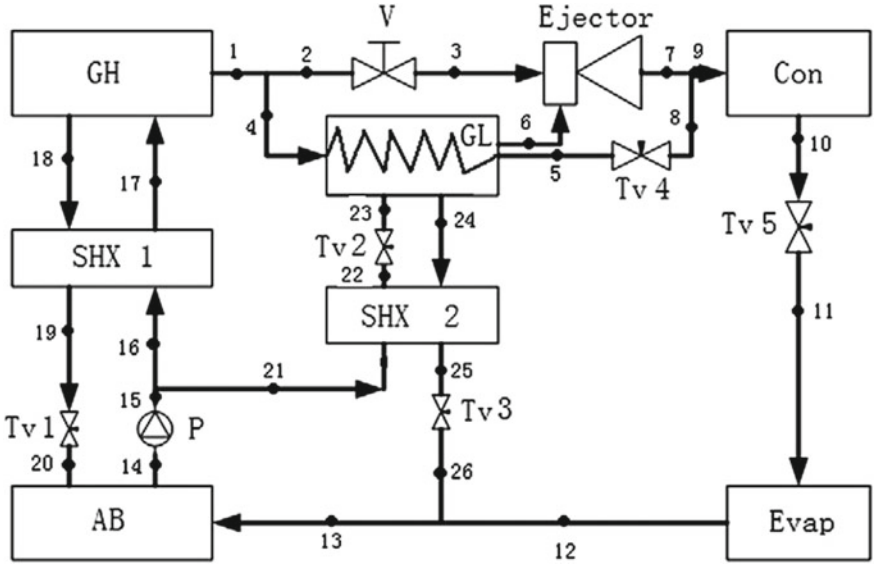

Fig. 12 Schematic diagram of a new ejector-absorption combined refrigeration cycle [53]

denser (condenser B). The use of ejector enhances the performance without making the system very complex. When the present system was compared with the similar system without the ejector, the refrigeration output for former system was 250 kW against 149 kW for the latter, for same operating conditions.

Some studies are also available on exergy and exergoeconomic analysis of ejector-coupled absorption refrigeration systems. Farshi et al. [22] studied a combined ejector double-effect absorption refrigeration system and compared it with standard series-flow double-effect absorption refrigeration system from the point of view of exergoeconomics.

5 Conclusions

The analysis on solar thermal energy-powered vapour absorption refrigeration systems clearly shows that a lot of research work has been done on VAR systems that utilize ammonia water and water–lithium bromide. However, studies related to VAR cycle combined with VCR cycles and ejectors are quite scant. Of the various studies conducted on hybrid absorption refrigeration systems, most of them are theoretical in nature and are confined to the first-law-based energy analysis only. There are only a few studies which analyse the hybrid absorption refrigeration cycles from the viewpoint of advanced concepts of exergy and exergoeconomics. Thus, there is a need to carry out the thermodynamic analysis of such systems from exergy and exergoe-

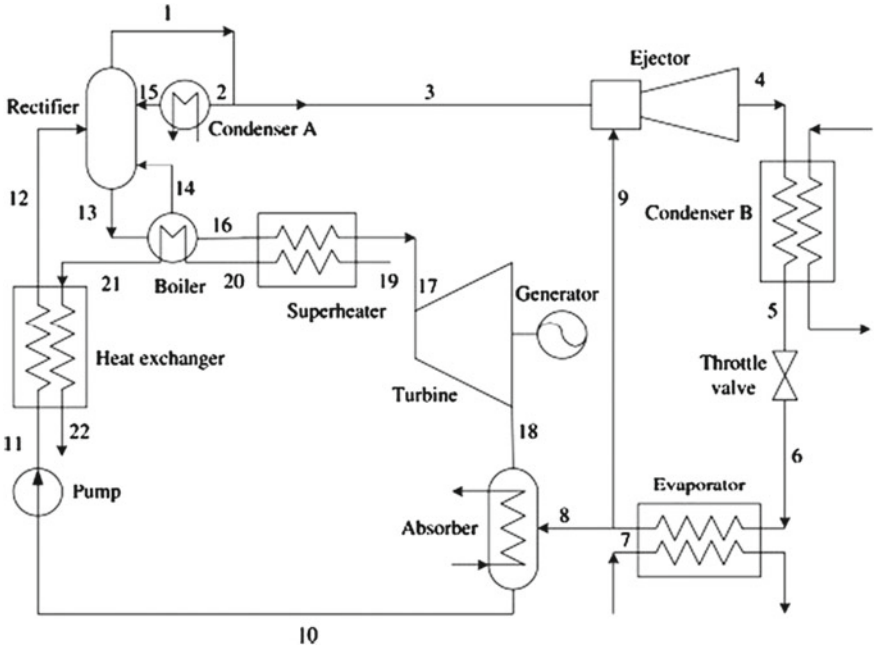

Fig. 13 Combined power and ejector-absorption refrigeration cycle [55]

conomic viewpoint. Also, the experimental validation of these cycles is absolutely necessary for their practical implementation.

References

1. Kalkan N, Young EA, Celiktas A (2012) Solar thermal air conditioning technology reducing the footprint of solar thermal air conditioning. Renew Sustain Energy Rev 16:6352–6383
2. Hanaoka T, Ishitani H, Matsuhashi R, Yoshida Y (2002) Recovery of fluorocarbons in Japan as a measure for abating global warming. Appl Energy 72:705–721
3. Dincer I, Rosen MA (2007) Exergy: energy, environment and sustainable development. Elsevier, Oxford, UK
4. Vliet GC, Lawson MB, Lithgow RA (1982) Water-lithium bromide double effect absorption cooling system analysis. ASHRAE Trans HO-82-5(2):811–823
5. Kaushik SC, Chandra S (1985) Computer modeling and parametric study of a double effect generation absorption refrigeration cycle. Energy Convers Manag 25(1):9–14
6. Kumar P, Devotta S (1990) Study of an absorption refrigeration system for simultaneous cooling and heating. ASHRAE Trans 92(2):291–298
7. Gommed K, Grossman G (1990) Performance analysis of staged absorption heat pumps: water lithium bromide systems. ASHRAE Trans 30(6):1590–1598
8. Xu GP, Dai YQ, Tou KW, Tso CP (1996) Theoretical analysis and optimization of a double-effect series-flow-type absorption chiller. Appl Therm Eng 16(12):975–987

9. Xu GP, Dai YQ (1997) Theoretical analysis and optimization of a double-effect parallel flow type absorption chiller. Appl Therm Eng 17(2):157–170
10. Sun DW (1997) Thermodynamic design data and optimum design maps for absorption refrigeration systems. Appl Therm Eng 17(3):211–221
11. Arun MB, Maiya MP, Murthy SS (2000) Equilibrium low pressure generator temperatures for double effect series flow absorption refrigeration systems. Appl Therm Eng 20:227–242
12. Arun MB, Maiya MP, Murthy SS (2001) Performance comparison of double effect parallel flow and series flow water lithium bromide absorption systems. Appl Therm Eng 21:1273–1279
13. Lee SF, Sherif SA (2001) Thermodynamic analysis of a lithium bromide/water absorption system for cooling and heating applications. Int J Energy Res 25:1019–1031
14. Lee SF, Sherif SA (2001) Second law analysis of various double effect lithium bromide/water absorption chillers. ASHRAE Trans 9(5):664–673
15. Gomri R, Hakimi R (2008) Second law analysis of double effect vapour absorption cooler system. Energy Convers Manag 49(11):3343–3348
16. Kaushik SC, Arora A (2009) Energy and exergy analysis of single effect and series flow double effect water-lithium bromide absorption refrigeration systems. Int J Refrig 32(6):1247–1258
17. Arora A, Kaushik SC (2009) Theoretical analysis of LiBr/H_2Oabsorption refrigeration systems. Int J Energy Res 33(15):1321–1340
18. Li Z, Ye X, Liu J (2014) Performance analysis of solar air cooled double effect LiBr/H_2O absorption cooling system in subtropical city. Energy Convers Manag 85:302–312
19. Bellos E, Tzivanidis C, Antonopoulos KA (2016) Exergetic, energetic and financial evaluation of solar driven absorption cooling system with various collector types. Appl Therm Eng 102:749–759
20. Misra RD, Sahoo PK, Sahoo S, Gupta A (2003) Thermoeconomic optimization of a single effect water/LiBr vapour absorption refrigeration system. Int J Refrig 26:158–169
21. Misra RD, Sahoo PK, Sahoo S, Gupta A (2005) Thermoeconomic evaluation and optimization of a double effect H_2O/LiBr vapour absorption refrigeration system. Int J Refrig 28(3):331–343
22. Farshi LG, Mahmoudi SMS, Rosen MA, Yari M, Amidpour M (2013) Exergoeconomic analysis of double effect absorption refrigeration systems. Energy Convers Manag 65:13–25
23. Grossman G, Wilk M, DeVault RC (1994) Simulation and performance analysis of triple-effect absorption cycles. ASHRAE Trans 100(2):452–462
24. Lee SF, Sherif SA (1999) Second law analysis of multi effect lithium bromide/water absorption chillers. ASHRAE Trans Ch-99-23-3: 1256–1266
25. Kaita Y (2002) Simulation results of triple-effect absorption cycles. Int J Refrig 25:999–1007
26. Herold KE, Radermacher R, Klein SA (1996) Absorption chillers and heat pumps. CRC Press, USA
27. Ma WB, Deng SM (1996) Theoretical analysis of low-temperature hot source driven two-stage LiBr/H_2O absorption refrigeration system. Int J Refrig 19(2):141–146
28. Sumathy K, Huang ZC, Li ZF (2002) Solar absorption cooling with low grade heat source—a strategy of development in south china. Sol Energy 72(2):155–165
29. Izquierdo M, Venegas M, Rodriguez P, Lecuona A (2004) Crystallization as a limit to develop solar air-cooled LiBr–H_2O absorption systems using low-grade heat. Sol Energy Mater Sol Cells 81(2):205–216
30. Crepinsek Z, Goricanec D, Krope J (2009) Comparison of the performances of absorption refrigeration cycles. WSEAS Trans Heat Mass Transf 3(4):65–76
31. Arivazhagan S, Murugesan SN, Saravanan R, Renganarayanan S (2005) Simulation studies on R134a—DMAC based half effect absorption cold storage systems. Energy Convers Manag 46:1703–1713
32. Arivazhagan S, Saravanan R, Renganarayanan S (2006) Experimental studies on HFC based two-stage half effect vapour absorption cooling system. Appl Therm Eng 26:1455–1462
33. Izquierdo M, Venegas M, García N, Palacios E (2005) Exergetic analysis of a double stage LiBr–H_2O thermal compressor cooled by air/water and driven by low grade heat. Energy Convers Manag 46:1029–1042

34. Gebreslassie BH, Medrano M, Boer D (2010) Exergy analysis of multi-effect water-LiBr absorption systems: from half to triple effect. Renew Energy 35:1773–1782
35. Gomri R (2010) Solar energy to drive half-effect absorption cooling system. Int J Therm Environ Eng 1(1):1–8
36. Lin P, Wang RZ, Xia ZZ (2011) Numerical investigation of a two stage air-cooled absorption refrigeration system for solar cooling: cycle analysis and absorption cooling performances. Renew Energy 36(5):1401–1412
37. Du S, Wang RZ, Lin P, Xu ZZ, Pan QW, Xu SC (2012) Experimental studies on air-cooled two-stage NH_3-H_2O solar absorption air-conditioning prototype. Energy 45(1):581–587
38. Domínguez-Inzunza LA, Hernández-Magallanes JA, Sandoval-Reyes M, Rivera, Florides GA, Kalogirou SA, Tassou SA, Wrobel LC (2014) Design and construction of a LiBr–water absorption machine. Energy Convers Manag 44:2483–2508
39. Cimsit C, Ozturk IT (2012) Analysis of compression–absorption cascade refrigeration cycles. Appl Therm Eng 40:311–317
40. Chinnappa JCV, Crees MR, Murthy SS, Srinivasan K (1993) Solar-assisted vapor compression/absorption cascaded air-conditioning systems. Sol Energy 50(5):453–458
41. Fernandez-Seara J, Sieres J, Va´zquez M (2006) Compression–absorption cascade refrigeration system. Appl Therm Eng 26:502–512
42. Kairouani L, Nehdi E (2006) Cooling performance and energy saving of a compression–absorption refrigeration system assisted by geothermal energy. Appl Therm Eng 26:288–294
43. Garimella S, Brown AM, Nagavarapu AK (2011) Waste heat driven absorption/vapor compression cascade refrigeration system for megawatt scale, high-flux, low-temperature cooling. Int J Refrig 34(8):1776–1785
44. Wang L, Ma A, Tan Y, Cui X, Cui H (2012) Study on solar-assisted cascade refrigeration system. Energy Procedia 16:1503–1509
45. Jain V, Kachhwaha SS, Sachdeva G (2013) Thermodynamic performance analysis of a vapor compression–absorption cascaded refrigeration system. Energy Convers Manag 75:685–700
46. Riffat SB, Shankland N (1993) Integration of absorption and vapour-compression systems. Appl Energy 46(4):303–316
47. Kim JS, Ziegler F, Lee H (2002) Simulation of the compressor-assisted triple-effect H_2O/LiBr absorption cooling cycles. Appl Therm Eng 22:295–308
48. Pratihar AK, Kaushik SC, Agarwal RS (2010) Simulation of an ammonia–water compression absorption refrigeration system for water chilling application. Int J Refrig 33:1386–1394
49. Kang YT, Hong H, Park KS (2004) Performance analysis of advanced hybrid GAX cycles, HGAX. Int J Refrig 27(4):442–448
50. Rameshkumar A, Udayakumar M (2007) Simulation studies on absorption compression cooler. Energy Convers Manag 48:2604–2610
51. Yari M, Zarin A, Mahmoudi SMS (2011) Energy and exergy analysis of GAX and GAX hybrid absorption refrigeration cycles. Renew Energy 36:2011–2020
52. Sun DW, Eames IW, Aphornratana S (1996) Evaluation of combined ejector-absorption refrigeration cycle-1: computer simulation. Int J Refrig 19(3):172–180
53. Hong D, Chen G, Tong L, He Y (2011) A novel ejector-absorption combined refrigeration cycle. Int J Refrig 34:1596–1603
54. Sozen A, Ozalp M, Arcaklioglu E (2004) Prospects for utilisation of solar driven ejector-absorption cooling system in Turkey. Appl Therm Eng 24:1019–1035
55. Wang J, Dai Y, Zhang T, Ma S (2009) Parametric analysis for a new combined power and ejector-absorption refrigeration cycle. Energy 34:1587–1593

Solid–Liquid Flow at Higher Concentration Through Bend

Navneet Kumar, D. B. Singh, D. R. Kaushal, S. K. Sharma, G. Singh and A. K. Singh

Abstract Slurry flow through a pipe bend is of most important concern as it contributes not only to high pressure drop and prone to extra erosion in the pipeline. Pipe bends also provide flexibility in a route of slurry pipelines. Pipe bends acquire relatively higher pressure drop. In this paper, experimental data generated for pressure drop 25 μm on fly ash slurry through 50 mm diameter of pipeline with velocity in the range 1–4 m/s at average efflux concentration of 32.52–46.61% (by volume) using the experimental setup (pilot test loop) facility and to carry out numerical simulations (CFD) using Ansys Fluent software intended for better visualization of complex flow pattern. Furthermore, simulated results have also been presented for qualitative analysis of fly ash slurry at the bend.

Keywords Slurry · Bend · CFD · Fly ash · Higher solids concentration

1 Introduction

The flow of slurry through pipe bend has a great significance to industries such as mineral processing plant, thermal power plants, and coal washeries. Slurry flow through pipeline bend is of very important part to the designers of slurry transportation systems. Present demand requires the fundamental accepting of the flow behavior of solid particles in such pipeline systems to get higher solid concentration. The researchers have attempted to develop models to forecast accurately the optimal design guideline for carrying solids using slurry pipeline system. The basic

N. Kumar (✉) · D. B. Singh · G. Singh · A. K. Singh
Department of Mechanical Engineering, Galgotias College of Engineering and Technology, Greater Noida, G.B. Nagar 201306, UP, India
e-mail: navneet_mech48@yahoo.com

D. R. Kaushal
Department of Civil Engineering, Indian Institute of Technology Delhi, Hauz Khas, New Delhi 110016, India

S. K. Sharma
Department of Mechanical Engineering, Amity University, Noida 201313, Uttar Pradesh, India

G. Zhang et al. (eds.), *Advances in Energy and Built Environment*, Lecture Notes in Civil Engineering 36, https://doi.org/10.1007/978-981-13-7557-6_20

slurry pipeline system comprised of three sub-systems is presented in Fig. 1, namely slurry preparation facility, pipeline and pumps, and terminal facility. In the slurry preparation sub-system, the solids are reduced to a convenient size by crushing and grinding and then mixed with the carrier fluid to achieve the desired value of concentration. The prepared slurry is stored in either agitated or non-agitated storage tanks. Before pumping the slurry, some additional precautions/treatments are carried out to transport for end use, and it depends on conveying solid materials. The second sub-system, namely the pipeline and the pumping equipments, is the main component of the transportation system, and its proper design determines the overall efficiency of the complete system. This system can primarily be divided into two main components, namely the pipeline and the pumping system. The design of the pumping system is reliant on the amount of the material to be conveyed and length of the pipeline. If intermediate pumping is required, intermediate pumping stations need to be provided. In the last sub-system, the slurry is received in storage tanks. It is then dewatered, filtered, and dried in accordance with the requirements of end utilization. Transporting solid particles through slurry pipelines will require the determination of physical and rheological properties and pressure drop for the flow of slurry through the pipeline. O'Brien [1] and Rouse [2] earliest studied and found that particles are kept in suspension for turbulent flow and proposed a simple one-dimensional diffusion model in turbulent streams like sediment transport in rivers and channels for predicting the particle concentration distribution. This model has a few serious restrictions for concentrated suspension having a large particle size distribution. Taking lead from above postulate, Ismail [3] modified the model of O'Brien [1] and Rouse [2] and correlated with mass transfer coefficient along shear stress–velocity gradient rapport employing von Karman universal velocity profile. Anderson and Jackson [4] used a model for the flow of fluid–solid mixtures to investigate the elbow erosion. This model employed to estimate the slurry flow field mechanism. Ayukawa [5] gave a theoretical approach to compute the pressure drop using energy considerations across the bend in a vertical plane for the flow of slurry. However, it is not weight due to the availability of limited experimental data. Kazanskij et al. [6] carried out the experiments to determine pressure drop in 100-mm pipeline to establish the effect of adding finer particles in coarse slurries. The percentage of fines was kept constant as 6.7% (by volume) of solid material for all the cases. From this study, they have concluded that for velocities close to deposition, the pressure drop reduces by up to 30% for medium sand and with increasing particle size and reduces pressure drop slightly. By increasing velocities, increases pressure drop and it is seen with addition of fine particles. They have identified the pressure drop reduction due to addition of fine particles, as a lubrication effect and partly due to an intensification of macro-turbulence in the two-phase flow. Wilson [7], based on the force balance concept, has also proposed a two-layer model. The concept involves dividing the moving solids into suspended and contact loads. Empirical correlations given by Wilson [8] and Wilson and Watt [9] are used to establish the suspended loads. The contribution to pressure loss by the contact load is evaluated following the force balance analysis originally proposed by Wilson [10] for stationary deposit. For transport of solid–liquid suspension, it is essential to evaluate the head loss for estimating

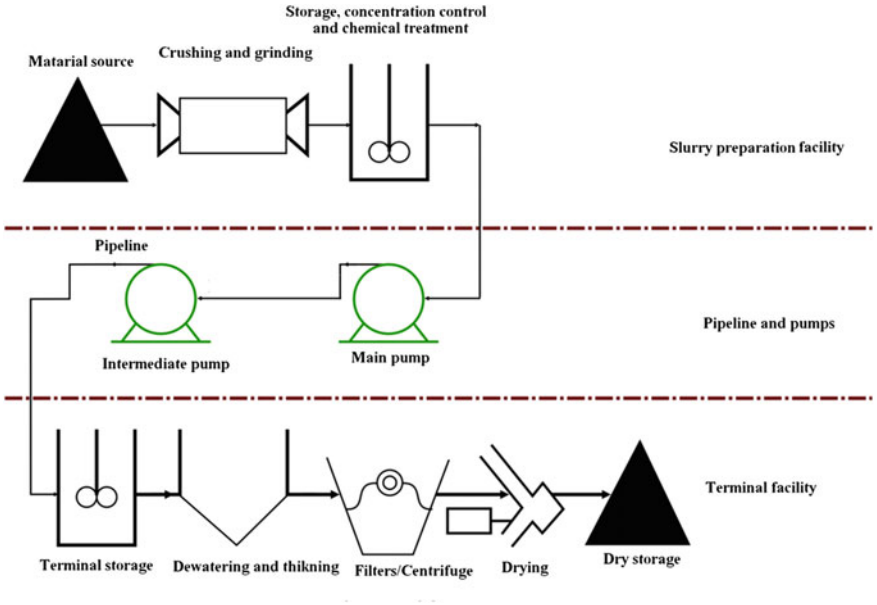

Fig. 1 Slurry transportation system for pipeline by Wasp et al. [11]

the power consumption. Wasp et al. [11] have proposed that the pressure drop in two parts; first as vehicle pressure drop (homogeneously distributed particles), and second is in the form of excess pressure drop owed to bed formation (heterogeneously distributed particles). Analytical technique recommended is repetitive one. The particular suspension is taken as altogether uniform for first iteration. Due to this condition, pressure gradient for slurry flow is calculated via Darcy–Weisbach equation which is expressed as follows:

$$i_{\text{vehicle}} = \frac{2 f_{\text{m}} V_{\text{m}}^2}{g D} \tag{1}$$

where

i_{vehicle} Vehicle pressure gradient, and
f_{m} Fanning friction factor determined by Wood's equation is given below:

$$f_{\text{m}} = a + b Re_{\text{m}}^{-c} \tag{2}$$

where

$$a = 0.026\left(\frac{\varepsilon}{D}\right)^{0.225} + 0.133\left(\frac{\varepsilon}{D}\right), \quad b = 22\left(\frac{\varepsilon}{D}\right)^{0.44}, \quad c = 1.62\left(\frac{\varepsilon}{D}\right)^{0.134}$$

Relative pipe roughness is (ε/D) which is evaluated (water data), normally taken prior from beginning of each measurement run with slurry and Reynolds number expressed as Re_{m} (solid–liquid mixture/slurry) which is calculated using Thomas [12] equation which is given as:

$$Re_{\mathrm{m}} = \frac{\rho_{\mathrm{m}} V_{\mathrm{m}} D}{\mu_{\mathrm{m}}} \tag{3}$$

$$\frac{\mu_{\mathrm{m}}}{\mu_1} = 1 + 2.5C_{\mathrm{Vf}} + 10.05C_{\mathrm{Vf}}^2 + 0.00273\ \exp(16.6C_{\mathrm{Vf}}) \tag{4}$$

where ρ_{m} is the mass density of slurry, carrier liquid (water) viscosity is μ_1, and C_{vf} is the average efflux concentration of slurry by vol., and V_{m} and g are the mixture velocity and acceleration due to gravity, respectively.

The rest solid particles are assumed to be suspended in the new carrier fluid, and its contribution is evaluated by the equation given by Durand [13]. Hayashi et al. [14], based on the experimental pressure drop versus velocity curves for iron ore concentrate slurries (particle size $d_{50} = 40$ μm and slurry concentration range 40–70% by weight), showed a curvature peculiar to a settling slurry when the velocity of flow is lower than the velocity at which solid particles start settling in the horizontal straight pipe (i.e., critical velocity), and the curve approaches a straight line parallel to that of water when the flow velocity exceeds the critical velocity. Shook et al. [15] have shown that mixing fine particles in coarse slurries in small fraction help to reduce the head loss. They have observed that 10% fine sand added to a slurry containing 18% coarse particles reduced the head loss nearly to that of 9% slurry. They have also concluded that two-layer model approach of Wilson [7] for coarse particle and mixed size flow works reasonably well for narrow size distributions. Verkerk [16] has investigated the flow of slurries in the concentration by weight of fly ash in the range of 5–73% in 100-mm pipeline. He has shown that addition of bottom ash in fly ash slurry at high concentration (in the past regime) reduces the pressure gradient significantly at low flow rates. Verkerk [17] has compared the performance of various models for the hydraulic design of pipeline and has concluded that pilot plant studies need to be conducted prior to the design stage for reliable hydraulic design of pipelines. Ahmed [18] modified the vehicle pressure drop calculations in Wasp et al. [11] model by incorporating of solid concentration effect on friction factor and achieved significant improvement in the pressure drop prediction at higher velocities. Kaushal [19] suggested that the velocity of flow minimum is generally kept more than deposition velocity of the solid particles as 0.5 m/s. On which deposition of solids takes place is known as deposition velocity. According to Wasp et al. [11] and Walton [20], particle diffusivity value increases with solid particle size. Kaushal et al. [21] modified their previous model for concentration profiles in pipe flow of multi-sized particulate slurries by in view of the reliance of particle diffusivity on particle size and efflux concentration. Again, Kaushal and Tomita [22] examined to predict pressure drops and concentration profiles of solids with experimental data and observed excellent results. Kim et al. [23] have performed experiments on sand–water slurry in circular and square pipes and found that hydraulic gradient for slurry flow in the square duct

is larger than the circular pipe. The selection of suitable multi-phase model of slurry pipeline flows for any numerical analysis has the key factor which subjects to the average efflux concentration of granular solid phase. As a result, researchers have developed some precise models for velocity profile, concentration distribution and pressure drop in hydraulic conveying of solids through pipelines. Kaushal and Kumar [24] have numerically simulated in the diameter of 50 mm at higher concentration for the flow of fly ash slurries to validate their experimental data. They proposed the optimum design methodology on the basis specific energy consumption for the disposal of fly ash slurry. CFD models require computer-based technique for fluid flow which uses numerical methods, and algorithms to the study of fluid flow, heat transfer systems, and related activities with the help of computer simulation and CFD modeling software by Versteeg and Malalasekra [25]. The continuity equations for conservation of mass, momentum, and energy could be derived with these models in the fluid flow. The selection of the appropriate multi-phase model (the discrete phase, Eulerian model, mixture) for differentiation of momentum transfer mechanism among the constituent phases depends on the concentration of solid particles and liquid proportion. Kumar et al. [26] have done CFD modeling of water-glass beads slurry of coarse particles using two-phase Eulerian model at different efflux concentration of solids in 54.9 mm horizontal pipeline. Recently, Kumar et al. [27] investigated experimentally on iron ore slurry in pipe diameter of 105 mm for seven different efflux concentrations, 0, 4.91, 7.83, 11.8, 16.6, 23.48, and 31% (by volume) using pilot plant test loop and found that the head loss increases due to an increase in solids concentration at any given flow velocity. As per literature review, it has been cleared that the experimental and computational studies on analysis of fly ash are limited at higher concentration. Due to attend these issues, experimental investigation and CFD modeling of 25 μm fly ash slurry flow have been performed through 50 mm horizontal 90° bend having higher solids concentration.

2 Experimental Investigation

2.1 Experimental Facility

Test loops are suitable for studying the effect of flow rates, mixture velocity and concentration on flow behavior, pressure drops, and solid concentration profiles. The pipe loop is available in the Fluid Mechanics Laboratory at IIT Delhi. Each test rig about 60 m long consists of the diameter of 50 and 105 mm pipes. A schematic view of loop is shown in Fig. 2. The pilot plant pipe loops are also described in details [27].

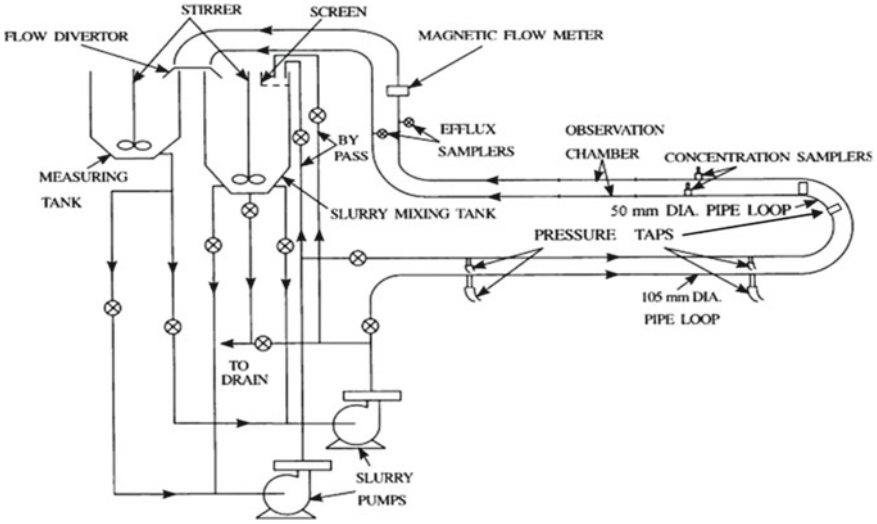

Fig. 2 Schematic diagram of experimental setup

2.2 Properties of Material Used and Range of Parameters

The experimentally determined specific gravity of fly ash is 2.03. The average particle size (d_{50}) of solid particles is 25 μm, and static settled concentration is 48.5% by volume (65.66% by weight). The slurry is having efflux concentration in the range of 0, 32.52, 36.55, 41.53, 43.52, and 46.61% (by volume), and mixture velocity ranges of 1–4 m/s, respectively.

2.3 Pressure Drop

Pressure drop in solid–liquid flow remains one of the most complex parameters to decide the slurry pump size. Figure 3 shows the variation of the observed pressure drop across a 90° bend with the flow velocity of fly ash slurries having different concentrations. Figure 3 gives the experimentally measured pressure drop for fly ash slurry in the pipe of 50 mm diameter at six different efflux concentrations, namely (0, 32.52, 36.55, 41.53, 43.52, and 46.61% by volume). It is observed that Fig. 3 shows higher pressure drop than that for water flow at all concentrations and at any given velocity. Therefore, it is also found that additional pressure drop due to solid particles increases with increase in concentration of slurry. This pattern is observed for all solid concentrations at different flow velocities.

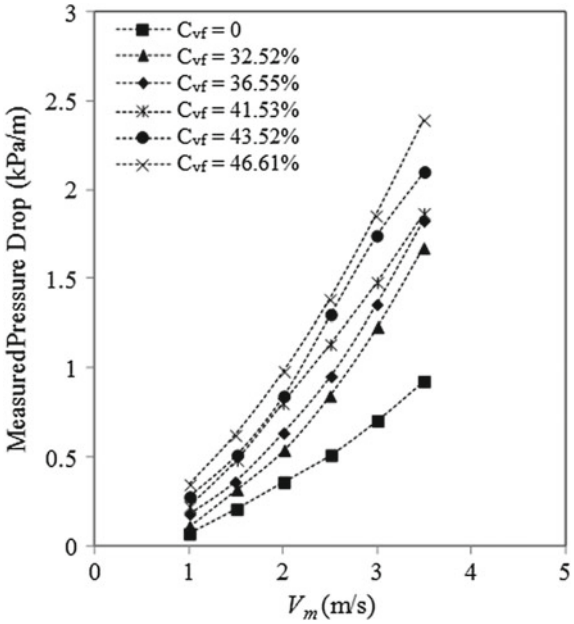

Fig. 3 Measured pressure drop across the test bend in 50 mm diameter of pipe

3 CFD Modeling

The slurry is not a dilute system of solid–liquid mixture through pipeline, and hence, the use of discrete phase model seems to be inappropriate to modeling the slurry flow. However, the mixture model and the Eulerian two-phase model seem suitable. Out of the two models, granular flow Eulerian model is adopted by the previous researchers with a presumption that the liquid and solid phases are continuous phases. The choice for adopting the granular flow model instead of simpler non-granular multi-fluid model is that the non-granular model does not account the effects of friction and collisions between the solid particles which are conceived to be essential for the complex solid–liquid flow.

3.1 Mathematical Model

Eulerian method uses volume averages by summation of the mass of every particle to measuring volume and divided by particulate phase volume. This model has need of averaging volume, which is large enough for the averaged property to yield a stationary value. The continuity equation provides conservation of mass, momentum, and energy of the particle and it is combined to expect the volume averaged properties of particle to entire the system. Eulerian model also proposed by Kumar et al. [26, 27] for slurry flow in pipe diameter of 54.9 and 105 mm, respectively. Slurry flow is

assumed as water "*f*" and solid "*s*" phases in Euler-Euler model which are separated to each one, yet retain interpenetrating continua so as to $\alpha_f + \alpha_s = 1$. Thus, the local concentration of fluid and solid phases is α_f and α_s by volume, respectively. Continuity and momentum equations are fulfilled by each one phase which is attached with coefficient of pressure and inter-phasial exchange. In the slurry, different forces acting on a single particle as:

1. Gradient due to static pressure, ∇P.
2. Gradient due to solid pressure, ∇Ps.
3. Drag force due to velocity difference between two phases, $K_{sf}\left(\vec{v}_s - \vec{v}_f\right)$ where K_{sf} is the inter-phasial drag coefficient, and solid and liquid phase velocity are $\vec{v}_s$ and $\vec{v}_f$, respectively.
4. Viscous forces, $\nabla.\overline{\overline{\tau_f}}$ where $\overline{\overline{\tau_f}}$ is the stress tensor for fluid.
5. Body forces, $\rho\vec{g}$, where density of concerned phase is ρ and acceleration due to gravity is g.
6. Virtual mass force, $C_{\text{vm}}\alpha_s\rho_f\left(\vec{v}_f.\nabla\vec{v}_f - \vec{v}_s.\nabla\vec{v}_s\right)$ where coefficient of virtual mass force is C_{vm} . Lift force, $C_{\text{L}}\alpha_s\rho_f\left(\vec{v}_s - \vec{v}_f\right) \times \left(\nabla \times \vec{v}_f\right)$ where lift coefficient is C_{L}.

Governing equations
Continuity equation

$$\nabla.(\alpha_t\rho_t\vec{v}_t) = 0 \tag{5}$$

where t is either s or f.

Momentum equations

For fluid phase:

$$\begin{aligned}\nabla.(\alpha_f\rho_f\vec{v}_f\vec{v}_f) = &-\alpha_f\nabla P + \nabla.(\overline{\overline{\tau_f}} + \overline{\overline{\tau_{t,f}}}) + \alpha_f\rho_f\vec{g} + K_{sf}(\vec{v}_s - \vec{v}_f)\\ &+ C_{\text{vm}}\alpha_s\rho_f(\vec{v}_s.\nabla\vec{v}_s - \vec{v}_f.\nabla\vec{v}_f) + C_{\text{L}}\alpha_s\rho_f(\vec{v}_f - \vec{v}_s) \times (\nabla \times \vec{v}_f)\end{aligned} \tag{6}$$

For solid phase:

$$\begin{aligned}\nabla.(\alpha_s\rho_s\vec{v}_s\vec{v}_s) = &-\alpha_s\nabla P - \nabla P_s + \nabla.(\overline{\overline{\tau_s}}) + \alpha_s\rho_s\vec{g}\\ &+ K_{fs}(\vec{v}_f - \vec{v}_s) + C_{\text{vm}}\alpha_s\rho_f(\vec{v}_f.\nabla\vec{v}_f - \vec{v}_s.\nabla\vec{v}_s)\\ &+ C_{\text{L}}\alpha_s\rho_f(\vec{v}_s - \vec{v}_f) \times (\nabla \times \vec{v}_f)\end{aligned} \tag{7}$$

Here, the Reynolds stress tensor is $\overline{\overline{\tau_{t,f}}}$, and viscous stress tensors for fluid and solid phases are $\overline{\overline{\tau_f}}$ and $\overline{\overline{\tau_s}}$, respectively, and are given below:

$$\overline{\overline{\tau_s}} = \alpha_s\mu_s\left(\nabla\vec{v}_s + \nabla\vec{v}_s^{tr}\right) + \alpha_s\left(\lambda_s - \frac{2}{3}\mu_s\right)\nabla.\vec{v}_s\overline{\overline{I}} \tag{8}$$

and

$$\overline{\overline{\tau_f}} = \alpha_f \mu_f \left(\nabla \vec{v}_f + \nabla \vec{v}_f^{tr} \right) \tag{9}$$

Here, indicates identity tensor is $\overline{\overline{I}}$ and superscript "*tr*" over velocity vector indicates transpose. λ_s is the bulk viscosity of solid and modeled using equation developed by Lun et al. [28] and is expressed as follows:

$$\lambda_s = \frac{4}{3} \alpha_s \rho_s d_s g_{o,ss} (1 + e_{ss}) \left(\frac{\Theta_s}{\pi} \right)^{\frac{1}{2}} \tag{10}$$

Particle diameter is d_s and the radial distribution function is $g_{o,ss}$, which gives the probability of particle touching another particle:

$$g_{o,ss} = \left[1 - \left(\frac{\alpha_s}{\alpha_{s,\max}} \right)^{\frac{1}{3}} \right]^{-1} \tag{11}$$

Here, static settled concentration of slurry is $\alpha_{s,\max}$.

3.1.1 Coupling Methodology

Pressure–velocity coupling with SIMPLE algorithm is selected for the simulations. In this method, velocities are calculated coupled with phases, but in a discriminative manner. Weiss et al. [29] proposed for block algebraic multi-grid scheme to simplify vector equation of velocity components of solid and liquid phases at the same time in the density-based solver.

3.1.2 Wall Functions

Because of extremely high gradients in flow parameters close to walls, concentration is required for this region. Very fine grids were adopted to acquire the accurate results near the wall region where gradient of flow quantities is high. So, a very fine boundary layer meshing is constructed in addition to selecting standard wall functions adjacent to the walls.

4 Numerical Result

4.1 Geometry Generation

The grid generated by GAMBIT which is having 266,670 cells. The number of cells adopted for the simulation was the same as that of the mesh used simulation for the simulation of pipe flow carrying single-phase fluid. The grid independence tests were conducted by doubling the number of cells present in the initial grid (266,670

cells). No improvement was found in simulation results. In this analysis, the flow domain having three boundaries as the inlet boundary, the outlet boundary and the wall boundary.

4.2 Solution Strategy and Convergence Criteria

The discretization scheme for the momentum was second-order upwind, whereas for volume fraction, turbulent kinetic and dissipation energies were first order. The continuing value for solution was fixed to 10^{-4} for each variable involved in simulation.

Modeling Results
Pressure Drop

Pressure profiles at mid-horizontal planes for solids concentrations ranging at 32.52 at different flow velocities are shown in Fig. 4. The pressure gradient across the

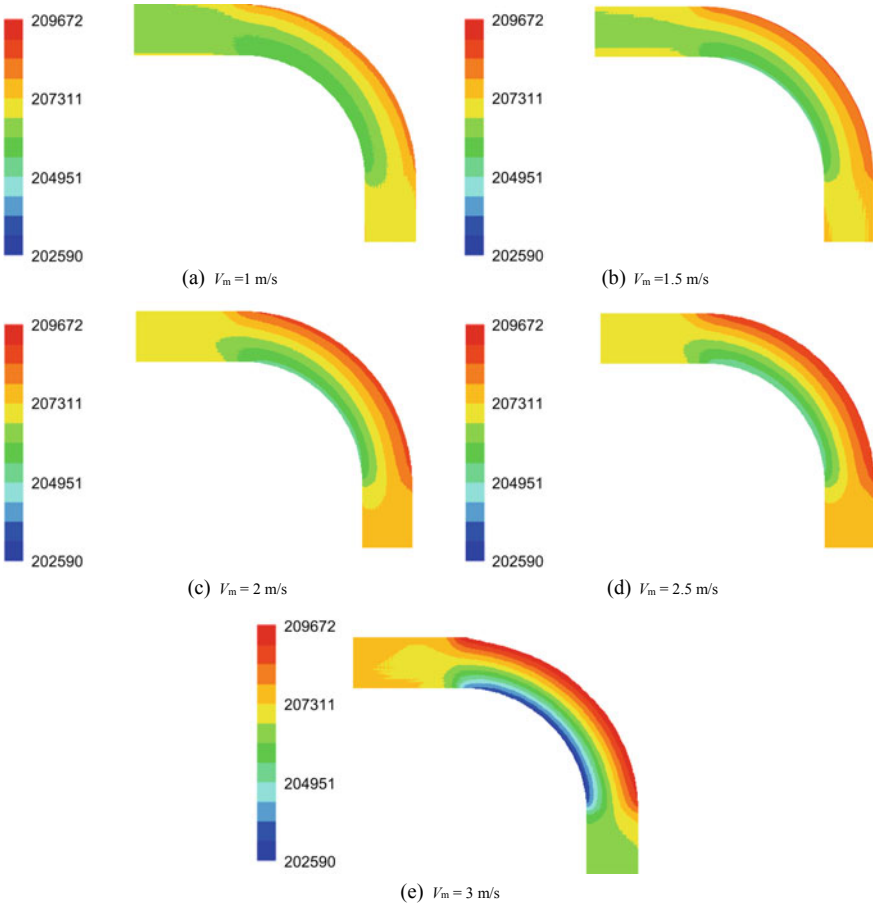

Fig. 4 Pressure profiles for fly ash slurry flow in pipe bend at mid-horizontal plane at $C_{vf} = 32.52\%$

bend increases with the increasing flow velocity. This increase in pressure gradient may be attributed to the increased interaction between particles. As the flow velocity increases, the larger pressure gradients take its effect to longer distances down the bend outlet.

5 Conclusions

A flow characteristic for solid–liquid mixture has been performed in diameter of 50 pipe loop in terms of pressure drop for pipe bend. Experimental data generated on 25 μm fly ash slurry at higher efflux concentrations. Pressure drops per meter have been presented experimentally. In this study, the Eulerian model of granular version has been adopted. It is most excellent suitable for slurry flows involving a wide range of volume fractions of solid phase. The use of the Eulerian model is owing to its capability to arrest the friction effect and collisions between particles. Also, contours of flow characteristics at bend have been presented by CFD simulations which are rather hard to be collected through experimentally. The practical gain to transport the solid at higher solid concentration through pipeline, and also when the pipeline is operated at the duration of low velocities, it will be subjected to minimum wear losses and less pressure drop.

References

1. O'Brien MP (1933) Review of the theory of turbulent flow and its relations to sediment transportation. Trans Am Geophys Union 14:487–491
2. Rouse H (1937) Modern conceptions of the mechanics of fluid turbulence. Trans ASCE 102:463–505
3. Ismail HM (1952) Turbulent transfer mechanism and suspended sediment in closed channels. Trans ASCE 117:409–446
4. Anderson TB, Jackson R (1967) A fluid mechanical description of fluidized beds equations of motion. Ind Eng Chem Fundam 6(4):527–539
5. Ayukawa K (1969) Pressure drop in hydraulic conveyance of solid materials through a bend in vertical plane. Bull Jpn Soc Mech Eng 12:1388–1396
6. Kazanskij I, Bruhl H, Hinsch J (1974) Influence of added fine particles on the flow structure and the pressure losses in sand-water mixture. In: Proceedings of hydrotransport 3, paper D2, BHRA fluid engineering, Colardo, USA, pp 11–12
7. Wilson KC (1976) A unified physically-based analysis of solid-liquid pipeline flow. In: Proceedings of the 4th international conference on the hydraulic transport of solids in pipes, Banff, Alberta, Paper A1, pp 1–16
8. Wilson KC (1972) A formula for the velocity required to initiate particle suspension in pipeline flow. In: Proceedings of hydrotransport 2, paper E2, BHRA fluid engineering, Cranfield, Badford England, pp 23–36
9. Wilson KC, Watt WE (1974) Influence of particle diameter on turbulent support of solids in pipeline. In: Proceedings of hydrotransport 3, paper D1, BHRA fluid engineering, Cranfield, Badford, England, pp 1–9

10. Wilson KC (1970) Slip point of beds in solid-liquid pipeline flow. Proc ASCE J Hydrol Div 96:1–12
11. Wasp EJ, Kenny JP, Gandhi RL (1977) Solid-liquid flow slurry pipeline transportation, 1st edn. Trans Tech Publications, London, England
12. Thomas DG (1965) Transport characteristics of suspensions: VIII. A note on the viscosity of Newtonian suspensions of uniform spherical particles. J Colloidal Sci 20:267–277
13. Durand R (1953) Basic relationships of the transportation of solids in pipe-experimental research. Proc Minnesota Int Hydraul Div ASCE, 89–103
14. Hayashi H, Sampei T, Oda S, Ohtomo S (1980) Some experimental studies on iron concentrate slurry transportation in pilot plant. In: Proceedings of the 7th international conference on the hydraulic transport of solids, Sendai, paper D2, pp 149–162
15. Shook CA, Gillies R, Hass DB, Husband WHW, Small M (1982) Flow of coarse and fine sand slurries in pipelines. J Pipeline 3:13–21
16. Verkerk CG (1982) Transport of fly ash slurries. In: Proceedings of 8th international conference on hydraulic transport of solids, Johannesburg, pp 307–316
17. Verkerk CG (1985) Some practical aspects of correlating empirical equations to experimental data in slurry pipeline transport. Bulk Solid Handling 5(4):21–31
18. Ahmed M (1991) Investigations of the flow of multi-sized heterogeneous slurries in straight pipe and pipe bends. Ph.D. Thesis, IIT Delhi
19. Kaushal DR (1995) Prediction of particle distribution in the flow of multi-sized particulate slurries through closed ducts and open channels. Ph.D. Thesis, Applied Mechanics Department, IIT Delhi
20. Walton IC (1995) Eddy diffusivity of solid particles in a turbulent liquid flow in a horizontal pipe. AIChE J (Am Inst Chem Eng) 41(7):1815–1820
21. Kaushal DR, Seshadri V, Singh SN (2002) Prediction of concentration and particle size distribution in the flow of multi-sized particulate slurry through rectangular ducts. Appl Math Model 26(10):941–952
22. Kaushal DR, Tomita Y (2002) Solid concentration profiles and pressure drop in pipeline flow of multisized particulate slurries. Int J Multiph Flow 28(10):1697–1717
23. Kim C, Lee M, Han C (2008) Hydraulic transport of sand-water mixtures in pipelines part I. Experiment. J Mech Sci Technol 22:2534–2541
24. Kaushal DR, Kumar N (2013) Optimum design of high concentration fly ash slurry disposal pipeline. Electron J Pol Agric Univ (EJPAU), 16–14
25. Versteeg HK, Malalasekera W (1995) An introduction to computational fluid dynamics: the finite volume method. Longman Scientific & Technical, Harlow
26. Kumar N, Gopaliya MK, Kaushal DR (2016) Modeling for slurry pipeline flow having coarse particles. Multiph Sci Technol 28(1):1–33
27. Kumar N, Gopaliya MK, Kaushal DR (2017) Experimental investigations and CFD modeling for flow of highly concentrated iron ore slurry through horizontal pipeline. Part Sci Technol An Int J, Taylor and Francis Publications (in press)
28. Lun CKK, Savage SB, Jeffrey DJ, Chepurniy N (1984) Kinetic theories for granular flow: inelastic particles in couette flow and slightly inelastic particles in a general flow field. J Fluid Mech 140:223–256
29. Weiss JM, Maruszewski JP, Smith WA (1999) Implicit solution of preconditioned Navier-Stokes equations using algebraic multigrid. AIAA J 37(1):29–36

Basin-Type Solar Distiller Associated with PVT Collectors—A Comprehensive Review

A. K. Singh, D. B. Singh, Navneet Kumar, V. K. Dwivedi, Gajendra Singh and Rajeev Kumar

Abstract Potable water is one of the prime needs for the existence of life on earth. However, the amount of water on earth is getting polluted due to industrial growth and fast urbanization. The need for potable water is gradually increasing due to exponential growth in human residents. The use of contaminated water is responsible for many waterborne diseases and it sometimes leads to death depending on the intensity of contamination . There are various methods for producing potable water; however, solar desalination is one of the best economical and user-friendly methods for potable water production as its operation resembles natural hydrological cycle and it works solely on solar energy. Basin-type active solar stills are capable of providing potable water as well as DC electric power to the society. The potable water yield for passive solar still ranges from 1 to 3 kg/m^2 and that for active solar still, it ranges from 4 to 15 kg/m^2. In this work, basin-type solar still integrated with PVT collectors has been reviewed and the future scope has been presented.

Keywords Basin-type solar still · PVT collectors · Productivity · Efficiency

1 Introduction

Filtered water is the basic necessity for survival and continued growth on the earth. More demand of fresh water by all sectors like agriculture, industry and domestic purposes forces to use more roughly to the freshly available and limited naturally available water sources like rivers, well, lake, and underground water. So, the controlled use with available sources and with new innovative and significant water purification techniques can manage the demand for potable water.

There are various techniques available for the purification of dirty water in which basin-type solar distillation method is the most versatile economic and self-sustainable technique which utilizes abundantly available solar energy.

A. K. Singh (✉) · D. B. Singh · N. Kumar · V. K. Dwivedi · G. Singh · R. Kumar
Department of Mechanical Engineering, Galgotias College of Engineering and Technology, Greater Noida, G.B. Nagar 201306, UP, India
e-mail: agashok26@gmail.com

G. Zhang et al. (eds.), *Advances in Energy and Built Environment*, Lecture Notes in Civil Engineering 36, https://doi.org/10.1007/978-981-13-7557-6_21

Basin-type solar still concept was initially mentioned by Nebbia and Menozzi [1]. Then, Malik et al. [2] presented the various methods of basin-type solar distillation techniques. Soliman [3] gave the utilization concept of flat plate collectors in the solar still. Basin-type active solar still was revealed by Rai and Tiwari [4]. A variety of different designs and different condensing covers in basin-type solar still were studied by various researchers [5–8]. Kumar et al. [9] studied active solar distiller with PVT collectors and reported better performance in comparison with the conventional solar still. Liu et al. [10] presented solar still with evacuated tubular collectors (ETC) than El-Baily et al. [11] reported the economic performance of active solar still. Singh and Tiwari [12] experimented on solar distiller with PVT collectors along with the partially covered system. Tiwari et al. [13] presented different active solar desalination systems with N number of PVT modules for the same climatic conditions and other design parameters.

2 Solar Still

Solar stills utilize solar energy as a primary source of energy and it may be either passive solar still or active solar still. Passive-type solar distiller consumes solar energy for heating basin water and producing potable distillate. Active solar distiller consumes solar energy for heating basin water and for further increase in potable water productivity, it uses secondary energy sources and related additional elements as electrical energy, PVT cells, flat plate collectors, etc. Active solar stills can also be the nocturnal type or high-temperature still type and active solar still in forced mode was presented by Rai and Tiwari [4], after that various active solar stills have been reported.

3 PVT Collectors

PVT collectors are photovoltaic–thermal modules associated with flat plate collectors which receive direct solar thermal energy useful for heating basin water and producing DC electrical power utilized for running pump and other electrical appliances. PVT collectors are applicable for active solar stills and other solar systems also and as a result, it shows better performance with greater efficiency than passive solar stills.

4 Solar Distiller Associated with PVT Collectors

Singh et al. [12] presented basin type active solar still of single and double slope type along with compound parabolic concentrator (CPC) and NPVT modules as shown in

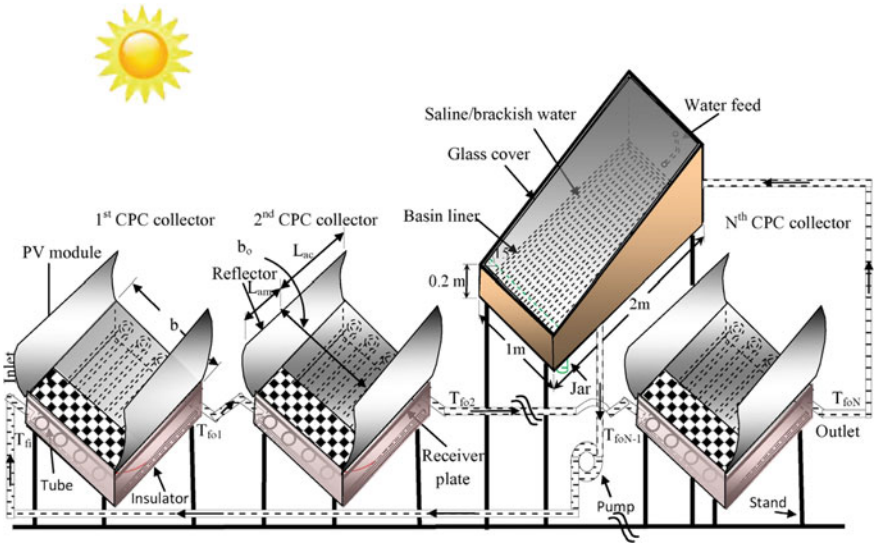

Fig. 1 Pictorial view of active basin-type solar distiller with NPVT CPC collectors [12]

Fig. 1 and result found double-slope solar still presents improved presentation than single-slope distiller as 4519.54 and 4757.70 kg annual distillate for single-slope and double-slope solar distiller correspondingly. It is because of more solar radiation gain in double slope solar still but single slope still is more economical than double-slope solar distiller as it has less embodied energy.

Sahota et al. [14] revealed double-slope active solar still with heat exchanger and nanofluids (water-based Al_2O_3, TiO_2, and CuO nanoparticles) as shown in Fig. 2. The result shows better performance for the combination of solar still with CuO water-based nanofluid and without heat exchanger as 2961.24 kg annual yield rather than other combinations of solar distillation systems with and without nanofluids and heat exchanger. As heat exchanger in the given set up in not much economical due to its high embodied energy and still with water-based CuO performs better due to its best suitability under recommended concentration ratio of nanofluid which is the best part of this type of solar stills.

Singh [15] presented the improved recital of single-slope basin-type solar distiller with NPVT flat plate collectors and found 21.98% cogeneration efficiency and 5845.23 kg annual yield which are much better than other solar systems with same configuration in similar climatic conditions due to better design parameters and optimum numbers of NPVT flat plate collectors as it utilizes maximum solar irradiation energy with minimum losses and minimum embodied energy.

Singh et al. [16] presented an experimental study for active double-slope solar distiller with CPC and NPVT collectors and found reasonable result as 4757.70 kg annual distillate output which is less than single-slope solar distiller with NPVT collectors.

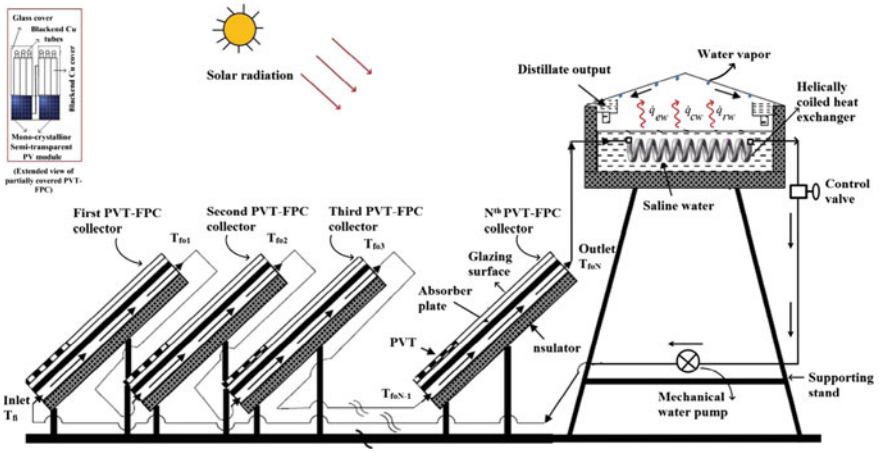

Fig. 2 Active double slope with NPVT flat plate collectors with helical heat exchanger and nanofluids [14]

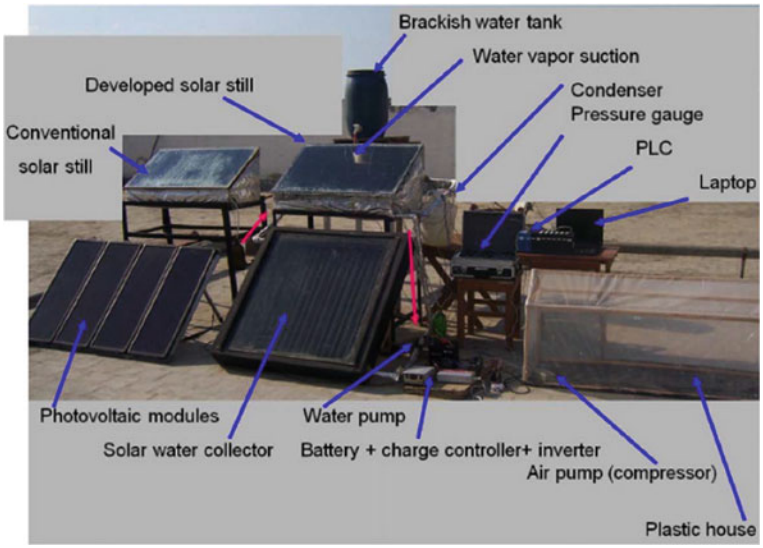

Fig. 3 Setup of conventional and developed solar still with NPVT and flat plate collectors [17]

Eltawil [17] presented an experimental study on conventional and developed single-slope solar still with PVT modules and flat plate collectors as shown in Fig. 3 and found developed single-slope solar still performs better with 5.450 l/m^2/day distillate amount produced as compared to usual single-slope solar distiller.

Al-Nimr Moh'd et al. [18] presented a novel concept of solar distiller with PVT and outside finned condenser as shown in Fig. 4 and reported better performance due to additional condensation and evaporation because of finned condenser as it

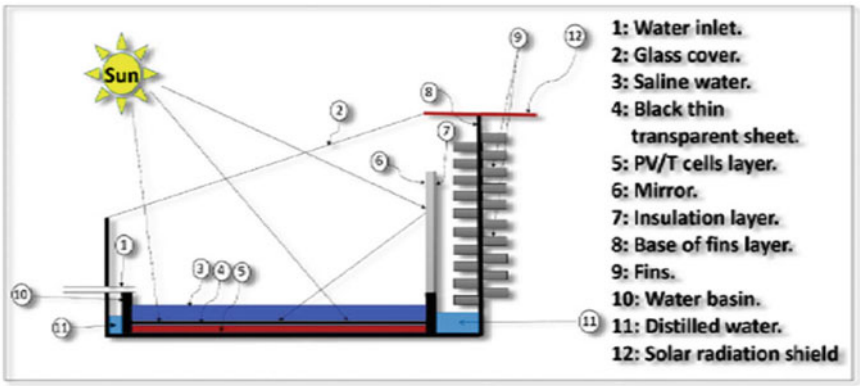

Fig. 4 Image of solar distiller with PV/T and outside finned condenser [18]

increases condensation surface area and a solar radiation shield provides a better environment for condensation which leads to more distillate output.

Yari et al. [19] gave another method for desalting impure water as well as electricity production with the help of PVT modules as shown in Fig. 5 which is solar distiller covered with transparent PVT module associated with ETC in natural circulation mode. The result was found with better effects as per the given Eq. 7 and shown in Fig. 6 as per the given thermal modeling of active single-slope solar distiller with ETC and semi-transparent PVT module.

Energy balance equation for semi-transparent photovoltaic module

$$R_g \alpha_c \beta_c I_s(t) A_c + h_{1w} A_b (T_{sw} - T_c) = h_o A_c (T_c - T_a) + \eta_m R_g \beta_c I_s(t) A_c \tag{1}$$

where α_c, β_c are the design parameters of the PVT module and the electrical efficiency (η_m) given as follows:

$$\eta_m = \eta_{r,m}[1 - \beta_{r,m}(T_c - 25) \tag{2}$$

Solar still basin liner energy balance equation

$$\alpha'_b (1 - \beta_c) R_g I_s(I) A_b = h_{bw} A_b (T_b - T_{sw}) + h_{ba} A_b (T_b - T_a) \tag{3}$$

Energy balance equation for the water mass inside the solar distillation system

$$N_c \dot{m} C_{cw} (T_{cw} - T_{sw}) + \alpha'_w (1 - \beta_c) R_g A_b I_s(t) + h_{bw} A_b (T_b - T_{sw}) = h_{1w} A_b (T_{sw} - T_c) + M_{sw} C_{sw} \frac{dT_{sw}}{dt} \tag{4}$$

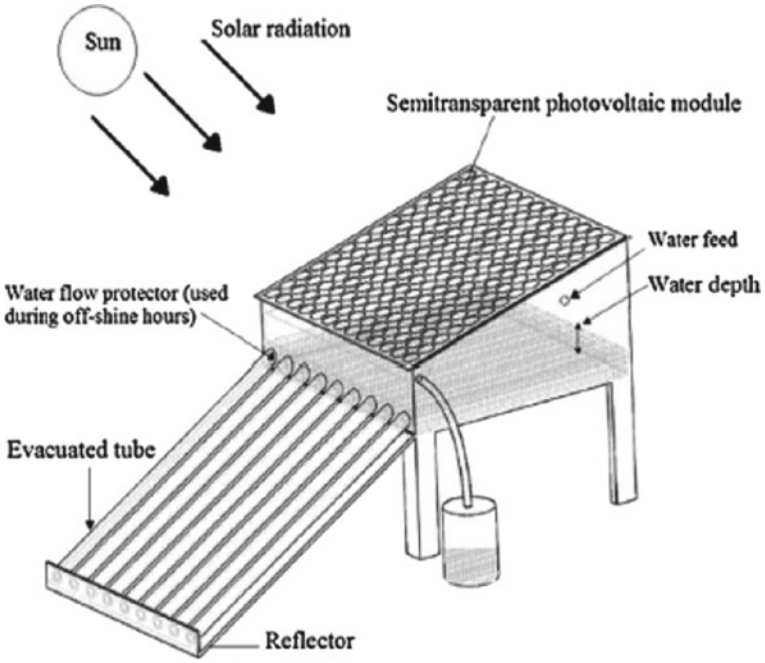

Fig. 5 Line diagram of solar distiller with ETC and semi-transparent PVT module [19]

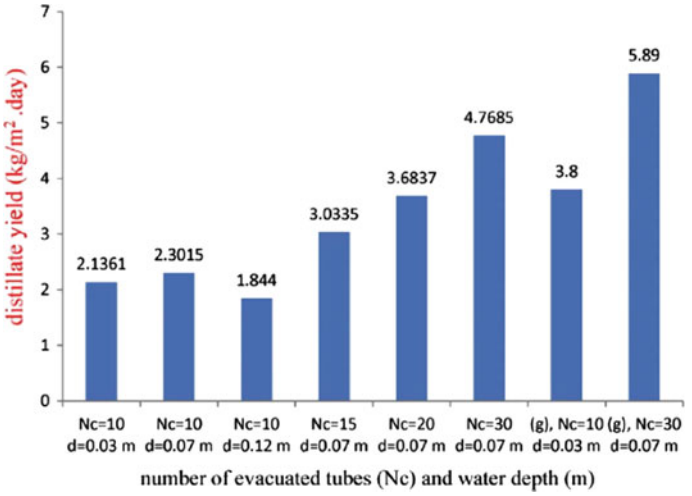

Fig. 6 Variation in yield for various combinations of evacuated tube number and water depth NETC and NPVT collectors [19], (g) [20]

Energy balance equation for ETC

$$Q_{u,\text{collector}} = M_{cw}C_{cw}\frac{\mathrm{d}T_{cw}}{\mathrm{d}t} + N_c\dot{m}C_{cw}(T_{cw} - T_{sw}) \tag{5}$$

where, $Q_{u,\text{collector}}$ represents the useful energy collected to the ETC.

$$T_{sw} = \frac{1}{(\lambda^+ - \lambda^-)}\left[\left(\frac{1-\mathrm{e}^{-c+t}}{c^+}\right)\left(g_1(t) + \lambda^+ g_2(t)\right) - \left(\frac{1-\mathrm{e}^{-c-t}}{c^-}\right)\left(g_1(t) + \lambda^- g_2(t)\right)\right.$$
$$\left. + T_{sw0}\left(\lambda^+\mathrm{e}^{c+t} - \lambda^-\mathrm{e}^{c-t}\right) + T_{cw0}\left(\mathrm{e}^{c-t} - \mathrm{e}^{c+t}\right)\right] \tag{6}$$

Equation for mass flow rate for distillate output

$$\dot{m}_y = \frac{h_{ew}(T_{sw} - T_c)}{L} \tag{7}$$

All the unknowns in the above equations may be referred by Yari et al. [19]. Further basin type of review studies have been given by the researchers [21, 22]

5 Conclusions

In the present review, various different types of solar distillers especially basin-type solar stills integrated with PVT collectors have been reviewed and the following conclusions have been made as follows:

- Both potable water output and electricity generation are mainly dependent on available solar energy, intensity, and absorbing capability.
- Numbers of solar collectors improve the efficiency and potable water productivity up to the optimized number of collectors with better design parameters.
- Higher temperature of PVT module decreases the efficiency of solar cells which leads to the poor performance of solar still and not economic as well.
- Solar distiller with NPVT module performs better with 5.450 l/m^2/day distillate as compared to others in comparison to distillate output.
- Solar still with PVT module flat plate collectors is itself efficient and self-sustainable for potable water production and electricity production.

6 Future Scope

PVT modules and collectors may be freely placed by the side walls of solar still and also it should be used with optimized dimensions for maximum economic benefits. Auto-cleaning system or some economic arrangement should be there for cleaning PVT module for maintaining better efficiency and utilization in the production of electrical power and distillate output as well.

References

1. Nebbia G, Menozzi GN (1966) Historical aspects of dissalzione. Acqua Ind 41(42):3–20
2. Malik MAS, Tiwari GN, Kumar A, Sodha MS (1982) Solar distillation. Pergamon Press, Oxford
3. Soliman HS (1976) Solar still coupled with solar water. Mosul University, Mosul
4. Rai SN, Tiwari GN (1983) Single basin solar still coupled with flat plate collector. Energy Convers Manage 23:145–149
5. Tiwari GN, Sharma SB, Sodha MS (1984) Performance of double condensing cover multi wick solar still. Energy Convers Manage 24:155–159
6. Tiwari GN, Garg HP (1985) Studies on various designs of solar distillation systems. Solar Wind Technol 1:161–165
7. Singh AK, Singh DB, Mallick A, Kumar N (2018) Energy matrices and efficiency analyses of solar distiller units: a review. Solar Energy 173:53–75
8. Singh AK, Chattopadhayaya S, Singh DB, Kumar N (2017) Performance study for active solar stills based on energy metrics: a short review. J Refrig Air Conditioning Heating Vent 4(3):21–26
9. Kumar S, Tiwari GN (2009) Life cycle cost analysis of single slope hybrid (PV/T) active solar still. Appl Eng 86:1995–2004
10. Liu X, Chen W, Gu M, Shen S, Cao G (2013) Thermal and economic analysis of solar desalination system with evacuated tubular collectors. Solar Energy 93:144–150
11. El-Bialy E, Shalaby SM, Kabeel AE, Fathy AM (2016) Cost analysis for several solar desalination systems. Desalination 384:12–30
12. Singh DB, Tiwari GN (2016) Effect of energy metrics on life cycle cost analysis of partially covered photovoltaic compound parabolic concentrator collector active solar distillation system. Desalination 397:5–91
13. Tiwari GN, Sahota L (2016) Review on the energy and economic efficiencies of passive and active solar distillation systems. Desalination. http://dx.doi.org/10.1016/j.desal.2016.08.023
14. Sahota L, Tiwari GN (2017) Exergoeconomic and enviroeconomic analysis of hybrid double slope solar still loaded with nanofluids. Energy Convers Manag 148:413–430
15. Singh DB (2017) Improving the performance of single slope solar still by including N identical PVT collectors. Appl Thermal Eng. https://doi.org/10.1016/j.applthermaleng.2017.11.146
16. Singh DB, Yadav JK, Dwivedi VK, Kumar S, Tiwari GN, Al-Helal IM (2016) Experimental studies of active solar still integrated with two hybrid PVT collectors. Sol Energy 130:207–223
17. Eltawil Mohmed A, Omara ZM (2014) Enhancing the solar still performance using photovoltaic, flat plate collector and hot air. Desalination 349:1–9
18. Al-Nimr Moh'd A, Al-Ammari Wahib A (2016) A novel hybrid PV-distillation system. Solar Energy 135:874–883
19. Yari M, Mazareh AE, Mehr AS (2016) A novel cogeneration system for sustainable water and power production by integration of a solar still and PV module. Desalination 398:1–11
20. Singh RV, Kumar S, Hasan MM, Khan ME, Tiwari GN (2013) Performance of a solar still integrated with evacuated tube collector in natural mode. Desalination 318:25–33
21. Singh DB, Singh AK, Navneet K, Dwivedi VK, Yadav JK, Singh G (2019) Performance analysis of special design single basin passive solar distillation systems: a comprehensive review. https://doi.org/10.1007/978-981-13-6469-3_27
22. Dharamveer, Samsher, Singh DB, Singh AK, Kumar N (2019) Solar distiller unit loaded with nanofluid—a short review. https://doi.org/10.1007/978-981-13-6577-55_24

An Easy-to-Understand Expert System for the Prediction of Direct, Diffuse and Global Solar Radiations in Indian Region

R. K. Tomar, Prakhar Duggal and N. D. Kaushika

Abstract Building is a modifier of indoor climate to provide comfort to its inhabitant. The building walls and roof often have sloppy surfaces, and the thermal performance evaluation of the building requires simultaneous values of direct, diffuse and global solar radiation. Such values are available only for limited locations. Consequently, the thermal evaluation of building in regions of complex climate and design of efficient air-conditioned system has continually suffered a setback. This paper presents an easy-to-understand expert system for the prediction of direct, diffuse and global solar radiation in the Indian region. The approach is based on a multi-frame output model of the artificial neural network analysis. The computational algorithm includes estimation of direct, diffuse and global components of solar radiation through clear sky conditions. The deviations of these estimates from measurements are considered to be due to random weather phenomena characterized by atmospheric clearness indices which are determined by an artificial neural network analysis based on interrelationship of direct, diffuse and global solar radiation. The target values of atmospheric clearness index achieved as a result of ANN analysis are expressed by an explicit polynomial representation which in turn enables the determination of atmospheric clearness index as a function of latitude and longitude of location, time of the day and month of the year. The whole computational scheme is embedded in a graphical user interface which is designed to assist a wide spectrum of users such as energy planner, engineers, architects, scientists and researchers to predict direct, diffuse and global solar radiation.

Keywords Expert system approach · Solar radiation prediction · Artificial neural network model

R. K. Tomar (✉) · P. Duggal
Department of Civil Engineering, Amity University,
Noida 201313, Uttar Pradesh, India
e-mail: rktomar@amity.edu

N. D. Kaushika
Centre for Energy Studies, Indian Institute of Technology, Hauz khas,
New Delhi 110016, India

G. Zhang et al. (eds.), *Advances in Energy and Built Environment*, Lecture Notes in Civil Engineering 36, https://doi.org/10.1007/978-981-13-7557-6_22

1 Introduction

The primary objective of building is to provide comfort to its inhabitants. The early buildings were in the form of primitive wooden huts and the habitats which focused on the use of locally available materials. These were followed by brick and concrete structures in both rural and urban areas. At the outset concerns of economy, utility, durability and common aspirations were indirectly linked to making structures as comfortable and convenient as possible. In urban areas owing to land use and other considerations, multi-storey buildings became popular. It is in this pursuit that present-day buildings stand as the third largest consumer of fossil energy next to industry and agriculture. When a number of multi-storey buildings are located in close proximity, they would create a heat-island effect. Consequently, thermal design of building is an essential element of greening the building.

In recent years, artificial-neural-network-based models have received steadily increasing attention for the estimation of solar radiation, a pragmatic approach to create a relationship among data with dynamic, nonlinear, complex and noise-ridden behaviour. The authors from various regions [1–18] of the world have investigated the efficacy of the ANN models. Recently, Tomar et al. [19] applied the ANN-based estimation and prediction model for direct solar radiation. This approach estimates the value of direct solar radiation through clear atmosphere through relationship between atmospheric transmittance factors and sun–earth geometry. The approach also takes into account variation owing to weather and climate phenomena through a mix parameter referring to atmospheric clearness index, which is found out with the help of ANN-based computational model estimation. The mentioned investigation determines parameter CI by using substantial sets of continuing assessment for climatic parameters like mean duration of sunshine per hour and mean hourly solar radiation. Consequently, the contour maps are drawn for atmospheric clearness index with respect to time of the day, latitude and month of the year.

In the end, using these maps, direct solar radiation estimation methodology at random region is presented. Result by this approach for arbitrary locations was exhibited to be compatible with NASA SSE insolation data set extracted from a physical model. More recently, Kaushika et al. [20] based and used the approach on multi-frame output model of the artificial neural network analysis. These authors predicted direct, diffuse and global solar radiation for several locations in the Indian region. In this paper, we extensively use multi-frame output ANN model for extensive number of stations covering the Indian continent and use an expert system approach to enable reliable prediction of diffuse, direct and global solar radiation in the Indian continent. The approach uses the computational scheme embedded in the graphical user interface (GUI) which is planned to benefit a wide spectrum of users such as energy planner, engineers, architects, researchers and scientists to anticipate diffuse, direct and global solar radiation.

2 Computational Algorithm

By following simple model given by Hottel [21], estimation of solar beam radiation on earth beneath cloudless upper atmosphere as first approximation, with the particulars from atmospheric transmittance, climate and sun–earth geometry type can be made. Model with superlative error of 0.4% suits an uncomplicated mixed-grey-gas model and works on cloudless day all wavelength transmittance of solar radiation through the 19,622 standard atmospheres. The model makes an allowance for the vertical distribution with consideration of climate type for water and ozone.

The model credits that estimation for the diffuse component can be combined and altered for percentage sunshine and cloudiness, etc. The relation for solar beam radiation

$$S_{\mathrm{bn}} = I_o\left(a_o + a_1 \mathrm{e}^{-k \sec \theta_z}\right) \tag{1}$$

The equation has all wavelength transmittance of solar radiation through the atmosphere [22] with day of the year, time of the day and position on earth as variables.

The expression for I_o, the extra-terrestrial radiation is

$$I_o = I_{\mathrm{Sc}}[1 + 0.033 \cos(360N/365)] \tag{2}$$

I_{sc} is the solar constant and N is the number of day and the θ_z is the solar zenith angle or solar incident angle on a horizontal plane.

The beam radiation indenting on a horizontal surface is hence given by

$$S_{\mathrm{bh}} = S_{\mathrm{bn}} \cos \theta_z \tag{3}$$

Liu and Jordan [23] give an equation for beam radiation in particular of atmospheric transmittance providing estimation for the diffuse component of solar radiation indenting on horizontal surface (S_{dh})

$$S_{\mathrm{dh}} = I_o \cos \theta_z\left[0.2710 - 0.2939\left(a_o + a_1 \mathrm{e}^{-k \sec \theta_z}\right)\right] \tag{4}$$

The above expression gives approximate result and should be used only as a guide. The global radiation is expressed as

$$S_{\mathrm{gh}} = S_{\mathrm{bh}} + S_{\mathrm{dh}} \tag{5}$$

Equations (3–5) can be used for the estimation of the values of diffuse, direct and global radiations. Deviation caused by climate and weather phenomena for these estimates may be considered, which are characterized by the atmospheric clearness indices [20] as follows

Atmospheric clearness index
= Observed value of solar radiation/Calculated value of solar radiation

Based on the result and analysis, we consequently develop an artificial neural network model to determine atmospheric clearness indices.

3 Artificial Neural Network (ANN) Model

3.1 Concept and Approach

ANN technique is inspired by the function of biological neuron, as the structural constituent of brain [24]. Biological neuron networks are nonlinear, parallel information processing systems and are bestowed with characteristics such as wholeness, fault sufferance and capability to learn by adapting to changes in the surrounding environment through connection strength. A simple biological neuron system is shown in Fig. 1. Dendrites are branching fibres extending from the cell body or soma. They receive stimuli (activation) from other neurons. The soma or cell body consists of nucleus and other structures, assisting chemical processes and generation of neurotransmitters.

Axon is a singular fibre that takes instructions far from the soma to the synaptic sites of other neurons (dendrites and soma). Axon hillock is the cumulativeness site for inbound instruction at any moment. The collective impact of all neurons conducting signals to a given neuron actuates whether or not to initiate an action potential at the axon hillock and to be propagated onwards axon to the synaptic sites of billions of interconnected neurons to form an intelligent system.

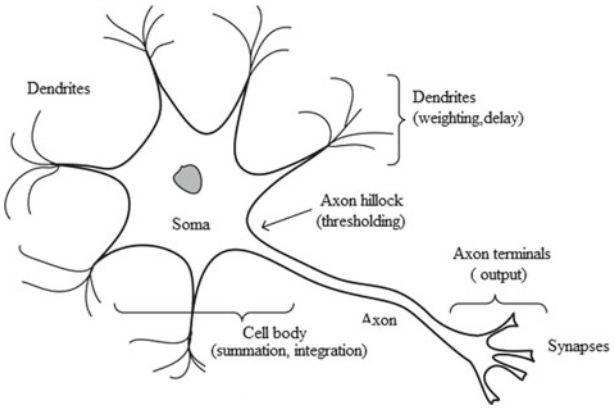

Fig. 1 Schematic of biological neural network

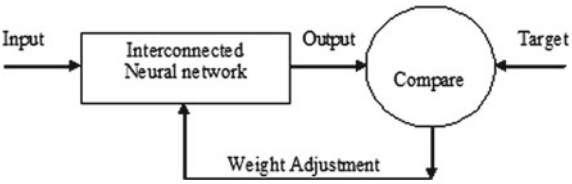

Fig. 2 Learning schematic of artificial neural network

Based on the above principle, the artificial neural network structures involve three types of layers: input layer, hidden layer and output layer, composed of simple elements (neurons) operating in parallel [25]. The artificial neural networks can be classified into two major categories: feedforward and feedback (recurrent) networks. The former involves loop-less network connections while one or more loop may prevail in the latter. The commonly used feedforward network is multi-layer perceptron (MLP). In this network, the input layer neurons act as interface between the input signal (x_i, $i = 1, 2, 3 \ldots$) and the hidden layer neurons. Each hidden layer neuron (jth) adds up the input signal modified with weight (w_{ji}) in input layer and computes its output y_j as a function f of the sum as follows

$$y_j = f\left[\sum_{i=1}^{n}\left(w_{ji}x_i\right)\right] \tag{6}$$

The output of the neurons in the output layer is computed in accordance with the learning rule which is a procedure for modifying the weights and biases; it is referred to as training algorithm. These are classified as follows;

(a) Unsupervised learning: There are no target outputs. Weights are modified in response to input only. They can perform clustering operations.
(b) Supervised learning: In supervised learning, the exacting input leads to distinct target output. Such a situation is shown in Fig. 2. The perceptron learning rule, back propagation algorithm, falls in this category.

3.2 Methodology of Using the MATLAB for the Determination of Clearness Indices

We have used the fitting tool (nftool). This tool provides the facility of mapping between a data set of numeric inputs and a set of numeric targets. The follow-up command opens up the selected data window which includes getting the input and target data from workspace in the matrix form (Fig. 3).

The atmospheric clearness indices $CI_{b,}$ CI_d and CI_g for beam, diffuse and global solar radiations are to be hold as numeric target variables in ANN analysis with latitude, longitude, altitude of location, local mean time, month of the year, monthly mean hourly total rainfall, monthly mean hourly relative humidity, atmospheric tem-

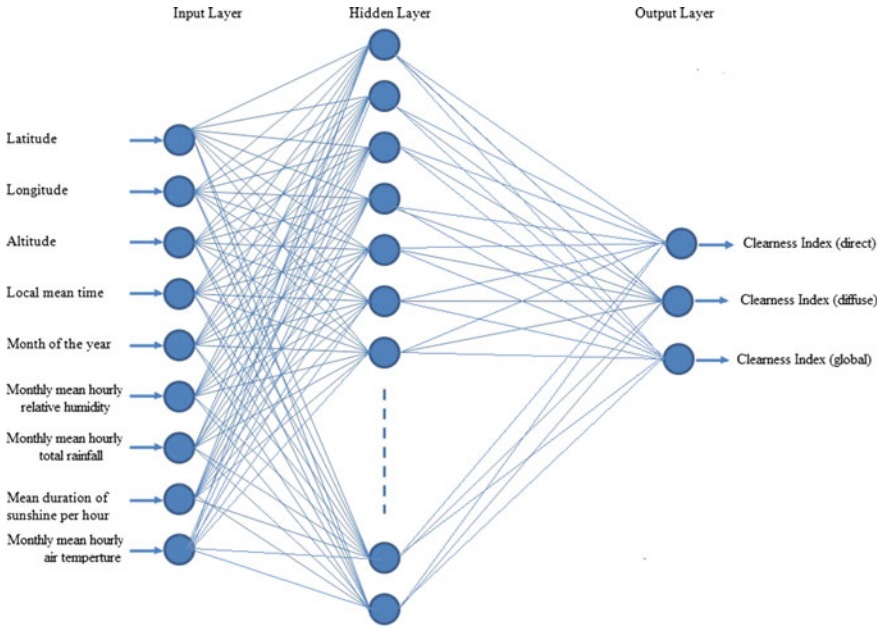

Fig. 3 Schematic of multi-frame output neural network

perature and monthly mean duration of sunshine per hour as input variable criterion. The data for 15 stations spread over the entire Indian continent published by Mani et al. [26, 27] have been used for input and output mapping of the network. The stations cover by far the widest range of latitudes (8.48° N to 34.08° N) and longitudes (72.18° E to 92.72° E) used for solar radiation estimation in the Indian region. The mapping process, therefore, used an input determinant of [9 × 2160] and an output determinant of [3 × 2160]. The wizard randomly divides up the sample in training, validation and testing categories. (e.g. 70, 15 and 15%, respectively). The next step is setting up the network architecture (e.g. the number of hidden neurons and the runs for optimal mapping). The training performance is evaluated regularly through the mean square error (MSE) (average squared difference between network output and target value) and the regression R value (correlation between network output and target value). Less the values of MSE, better they are and zero stands for perfect fitting. Similarly, R values of one mean a close relationship and zeros a causal relationship. Optimal number for neurons was estimated as thirteen and at the third run, best fitting was achieved as illustrated in Fig. 4. Finally, the target CI values were achieved and were transferred to the workspace for further analysis.

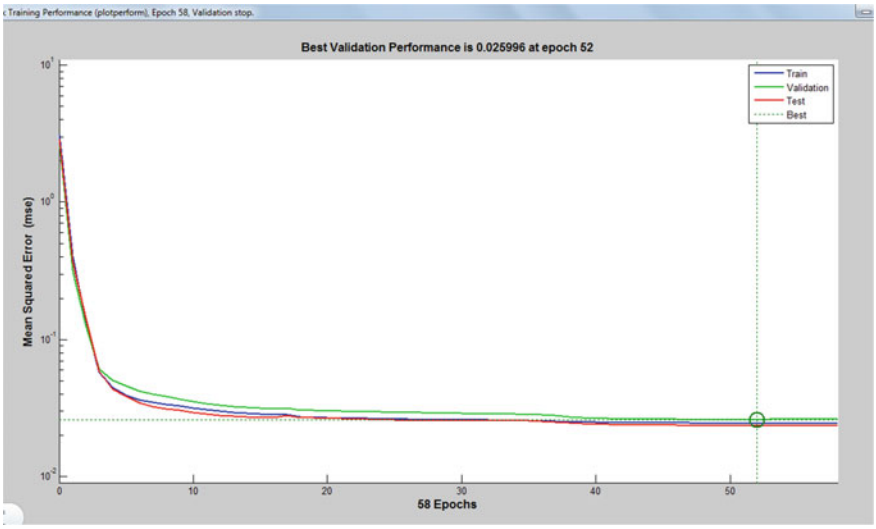

Fig. 4 MATLAB window exhibiting the training performance of ANN analysis

4 Prediction Methodology

The result of ANN analysis gives target values of atmospheric clearness indices which may be used to develop a technique predicting diffuse, direct and global components of solar radiation as the objective of time of the day, month of the year and geographical coordinates of the location as follows

1. Contour map approach
2. An approach involving polynomial representation of clearness index and its variations.

4.1 Contour Map Representation of Clearness Index

The approach to diffuse, direct and global radiations is simple through contour maps of the clearness indices. The value of these radiations upon multiplication with the corresponding values intended from the simple cloudless sky model will yield the values of direct, diffuse and global solar radiations compatible with observed values. Illustrative contour maps for clearness indices of diffuse, direct and global solar radiations of 09:00, 12:00, 15:00 h (local mean time) as an outcome of month of the year, latitude of the location at various hours of the day are shown in Figs. 5a–c, 6a–c and 7a–c, respectively.

In practice, using simple estimation, contours can be used for the prediction of solar radiation for arbitary location in the Indian region. However, the process of

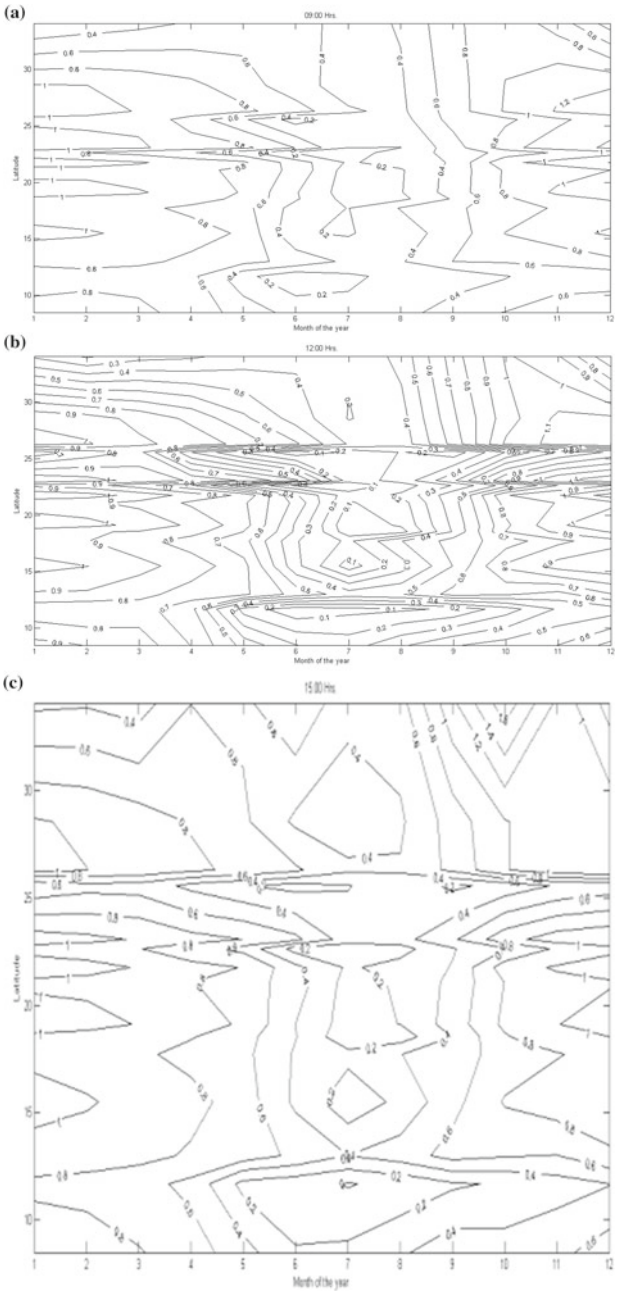

Fig. 5 Contour map of CI of direct solar radiation for Indian region at **a** 09.00 h (local mean time), **b** 12.00 h (local mean time) and **c** 15.00 h (local mean time)

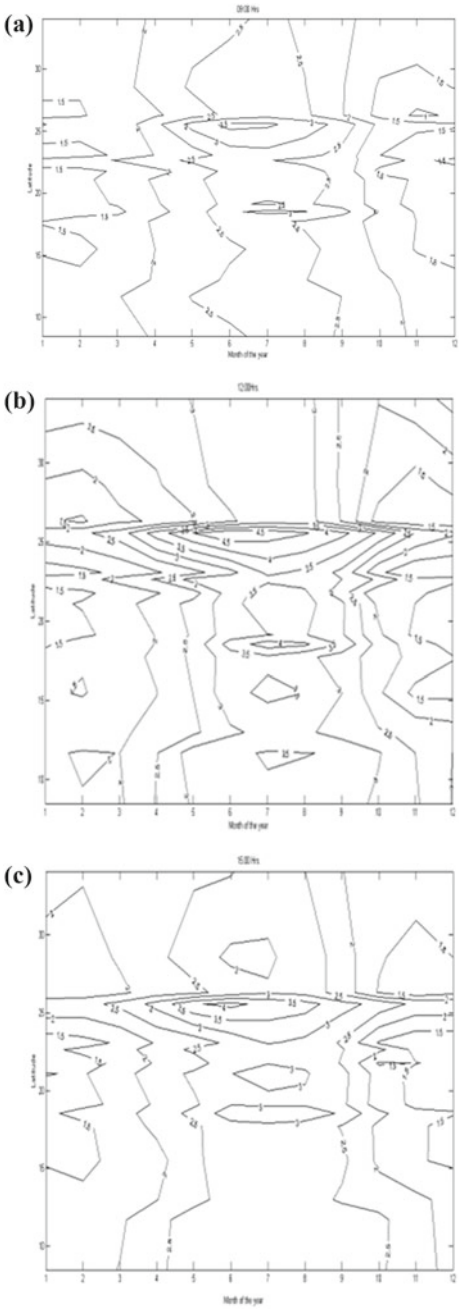

Fig. 6 Contour map of CI of diffuse solar radiation for Indian region at **a** 09.00 h (local mean time), **b** 12.00 h (local mean time) and **c** 15.00 h (local mean time)

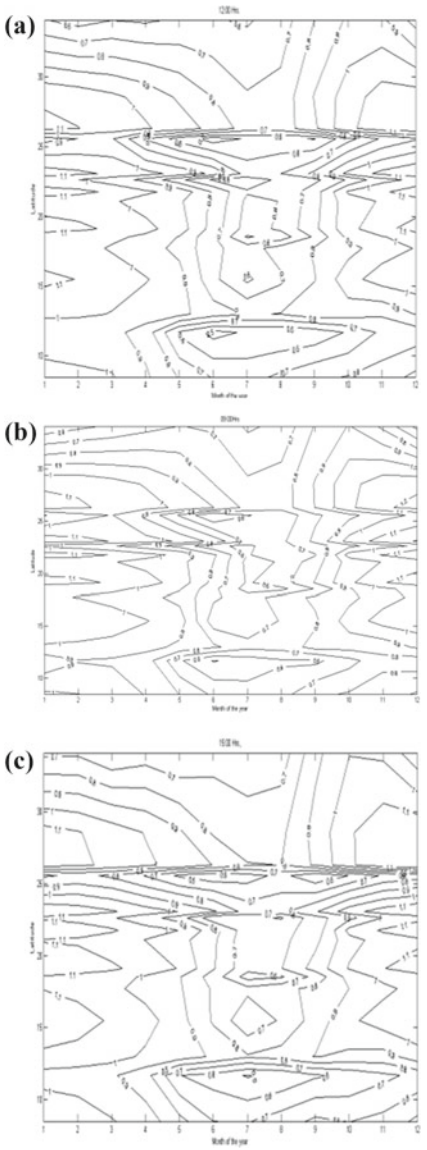

Fig. 7 Contour map of CI of global solar radiation for the Indian region at **a** 09.00 h (local mean time), **b** 12.00 h (local mean time) and **c** 15.00 h (local mean time)

estimation of CI at an arbitrary location involves errors in those regions where the contours are widely spaced.

4.2 Polynomial Representation of Clearness Index

Use of the contour map for the determination of clearness indices at an arbitrary location will involve the manual extrapolation between consecutive contours if the location does not fall on the contour. Alternatively, the extensive data set of clearness indices may be represented by polynomials where manual extrapolation will not be needed. In the following, we present the polynomial representation of clearness indices with multiple functional dependence on latitude, longitude, month of the year and time of the day.

4.2.1 Direct Solar Radiation

Variation of clearness index for direct solar radiation at 12:00 h (local mean time) with month of the year at different locations in the Indian zone is shown in Fig. 8. The mean curve through these variations is shown by the thick curve.

As a matter of fact, the atmospheric clearness index is an outcome of the time of the day, month of the year, longitude and latitude of location. In terms of Fig. 8, the value of CI at random location can be expressed as

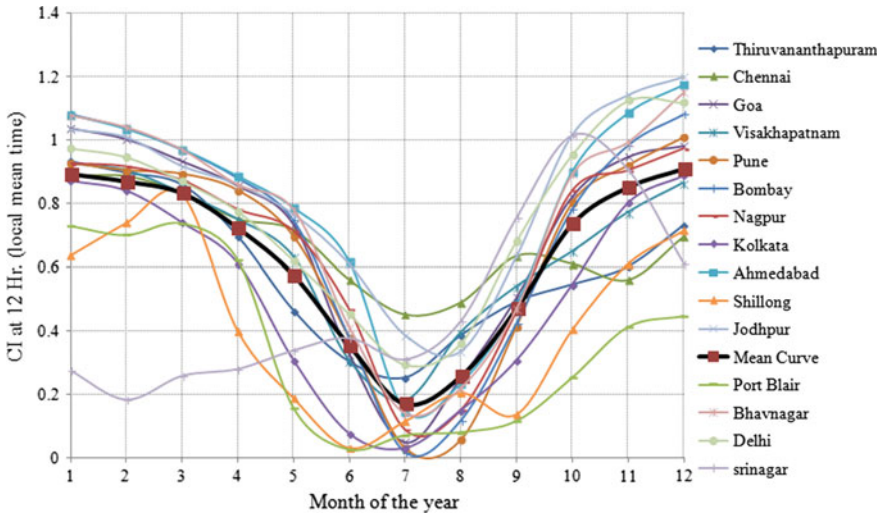

Fig. 8 Variation of clearness index for direct solar radiation at 12:00 h (local mean time) with month of the year at different locations in the Indian zone

$$\mathbf{CI}_{(m,L,\Phi,t)} = [\mathbf{CI}_{(m,\text{mean location},12)} + \textbf{longitudinal correction} + \textbf{Latitude correction}] \times \textbf{time correction} \quad (7)$$

where

m = month of the year
L = longitude of location
ϕ = latitude of location
t = local mean time

The above corrections can be expressed mathematically as follows

a. **longitudinal correction for direct solar radiation**

The variation of longitudinal correction as a function of longitude is obtained from the deviations of the curves of various stations from the mean curve Fig. 8. It can be mathematically expressed as follows

$$\Delta \mathrm{CI}_{(L,12)} = \left[\sum_{m=1}^{m=12} \mathrm{CI}_{(L,12)} - \mathrm{CI}_{(\text{mean},12)} \right] \times \frac{1}{12} \quad (8)$$

b. **Latitude correction for direct solar radiation**

The variation of the latitude correction can be mathematically expressed as

$$\Delta \mathrm{CI}_{(\phi,12)} = \left[\sum_{m=1}^{m=12} \mathrm{CI}_{(\phi,12)} - \mathrm{CI}_{(\text{mean},12)} \right] \times \frac{1}{12} \quad (9)$$

c. **Time correction for direct solar radiation**

Mathematically, it can be expressed as

$$\Delta \mathrm{CI}_{(t)} = \left[\sum_{1}^{n} \mathrm{CI}_{(t,\text{location})} \right] \times \frac{1}{n} \quad (10)$$

where

$$\Delta \mathrm{CI}_{(t,\text{location})} = \left[\sum_{1}^{12} \frac{\mathrm{CI}_{(m,t)}}{\mathrm{CI}_{(m,12)}} \right] \times \frac{1}{12} \quad (11)$$

Now, the above corrections may be expressed in the polynomial form as follows. The polynomial representation of the mean curve at 12:00 h (Fig. 8) is as follows

$$\mathrm{CI}_{(m,\text{mean location},12)} = \begin{bmatrix} 4.35737044642837 \times 10^{-5} m^6 - 1.90102878751719 \\ \times 10^{-3} m^5 + 3.11078143567024 \times 10^{-2} m^4 \\ - 2.35162560426871 \times 10^{-1} m^3 \\ + 8.28001469377956 \times 10^{-1} m^2 \\ - 1.30655439848619 \times m + 1.58509888400695 \end{bmatrix} \tag{12}$$

where m is the month of the year.

The graphical representation of longitudinal correction is shown in Fig. 9.

Its polynomial representation is as follows

$$\Delta\mathrm{CI}_{(L,12)} = \begin{bmatrix} - 2.29541922313475 \times 10^{-7} L^6 + 1.1149425230271 \times 10^{-4} L^5 \\ - 2.25094555605321 \times 10^{-2} L^4 \\ + 2.41756693290395 L^3 - 145.675789557959 L^2 \\ + 4669.16059344188 \times L - 62,186.0484190766 \end{bmatrix} \tag{13}$$

where L is the longitude of location.

Similarly, the variation of latitude correction as a function of latitude is obtained from Fig. 8 and is shown in Fig. 10.

Its polynomial representation is as follows

$$\Delta\mathrm{CI}_{(\phi,12)} = \begin{bmatrix} 3.43986477716442 \times 10^{-7} \phi^6 - 4.13911107358435 \times 10^{-5} \phi^5 \\ + 1.98575624686657 \times 10^{-3} \phi^4 - 4.84684580330475 \\ \times 10^{-2} \phi^3 + 6.32952035473224 \times 10^{-1} \phi^2 \\ - 4.17433341969507 \times \phi + 10.8166447274777 \end{bmatrix} \tag{14}$$

where ϕ is the latitude of location.

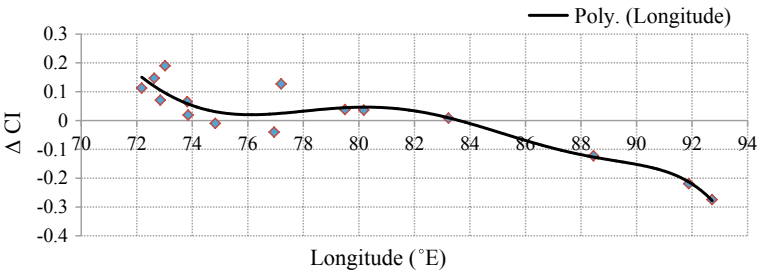

Fig. 9 Longitudinal correction for direct solar radiation

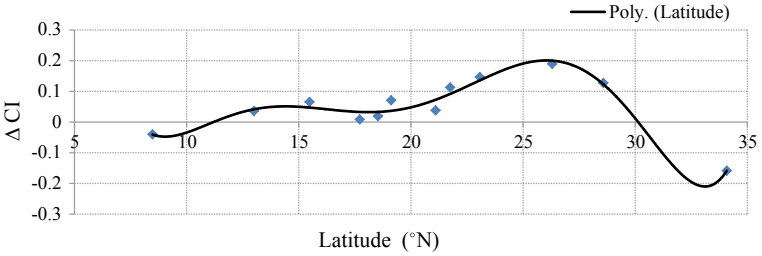

Fig. 10 Latitude correction for direct solar radiation

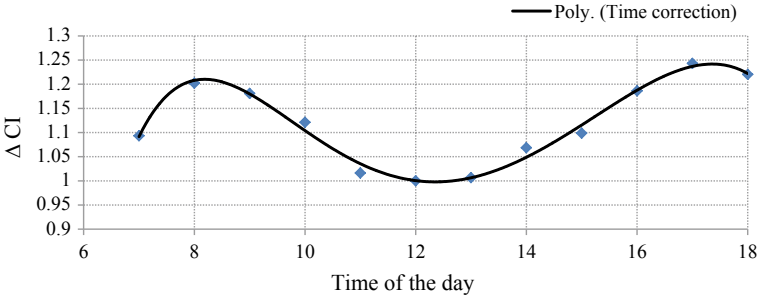

Fig. 11 Time correction for direct solar radiation

Similarly, the atmospheric clearness index values have been expressed as the ratio of atmospheric clearness index values of the corresponding 12:00 h value and the daily variation of the mean value of the ratio for all the months and location are drawn in Fig. 11 and its polynomial representation is given as follows

$$\Delta \mathrm{CI}_{(t)} = \left[\begin{array}{l} -4.16223256194392 \times 10^{-6} t^6 + 3.45593256942944 \times 10^{-4} t^5 \\ -1.22170111761604 \times 10^{-2} t^4 + 2.32627054561985 \times 10^{-1} t^3 \\ -2.47536199905327 t^2 + 13.7262494684557 t \\ -29.4762759933273 \end{array} \right] \tag{15}$$

where t is the time (local mean time).

Similarly, the polynomials for diffuse and global solar radiation can be obtained and are expressed as follows.

4.2.2 Diffuse Solar Radiation

The polynomial equations for diffuse solar radiation are as follows.

a. **Mean curve**

$$\mathrm{CI}_{(m,12)} = \begin{bmatrix} -5.26362808779268 \times 10^{-5} m^6 + 2.47553359451835 \times 10^{-3} m^5 \\ -4.18191249279678 \times 10^{-2} m^4 + 3.09264044423802 \times 10^{-1} m^3 \\ -9.91007654722956 \times 10^{-1} m^2 + 1.43922406022673 \times m \\ +1.00811892026567 \end{bmatrix} \tag{16}$$

where m is the month of the year.

b. **Longitudinal correction**

$$\Delta\mathrm{CI}_{(L,12)} = \begin{bmatrix} -4.11493492771461 \times 10^{-6} L^6 + 2.00764059291301 \times 10^{-3} L^5 \\ -4.07567285636087 \times 10^{-1} L^4 + 44.068689629996 L^3 \\ -2676.82246983027 L^2 + 86,608.6270631919 \\ \times L - 1,166,170.62652659 \end{bmatrix} \tag{17}$$

where L is the longitude of location.

c. **Latitude correction**

$$\Delta\mathrm{CI}_{(\phi,12)} = \begin{bmatrix} -1.69552706308384 \times 10^{-6} \phi^6 + 2.0920613134964 \times 10^{-4} \phi^5 \\ -1.03648813626344 \times 10^{-2} \phi^4 + 2.6329505422082 \times 10^{-1} \phi^3 \\ -3.60532366799459 \phi^2 + 25.0966245913471 \times \phi \\ -68.8545170154258 \end{bmatrix} \tag{18}$$

where ϕ is the latitude of location.

d. **Time correction**

$$\Delta\mathrm{CI}_{(t)} = \begin{bmatrix} 2.47930729361245 \times 10^{-5} t^6 - 1.85645541180723 \times 10^{-3} t^5 \\ +5.7009837367242 \times 10^{-2} t^4 - 9.18313440702574 \times 10^{-1} t^3 \\ +8.16274366104442 t^2 - 37.7826115282061 t \\ +71.560558883972 \end{bmatrix} \tag{19}$$

where t is the time (local mean time).

4.2.3 Global Solar Radiation

The polynomial equations for global solar radiation are s under

a. **Mean curve**

$$\mathrm{CI}_{(m,12)} = \begin{bmatrix} 2.02222089904502 \times 10^{-5} m^6 - 8.95954961285916 \times 10^{-4} m^5 \\ + 1.48234484849445 \times 10^{-2} m^4 - 1.12592270583947 \times 10^{-1} m^3 \\ + 3.95097192197459 \times 10^{-1} m^2 - 6.25021732141298 \times 10^{-1} m \\ + 1.35839796735731 \end{bmatrix} \tag{20}$$

where m is the month of the year.

b. **Longitudinal correction**

$$\Delta\mathrm{CI}_{(L,12)} = \begin{bmatrix} 2.125459904298 \times 10^{-7} L^6 - 1.04667878652755 \times 10^{-4} L^5 \\ + 2.14518311172014 \times 10^{-2} L^4 - 2.34227865877322 L^3 \\ + 143.707537331333 L^2 - 4697.66249351238 \times L \\ + 63{,}922.3125574916 \end{bmatrix} \tag{21}$$

where L is the longitude of location.

c. **Latitude correction**

$$\Delta\mathrm{CI}_{(\phi,12)} = \begin{bmatrix} 2.27081102399532 \times 10^{-7} \phi^6 - 2.73568732143344 \times 10^{-5} \phi^5 \\ + 1.31410790194013 \times 10^{-3} \phi^4 - 3.2117918945487 \times 10^{-2} \phi^3 \\ + 4.2005891299052 \times 10^{-1} \phi^2 - 2.77563403424049 \times \phi \\ + 7.22171312438999 \end{bmatrix} \tag{22}$$

where ϕ is the latitude of location.

d. **Time correction**

$$\Delta\mathrm{CI}_{(t)} = \begin{bmatrix} 2.98589162950336 \times 10^{-7} t^6 - 1.32560642849278 \times 10^{-5} t^5 \\ + 2.54326663242654 \times 10^{-5} t^4 + 7.619622082831413 \times 10^{-3} t^3 \\ - 1.5586852881935 \times 10^{-1} t^2 + 1.20472869699795 t \\ - 2.29796027988015 \end{bmatrix} \tag{23}$$

where t is the time (local mean time).

5 Expert System Approach

We now make an effort to widen the usability of the ANN estimation model for larger cross section of the users. This approach may be referred to as the expert system approach. It is basically a computational scheme that is envisioned to provide the general users the ability of an expert. For this purpose, we use the set of polynomial equations (Eqs. 12–23) to calculate atmospheric clearness indices corresponding to direct, diffuse and global solar radiation as a function of time of the day, month of the year, latitude and longitude of location which in turn can be used to calculate direct, diffuse and global solar radiations at an arbitrary location in a given month and at a given time of the day using the computational scheme illustrated in the flow chart (Fig. 12).

The input and output operation of the above scheme is accomplished through the graphical user interface (GUI) for the above-mentioned computational scheme is shown in Table 1. The graphical user interface has been developed with MS Office-Excel sheet and is designed to assist a wide spectrum of users such as energy planner, engineers, architects, scientists and researchers.

6 Validation of the Results

With a view to examine the compatibility of the predictions of the expert system approach, we have investigated the RMSE (%) values of the predictions for all the stations spread all over India. The mean values of RMSE (%) values of all 15 stations used in the analysis were calculated as 27.63, 14.87 and 18.58 for direct, diffuse and global solar radiations, respectively. These values are of the right order of magnitude in view of the prediction errors reported by earlier researchers, for example, 22.73% reported by NASA SSE data sets [28]. However, it was noticed that the RMSE (%) values of costal locations are relatively higher owing to intensive monsoon activities and their effect on observed data.

Furthermore, recently, some limited measurements for stations not used in the present analysis have been reported [27]. We have examined the compatibility of the results of the proposed expert system approach with these measurements. This is illustrated in Fig. 13 for a location Bangalore which has not been used in the analysis.

RMSE (%) values of the deviations of observations from the results obtained from the present expert system approach for several stations are shown in Table 2. The result exhibits good compatibility.

Table 1 Graphical user interface of the expert system approach

The Graphical User Interface

Enter the input data below

Name of location	New Delhi
Latitude of location	28.58
Longitude of location	77.2
Altitude in Km	0.216
Month of the year	1
Day of the year	17

SUN RISE (LMT) :	6.81	SUN SET (LMT) :	5.19

Results

Solar Radiation W/m^2			
L.M.T.	Direct	Diffuse	Global
1	0.00	0.00	0.00
2	0.00	0.00	0.00
3	0.00	0.00	0.00
4	0.00	0.00	0.00
5	0.00	0.00	0.00
6	0.00	0.00	0.00
7	22.42	1.40	1.98
8	353.21	46.23	84.33
9	658.83	95.63	246.61
10	801.96	131.59	406.02
11	832.35	154.15	522.28
12	824.80	164.18	582.85
13	813.00	164.72	584.46
14	799.21	157.09	526.88
15	758.44	139.11	413.05
16	631.23	106.06	254.69
17	364.45	51.09	89.55
18	25.40	1.41	2.18
19	0.00	0.00	0.00
20	0.00	0.00	0.00
21	0.00	0.00	0.00
22	0.00	0.00	0.00
23	0.00	0.00	0.00
24	0.00	0.00	0.00

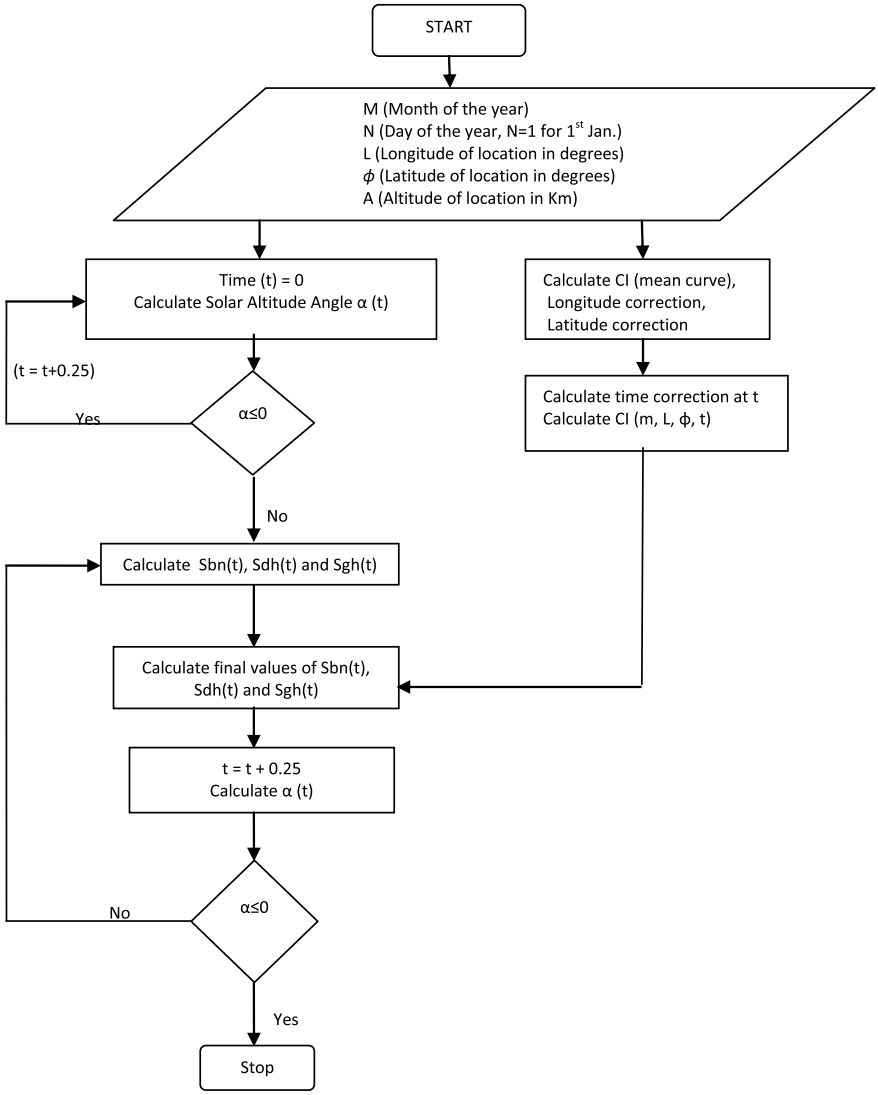

Fig. 12 Flow chart for the computational scheme using GUI

7 Summary and Conclusion

The estimation and prediction of direct, diffuse and global solar radiations are useful for a wide spectrum of users such as energy planner, engineers, architects, solar scientists and researchers. In this paper, a multi-frame output artificial-neural-network-based computational model for the estimation and prediction of solar radiation in

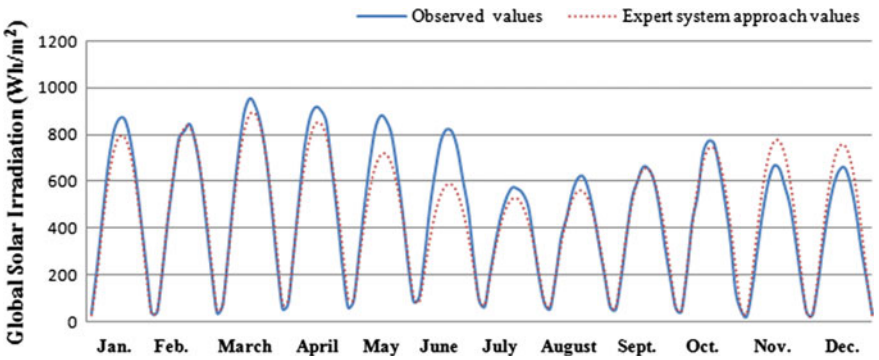

Fig. 13 Comparison of calculated (expert system approach) values with observed values of global solar irradiation for Bangalore

Table 2 RMSE (%) of the expert system approach prediction

Sr. No.	Name of the station	Latitude (°N)	Longitude (°E)	Height above mean sea level (km)	RMSE (%) of global solar radiation
1	Hyderabad	17.45	78.47	0.53	15.08
2	Jaipur	26.81	75.80	0.39	7.61
3	Bangalore	12.97	77.58	0.921	12.08
4	Varanasi	25.30	83.02	0.09	10.41
5	Ranchi	23.32	85.32	0.652	7.25
6	Bhopal	23.28	77.35	0.523	8.67

the Indian zone is developed. The analysis is based on the data of 15 stations spread over the entire Indian continent. The stations used in the analysis cover by far the widest range of latitude and longitude, used for solar radiation estimation in the Indian region. The results of ANN analysis are expressed by an explicit polynomial representation which in turn enables the estimation of atmospheric clearness index and hence solar radiation as a function of latitude and longitude of location, time of the day and month of the year. The computational scheme is embedded in a graphical user interface designed to be usable by a wider cross section of investigators. The computational results obtained from GUI exhibit good compatibility with earlier models and recent measurements carried out at arbitrary locations in the Indian region.

References

1. Mohandes M, Rehman S, Halawani TO (1998) Estimation of global solar radiation using artificial neural networks. Renew Energy 14(1–4):179–184
2. Alawi SM, Hinai HA (1998) An ANN-based approach for predicting global radiation in locations with no direct measurement instrumentation. Renew Energy 14:199–204
3. Mihalakakou G, Santamouris M, Asimakopoulos DN (2000) The total solar radiation time series simulation in Athens, using neural networks. Theoret Appl Climatol 66:185–197
4. Sfetsos A, Coonick AH (2000) Univariate and multivariate forecasting of hourly solar radiation with artificial intelligence techniques. Sol Energy 68(2):169–178
5. Dorvlo ASS, Jervase JA, Al-Lawati A (2002) Solar radiation estimation using artificial neural networks. Appl Energy 71:307–319
6. Reddy KS, Ranjan M (2003) Solar resource estimation using artificial neural networks and comparison with other correlation models. Energy Convers Manage 44:2519–2530
7. Sozen A, Arcaklioglu E, Ozalp M (2004) Estimation of solar potential in Turkey by artificial neural networks using meteorological and geographical data. Energy Convers Manage 45(18–19):3033–3052
8. Tymvios FS, Jacovides CP, Michaelides SC, Scouteli C (2005) Comparative study of Angstroms and artificial neural networks methodologies in estimating global solar radiation. Sol Energy 78:752–762
9. Shah A, Kaushik SC, Garg SN (2006) Computation of beam solar radiation at normal incidence using artificial neural network. Renew Energy 31(10):1483–1491
10. Krishnaiah T, Srinivasa Rao S, Madhumurthy K, Reddy KS (2007) Neural network approach for modelling global solar radiation. J Appl Sci Res 3(10):1105–1111
11. Lam JC, Kevin KW, Yang L (2008) Solar radiation modeling using ANNs for different climates in China. Energy Convers Manage 49(5):1080–1090
12. Mishra A, Kaushika ND, Zhang G, Zhou J (2008) Artificial neural network model for the estimation of direct solar radiation in the Indian zone. Int J Sustain Energy 27(3):95–103
13. Fadare D (2009) Modeling of solar energy potential in Nigeria using an artificial neural network model. Appl Energy 86:1410–1422
14. Shah A, Kaushik SC, Garg SN (2009) Assessment of diffuse solar energy under general sky condition using artificial neural network. Appl Energy 86:554–564
15. Tang W, Yang K, He J, Qin J (2010) Quality control and estimation of global solar radiation in China. Sol Energy 84(3):466–475
16. Paoli C, Voyant C, Muselli M, Nivet ML (2010) Forecasting of preprocessed daily solar radiation time series using neural networks. Sol Energy 84:2146–2160
17. Sahin M, Kaya Y, Uyar M (2012) Comparison of ANN and MLR models for estimating solar radiation in Turkey using NOAA/ AVHRR data. Adv Space Res 51:891–904
18. Khatib T, Mohamed A, Mahmoud M, Sopian K (2012) Estimating global solar energy using multilayer perception artificial neural network. Int J Energy 6(1):25–33
19. Tomar RK, Kaushika ND, Kaushik SC (2012) Artificial neural network based computational model for the prediction of direct solar radiation in Indian zone. J Renew Sustain Energy 4:063146
20. Kaushika ND, Tomar RK, Kaushik SC (2014) Artificial neural network model based on Interrelationship of direct, diffuse and global solar radiations. Sol Energy 103:327–342
21. Hottel HC (1976) A sample model for estimating the transmittance of direct solar radiation through clear atmosphere. Sol Energy 18:129
22. Duffie JA, Beckman WA (1991) Solar engineering of thermal processes. Wiley, New York
23. Liu BYH, Jordan RC (1960) The interrelationship and characteristics distribution of direct, diffuse and total solar radiation. Sol Energy 4:1–19
24. Haykin S (1998) Neural networks: a comprehensive foundation. Macmillan College Publishing Co., New York
25. Zurada JM (1992) Introduction to artificial neural systems. West, St. Paul

26. Mani A (1981) Handbook of solar radiation data for India. Allied, New Delhi
27. Tyagi AP (2009) Solar radiant energy over India. India Meteorological Department, Ministry of Earth Sciences, New Delhi
28. See portal http://eosweb.larc.nasa.gov/sse/ for NASA SSE